Space Programs Summary 37-44, Vol. III

The Deep Space Network

For the Period January 1 to February 28, 1967

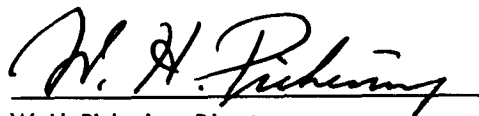*SPACE PROGRAMS SUMMARY 37-44, VOL. III*

Preface

The Space Programs Summary is a six-volume bimonthly publication designed to report on JPL space exploration programs and related supporting research and advanced development projects. The titles of all volumes of the Space Programs Summary are:

Vol. I.   *The Lunar Program* (Confidential)

Vol. II. *The Planetary–Interplanetary Program* (Confidential)

Vol. III. *The Deep Space Network* (Unclassified)

Vol. IV. *Supporting Research and Advanced Development* (Unclassified)

Vol. V.   *Supporting Research and Advanced Development* (Confidential)

Vol. VI. *Space Exploration Programs and Space Sciences* (Unclassified)

The Space Programs Summary, Vol. VI, consists of: an unclassified digest of appropriate material from Vols. I, II, and III; an original presentation of the JPL quality assurance and reliability efforts, and the environmental- and dynamic-testing facility-development activities; and a reprint of the space science instrumentation studies of Vols. I and II.

Approved by:

W. H. Pickering, *Director*

Jet Propulsion Laboratory

Contents

Contents (contd)

I. Introduction

The Deep Space Network (DSN), established by the NASA Office of Tracking and Data Acquisition, is under the system management and technical direction of JPL. The DSN is responsible for two-way communications with unmanned spacecraft traveling from approximately 10,000 miles from Earth to interplanetary distances. Tracking and data-handling equipment is provided to support these missions. Present facilities permit simultaneous control of a newly launched spacecraft and a second one already in flight. In preparation for the increased number of U.S. activities in space, a capability is being developed for simultaneous control of either two newly launched spacecraft plus two in flight, or four spacecraft in flight. Advanced communications techniques are being implemented to make possible obtaining data from, and tracking spacecraft to, planets as far out in space as Jupiter.

The DSN is distinct from other NASA networks such as the Space Tracking and Data Acquisition Network (STADAN), which tracks Earth-orbiting scientific and communication satellites, and the Manned Space Flight Network (MSFN), which tracks the manned spacecraft of the *Gemini* and *Apollo* programs.

The DSN supports, or has supported, the following NASA space exploration projects: (1) *Ranger, Surveyor, Mariner,* and *Voyager* Projects of JPL; (2) *Lunar Orbiter* Project of the Langley Research Center; (3) *Pioneer* Project of the Ames Research Center; and (4) *Apollo* Project of the Manned Spacecraft Center (as backup to the Manned Space Flight Network). The main elements of the network are: the Deep Space Instrumentation Facility (DSIF), with space communications and tracking stations located around the world; the Ground Communications System (GCS), which provides communications between all elements of the DSN; and the JPL Space Flight Operations Facility (SFOF), the command and control center.

The DSIF tracking stations are situated such that three stations may be selected approximately 120 deg apart in

longitude in order that a spacecraft in or near the ecliptic plane is always within the field of view of at least one of the selected ground antennas. The DSIF stations are:

Deep Space Communication Complex (DSCC)	Deep Space Station (DSS)	DSS serial designation
Goldstone	Pioneer	11
	Echo	12
	Venus	13
	Mars	14
Canberra	Woomera	41
	Tidbinbilla	42
	Booroomba*	43
	Johannesburg	51
Madrid	Robledo	61
	Cebreros	62
	Rio Cofio*	63
	Cape Kennedy (Spacecraft Monitoring)	71
	Ascension Island (Spacecraft Guidance and Command)	72
*Station not yet authorized.		

JPL operates the U.S. stations and the Ascension Island Station. The overseas stations are normally staffed and operated by government agencies of the respective countries, with assistance of U.S. support personnel.

The Cape Kennedy Station supports spacecraft final checkout prior to launch, verifies compatibility between the DSN and the flight spacecraft, measures spacecraft frequencies during countdown, and provides telemetry reception from lift-off to local horizon. The other DSIF stations obtain angular position, velocity (doppler), and distance (range) data for the spacecraft, and provide command control to (up-link), and data reception from (down-link), the spacecraft. Large antennas, low noise phase-lock receiving systems, and high-power transmitters are utilized. The 85-ft-diameter antennas have gains of 53 db at 2300 MHz, with a system temperature of 55°K, making possible the receipt of significant data rates at distances as far as the planet Mars. To improve the data rate and distance capability, a 210-ft-diameter antenna has been built at DSS 14, and two additional an-

tennas of this size are planned for installation at overseas stations.

In their present configuration, all stations with the exception of Johannesburg are full S-band. The Johannesburg receiver has the capability for L- to S-band conversion.

It is the policy of the DSN to continuously conduct research and development of new components and systems and to engineer them into the network to maintain a state-of-the-art capability. Therefore, the Goldstone stations are also used for extensive investigation of space tracking and telecommunications techniques, establishment of DSIF–spacecraft compatibility, and development of new DSIF hardware and software. New DSIF system equipment is installed and tested at the Goldstone DSCC before being accepted for system-wide integration into the DSIF. After acceptance for general use, it is classed as Goldstone Duplicate Standard (GSDS) equipment, thus standardizing the design and operation of identical items throughout the system.

The GCS consists of voice, teletype, and high-speed data circuits provided by the NASA Communications Network (NASCOM) between each overseas station, the Cape Kennedy Station, and the SFOF. Voice, teletype, high-speed data, and video circuits between the SFOF and the Goldstone stations are provided by a DSN microwave link. NASCOM is a global network consisting of more than 100,000 route miles and 450,000 circuit miles interconnecting 89 stations, 34 of which are overseas in 18 foreign countries. It is entirely operationally oriented and comprises those circuits, terminals, and switching equipments interconnecting tracking and data acquisition stations with, for example, mission control, project control, and computing centers. Circuits used exclusively for administrative purposes are not included.

The SFOF at JPL controls the DSN operation during the support of a spacecraft and also performs spacecraft commands, data processing, and data analysis. The SFOF utilizes operations control consoles, status and operations displays, computers, and data-processing equipment for the analysis of spacecraft performance and space science experiments. Spacecraft control is accomplished by generating trajectories and orbits, as well as command and control data, from tracking and telemetry data received from the DSIF in near-real time. The SFOF also reduces the DSIF-recorded data to information for use by scientific experimenters and spacecraft engineers.

N67- 25062

II. Tracking and Navigational Accuracy Analysis

A. DSN Inherent Accuracy Project, T. W. Hamilton and D. W. Trask

The DSN Inherent Accuracy Project was formally established by the DSN Executive Committee in July 1965. The objectives of the Project are:

(1) Determination (and verification) of the inherent accuracy of the DSN as a radio navigation instrument for lunar and planetary missions.

(2) Formulation of designs and plans for refining this accuracy to its practical limits.

Achievement of these goals is the joint responsibility of the Telecommunications Division (33) and the Systems Division (31) of JPL. To this end, regular monthly meetings are held to coordinate and initiate relevant activities. The Project leader and his assistant (from Divisions 31 and 33, respectively) report to the DSN Executive Committee, and are authorized to task Project members to (1) conduct analyses of proposed experiments, (2) prepare reports on current work, and (3) write descriptions of proposed experiments. The Project is further authorized to deal directly with those flight projects using the DSN regarding data-gathering procedures that bear on inherent accuracy.

The various data types and tracking modes provided by the DSIF in support of lunar and planetary missions are discussed in SPS 37-39, Vol. III, pp. 6–8. Technical work directly related to the Inherent Accuracy Project is presented in SPS 37-38, Vol. III, and in subsequent issues, and is continued in the following sections of this volume.

In this issue the results of the first DSN use of distance space probe tracking for station location determination are described. This self-calibration method is considered an experiment directed toward determining the feasibility of the eventual replacement of usual survey methods. Also included is a technical description of the proposed doppler–ranging calibration experiment to be performed on *Lunar Orbiter* spacecraft. This experiment, which is the first to be formally identified by the Inherent Accuracy Project, involves use of both Mark IA and Mark II ranging systems, and will test the feasibility of extremely precise calibration of doppler and range tracking data. That is, the doppler and range measurements will be combined in such a way that charged particle effects can be detected and removed.

Numerous other problems are anticipated, such as calibration stability of the ground and spacecraft systems,

dynamic tracking errors, and the subtle effects of procedures upon system performance at the 1-m level.

B. Critical Parameters in Determining the Navigational Accuracy for a Deep Space Probe During the Planetary Encounter Phase,
T. W. Hamilton, D. C. Grimes, and D. W. Trask

1. Introduction

The level of navigational accuracy obtainable during the planetary encounter phase is a critical question for most interplanetary missions because of the need for (1) precise scan platform pointing, (2) insertion into orbit about the target body, or (3) the avoidance of biological contamination of the target.

In this article an approximate method for determining the navigational accuracy obtainable during the encounter phase of a planetary mission is presented, and the parameters that limit this accuracy are discussed. Numerical examples are given comparing the results from this approximate approach with those of a sophisticated orbit determination (OD) computer program. The methods agree within 2.3% for the two typical trajectories selected as representative of those being considered for the 1969 Mars opportunity by the *Mariner* Project (*Mariner* Mars 1969). The approximate method, however, does break down when the declination of the target planet near encounter is small.

When Earth-based tracking data are used for space-craft navigation, several factors combine to provide information for orbit determination. The information content of the data is produced principally by parallax effects.[1] The "position parallax" includes such factors as barycenter motion, position change of the tracking stations, and the changing Earth-probe geometry due to gravitational effects. The so-called "velocity parallax" arises from the velocities of the tracking stations. For a probe with a reasonably large geocentric declination, velocity parallax contributes the greatest amount of information (and is treated exclusively in SPS 37-39, Vol. III, pp. 18–23), but for low declinations, the other factors become relatively more significant because the velocity parallax no longer provides adequate information.

---

[1] J. Light, "An Investigation of the Orbit Redetermination Process Following the First Midcourse Maneuver," Space Programs Summary 37-33, Vol. IV, pp. 8–17.

The navigational accuracy obtainable depends on the quality of the tracking data, the sophistication of the software employed to process these tracking data, and the degree to which the probe is free of attitude-control-system gas leakages and similar annoying characteristics. Also, the operational needs of the project are an important consideration. For example, must a given navigational accuracy be obtained before the presence of the target planet has a chance to influence the tracking data significantly?

The numerical examples use tracking data from five days before encounter $(E-5^d)$ to $E-1^d$. Under these conditions the accuracy is limited by uncertainties in the locations of the tracking stations and by the "effective" quality of the tracking data. The concept of "effective" tracking data quality includes the degradation introduced by the incompleteness of the model of the "real universe" built into the software. Ephemeris errors are considered and a method is presented to account for the additional information provided by the influence of the target body on the probe.

This article ties together the results of several past Space Programs Summary articles to predict the range of capability that may be expected in the 1969 time period. Of particular interest is the improved performance expected from the orbit determination program now under development over the one presently in use. The ability to determine and adequately represent tracking station locations even to the anticipated 1.5- to 3-m level is seen to be a basic limitation to navigational accuracy.

2. Tracking Patterns and A Priori Statistics

The encounter phase for this study was assumed to start at five days before encounter $(E-5^d)$. This time was chosen to allow for a "final" midcourse correction maneuver relatively close to the target planet as well as for the reasons stated below. The probe is tracked from two deep space stations, DSS 11 (Pioneer, Goldstone) and DSS 51 (Johannesburg), which obtained two-way doppler (f_2) beginning at $E-5^d$ and ending at $E-1^d$.

At the start of the encounter phase during a planetary mission, the "claimed" knowledge of the probe coordinates with respect to Earth is relaxed. This has the effect of "freeing" the orbit determination process from an accumulation of errors that build up during the cruise phase because of deviations between the software "fitter's universe" and the real universe. As the probe trajectory becomes sufficiently perturbed by the gravitational effect

of the target body, the information content of the doppler data accurately determines several parameters of the spacecraft orbit with respect to the target body. The relaxation of the probe coordinates at an epoch near encounter allows a trajectory discontinuity such that the spacecraft can be moved in the inexact "fitter's universe" to match the observations better as the probe nears the target body. As the tracking data quality increases, less of a tie is needed with the previous information. At the same time, the doppler data are still sensitive to model errors (such as Earth–Sun–target ephemeris errors). The effect of these model errors will be introduced into the encounter phase orbit and will increase in importance as the length of the data arc and the quality of the tracking data increase. For these reasons, this study essentially discards previous probe position $(\tilde{\sigma}_x, \tilde{\sigma}_y, \tilde{\sigma}_z)$ and velocity $(\tilde{\sigma}_{\dot{x}}, \tilde{\sigma}_{\dot{y}}, \tilde{\sigma}_{\dot{z}})$ information at $E-5^d$ by starting the OD process with the following a priori values:

$$\tilde{\sigma}_x = \tilde{\sigma}_y = \tilde{\sigma}_z = 1000 \text{ km}$$

$$\tilde{\sigma}_{\dot{x}} = \tilde{\sigma}_{\dot{y}} = \tilde{\sigma}_{\dot{z}} = 1 \text{ km/sec}$$

3. Principal Study Parameters

a. Tracking data quality. The quality of the tracking data and the uncertainty in the tracking station locations are the two controlling parameters for planetary encounter orbit determination capability (for reasonable declination angles as discussed on page 7). In the case of tracking data quality, an effective data weight is assigned which is a measure not only of the noise on the raw data but also of the degradation introduced by the software that processes these data. The numbers used in this article refer to the data weight $\sigma_{f_2(eff)}$ that must be applied to f_2 so that the noise on data points taken at 1-min intervals can be considered uncorrelated.[2]

---

[2]The general form for the effective data-weighting sigma is

$$\sigma_{f_2(eff)} = \left[\sum_{i=1}^{n} \sigma_i^2 \max\left(1, \frac{T_{l_i}}{T_s}\right) \right]^{1/2}$$

where

σ_i is the standard deviation of the ith error source

T_{l_i} is the correlation width of the ith error source

T_s is the sample spacing of data points (60 sec for this article)

$$\max\left(1, \frac{T_{l_i}}{T_s}\right) = \begin{cases} 1, & \dfrac{T_{l_i}}{T_s} \leq 1 \\[2ex] \dfrac{T_{l_i}}{T_s}, & \dfrac{T_{l_i}}{T_s} > 1 \end{cases}$$

For the current JPL single precision orbit determination program (SPODP), degradation results from a limited precision in the computation of probe acceleration near the target. Studies for Mariner Mars 1964 (Mariner IV) have shown this effect to be approximately 5 mm/sec (SPS 37-41, Vol. III, pp. 12–18). This problem increases with small probe-target planet and/or large Earth-probe distances. These parameters are compared in Table 1 for Mariner Venus 1962 (Mariner II), Mariner IV, a typical Mariner Venus 67 trajectory, plus two nominal trajectories for Mariner Mars 1969. The Earth–Mars distance for Mariner Mars 1969 is less than half that for Mariner IV (although still greater than that for Mariner Venus 67), but the Mars-probe distance at encounter is considerably less than that for any of the previous missions. These considerations are expected to limit the SPODP effective data quality to 3 to 6 mm/sec for the Mariner Mars 1969 examples considered here.

Also related to this problem is the fact that model inadequacies limit the length of data arc that can be handled without increasing $\sigma_{f_2(eff)}$. As an example, during the cruise phase of Mariner IV, systematic f_2 residuals appear as the data arc increases so that when one month

Table 1. Trajectory characteristics

Parameter	Mariner II (actual)	Mariner IV (actual)	Mariner Venus 67 (typical)	Mariner Mars 1969 (A) (typical)	Mariner Mars 1969 (B) (typical)
Target	Venus	Mars	Venus	Mars	Mars
Launch date	8/28/62	11/28/64	6/17/67	4/1/69	3/8/69
Encounter date	12/14/62	7/15/65	10/19/67	8/10/69	8/1/69
B, km	50874	15251	25000	7000	6700
R_{CA}, km	40500	13200	8300	6200	5900
$R_{\oplus}$ at E, km × 10⁶	57.8	216.3	79.7	103.4	96.6
δ at E-20ᵈ, deg	−7.8	+1.1	+8.4	−24.3	−24.3
δ at E-10ᵈ, deg	−10.5	−1.1	+7.7	−24.6	−24.4
δ at E, deg	−13.5	−3.3	+6.0	−25.0	−24.5

B = distance from center of target body perpendicular to incoming asymptote
R_{CA} = radius of closest approach
$R_\oplus$ = geocentric radius to probe
E = time of encounter
δ = geocentric declination of probe

of data is in the fit the systematic residual has an amplitude of 0.7 mm/sec and an "apparent" correlation width of 300 min:

$$\sigma_i \sqrt{\frac{T_1}{1 \text{ min}}} = 10 \text{ mm/sec}$$

This is probably caused by miscellaneous forces (attitude-control system, variations in solar pressure constant, and/or effective reflecting area). The effect of these on the data fit grows as the square of the data time span; this accounts for the relatively short data span chosen for this study.

Because of its more sophisticated model and more efficient estimator, the JPL double precision orbit determination program (DPODP) now under development[3] will be able to use longer data arcs profitably. Although no operational experience has been obtained on the DPODP, it is designed with the SPODP's limitations in mind and will not be a major contributor to $\sigma_{f_2(eff)}$ for a data arc this short. The noise on the raw data, however, may limit $\sigma_{f_2(eff)}$ to 1 to 3 mm/sec. The lower bound assumes that the charged particle (space plasma and ionosphere) effects (SPS 37-41, Vol. III, pp. 3–11) are directly calibrated by using the ranging system (group velocity effect) in conjunction with the counted doppler system (phase velocity effect), while the upper bound (3 mm/sec) assumes a simple model of the effect of charged particles in the ionosphere but no correction for the space plasma. Although it is assumed that the ranging system is used to calibrate out the effects of charged particles, the encounter accuracies quoted here do not use ranging data directly as tracking data.

From the analysis presented in SPS 37-39, Vol. III, pp. 18–23, it is possible to compute the uncertainty in the declination direction due to data noise alone. Using this method for trajectory A (Table 1) and range-rate data ($\sigma\dot{\rho} = 3$ mm/sec) from $E-5^d$ to $E-1^d$, the uncertainty predicted is 36 km, whereas the SPODP computation yields 53 km. For this case, the agreement is to 32%.

There are two major discrepancies between the formulation given in SPS 37-32, Vol. III, and that contained in the SPODP. The former assumes symmetric passes of data and constant data weighing across the pass; the SPODP, however, allows for asymmetric passes and

---

[3]T. D. Moyer, "Theoretical Basis for the Double Precision Orbit Determination Program," Space Programs Summary 37-38, Vol. III, pp. 24–26, and subsequent issues of Vol. III.

assigns less significance to data points taken at low elevations. In obtaining the above comparison, these discrepancies were taken into account. Notice that the SPODP value must be used for the $\sigma_{r_s} = 0$ case to achieve the 2.3% accuracy illustrated in Table 2.

b. Tracking station location uncertainties. Uncertainties in the distance of a tracking station from the Earth's spin axis ($\sigma_{r_s} \sim$ m), and sometimes in the station's longitude ($\sigma_\lambda \sim$ m), can be critical with respect to encounter orbit determination accuracies. The uncertainty in the tracking station coordinate parallel to the Earth's spin axis is of no consequence. An error in r_s displaces the predicted probe position in the direction of declination δ, while an error in λ moves it in the direction of the right ascension α, both of which are normal to the Earth-probe direction (SPS 37-39, Vol. III).

Substantial postflight analysis has been performed on each deep space mission of consequence (*Ranger, Mariner, Surveyor*) tracked by the deep space stations (DSS). For the case of the *Ranger* Block III mission (*Rangers VI–IX*), these individual determinations generally fall within 20 m of the mean for r_s and 25 m of the mean for λ (SPS 37-43, Vol. III, pp. 3–18). Although these variations are due in part to noise on the raw tracking data, the main contribution lies in discrepancies between the "SPODP universe" and the real universe. The SPODP makes no provision for modeling the small nongravitational forces that can produce quite significant errors for planetary missions. The wandering of the pole and refraction due to charged particles (ionosphere and space plasma), which are not modeled in the SPODP, affect both r_s and λ to several meters, as do imperfections in the ephemerides. In addition, a 5-msec error in determining DSS times (typical during *Ranger* flights) will shift λ by 2 m.

In particular, the relatively large variations in r_s and λ that occur among the *Ranger* solutions are caused primarily by "known" errors in the lunar ephemeris and failure to account for ionospheric (charged particle) refraction. A corrected "experimental" ephemeris tape is now in use, and work is progressing toward determining the necessary ionospheric corrections. Significantly, the charged particle effects are six times greater for the L-band system used during the *Ranger* missions than for the S-band system used on subsequent missions. (The effect varies inversely as the square of the carrier frequency.)

Even if it is not used in the *Mariner* Mars 1969 operations, the DPODP will be running in a research mode

---

before that mission. The more sophisticated model (including pole wandering and effects of charged particles) of the DPODP, the results of ephemeris improvement work (lunar and planetary) now under way, and the improved time synchronization and control policies slated for the DSS will allow r_s and λ solutions to approximately 1 m during postflight analysis.

This will be accomplished not only by minimizing the contribution of the above-mentioned error sources, but also by the analysis and combination of results from several missions. For example, tracking data from the extended *Lunar Orbiter* missions are extremely attractive for determining DSS locations; i.e., absolute longitudes, which are relatively poorly determined from cruise tracking data, can be well defined because of the continuous direct tie between the probe and the Moon. In addition, because of the variations that occur throughout the lunar month the results are less susceptible to undetected systematic errors. (The *Ranger* series all occurred during the third quarter of the lunar month.) In general, the longitude difference between stations is determined better than the absolute longitude of either station. Therefore, it is not necessary that this postflight analysis concentrate on the deep space station to be used during the encounter phase of a mission whose navigational accuracy requirements demand precise knowledge of the DSS coordinates.

Information on pole wandering and on the relationship between the U.S. Bureau of Standards broadcast time reference, Universal Time Coordinated (UTC), and the best estimate of universal time, Universal Time One (UT1), is available one week[4] to one year after the fact (depending upon the accuracy desired). These effects will probably be extrapolated from two to four months ahead for the encounter phase of the *Mariner* Mars 1969 mission. Therefore, operationally, σ_{r_s} and σ_{λ} ~1.5 to 3 m for the DPODP. The SPODP, however, will suffer because of its more limited model of the universe, so that σ_{r_s} and σ_{λ} ~ 5 to 10 m for encounter operational use.

An error in the knowledge of a station's distance off the spin axis r_s produces an error in the calculation of the probe's geocentric declination, which is given by

$$\Delta k_\delta = R_\oplus \, (\cot \delta) \left(\frac{\Delta r_s}{r_s} \right)$$

where

Δk_δ is the error in the direction of declination, km

$R_\oplus$ is the geocentric distance to the probe, km

δ is the geocentric declination of the probe

It should be noted that Δk_δ becomes large as δ approaches zero. In such cases, information must be gathered from other sources, as discussed earlier. Similarly, a longitude error leads to an error in the knowledge of the right ascension of the probe:

$$\Delta k_\alpha = R_\oplus \, (\cos \delta) \left(\frac{\Delta \lambda}{r_s} \right)$$

where

Δk_α is the error in the direction of the right ascension α, km

$\Delta \lambda$ is expressed in meters

Although σ_{r_s} and σ_λ will be of comparable size by 1969, σ_{r_s} will be the more important contributor for the *Mariner* Mars 1969 trajectories considered, because

$$\frac{\Delta b_\delta}{\Delta r_s} = 39 \text{ km/m}$$

while

$$\frac{\Delta b_\alpha}{\Delta \lambda} = 16 \text{ km/m}$$

b_δ = projection on the B-plane[5] of the error due to Δr_s, km

b_α = projection of the error due to $\Delta \lambda$, km

The B-plane concept is used here to facilitate comparison with the SPODP, where the output is presented in terms of the B-plane coordinates and uncertainties.

c. Total error due to data noise and station location uncertainty. Fig. 1 depicts the total errors due to data noise and station location uncertainties for the *Mariner* Mars 1969 trajectories before the target planet's influence

---

[4]The U.S. Naval Observatory issues a weekly time bulletin. The best estimate of UT1–UTC is one week old, while the last data point used in extrapolating the polar motion is taken 45 to 90 days before receipt of this weekly bulletin.

[5]If **S** is the probe velocity vector on the incoming asymptote and **T** is a vector in the ecliptic plane perpendicular to **S**, then **R** = **S** × **T**. The B-plane is that plane perpendicular to **S** that contains the vector **B** from the center of mass of the target body perpendicular to **S**.
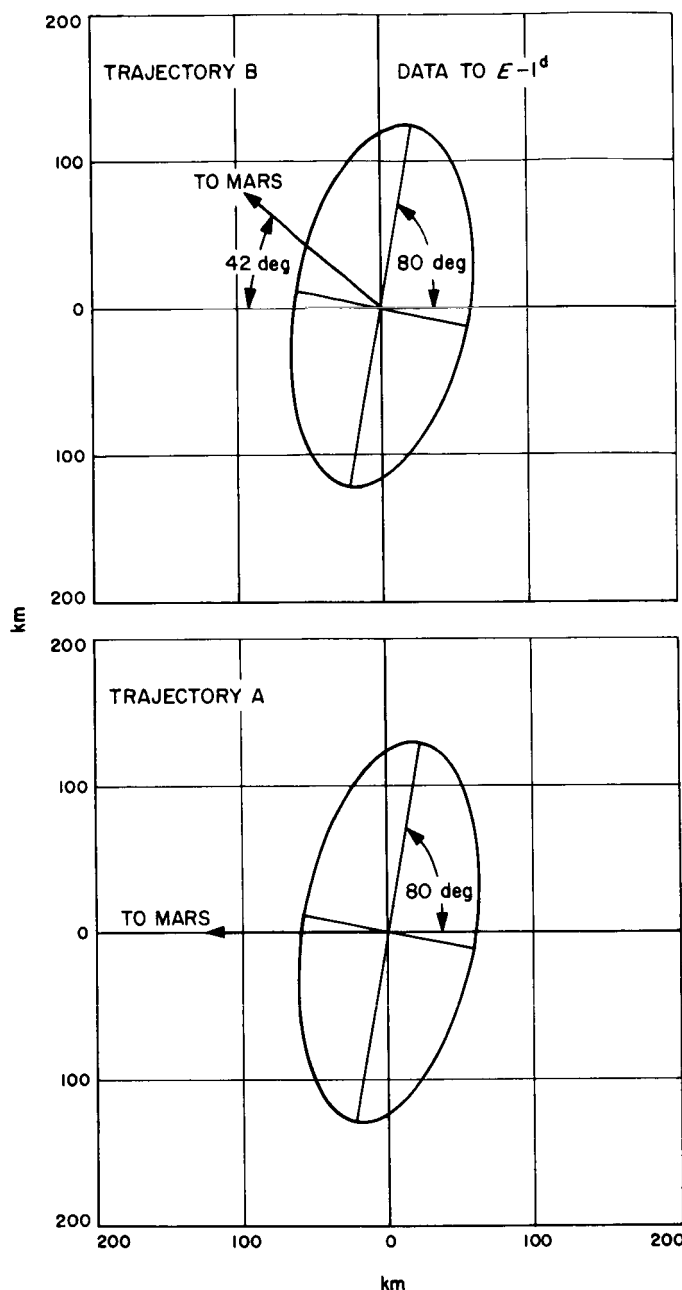
Fig. 1. B-plane errors due to data noise and station location uncertainties

becomes a significant factor. The uncertainty ellipsoids for these trajectories are almost identical, since the geocentric declinations, the Earth-probe distances, and the data spans are very nearly the same.[6] These results were

---

[6]If the declinations and encounter geometries were identical, one would expect the uncertainties for trajectory A to be 1.07 times those for trajectory B, because of the greater Earth-probe distance for trajectory A.

obtained using the upper limits for DPODP ($\sigma_{f_2} = 3$ mm/sec, $\sigma_{r_s} = \sigma_\lambda = 3$ m) and tracking data from $E-5^d$ to $E-1^d$.

Neglecting ephemeris errors, the uncertainty at the target (in the B-plane), with data to $E-1^d$, is approximately the square root of the sums of the squares of the data noise error and the declination contribution. The strength of this method is easily seen by referring to Table 2. The uncertainties obtained in this manner all lie within 2.3% of the actual uncertainties as computed by the SPODP. In light of the complexity of the SPODP, such agreement is quite phenomenal. Thus it should be possible in the future to predict encounter accuracies in many cases without resorting to an expensive computer program such as the SPODP.

Table 2. Errors due to data noise and station location uncertainty

σ_{r_s}, m	$\dfrac{\Delta SMAA}{\Delta r_s}\sigma_{r_s}$, km	$SMAA_{\hat\rho}$, km	$\sqrt{\Sigma k^2}$, km	SMAA (SPODP), km	$\Delta SMAA$, km
0	0	52.87	52.87	52.87	0
1.58	60.75	52.87	80.53	80.25	0.28
2.81	108.04	52.87	120.28	121.33	−1.05
4.02	154.57	52.87	163.36	166.18	−2.82
5.26	202.25	52.87	209.06	213.33	−4.27
6.48	249.16	52.87	254.71	260.71	−6.00

$\dfrac{\Delta SMAA}{\Delta r_s}\sigma_{r_s} =$ contribution to semimajor axis due to uncertainty in r_s

$SMAA$ (SPODP) = uncertainty computed by SPODP

$SMAA_{\hat\rho} =$ data noise contribution; i.e., SMAA(SPODP) for $\sigma_{r_s} = 0$

$$\sqrt{\Sigma k^2} = \left[\left(\frac{\Delta SMAA}{\Delta r_s}\sigma_{r_s}\right)^2 + (SMAA_{\hat\rho})^2\right]^{1/2}$$

$\Delta SMAA =$ difference between the simplified estimate and the actual computed uncertainty $= \sqrt{\Sigma k^2} - SMAA(SPODP)$

The agreement is again illustrated in Fig. 2 for trajectory A. In this figure the straight line represents the error due to station location uncertainties, indicating a lower bound for attainable orbit determination accuracies, while the curves result from inclusion of the appropriate levels of effective data noise. $SMAA$ is the semimajor axis of the 1-σ dispersion ellipse in the B-plane.

This figure also presents the expected ranges of performance of the SPODP and the DPODP. As mentioned, the SPODP performance is bounded by station location
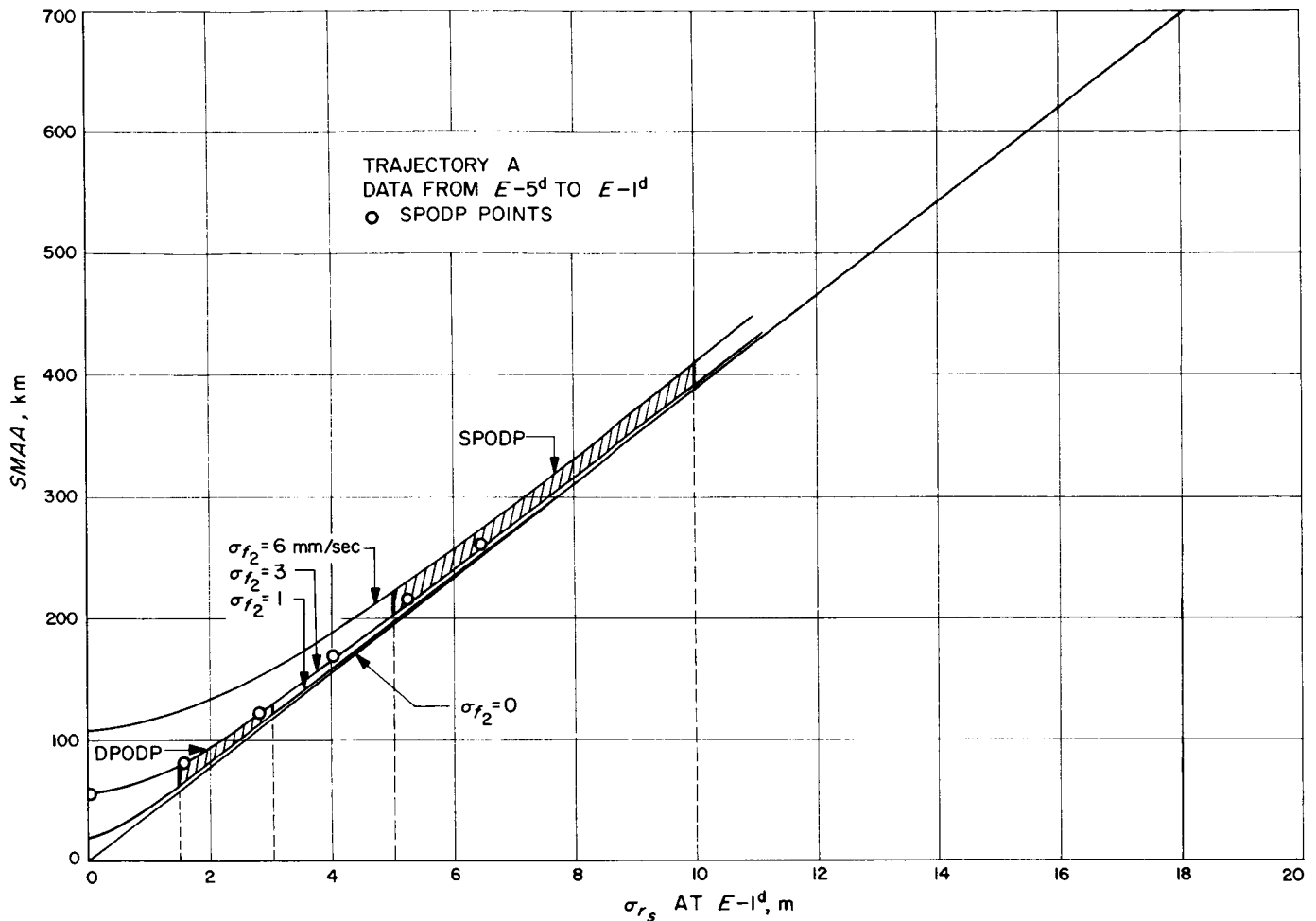
Fig. 2. SMAA versus σ_{r_s}

uncertainties of 5 to 10 m and data noise levels of 3 to 6 mm/sec. The corresponding DPODP figures are 1.5 to 3 m in station locations and 1 to 3 mm/sec in data noise.

d. Effect of ephemeris errors. The JPL Ephemeris Development Project estimates that, prior to the *Mariner Mars 1969* mission, the Martian ephemeris errors will project onto the B-plane as illustrated in Fig. 3. The major axis of the dispersion ellipse lies along the velocity vector of Mars with respect to the Sun. The resulting B-plane uncertainties are 118 km in a direction 1.5 deg below **T** and 40 km perpendicular to this for trajectory A, with 125 km and 40 km the corresponding values for trajectory B. If the SPODP were used, these ephemeris errors would be small relative to the contributions from data noise and station location uncertainties.

Since the DPODP is not yet available, it is not possible at this time to provide an *exact* evaluation of the DPODP

ephemeris estimation capability. However, it is possible to approximate the DPODP operational situation by first adding the ephemeris error ellipsoid to that obtained from data noise and station location uncertainties before entering the target planet's sphere of influence, and then assuming that the near-target tracking provides an accurate orbit with respect to the planet in the direction of the probe-target vector. This produces a reasonable approximation to the accuracy to be expected in the θ direction (perpendicular to **B**).

If Γ_T is the total covariance matrix, Γ_0 the contribution due to data noise and station locations, Γ_E the ephemeris covariance, and Γ_g a dispersion having an infinite component along the θ direction and a very small component in the probe-target direction, then

$$\Gamma_T = [(\Gamma_0 + \Gamma_E)^{-1} + \Gamma_g^{-1}]^{-1}$$
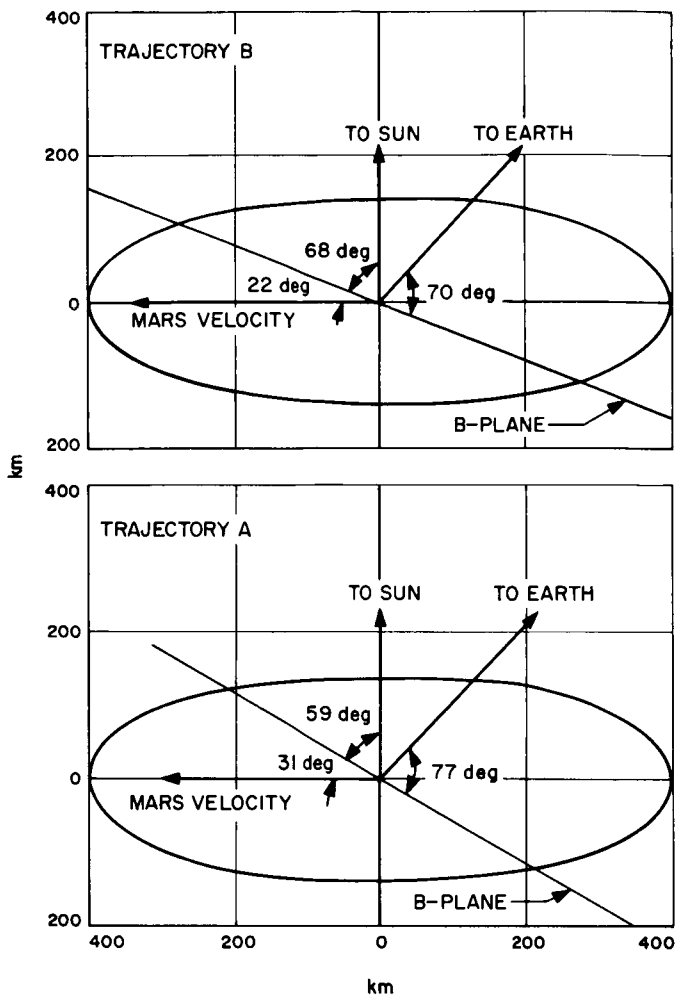
Fig. 3. Mars ephemeris errors (3 σ)

Fig. 4. Encounter orbit determination effects

A geometric interpretation of this procedure is presented in Fig. 4. The above equation is valid only for the θ direction; i.e., the Γ_g assumptions are an artifice to approximate the effect of near-target tracking. Again, these results are obtained for the DPODP "worst case."

Using this approach for the 1969 sample trajectories leads to the following results:

$$\sigma_\theta(A) = 120\,\text{km}$$

$$\sigma_\theta(B) = 150\,\text{km}$$

If Fig. 2 is consulted and the above procedure continued, the performance ranges for the SPODP and DPODP, respectively, are found to be

$$\sigma_\theta = 200\text{ to }405\,\text{km}$$

$$\sigma_\theta = 61\text{ to }150\,\text{km}$$

4. Summary

For the encounter phase of a planetary mission, a simple method may be used to predict the navigational accuracy

before the probe enters the target planet's sphere of influence. It has been shown that this procedure yields results that agree remarkably well with the values computed by the SPODP. This demonstrates that data noise and station location uncertainty are the important contributors to encounter uncertainty.

To attain the extremely high accuracies necessary for future planetary missions, station location solutions on the order of 1 to 3 m are required. This area, therefore, is the target of a concentrated effort expected to produce absolute DSS locations to better than 1 m in the r_s and λ coordinates.

C. *Ranger* Combined Analysis, Part II: Determination of the Masses of the Earth and Moon From Radio Tracking Data, C. J. Vegos and D. W. Trask

1. Introduction

This report is the second in a series presenting the combined results of information obtained through the processing of radio tracking data from the four *Ranger* Block III (*Ranger VI–IX*) lunar missions. In Part II the $GM_\oplus$ and $GM_{\mathcal{C}}$ are discussed,[7] while Part I (SPS 37-43, Vol. III, pp. 3–18) presents the determination of the tracking station locations. Both the tracking station locations and the GM determinations are natural by-products from the postflight analysis of the Ranger tracking data and result, in fact, from the same computer runs. These determinations are published separately to emphasize the details peculiar to these two groups of parameters.

This article reviews the method of statistically combining the radio tracking data information from the four individual flights, compares the $GM_\oplus$ and $GM_{\mathcal{C}}$ results with those of other investigators, presents the tracking data residuals for each mission that result when the combined parameters are used, and discusses the limitations to this analysis. In the case of $GM_\oplus$ and $GM_{\mathcal{C}}$ the inaccuracy of the Earth–Moon ephemeris is the limiting factor.

---

[7] $GM_\oplus$ and $GM_{\mathcal{C}}$ are the universal gravitational constant times the mass of the Earth and Moon, respectively. For convenience, they are expressed in units of km³/sec² (and are also loosely referred to as masses). The actual unit of length is the light meter (i.e., the distance the electromagnetic signal travels in a unit time is the basic unit of length in the "radio tracking world"). Throughout the analysis, lengths (in meters) depend on the adopted value of $c = 299792.5$ km/sec.
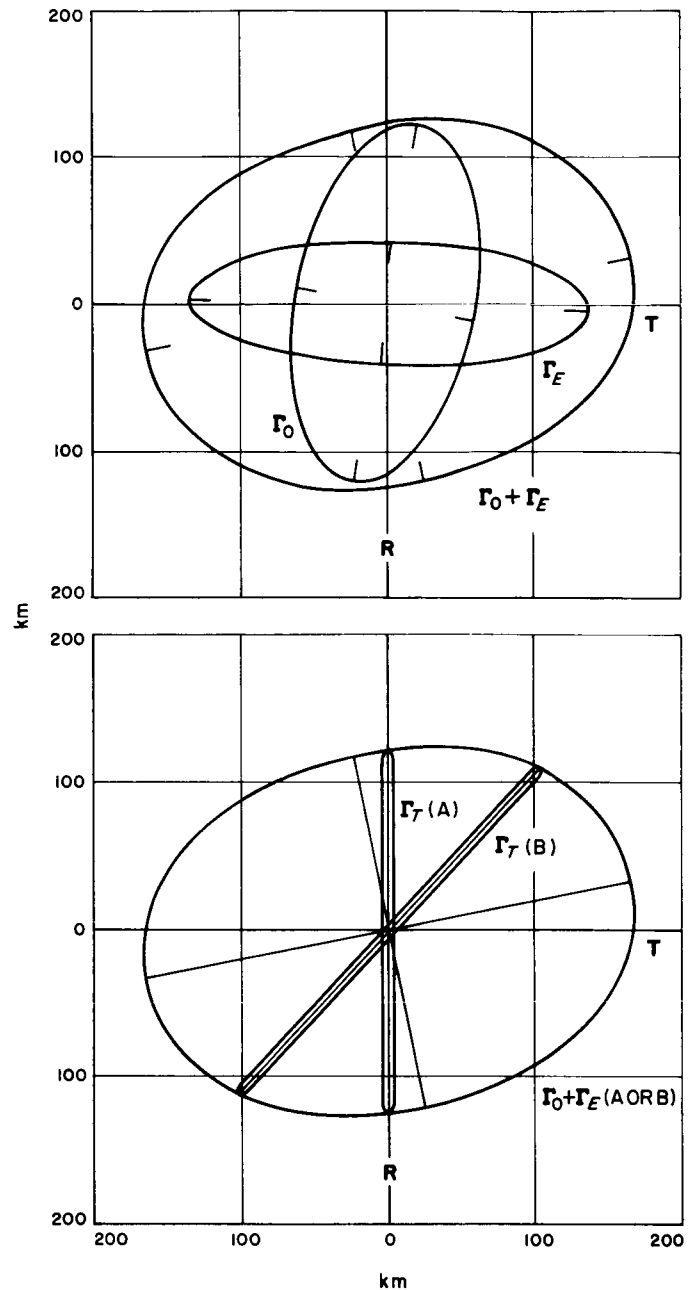
The combined *Ranger* analysis produces

$$GM_\oplus = 378601.2 \pm 0.7 \text{ km}^3/\text{sec}^2$$

$$GM_{\mathcal{C}} = 4902.6 \pm 0.1 \text{ km}^3/\text{sec}^2$$

where the uncertainties[8] for the Earth and Moon have been adjusted upward from 0.37 and 0.07 km³/sec², respectively, as discussed in Section 3. Not only do these results compare favorably with the individual *Ranger III–IX* solutions, but in the case of the Earth–Moon mass ratio[9] μ^{-1}, the combined *Ranger* value, as well as the values from the *Mariner II* (Venus) and *Mariner IV* (Mars) missions, falls within the spread of previous determinations from optical observations. However, the *Mariner* values of μ^{-1} are 2 to 3 σ lower than the combined *Ranger* μ^{-1}.

2. Discussion

The results presented here were obtained using tracking data from the *Ranger* Block III missions. All four flights were tracked continuously from injection to impact on the lunar surface by use of three deep space stations: DSS 12 (Echo, Goldstone, California), DSS 41 (Woomera, Australia), and DSS 51 (Johannesburg, South Africa). Only two-way doppler was used during the postflight analysis because the information content of the angle data also obtained during the mission is completely overshadowed by that provided by the two-way doppler. A summary of the data used and the analysis performed for the *Ranger* missions is contained in Ref. 1, and a detailed description of the immediate postflight analysis for the individual *Ranger* Block III missions is given in Refs. 2–5. Although tracking data are available from such missions as *Rangers III–V, Mariner II* (Venus), and *Mariner IV* (Mars), they are not included in this analysis.

Successful combination of the radio tracking results from several missions depends on a thorough postflight analysis of the tracking data from each mission. It is extremely important to detect and reject (or appropriately take into account) and *nonstandard* tracking data. Such data may be due to anomalistic performance of the tracking stations or even of the spacecraft itself (attitude-control-system leakage, spacecraft tumbling, etc.). In addition, for a mission to be a logical candidate for

---

[8] Uncertainties are quoted in this report as 1-σ values.

[9] $$\mu^{-1} = \frac{GM_\oplus}{GM_{\mathcal{C}}}$$

inclusion in a combined analysis, its results must be competitive in quality with the other missions or must add information of a different nature than that provided by the other missions.

Taking the above reasoning into account, the *Ranger* Block III missions were selected for the combined analysis. This selection of a subset of four missions from all the available candidates was made not only to limit the size of the extensive data analysis task but also because of the extent of the tracking coverage (launch to lunar impact for all four of the missions), the improvement in the tracking data quality over previous missions, and the adequacy of the software to accomplish the job.[10]

To statistically combine the *Ranger* Block III missions the covariance matrices and the solution vectors of the individual flights are used as follows:[11] the variations in the two-way doppler z_i associated with the ith experiment are given by

$$\delta z_i = \mathbf{A}_i \, \delta q_i + \mathbf{B}_i \, \delta a$$

where

z_i = doppler data from the ith probe where $i =$ *Rangers VI–IX*

q_i = parameters unique to each mission; i.e., position and velocity vector for Earth probe plus the Earth–Moon ephemeris scale factor

a = parameters common to all the missions; i.e., DSS locations, mass of the Earth, mass of the Moon, and the effect of solar pressure

$\mathbf{A}_i = \dfrac{\partial z_i}{\partial q_i}$

$\mathbf{B}_i = \dfrac{\partial z_i}{\partial a}$

$\delta(\ ) =$ variation in $(\ )$

---

[10] Single precision software and a limited ability to model forces on the spacecraft due to solar pressure and the attitude control system are more limiting factors for the analysis of planetary missions.

[11] This method is described by J. D. Anderson in JPL Interoffice Technical Memorandum 312-284, *Average of Least Squares Parameter Estimates Over Several Experiments*, March 12, 1963.

The normal matrix $\mathbf{J}$ that results from the least-square formulation of the orbit-determination program is used in the following partitioned form:

$$\mathbf{J}_i = \left(\begin{array}{c|c} \mathbf{L}_i & \mathbf{X}_i \\ \hline \mathbf{X}_i^T & \mathbf{K}_i \end{array} \right) = \left(\begin{array}{c|c} \mathbf{A}_i^T \mathbf{W}_i \mathbf{A}_i & \mathbf{A}_i^T \mathbf{W}_i \mathbf{B}_i \\ \hline \mathbf{B}_i^T \mathbf{W}_i \mathbf{A}_i & \mathbf{B}_i^T \mathbf{W}_i \mathbf{B}_i \end{array} \right) \tag{2}$$

where $\mathbf{J}_i$ is obtained from each mission and $\mathbf{W}_i$ is the weighting matrix for the doppler data. Next designate the least-squares estimates of the parameters for the ith experiment by $\tilde{q}_i$ and $\tilde{a}_i$ and form differences between the $\tilde{a}_i$ and some standard value of a (e.g., $a = \tilde{a}_1$), where

$$\delta \tilde{a}_i = \tilde{a}_i - a \tag{3}$$

Finally, for each experiment, form the matrix

$$\mathbf{M}_i = \mathbf{K}_i - \mathbf{X}_i^T \mathbf{L}_i^{-1} \mathbf{X}_i \tag{4}$$

where, of course, $\mathbf{J}_i$ must be nonsingular.

Then the least-squares estimate a^* of a over all of the data $z_1, z_2, \cdots, z_n$ is given by

$$a^* = a + \delta a^* \tag{5}$$

where

$$\delta a^* = \left(\sum_{i=1}^{n} \mathbf{M}_i \right)^{-1} \sum_{i=1}^{n} \mathbf{M}_i \, \delta \tilde{a}_i \tag{6}$$

The covariance matrix of δa^* is given by

$$\left(\sum_{i=1}^{n} \mathbf{M}_i \right)^{-1}$$

The above procedure was programmed (by P. Muller of JPL Section 312) to accept the standard double precision $\mathbf{J}$ matrix punched output of the JPL single precision orbit determination program (SPODP)[12] described in Refs. 6 and 7.

Notice that the Earth–Moon ephemeris scale factor *REM* was computed as an independent parameter in

---

[12] Although SPODP is a single precision program, it accumulates the normal matrix in double precision.

all the calculations of this analysis. In reality, *REM* is related to the Earth and Moon gravitational constants. The constraint equation for *REM* is

$$REM = k(GM_\oplus + GM_\mathbb{C})^{1/3}$$

where

$$k = 86.315745 \text{ (described below)}[13]$$

The *REM* value obtained from the above equation, using $GM_\oplus$ and $GM_\mathbb{C}$ values computed from the combined *Rangers*, is 6378.3106 km.

It should be noted that although $GM_\oplus$ and $GM_\mathbb{C}$ are included as common parameters in the combined solutions, *REM* is not. That is, the constraint that matches the calculated period of the Moon with the observed period (see above equation) was not applied because the statistics associated with the *REM* are competitive with the quality of the lunar ephemeris which is determined independently. Therefore, *REM* is left unconstrained to compensate for the ephemeris errors.

The results of the physical constants $GM_\oplus$ and $GM_\mathbb{C}$ obtained from the *Ranger* and *Mariner* postflight analysis and the combined *Ranger VI*, *VII*, *VIII*, and *IX* values are shown in Tables 3 and 4. The combined *Ranger* value for $GM_\oplus$ is 389601.22 ±0.37 km³/sec², which is clustered among the other values obtained from individual flight analysis, and is comparable to but lower than the value of $GM_\oplus$ = 398603.2 ±4.0 adopted by the ad hoc NASA Standards Committee (Ref. 9) and the value of $GM_\oplus$ = 398603 adopted by resolution at the 21st International Astronomical Union (IAU) Symposium (Paris, May 1963), as reported in Ref. 10. The $GM_\mathbb{C}$ results for the various missions are also given in Table 4. For the combined analysis, $GM_\mathbb{C}$ = 4902.63 ±0.07 km³/sec². Notice that although *Ranger* results are 2 to 3 σ from the *Mariner* values, there is still relatively close agreement in light of

---

[13] $k = F_2 [\sin \pi_\mathbb{C}] n_\mathbb{C}^{-2/3}$ and is a constant depending on the ephemeris used. The ephemeris used for this analysis (Ephemeris Tape E9537) is based on the constants given in Ref. 8.

F_2 = 0.999093142 ↪ a constant that relates the perturbed mean distance of the Moon to the semimajor axis as calculated from Kepler's law.

$n_\mathbb{C}$ = 2.661699489 × 10⁻⁶ rad/sec ↪ sidereal mean motion of the Moon (1900).

$\sin \pi_\mathbb{C}$ = 3422."54 ↪ sine parallax for the Moon.

Table 3. $GM_\oplus$ solutions from *Ranger* and *Mariner* postflight analysis

Mission	Value, km³/sec²	Standard deviation, km³/sec²	Remarks
Nominal	398603.20	4.0	Adopted by the ad hoc NASA Standard Constant Committee (Ref. 9)
Ranger III	398601.63	2.5	Data, 4 days ⎫
Ranger IV	398601.87	13.3	Data, 8 hr ⎬ Ref. 1
Ranger V	398599.20	13.2	Data, 8 hr ⎭
Ranger VI	398600.69	1.13	Data, 65 hr
Ranger VII	398601.34	1.55	Data, 68 hr
Ranger VIII	398601.14	0.72	Data, 65 hr
Ranger IX	398601.42	0.60	Data, 65 hr Vegos[a]
Combined Rangers	398601.22	0.37	Combined estimate of Rangers VI, VII, VIII, IX
Mariner IV	398601.83	1.4	Data, 7 days Ref. 12

[a] Vegos, C. J., *Combining of Ranger Block III Data for Determination of DSS Locations and Physical Constants*, Technical Memorandum 312-779, Jet Propulsion Laboratory, Pasadena, Calif., January 13, 1967.

Table 4. $GM_\mathbb{C}$ solutions from *Ranger* and *Mariner* postflight analysis

Mission[a]	Value, km³/sec²	Standard deviation, km³/sec²	Remarks
Ranger VI	4902.66	0.19	To impact
Ranger VII	4902.54	0.17	To impact
Ranger VIII	4902.63	0.12	To impact
Ranger IX	4902.71	0.30	To impact, last 10 min before impact
Combined Rangers	4902.63	0.07	Combined estimate of Rangers VI, VII, VIII, IX Vegos[c]
Mariner II[b]	4902.84	0.07	Ref. 11, 2½ mo of data
Mariner IV	4902.76	0.10	6 mo of cruise data

[a] The Ranger III, IV, and V missions did not produce significant $GM_\mathbb{C}$ solutions [$\sigma_{GM_\mathbb{C}}$ > 4 km³/sec²]. Rangers IV and V had only near-Earth two-way doppler coverage, while the closest approach of Ranger III to the Moon was 35,000 km with relatively poor tracking coverage compared with the Ranger Block III missions.

[b] Based on $GM_\oplus$ = 398601.27 km³/sec².

[c] Vegos, C. J., *Combining of Ranger Block III Data for Determination of DSS Locations and Physical Constants*, Technical Memorandum 312-779, Jet Propulsion Laboratory, Pasadena, Calif., January 13, 1967.
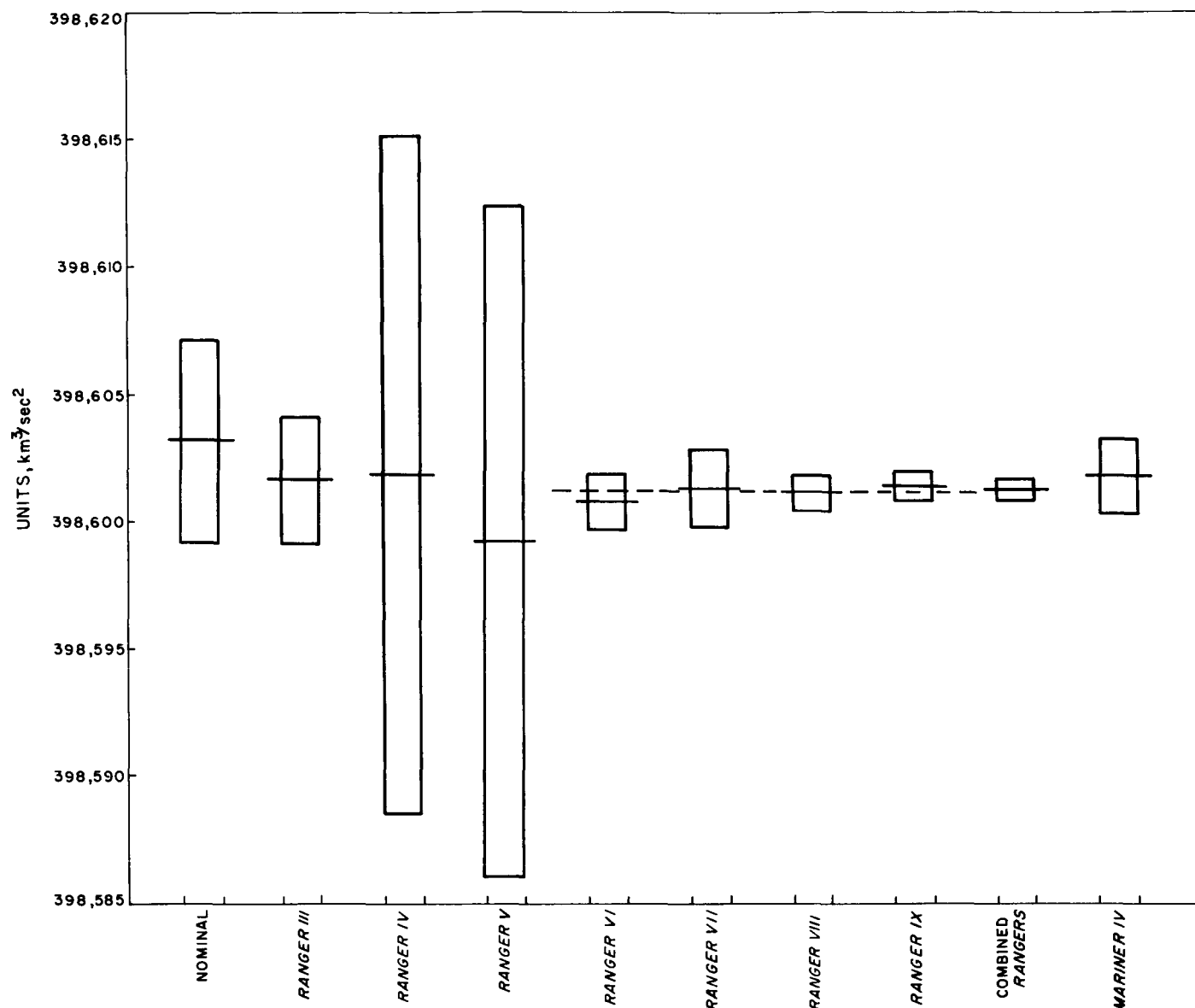
Fig. 5. Earth gravitational constant

the spread of the Earth–Moon mass ratios obtained by other investigators (as discussed in the following paragraph). This is significant because the *Mariner* results are obtained by the 28-day periodic effect of the Earth–Moon system on the cruise phase data (Refs. 11 and 12), while the strength of the *Ranger* missions $GM_{\mathbb{C}}$ solution came from the last few hours of tracking data, where the direct effect of the lunar potential is present. Figs. 5 and 6 show the results from each mission for $GM_{\oplus}$ and $GM_{\mathbb{C}}$, with their associated uncertainties.

The Earth–Moon mass ratio values $(\mu^{-1} = GM_{\oplus}/GM_{\mathbb{C}})$ obtained from the *Ranger* and *Mariner* missions, as well as the inferred results from optical determinations, are presented in Table 5. For the combined analysis, $\mu^{-1} = 81.3035 \pm 0.0012$. The optical values are derived from determinations of the lunar inequality L, which is the coefficient of the periodic displacement of an object at a distance of one astronomical unit in the plane of the Moon's orbit caused by the motion of the Earth's center about the center of mass of the Earth–Moon

14
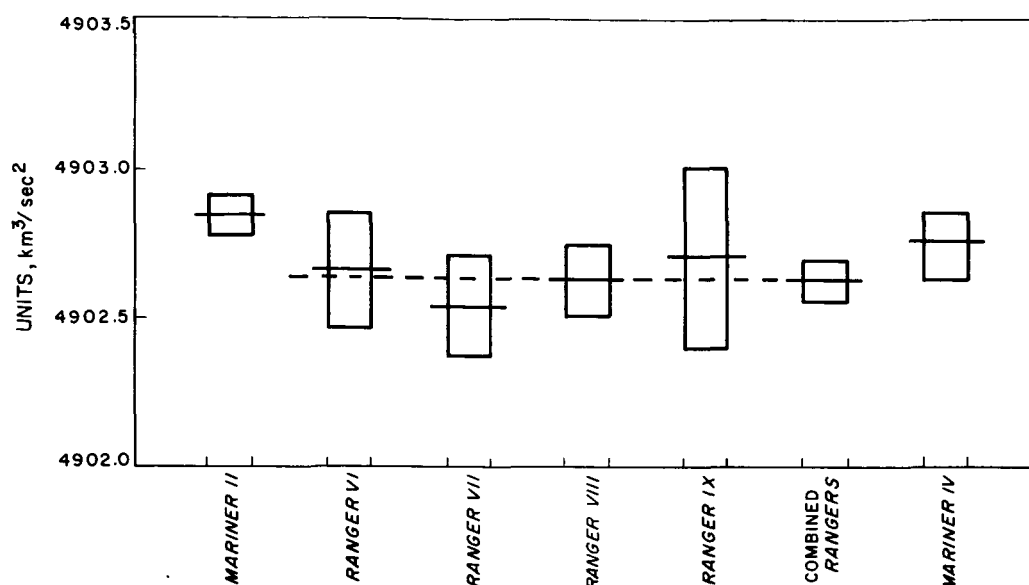
Fig. 6. Moon gravitational constant

Table 5. Earth–Moon mass ratio $GM_\oplus/GM_\mathbb{C}$

Source	Value	Standard deviation	Remarks		Source	Value	Standard deviation	Remarks
Ranger VI	81.3030	0.0023			Hinks	81.4213		(1900-1901) EROS[a]
Ranger VII	81.3051	0.0029			Morgan & Scott	81.1721		Sun[a]
Ranger VIII	81.3035	0.0018			Jones & Jeffreys	81.3278		(1930-1931) EROS[a]
Ranger IX	81.3023	0.0043			Spencer Jones	81.3125	0.021	(1941) EROS[b]
Combined *Rangers VI, VII, VIII, IX*	81.3035	0.0012			Delano	81.2639	0.027	(1950) Right ascension of EROS[b]
Mariner II	81.3001	0.0013			Delano	81.2614	0.030	From delineations of EROS[b]
Mariner IV	81.3015	0.0016						

[a] Ref. 13.
[b] Ref. 14.

system. The relationship among L and other astronomical quantities (Ref. 10, p. 102) is given as [14]

$$L = \frac{\mu}{1+\mu} \frac{a_\mathbb{C}}{A} \ (206262.81 \text{ arc sec/rad})$$

---

[14] The authors are indebted to J. D. Anderson for his assistance in researching and interpreting the results from optical tracking.

where

L is given in seconds of arc

A = astronomical unit, for this analysis $A = 149597546$ km (Ref. 11)

$a_\mathbb{C} = 384400.2$ km = the mean distance between the centers of the Earth and the Moon (Ref. 11)

Assuming that L is determined to five significant digits, μ^{-1} can also be calculated to five significant digits because

$a_{\mathbb{C}}$ and A are both known to a higher precision; i.e.,

$$\mu^{-1} = \frac{1}{L} \frac{a_{\mathbb{C}}}{A} \, 206262.81 \, -1$$

The optical values quoted in this report were computed from the values of L given in Refs. 13 and 14, using the above equation. These inferred optical values vary from 81.172 to 81.421. It is interesting to note that if the optical values presented in this report were averaged, the mean value would be 81.293. Fig. 7 shows the Earth–Moon mass ratio mean values and their associated uncer-

tainties obtained from the radio and optical data. At the 21st IAU Symposium (Ref. 10) the value $\mu^{-1} = 81.30$ was adopted on the basis of provisional *Mariner II* results.

3. Limitations

This section discusses those limitations to the analysis that affect the Earth and lunar mass solutions, presents the two-way doppler residuals (observed minus computed values) based on the solution parameters that result from the combined analysis, discusses the role of *REM*, and interprets the uncertainties that should be associated with the mass solutions from this analysis.

Fig. 7. Earth–Moon mass ratio

On the chart:

ON VCO

$12^h 13^m 38^s$ GMT, COMPLETION OF MIDCOURSE MOTOR BURN

3.12 mm/sec

ON VCO

DSS 12 — DSS 41 — DSS 12 — DS

MARCH 23, 1965

TWO-WAY DOPPLER RESIDUALS, cps

17
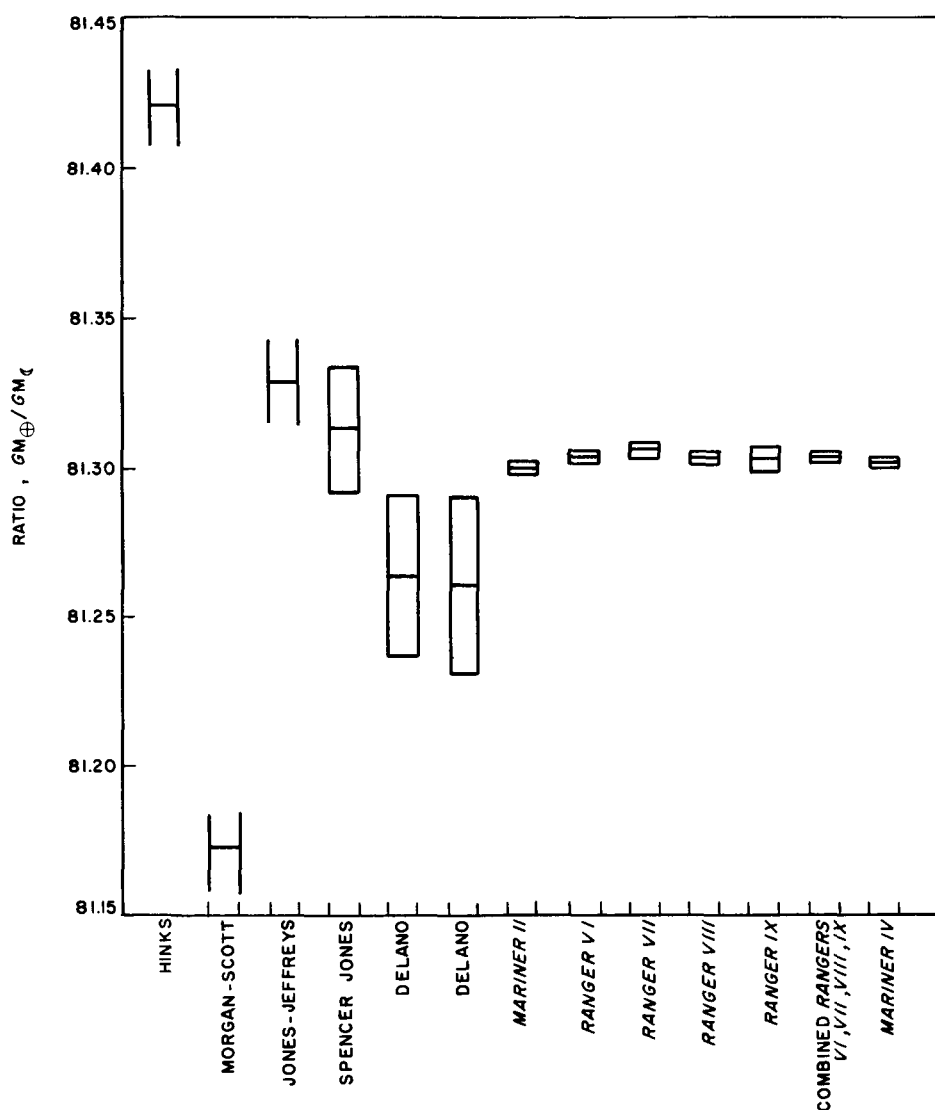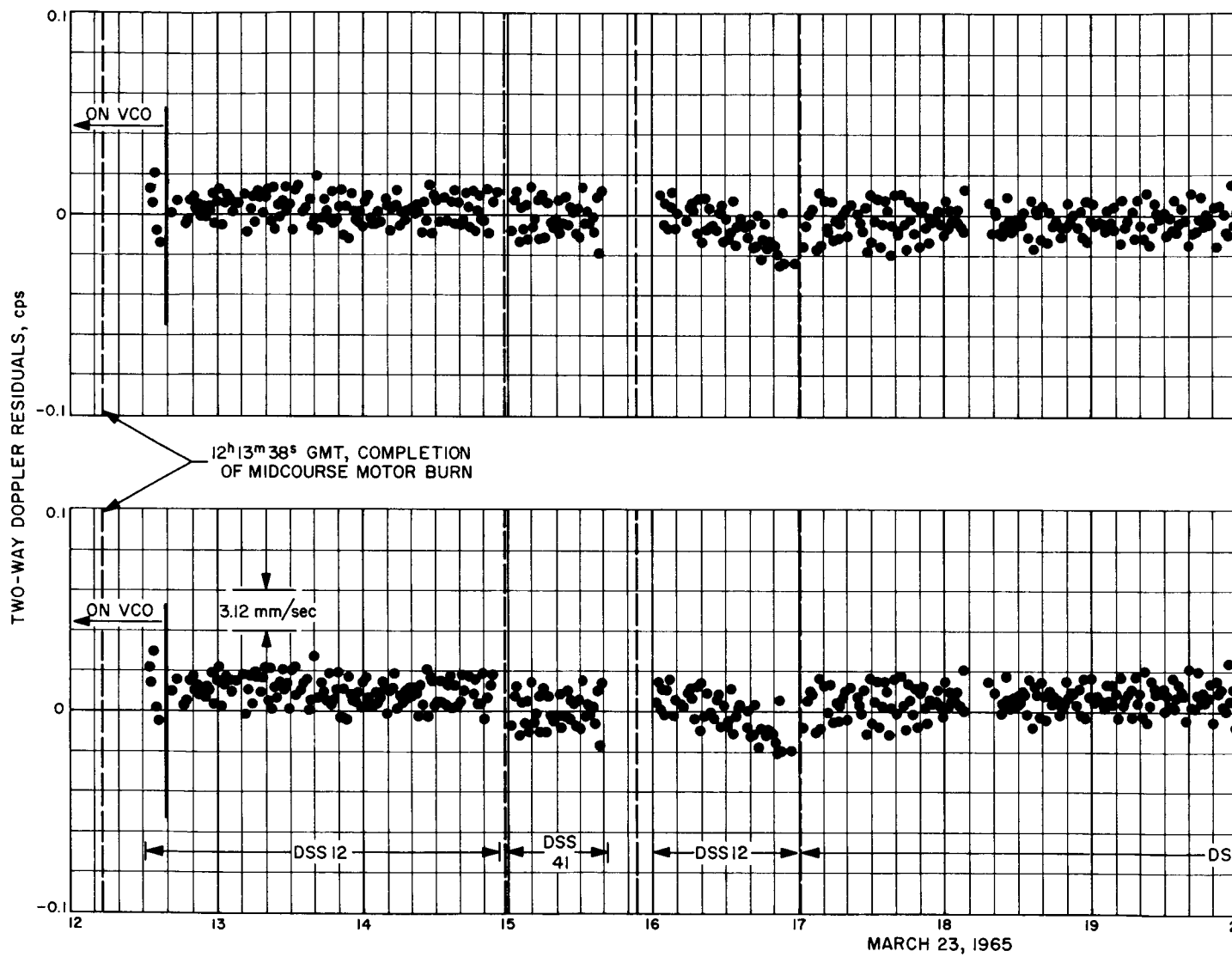
SINGLE MISSION RESIDUALS

COMBINED PARAMETER RESIDUALS

S 41 ├──────── DSS 51 ──── DSS 41 ──── DSS 51 ─

| 0 | 21 | 22 | 23 | 0 | | 2 | 3 | 4 | 5 |

GMT, hr

18-1

IMPACT AT 14^h 08^m 19.9^s GMT

ON VCO

ON VCO

DSS 12

MARCH 24, 1965
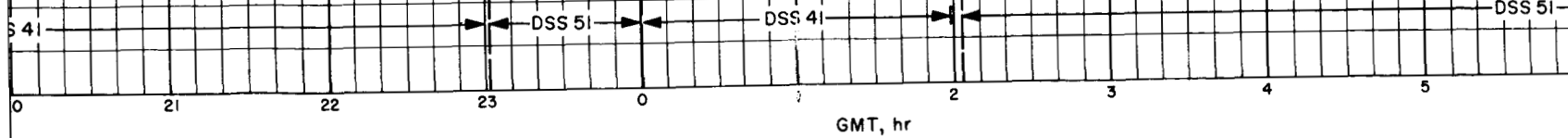
Fig. 8. *Ranger IX two-way doppler residual comparison*

18-2

A similar section in Part I of this analysis (SPS 37-43, Vol. III) discusses ionospheric refraction, inaccuracies in the Earth–Moon ephemeris, and errors in certain timing relationships as they affect the solutions for tracking station locations. Of these, the Earth–Moon ephemeris inaccuracies are the most serious with respect to the mass solutions. In addition, the numerical precision of the calculations themselves may be a limiting factor.

The data residuals are a guide to the quality of the results. The degree to which the computed tracking data agree with the observed tracking data is illustrated in Fig. 8. Two cases are presented for the *Ranger IX* post-midcourse data; namely, the residuals that result from the best fit to the *Ranger IX* data (single-mission *Ranger IX* residuals) and the residuals based on the parameters (common and unique) derived from the combined *Ranger* analysis (combined-mission *Ranger IX* residuals).

The residuals for the postmidcourse phase of the *Ranger VI*, *VII*, and *VIII* missions (derived from the combined *Ranger* analysis) are illustrated in Figs. 9–11, respectively. In computing the combined-mission residuals, the common parameters a which include the DSS locations, mass of the Earth, and mass of the Moon are those obtained from the use of Eq. (6). The remaining parameters, i.e., the parameters unique to the individual mission, which include the position and velocity of the probe shortly after the midcourse maneuver plus the Earth–Moon ephemeris scale factor, are computed as follows:

$$q_i^* - \widetilde{q}_i = \mathbf{L}_i^{-1} \mathbf{X}_i \left(\delta \widetilde{a}_i - \delta a^* \right) \qquad (8)$$

where

q_i^* is the new estimate of the unique (state vector) parameters for the probe

$\widetilde{q}_i$ is the unique parameter from least-squares fit to the probe tracking data

$\mathbf{L}_i$, $\mathbf{X}_i$, $\delta \widetilde{a}_i$, and δa^* are defined in Eqs. 2, 3, and 6, respectively

The single-mission residuals represent the best obtainable given the software model of the universe used for the analysis. Although the visible noise on a residual plot such as Fig. 8 may not include all the data error (low-frequency noise may be partially absorbed by a "false" solution vector), the high frequency noise caused by transmitter instability, doppler counter quantization error, and phase jitter is evident. For example, Figs. 8–11 illustrate the increased "visible" data noise when the voltage controlled oscillator (VCO) is being used instead of the more stable rubidium frequency standard.

It is interesting to note that doppler counter quantization error[15] is the major contributor to the visible noise (when the rubidium standard is used). This source contributes 1.1 mm/sec of a standard deviation[16] of 1.3 mm/sec for the combined errors for the single-mission residuals of Fig. 8. However, because of the "nonvisible" low frequency noise, the data taken at one sample/min were assigned a data weighting sigma of 13 mm/sec (for the data taken with the rubidium stan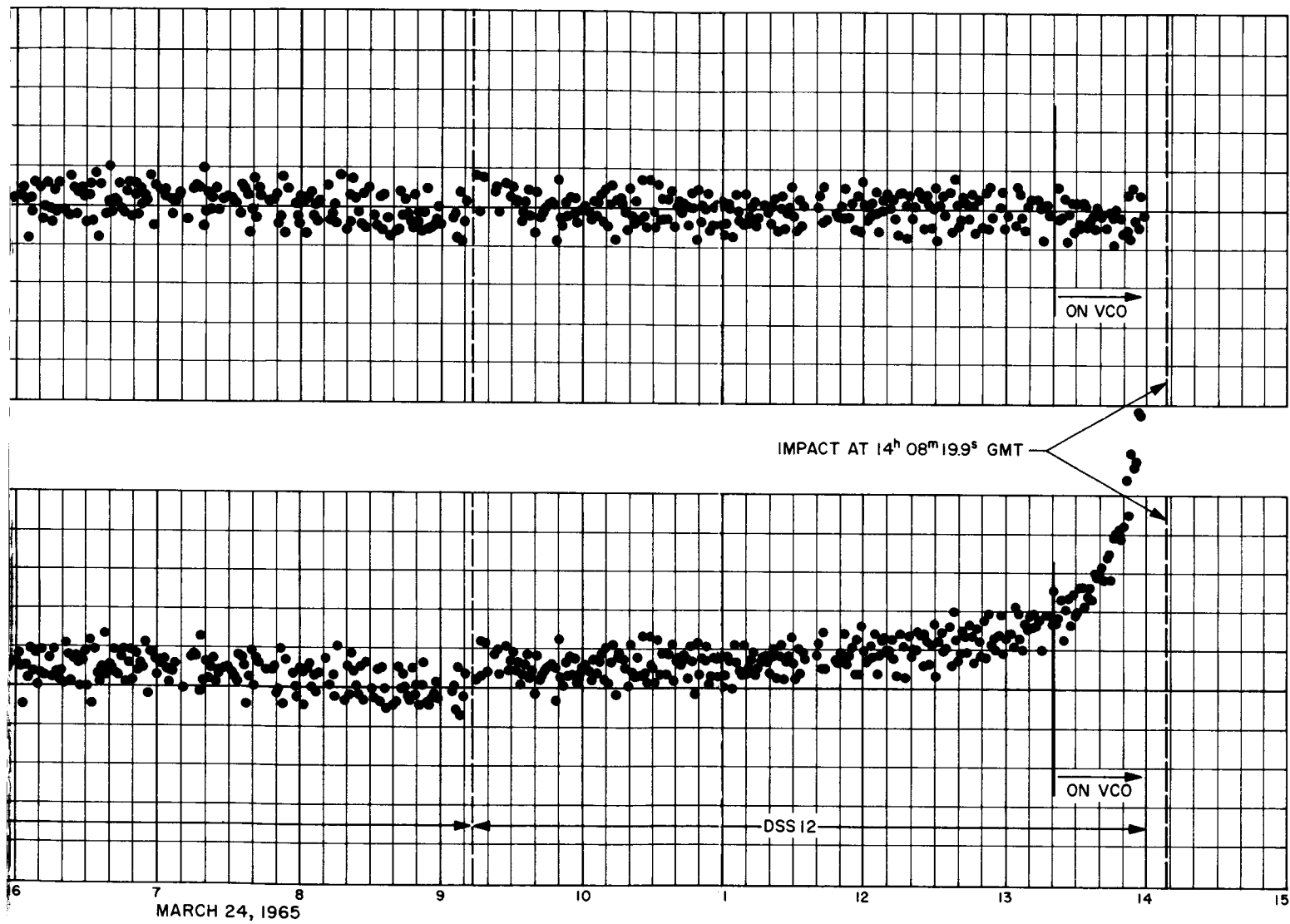dard). The principal component of this weighting sigma is a result of errors due to interpolation and the buildup of roundoff error introduced during computations. This means that the full potential of the DSS tracking data is not realized in the combined *Ranger* analysis. The two-way-doppler weighting sigma (for 1 sample/min) can be reduced from 13 mm/sec to less than 5 mm/sec if the computing noise is made negligible compared with the other error sources. The next-generation orbit determination program (described in SPS 37-38, Vol. III, pp. 24–26, and subsequent issues of Vol. III) will minimize these errors.

Although the combined parameters are optimum when taken over the set of *Ranger* Block III missions, they are not optimum in the sense of a single mission. Except for the region near the Moon, this is primarily reflected by biases (generally less than 1.6 mm/sec) in the combined-mission residuals of Figs. 8–11. The solution vectors derived from a single mission may to some extent "fit out" model inadequacies. However, this freedom is generally not available to the combined solution. Therefore the relatively large deviation in the combined-mission residuals starting ≈ 1 hr prior to impact is to be expected in light of the extreme sensitivity of the tracking data near the Moon to small changes in the probe orbital parameters and certain physical constants. However, the general behavior of the combined-mission residuals is encouraging and lends confidence to the method of analysis employed in combining the *Ranger* Block III results to obtain a "best estimate" for $GM_\oplus$ and $GM_\mathbb{C}$ based on radio tracking data.

[15]The doppler is continuously counted and sampled once a minute. The data used in Figs. 8–11 are obtained by differencing successive samples and dividing by the count time. The resulting "normalized" range difference can have a quantization error as large as one cycle/count time or 156 mm/60 sec.

[16]For elevation angles greater than 17 deg and excluding the last pass of DSS 12 data.
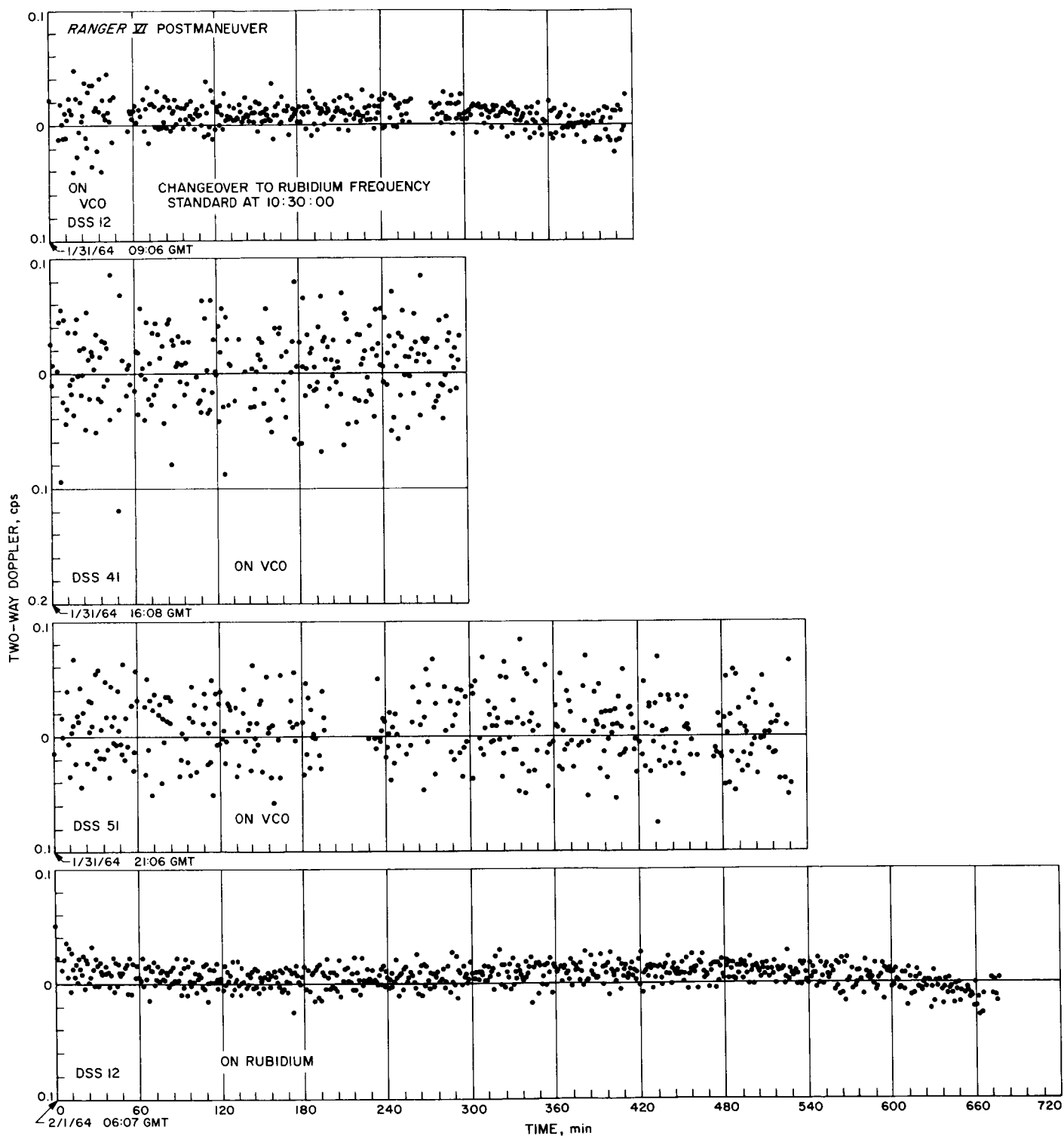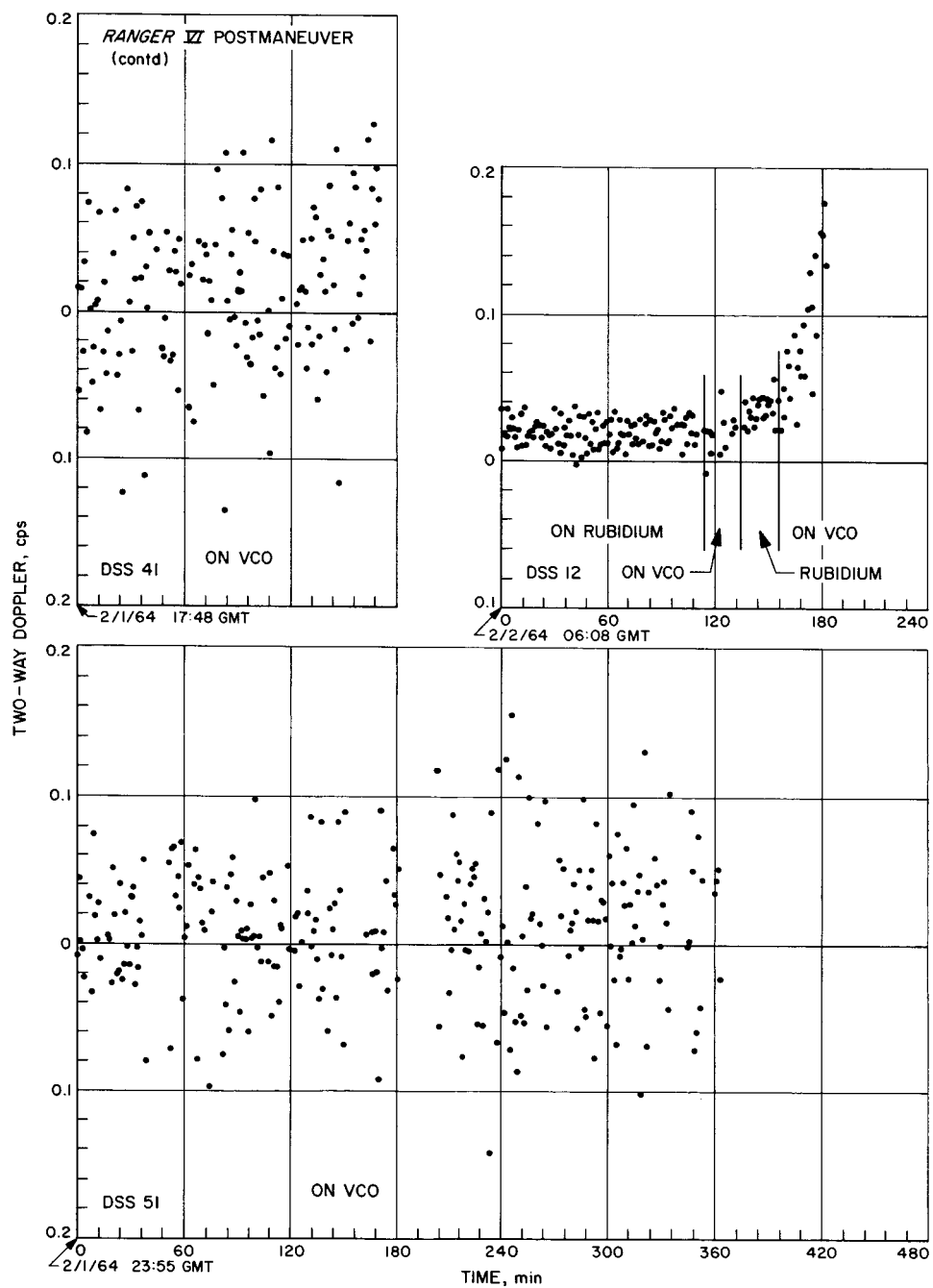
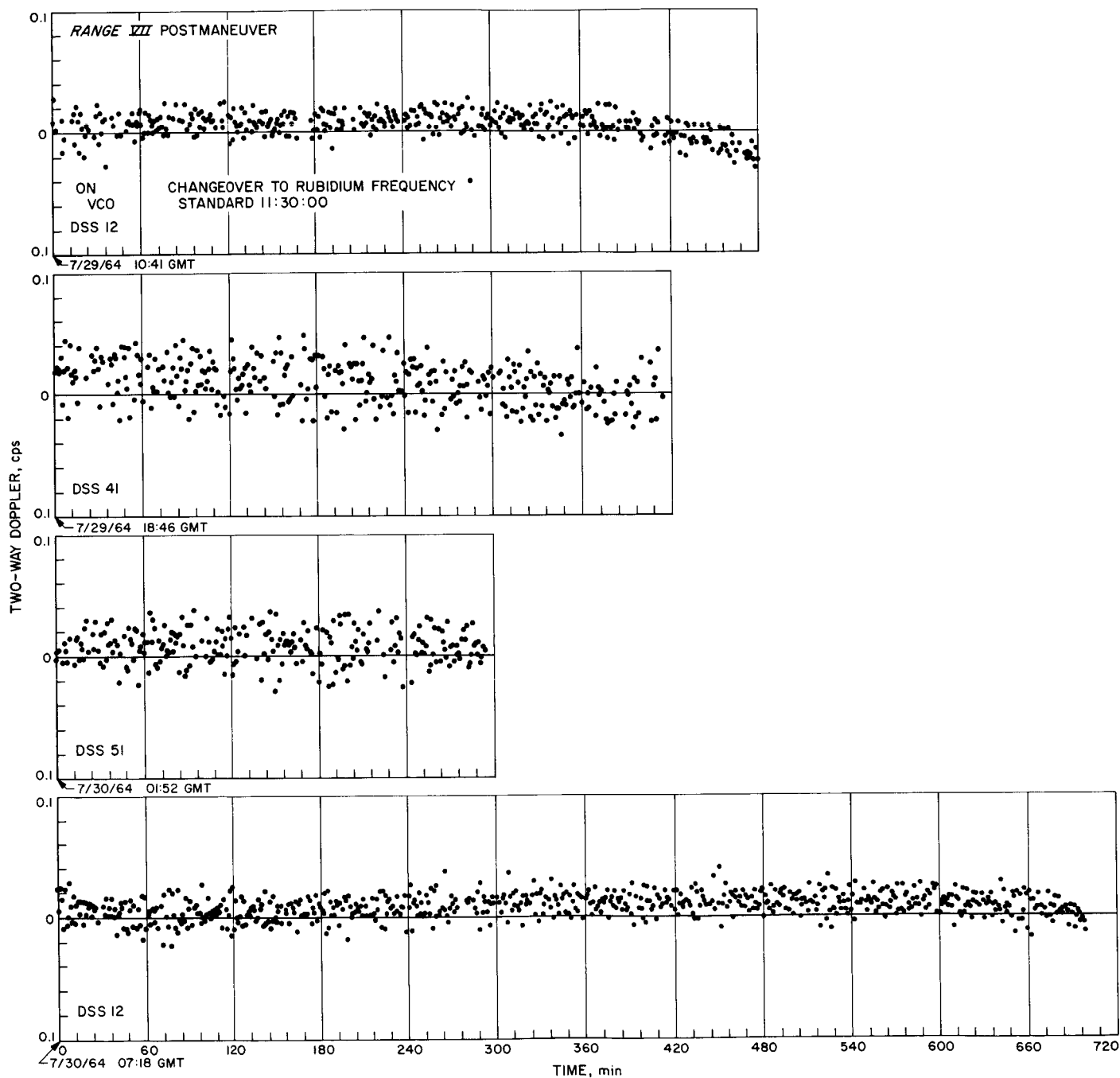**Fig. 9.** *Ranger VI two-way doppler residual comparison*

Fig. 9 (contd)

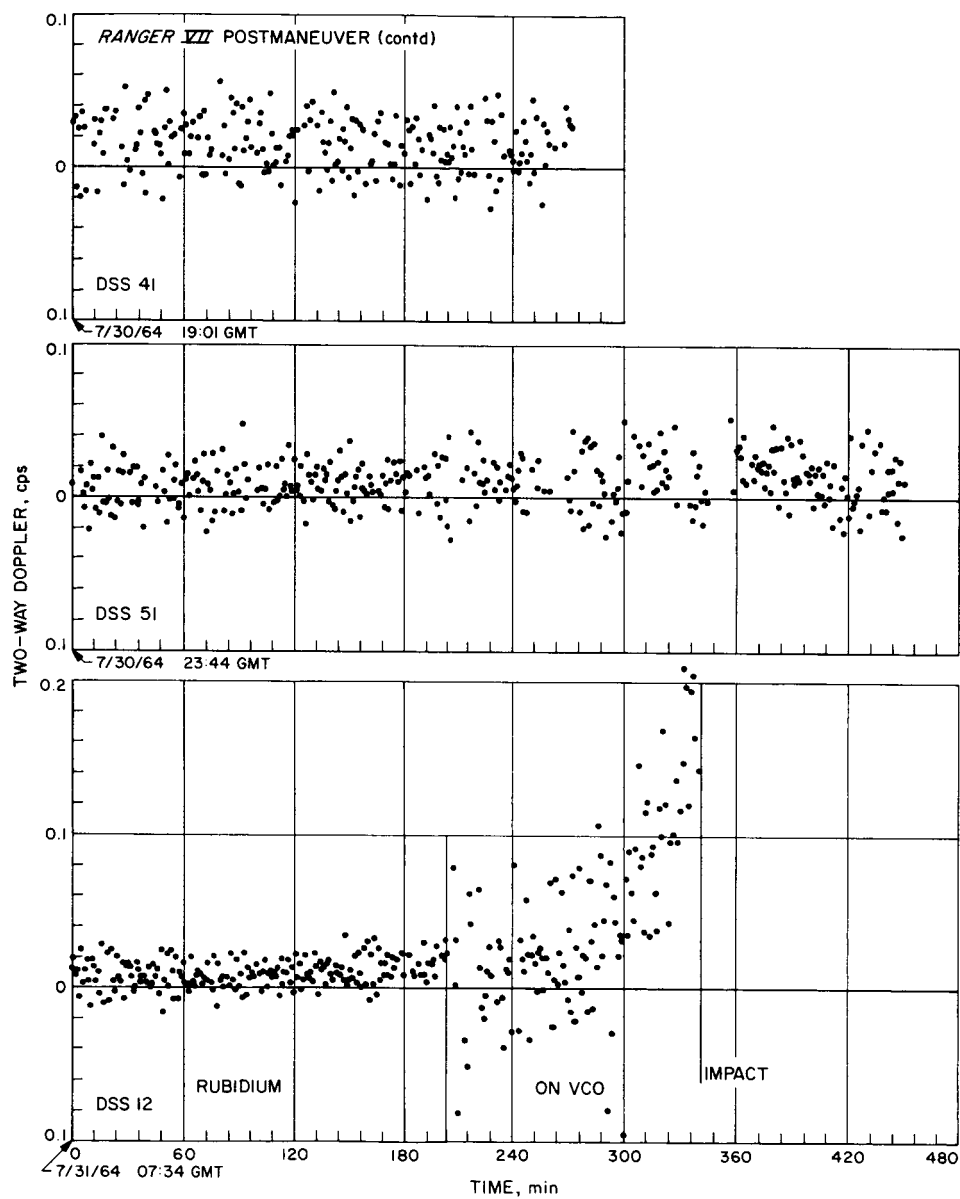Fig. 10. *Ranger VII* two-way doppler residual comparison

Fig. 10 (contd)

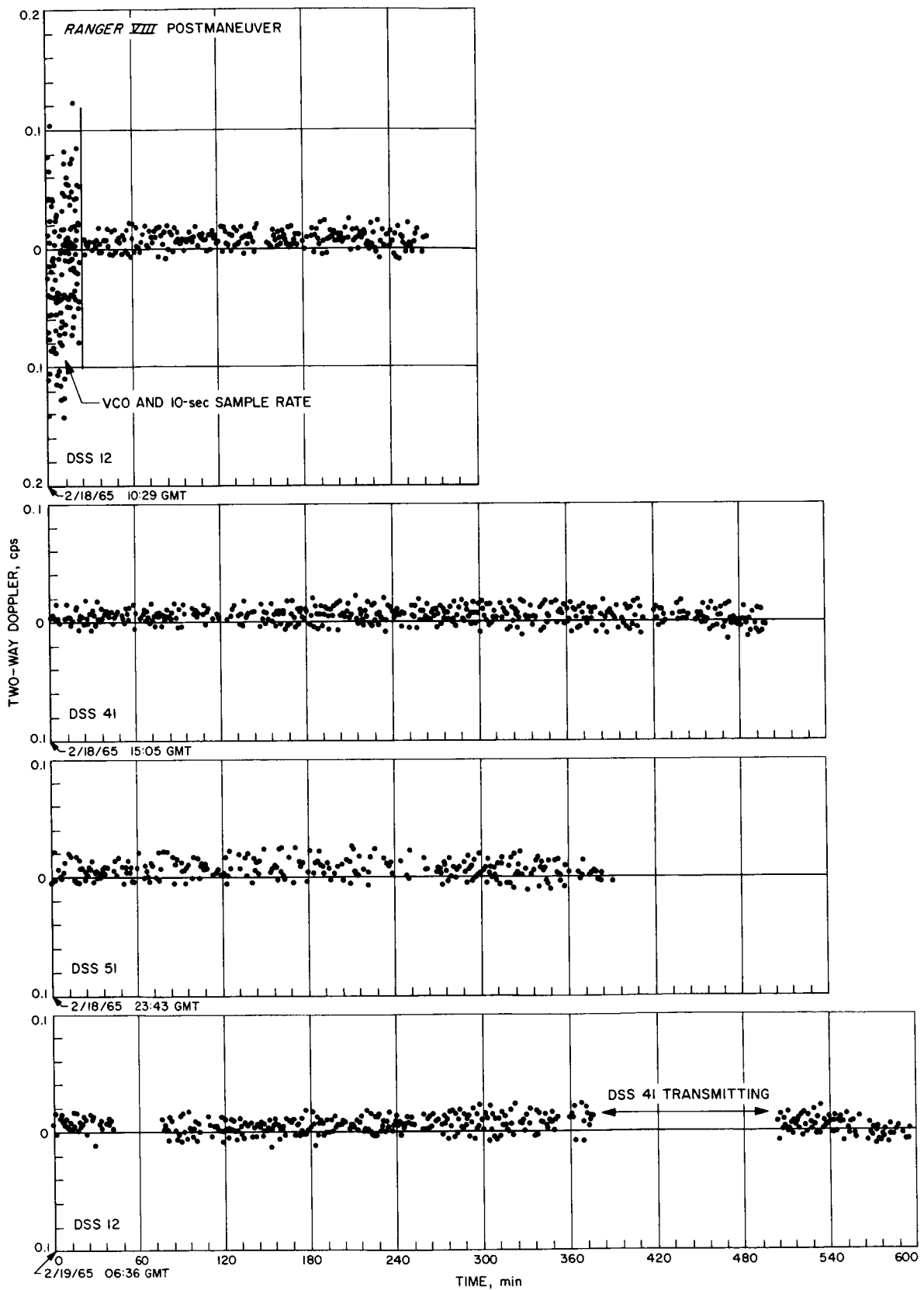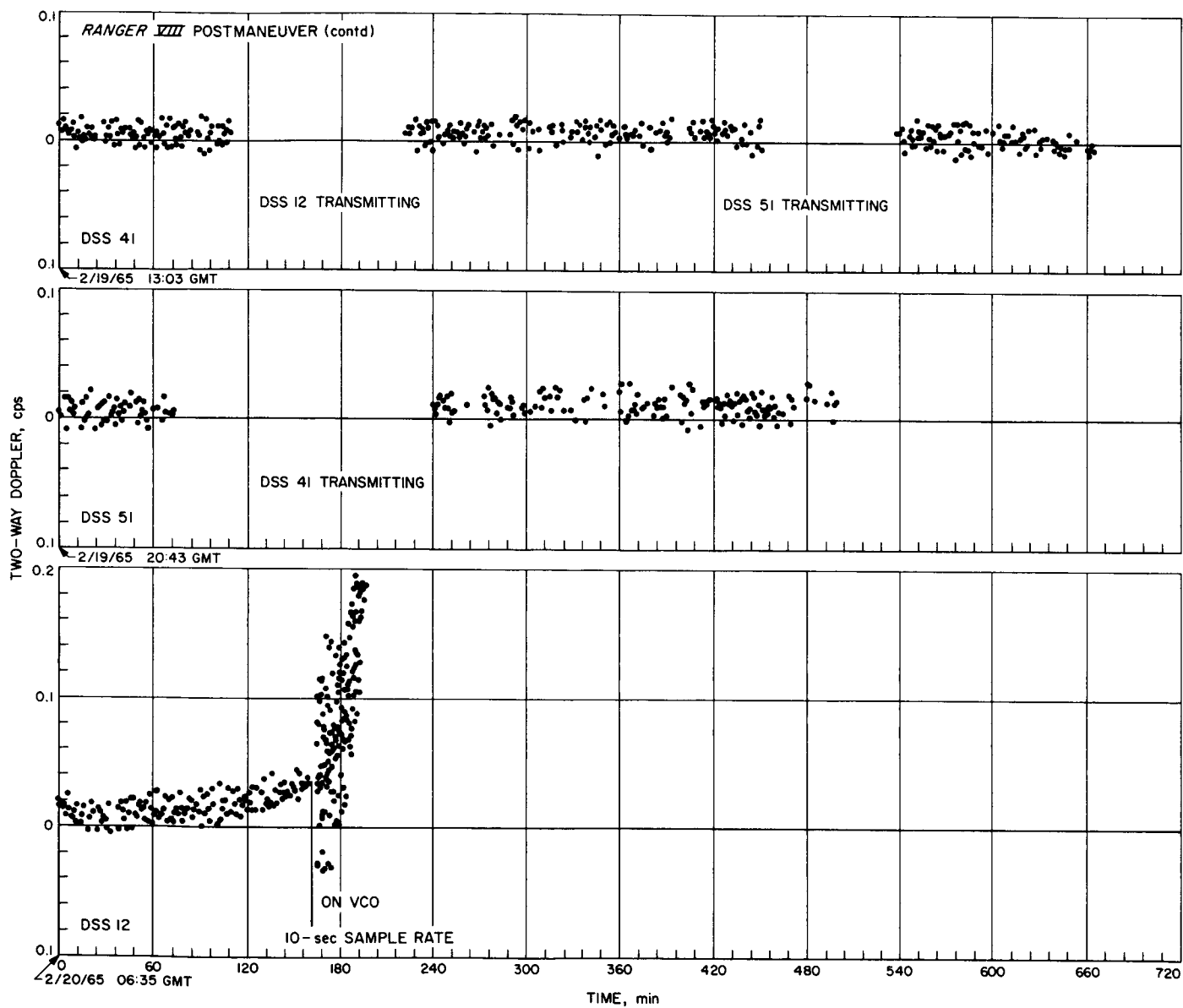**Fig. 11.** *Ranger VIII* two-way doppler residual comparison

Fig. 11 (contd)

The suspected causes for the degraded residuals near the Moon include the omission of ionospheric refraction corrections (mainly through their influence on station location parameters), the Earth–Moon ephemerides, and uncertainties among the time relationships utilized in the orbit-determination process. Known discrepancies in the improved lunar ephemeris are pointed out by W. J. Eckert in Ref. 15. These errors were incurred when insufficient accuracy was maintained in transforming from the original coordinates computed by Brown to those presently in use. The discrepancies in Earth–Moon distance and lunar longitude and latitude that existed at lunar encounter for Rangers VI–IX are shown in Table 6.[17] For Ranger VIII, the Earth–Moon distance had a known error of 1 km. These errors have a relatively high frequency and can change by 100 m/day. Recently these errors have been observed through tracking of the Lunar Orbiter with the DSS range and doppler system. These results are reported in SPS 37-43, Vol. III, pp. 24–28. A version of the Earth–Moon ephemeris produced by JPL has also been updated to included these as well as other corrections (SPS 37-42, Vol. IV, p. 2). Ephemeris errors will affect the $GM_\oplus$ and $GM_\emptyset$ solutions if the REM constraint is applied and the probe position coordinates are constrained at the midcourse maneuver epoch to be consistent with the best estimate of the maneuver. Under these conditions, if the REM (the artificial Earth radius that scales the ephemeris) shifts to yield the correct Earth–Moon distance $a_\emptyset$, a 1-km error in $a_\emptyset$ will cause a 3.0 km³/sec² shift in $GM_\oplus + GM_\emptyset$. Notice the comparatively small variation (0.4 km³/sec² from the mean) of $GM_\oplus + GM_\emptyset$ over the Ranger VI–IX flights as opposed to the known errors in $a_\emptyset$ shown in Table 6. Because of the relative inaccuracy of the lunar ephemeris compared with the ability of the tracking data to independently

---

[17]These values are based on a communication from W. J. Eckert, March 7, 1966.

determine $GM_\oplus$, $GM_\emptyset$, and REM, the REM constraint was not applied for the Ranger results contained in this report. As the lunar ephemeris is improved, the additional knowledge supplied by the application of the REM constraint will become meaningful.

The power of the tracking data to properly locate the Moon even without the lunar constraint is demonstrated in Table 7, where three sets of REM as well as the "stated" uncertainties are considered. The single-mission REM (REM_S) refers to those values that result from processing the data, one mission at a time, without applying the REM constraint. Little information with respect to the Eckert corrections can be gained from analyzing these values, because of their relatively large uncertainties combined with the correlations among REM_S, $GM_\oplus$, and $GM_\emptyset$, and the size of the errors that exist in the single-mission values of $GM_\oplus$ and $GM_\emptyset$.

The combined REM (REM_C) is computed from the constraint equation (Eq. 7) using the $GM_\oplus$ and $GM_\emptyset$ values that result from the combined analysis. This represents an average REM over the set of Ranger Block III missions and is the REM necessary to produce the correct computed lunar period. (Actually the lunar period is fixed to the correct value for this analysis; i.e., the lunar positions are "locked up" from a fixed ephemeris tape except for the REM scale factor.)

The nonconstrained REM (REM_N) results from Eq. (8) and represents the best estimate of REM on a single-mission basis, given the $GM_\oplus$, $GM_\emptyset$, and tracking station locations as determined from the combined analysis. REM_N should produce a realistic best estimate of the true Earth–Moon distance $(a_\emptyset)$ during a particular mission. The difference

$$\Delta REM \equiv REM_N - REM_C$$

$$\text{scaled by } \frac{\text{mean lunar distance}}{\text{Earth equatorial radius}} = 60.27$$

should and does follow the Eckert correction, as shown in Table 7. The agreement implies that $\sigma_{\Delta REM_N} \sim 2\,\text{m}$ which is small compared with σ_{REM_C} and σ_{REM_N} (however, REM_C and REM_N are highly correlated).

In addition to the computing noise and ephemeris noise, other numerical limitations exist in the current analysis. This is indicated by the fact that certain constraints hold only to a limited precision. An example of this is the variations in physical-constant solutions that

Table 6. Eckert corrections to Brown's lunar ephemeris

Mission	Encounter date	Correction, m		
		Earth–Moon distance $\Delta a_\emptyset - \dfrac{-a_\emptyset^2}{a_e}\Delta\left(\sin\dfrac{a_e}{a_\emptyset}\right)$	Lunar longitude $a_\emptyset\,\Delta\Psi$	Lunar latitude $a_\emptyset\Delta\beta$
Ranger VI	2/2/64	−244	+64	−31
Ranger VII	7/31/64	410	−24	−21
Ranger VIII	2/20/65	1024	+63	−80
Ranger IX	3/24/65	500	−11	+2

Table 7. Sensitivity of REM to ephemeris errors in the Earth–Moon distance

Mission	REM, m						Correction to lunar distance, m		$\epsilon_{\Delta REM} \equiv \Delta REM - \dfrac{E}{60.27}$, m
	Single mission		Nonconstrained		Combined Rangers		$\dfrac{a_\zeta}{a_e}$ $\Delta REM = 60.27$ $(REM_N - REM_C)$	Eckert correction E	
	REM_S	σ_{REM_S}	REM_N	σ_{REM_N}	REM_C	σ_{REM_C}			
Ranger VI	6378309.4	18.9	6378307.1	8.4	6378310.6	2.5	−211	−244	+0.6
Ranger VII	6378309.1	35.8	6378319.5	18.3			536	410	+2.1
Ranger VIII	6378327.0	26.4	6378324.4	2.8			832	1024	−3.2
Ranger IX	6378305.5	33.1	6378320.0	8.3			567	500	+1.1

result from processing the same tracking data in a different order. The solutions obtained should be identical, whether using the results of premaneuver data as *a priori* information when processing postmaneuver data, or vice versa, because both orbits use the same set of data but in a different order. In general, these solutions were not identical, but in no case did the discrepancy between the "forward" and "backward" solution for a parameter exceed its standard deviation. The worst comparison was experienced with the GM_ζ solution for *Ranger VII* as reported in Ref. 3. A variation was experienced between the two solutions of $\Delta GM_\zeta = 0.09$ km³/sec² ($\sigma GM_\zeta = 0.15$ km³/sec²). This is an unexpected discrepance in the sixth digit. Roundoff may cause a variation of the seventh or eighth digit since, although the same computations are performed, they are accomplished in a different sequence for the two solutions. Similarly, for the same mission $\Delta GM_\oplus = 0.9$ km³/sec² ($\sigma GM_\oplus = 1.5$ km³/sec²); however, this represents an error in the seventh rather than the sixth digit. The major portion of this numerical problem seems to be related to the backward mapping process associated with using the postmidcourse data as *a priori* information when processing the premaneuver data. Therefore only the "forward" version of the analysis was used here.

Even though the effective weighting scheme employed for this analysis compensates for model inadequacies, this is not the most efficient way to handle the problem. Certain model errors may be known to exist, but cannot be effectively modeled with the present estimator because an unreasonable number of parameters are required in the solution vector. Work is presently underway at JPL to mechanize an estimator that more properly accounts

for these types of model errors or process noise. In addition to computational noise, model errors will be applied to the tracking data. These may take such forms as (1) unaccounted-for unbalanced attitude-control forces; (2) varying solar-pressure force (either because the spacecraft presents a variable effective area to the Sun or the Sun expels a variable photon flux); (3) incorrect ephemerides; and (4) an inadequate model for corrections, such as refraction due to the Earth's atmosphere (tropospheric and ionospheric) and the effect of space plasma.

Although of minor concern for the *Ranger VI–IX* missions, the effects of the attitude-control system, varying solar pressure, and space plasma are significant items for the *Mariner II* (Venus) and *Mariner IV* (Mars) flights and should be kept in mind when comparing the *Mariner II* and *Mariner IV* GM_ζ solutions with the solutions obtained from the *Ranger* missions. As an example, the *Mariner II* attitude-control forces that existed during the flight are rather ill-defined. A solution of GM_ζ using cruise data and assuming no attitude-control forces differed by 0.2 km³/sec² from a solution obtained when a "reasonable" attitude-control-force time history was assumed.

It should be noted that the previously quoted statistics in this report assume that the "fitter's universe" exactly matches the "real universe." The most significant deviation between the two is the representation of the Earth–Moon system for the case of the Earth and lunar masses; however, the error sources (ionospheric and timing) discussed in Part I of this analysis are also important. Taking the above into account, the actual statistics of the combined *Ranger* analysis are probably on the order of

$\sigma_{GM_\oplus} \sim 0.7$ km^3/sec^2, $\sigma_{GM_\mathbb{C}} \sim 0.1$ km^3/sec^2, and consequently $\sigma_{\mu^{-1}} \sim 0.0017$.

4. Conclusion

Radio tracking of deep space probes provides a powerful means of determining certain physical constants, such as $GM_\oplus$ and $GM_\mathbb{C}$, which exhibit a high degree of consistency among the individual *Ranger* missions. When the radio tracking information from the four *Ranger* missions is combined, the solutions that result are

$$GM_\oplus = 398601.2 \pm 0.7 \text{ km}^3/\text{sec}^2$$

$$GM_\mathbb{C} = 4902.6 \pm 0.1 \text{ km}^3/\text{sec}^2$$

and

$$\mu^{-1} = 81.302 \pm 0.0017$$

where the statistics are adjusted to compensate for known limitations to the analysis.

The results of the combined *Ranger* analysis were compared with results from the *Mariner* planetary flights and with those from optical tracking data. The comparison among the *Ranger* and *Mariner* missions is quite good considering the size of systematic errors which may be caused by known limitations that affect the data reduction process. This is particularly true when comparing the *Ranger* and *Mariner* $GM_\mathbb{C}$ solutions, which are relatively independent though both depend on radio tracking data. That is, the *Ranger* $GM_\mathbb{C}$ is a gravitational determination (doppler data are affected by the motion of the probe caused by the Moon), while the *Mariner* $GM_\mathbb{C}$ solutions are not (i.e., the doppler data are affected by the motion of the Earth about the Earth–Moon barycenter). Also, the combined *Ranger* μ^{-1} determinations fall within the spread of the μ^{-1} values inferred from the determination of the lunar inequality based on optical data. An interesting by-product of the analysis is the extent to which the *REM* solutions follow the trend predicted by the Eckert corrections to the ephemeris used for this study.

Limitations to this analysis due to inaccuracies in the Earth–Moon ephemeris and software inadequacies do not allow the full utilization of the radio tracking data accuracy. A version of an improved Earth–Moon ephemeris is already available and work is actively proceeding on the development of more sophisticated software for the processing of the tracking data.

D. Doppler–Ranging Calibration Experiment Proposed for *Lunar Orbiter*, A. S. Liu and R. L. Motsch

1. Introduction

Experiments are planned during the *Lunar Orbiter* missions to use data from the DSIF Mark IA ranging system in conjunction with doppler measurements for the following purposes:

(1) To extract information on the effects of the ionosphere's charged particles on tracking data.

(2) To evaluate the Mark IA ranging system performance.

(3) To measure transponder differential delay versus temperature.

(4) To measure effects of system signal-to-noise ratio on ranging accuracy.

(5) To produce valuable calibrated tracking data for selenodesy, landed *Surveyor*, lunar ephemeris projects, etc.

This article is limited to a discussion of the first three listed items.

2. Discussion

In a dispersive medium such as the ionosphere, the range is propagated with group velocity and the doppler is propagated with phase velocity. The difference between cumulative doppler count and two independent ranging measurements gives a measure of twice the change due to group or phase velocity. At low elevation angles, during daylight hours at times of high solar activity, the effect can be on the order of 20 to 30 m maximum. Fig. 12 shows the range corrections in meters for a pass of data taken from Madrid during the translunar phase of *Lunar Orbiter II* for various indices $\bar{R}$ (sunspot activity index) of ionospheric activity. Fig. 13 shows a comparison between actual ranging data and counted doppler data from DSS 61 (Robledo DSS, Madrid) which were taken during the translunar phase of the *Lunar Orbiter II* mission. The figure shows a scatter of points centered about -100 counts. Each range unit, (about 1.06 m) corresponds to 32 counts, so that the total scatter about the mean amounts to ± 3 m.

From satellite drag analyses and from ionosonde data, it has been determined that the electron concentration reaches a maximum at about 3 p.m. local time and a
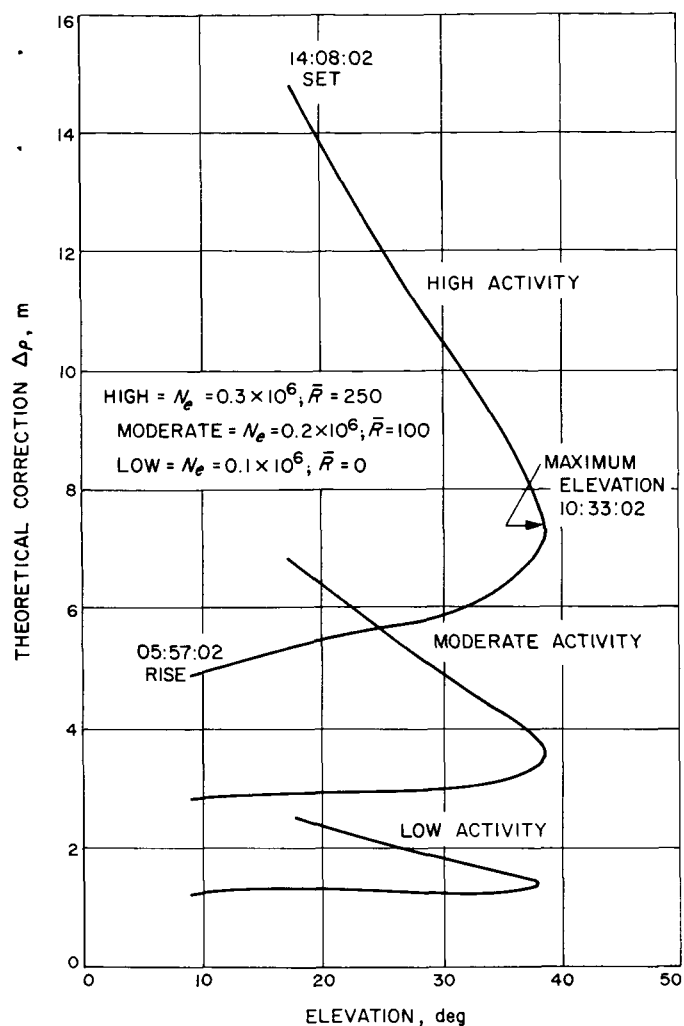
Fig. 12. Range correction versus elevation angle, *Lunar Orbiter II* Madrid pass
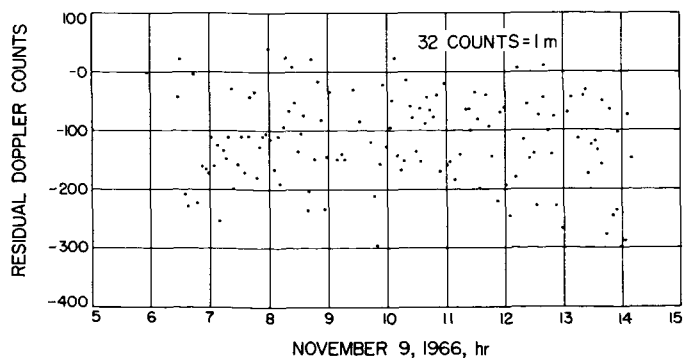
Fig. 13. Difference in counts between doppler and range

minimum at about 3 a.m. local time. Fig. 14 shows an equidensity contour plot of particle concentration for geomagnetic latitudes ±15 deg for an assumed shape of the diurnal bulge. The shape depends upon the location of the Sun; hence we may view the ionosphere as being fixed over one day and the tracking station as rotating underneath the ionosphere. Fig. 15 compares an actual diurnal variation with the assumed variation based upon Fig. 14 (corrected for latitude effects). These data, taken by Stanford experimenters (Ref. 16), represent measurements of Faraday rotations of signals received from *Syncom* over a Hawaii station. Total electron contents in numbers/m² is plotted along the vertical axis. At S-band frequencies, 1×10^{17} numbers/m² correspond to approximately 1-m correction in range. Fig. 16, taken from the same source, shows not only an hourly variation in electron content but also a daily variation.

To maximize the effects of the diurnal bulge of the ionosphere, tracking data are required when the elevation angle of the Moon (i.e., *Lunar Orbiter*) is low, at about 3 p.m. local station time. Moonrise or moonset is dependent upon the declination of the Moon and the time of station meridian crossing. Table 8 gives the approximate dates when the Moon is near the horizon at

Table 8. Approximate dates of maximum ionospheric effects (Goldstone)

Date, 1967	Pass length, hr
4/7–9	11.5
4/15–17	14
5/8–10	12.5
5/15–17	13
6/6–8	13
6/13–15	12
7/6–8	12.5
7/12–14	11.5
8/4–6	13
8/11–13	10
9/2–4	12.5
9/9–11	9
10/2–4	11.5
10/9–11	8
10/31–11/2	12
11/7–9	9
11/30–12/2	11
12/6–8	7.5
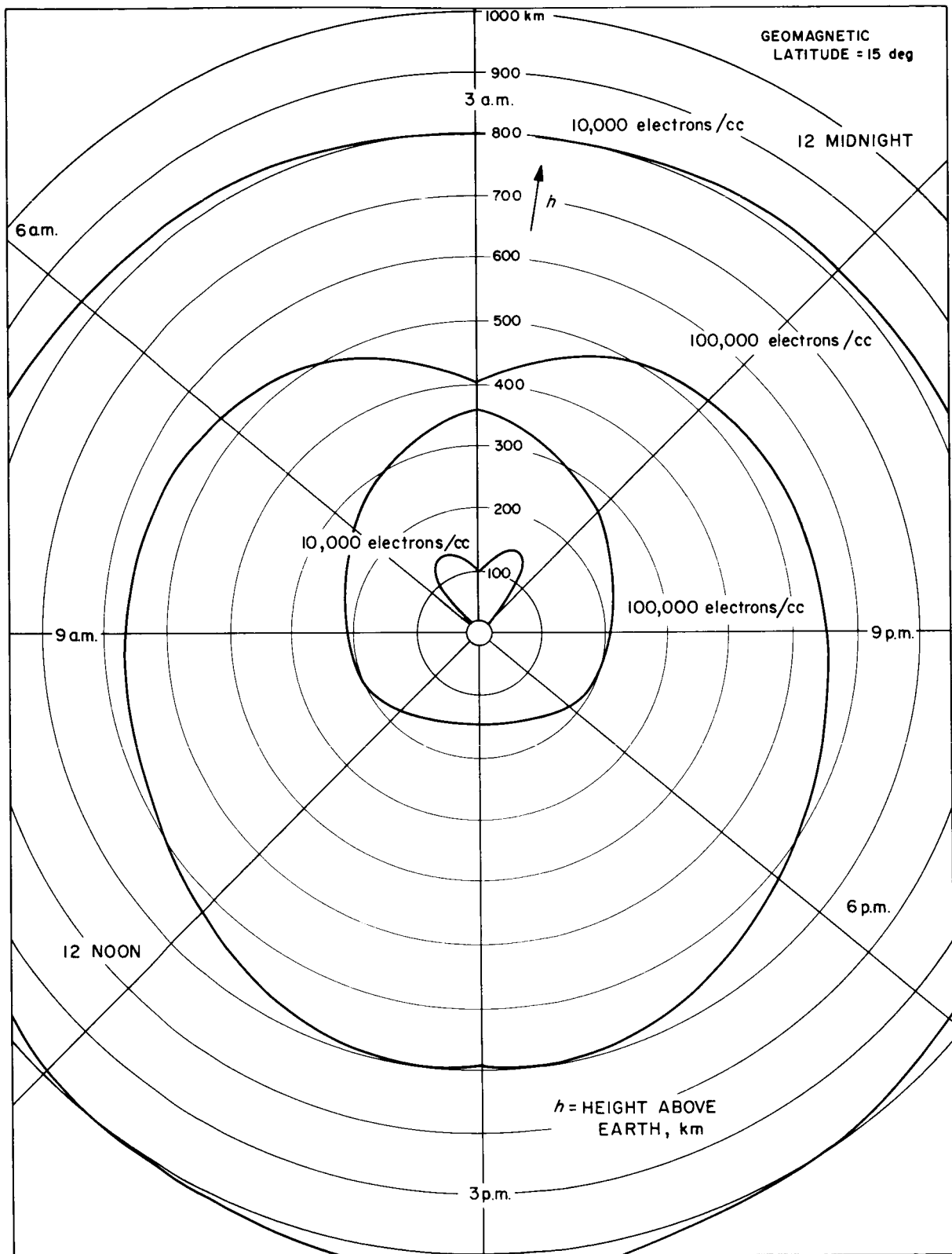
Fig. 14. Ionospheric equidensity plot
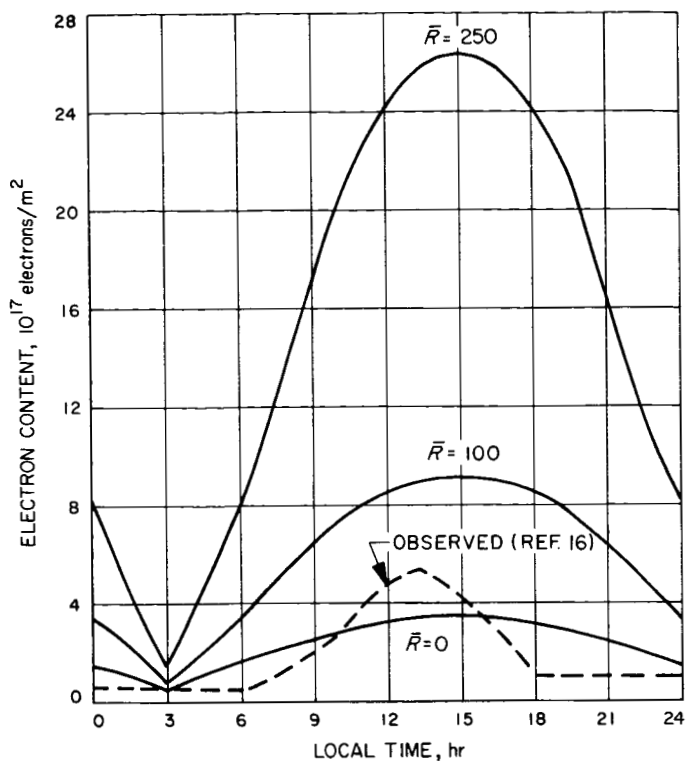
Fig. 15. Diurnal variation of electron content

Fig. 16. Variation of electron content
by day and hour

Fig. 17. Plot of pass duration versus lunar
declination δ for Goldstone

temporal asymmetry of the ionosphere, to analyze the density distribution of the ionosphere with time by examining plots such as Fig. 13.

As can be seen from Fig. 13, there is considerable scatter of the ranging measurements about the mean. It is believed at this time that the noise observed is an overall ground system noise due to a phase jitter of about ± 5 deg in the 498-kHz clock loop. For the future planned experiment we hope to have a better picture of the system performance and to ascertain the correctness of the phase-jitter hypothesis.

From ground calibration tests performed on the transponder of *Lunar Orbiters I* and *II*, it was determined that the delay time (or an error in range) is sensitive to temperature variations (Figs. 18 and 19). This sensitivity seems to vary from transponder to transponder; the slope is positive for *Lunar Orbiter I* and negative for *Lunar Orbiter II*. During the transluner phase, the temperature of the spacecraft is nearly constant; however, during the orbital phase, because the spacecraft is periodically

3 p.m. and the approximate time duration of the pass. The dates could be in error on the order of two days. Fig. 17 plots duration of the pass over Goldstone against lunar declination.

It is possible, therefore, on the basis of the differing propagation speed between range and doppler and the
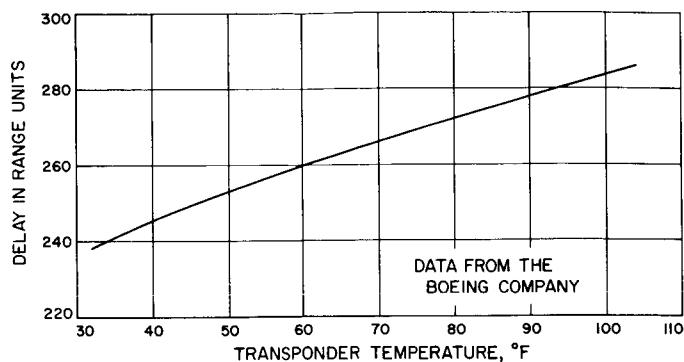
Fig. 18. Ranging delay in range units for Lunar Orbiter I
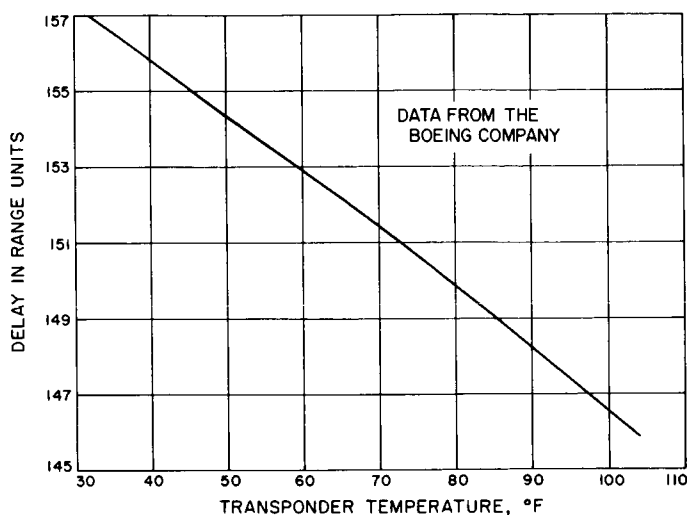
Fig. 19. Ranging delay in range units for Lunar Orbiter II

shielded from sunlight by the Moon (Fig. 20), the temperature will vary. Figs. 21 and 22 show telemetered temperature measurements taken during the *Lunar Orbiter II* mission that revealed a variation of about 20°F. This variation, which has a rise time of about 2 hr and a cooling time of about 1 hr, will cause an approximate 3-m error in the range measurements.
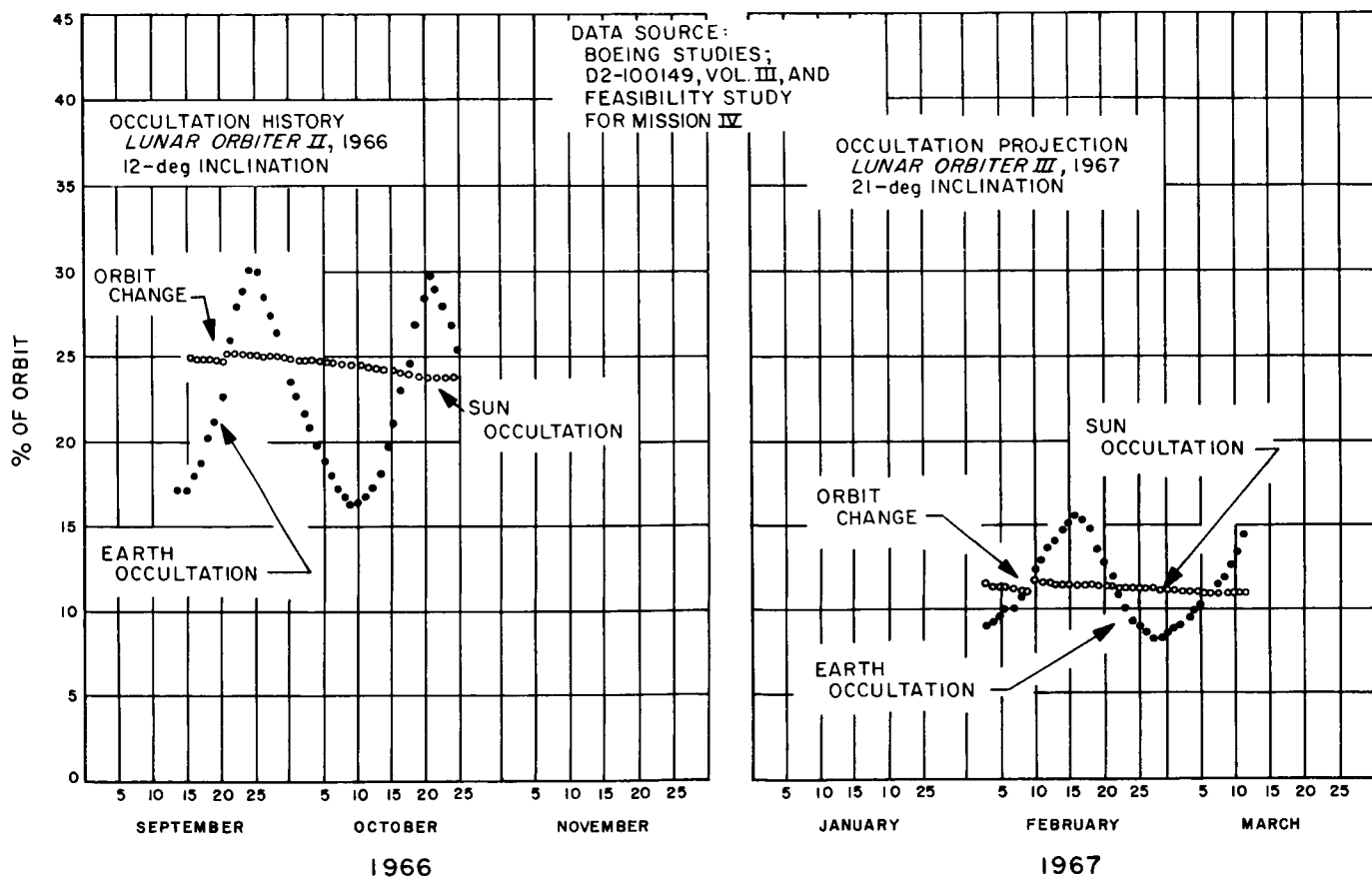
Fig. 20. Occultation history for *Lunar Orbiter II*, 1966, 12-deg inclination; occultation projection for *Lunar Orbiter III*, 1967, 21-deg inclination
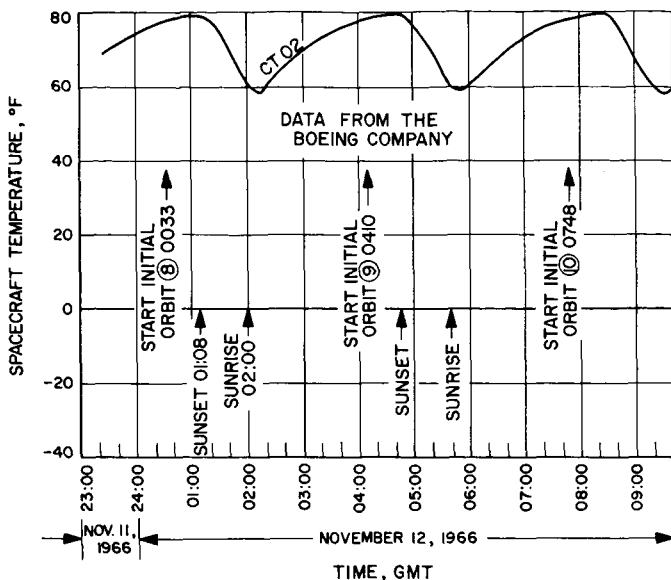
Fig. 21. *Lunar Orbiter II* temperatures
(initial orbits 8, 9 and 10)
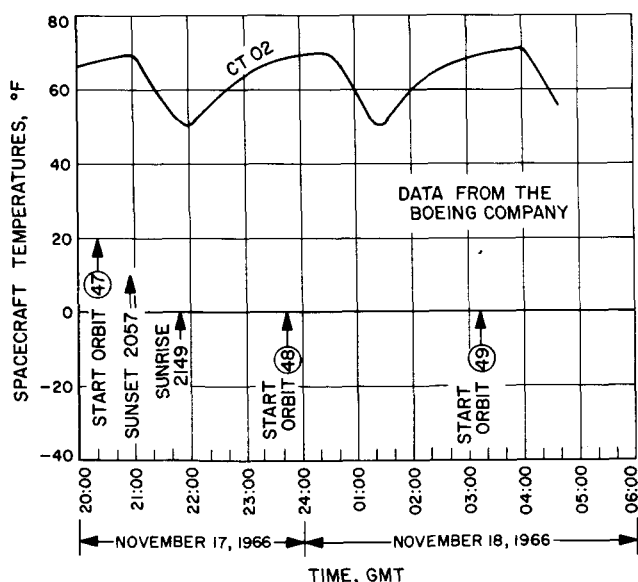
Fig. 22. *Lunar Orbiter II* temperatures
(orbits 47, 48 and 49)

3. Summary

During this experiment, plans include:

1. Demonstration of the use of the difference between group velocity of range increment and phase velocity of counted doppler to measure the ionospheric effects.

2. Evaluation of the range system performance.

3. Correlation of temperature data received from the spacecraft with errors in range measurements.

The success of this experiment will depend primarily upon how small the phase jitter in the ground system can be made and upon the constancy of the ground system calibration.

E. Theoretical Basis for the Double Precision Orbit Determination Program: VII. Variational Equations, *T. D. Moyer*

1. Introduction

This seventh article in the series presenting the theoretical basis for the double precision orbit determination program (DPODP) gives the formulation for the solution of the variational equations. The partial derivative of the probe acceleration vector with respect to the parameter vector **q** is integrated numerically by the second-sum procedure to give the partial derivatives of the probe velocity and position vectors with respect to **q**.

These subpartial derivatives are used to form the partial derivatives of the observable quantities with respect to **q**, which are used along with the observed minus-computed residuals to differentially correct the *a priori* estimates of **q**.

2. Variational Equations and Method of Integration

The acceleration of the probe relative to the center of integration has been described in Part III of this series (SPS 37-41, Vol. III, pp. 24–31). In functional form, it is given by

$$\ddot{\mathbf{r}} = \ddot{\mathbf{r}}\,(\mathbf{r}, \dot{\mathbf{r}}, \mathbf{q}) \tag{1}$$

where

$\mathbf{r}, \dot{\mathbf{r}}, \ddot{\mathbf{r}}$ = position, velocity, acceleration vectors of probe relative to center of integration with rectangular components referred to the mean Earth equator and equinox of 1950.0. The argument is ephemeris time

$\mathbf{q}$ = solve-for parameter vector

$$= \begin{bmatrix} \mathbf{X}_0^B \\ \hline \mathbf{a} \end{bmatrix}$$

where

$$\mathbf{X}_0^B = \begin{bmatrix} \mathbf{r}_0^B \\ \dot{\mathbf{r}}_0^B \end{bmatrix} = \text{position and velocity components of}$$

position and velocity components of probe relative to body B (not necessarily the center of integration C) at injection epoch

$\mathbf{a}$ = dynamic constants affecting probe trajectory

The state vector of the probe $\mathbf{X}_0$ relative to the center of integration at the injection epoch is given by

$$\mathbf{X}_0 = \mathbf{X}_0^B + (\mathbf{X}_B^C)_0 \qquad (2)$$

Differentiating Eq. (1) with respect to $\mathbf{q}$ gives

$$\frac{\partial \ddot{\mathbf{r}}}{\partial \mathbf{q}} = \frac{\partial \ddot{\mathbf{r}}}{\partial \mathbf{r}}\frac{\partial \mathbf{r}}{\partial \mathbf{q}} + \frac{\partial \ddot{\mathbf{r}}}{\partial \dot{\mathbf{r}}}\frac{\partial \dot{\mathbf{r}}}{\partial \mathbf{q}} + \frac{\partial \ddot{\mathbf{r}}}{\partial \mathbf{q}}\bigg|_{\mathbf{r},\dot{\mathbf{r}}=\text{constant}} \qquad (3)$$

Let

$$A = \frac{\partial \ddot{\mathbf{r}}}{\partial \mathbf{r}} = \begin{bmatrix} \dfrac{\partial \ddot{x}}{\partial x} & \dfrac{\partial \ddot{x}}{\partial y} & \dfrac{\partial \ddot{x}}{\partial z} \\[2mm] \dfrac{\partial \ddot{y}}{\partial x} & \dfrac{\partial \ddot{y}}{\partial y} & \dfrac{\partial \ddot{y}}{\partial z} \\[2mm] \dfrac{\partial \ddot{z}}{\partial x} & \dfrac{\partial \ddot{z}}{\partial y} & \dfrac{\partial \ddot{z}}{\partial z} \end{bmatrix} \qquad (4)$$

$$B = \frac{\partial \ddot{\mathbf{r}}}{\partial \dot{\mathbf{r}}} \qquad (5)$$

$$C = \frac{\partial \ddot{\mathbf{r}}}{\partial \mathbf{q}}\bigg|_{\mathbf{r},\dot{\mathbf{r}}=\text{constant}} \qquad (6)$$

$$Z = \frac{\partial \mathbf{r}}{\partial \mathbf{q}} = \left[\frac{\partial \mathbf{r}}{\partial q_1}, \frac{\partial \mathbf{r}}{\partial q_2}, \cdots, \frac{\partial \mathbf{r}}{\partial q_n} \right] \qquad (7)$$

$$\dot{Z} = \frac{\partial \dot{\mathbf{r}}}{\partial \mathbf{q}} \qquad (8)$$

$$\ddot{Z} = \frac{\partial \ddot{\mathbf{r}}}{\partial \mathbf{q}} \qquad (9)$$

Then,

$$\ddot{Z} = AZ + B\dot{Z} + C \qquad (10)$$

where the first six columns of C corresponding to the injection conditions $\mathbf{X}_0^B$ are zero. The variational equation (Eq. 10) is integrated numerically by the second-sum method to give Z and $\dot{Z}$ as functions of ephemeris time t. The partial derivative of the probe state vector $\mathbf{X}$ with respect to $\mathbf{q}$ at any time t is

$$\frac{\partial \mathbf{X}}{\partial \mathbf{q}} = \begin{bmatrix} Z \\ \dot{Z} \end{bmatrix} = [U \mid V] \qquad (11)$$

where (noting Eq. 2),

$$U = \frac{\partial \mathbf{X}}{\partial \mathbf{X}_0^B} = \frac{\partial \mathbf{X}(t)}{\partial \mathbf{X}(t_0)} = U(t, t_0) \qquad (12)$$

$$V = \frac{\partial \mathbf{X}}{\partial \mathbf{a}} \qquad (13)$$

For each parameter q_i, three sum and difference numerical integration arrays, each having two sums and 10 differences, are generated. These three sums and difference arrays may be interpolated at any time t to give ∂x, $\dot{x}/\partial q_i$, $\partial \dot{y}, y/\partial q_i$, and $\partial \dot{z}, z/\partial q_i$, respectively, which are the elements of the q_i column of U or V.

When the injection conditions are referred to the center of integration, the initial value of $\partial \mathbf{X}/\partial \mathbf{q}$ at the injection epoch is

$$\left[\frac{\partial \mathbf{X}}{\partial \mathbf{q}} \right]_0 = [I \mid 0] \qquad (14)$$

where I is a 6×6 identity matrix. When the injection conditions are referred to a body B other than the center of integration C,

$$\left[\frac{\partial \mathbf{X}}{\partial \mathbf{q}} \right]_0 = \left[I \mid \frac{\partial (\mathbf{X}_B^C)_0}{\partial \mathbf{a}} \right] \qquad (15)$$

The eighteen sum and difference arrays for the six injection parameters are started at the injection epoch t_0, with $\partial \mathbf{X}/\partial \mathbf{X}_0^B = I$ (6×6) as initial conditions. For reasons that will become evident later, these sum and difference arrays are restarted with initial values I at a number of intermediate epochs t_1, t_2, t_3, $\cdots$, t_n. The U matrix of Eq. (12) is then formed by the chain rule as:

$$U = \frac{\partial \mathbf{X}}{\partial \mathbf{X}_0^B} = \frac{\partial \mathbf{X}(t)}{\partial \mathbf{X}(t_0)} = \frac{\partial \mathbf{X}(t)}{\partial \mathbf{X}(t_n)} \frac{\partial \mathbf{X}(t_n)}{\partial \mathbf{X}(t_{n-1})} \cdots \frac{\partial \mathbf{X}(t_1)}{\partial \mathbf{X}(t_0)}$$

$$= U(t, t_n)U(t_n, t_{n-1}) \cdots U(t_1, t_0) \qquad (16)$$

Similarly, a U matrix from any intermediate epoch t_i to any time t is formed by

$$U(t, t_i) = U(t, t_n)U(t_n, t_{n-1}) \cdots U(t_{i+1}, t_i) \qquad (17)$$

For a dynamic parameter a_i, if the corresponding column of the C matrix is always nonzero, the three sum and difference arrays are started at the injection epoch and continued for the duration of the mission. For each of these parameters, the elements of the column of the V matrix can be obtained by interpolation of the three sum and difference arrays at the desired time t.

For certain other parameters a_i, the C matrix is non-zero only for $t_a < t < t_b$, and the sum and difference arrays are generated only for this interval of time. For $t < t_a$, $\partial X / \partial a_i = 0$. For $t_a < t < t_b$, the column of V is obtained by interpolation of the sum and difference arrays. For $t > t_b$,

$$\frac{\partial X(t)}{\partial a_i} = \frac{\partial X(t)}{\partial X(t_b)} \frac{\partial X(t_b)}{\partial a_i} = U(t, t_b) \frac{\partial X(t_b)}{\partial a_i} \qquad (18)$$

where $\partial X(t_b) / \partial a_i$ is obtained from the sum and difference arrays at the stop time t_b, and $U(t, t_b)$ is obtained from Eq. (17) using $t_i = t_b$.

Some parameters have an initial value $\partial X(t_b) / \partial a_i$ at a discontinuity epoch t_b, and the column of the C matrix is zero for all time. For this case, $\partial X(t) / \partial a_i$ is computed directly from Eq. (18); no sum and difference arrays are generated for this type of parameter.

Some parameters are a combination of the two previous cases. A period of time $t_a < t < t_b$ exists when the column of C is nonzero and sum and difference arrays are generated; also there are several epochs where discontinuities to the partial derivatives occur. At each discontinuity epoch or stop time for sum and difference arrays, the increment to the partial derivative is added to the accumulated partial and mapped to the next discontinuity epoch or start time for sum and difference arrays (using Eq. 17). If the discontinuity occurs during the integration of the sum and difference arrays, they must be restarted using the incremented partial derivatives as initial values. For $t_a < t < t_b$, $\partial X / \partial a_i$ may be obtained directly by interpolation. Otherwise, the accumulated value of $\partial X / \partial a_i$ at the last discontinuity epoch or stop time for sum and difference arrays is mapped to the current time, using Eqs. 17 and 18.

3. Computation of A Matrix

a. Introduction. The formulation for computing the acceleration of the probe relative to the center of integration appears in Part III of this series (SPS 37-41, Vol. III, pp. 24–31). The terms of the probe acceleration vector that are a function of the probe position vector are:

(1) The direct Newtonian point mass acceleration due to each celestial body i (nine planets, Sun, and Moon).

(2) The direct Newtonian acceleration due to oblateness for each oblate body j.

(3) The acceleration due to the solar radiation pressure (SRP) and attitude control (AC) models.

The A matrix is computed from the following sum of terms:

$$A = \sum_i \frac{\partial \ddot{\mathbf{r}}_{Newtonian}^{(i)}}{\partial \mathbf{r}} + \sum_j \frac{\partial \ddot{\mathbf{r}}_{oblate}^{(j)}}{\partial \mathbf{r}} + \frac{\partial \ddot{\mathbf{r}}(SRP - AC)}{\partial \mathbf{r}} \qquad (19)$$

The formulation for computing each of these terms is given in the succeeding sections. The notation used is that of Part III. All vectors appearing in the formulation are column vectors.

b. Contribution from Newtonian point mass acceleration. From Eq. (9) of Part III, the direct term of the Newtonian point mass acceleration due to body i is

$$\ddot{\mathbf{r}} = - \frac{\mu_i (\mathbf{r} - \mathbf{r}_i)}{\|\mathbf{r} - \mathbf{r}_i\|^3} \qquad (20)$$

Differentiating with respect to $\mathbf{r}$ gives

$$\frac{\partial \ddot{\mathbf{r}}}{\partial \mathbf{r}} = \frac{3\mu_i (\mathbf{r} - \mathbf{r}_i)(\mathbf{r} - \mathbf{r}_i)^T}{\|\mathbf{r} - \mathbf{r}_i\|^5} - \frac{\mu_i I}{\|\mathbf{r} - \mathbf{r}_i\|^3} \qquad (21)$$

where I is a 3×3 identity matrix.

c. Contribution from oblateness acceleration. The acceleration due to the oblateness of one celestial body

is given by Eqs. (23), (27), (28) and associated formulas of Part III. Differentiating Eq. (23) with respect to $\mathbf{r}$ gives

$$\frac{\partial \ddot{\mathbf{r}}}{\partial \mathbf{r}} = \left[\frac{\partial G^T}{\partial x} \ddot{\mathbf{r}}', \frac{\partial G^T}{\partial y} \ddot{\mathbf{r}}', \frac{\partial G^T}{\partial z} \ddot{\mathbf{r}}' \right] + G^T \left[\frac{\partial \ddot{\mathbf{r}}'(J)}{\partial \mathbf{r}'} + \frac{\partial \ddot{\mathbf{r}}'(C,S)}{\partial \mathbf{r}} \right] G \qquad (22)$$

where

$$\frac{\partial G^T}{\partial x} = G^T \text{ with each term differentiated with respect to } x$$

$$\frac{\partial G^T}{\partial x} \ddot{\mathbf{r}}' = \text{first column of first term}$$

$$\ddot{\mathbf{r}}' = \ddot{\mathbf{r}}'(J) + \ddot{\mathbf{r}}'(C,S) \qquad (23)$$

$$\frac{\partial \ddot{\mathbf{r}}'}{\partial \mathbf{r}'} = \left[\frac{\partial \ddot{\mathbf{r}}'}{\partial x'}, \frac{\partial \ddot{\mathbf{r}}'}{\partial y'}, \frac{\partial \ddot{\mathbf{r}}'}{\partial z'} \right] = \left[\frac{\partial \ddot{\mathbf{r}}'}{\partial r}, \frac{1}{r \cos \phi} \frac{\partial \ddot{\mathbf{r}}'}{\partial \lambda}, \frac{1}{r} \frac{\partial \ddot{\mathbf{r}}'}{\partial \phi} \right] \qquad (24)$$

Differentiating Eqs. (27) and (28) of Part III gives

$$\frac{\partial \ddot{\mathbf{r}}'(J)}{\partial x'} = -\frac{1}{r} \sum_{n=1}^{n_1} (n+2)\ddot{\mathbf{r}}'(J_n) \qquad (25)$$

$$\frac{\partial \ddot{\mathbf{r}}'(J)}{\partial y'} = 0 \qquad (26)$$

$$\frac{\partial \ddot{\mathbf{r}}'(J)}{\partial z'} = \frac{\mu}{r^3} \sum_{n=1}^{n_1} J_n \left(\frac{a_p}{r} \right)^n \begin{bmatrix} (n+1) \cos \phi \, P'_n \\ 0 \\ \sin \phi \, P'_n - \cos^2 \phi \, P''_n \end{bmatrix} \qquad (27)$$

$$\frac{\partial \ddot{\mathbf{r}}'(C,S)}{\partial x'} = -\frac{1}{r} \sum_{n=1}^{n_2} (n+2) \sum_{m=1}^{n} \left[\ddot{\mathbf{r}}'(C_{nm}) + \ddot{\mathbf{r}}'(S_{nm}) \right] \qquad (28)$$

$$\frac{\partial \ddot{\mathbf{r}}'(C,S)}{\partial y'} = \frac{\mu}{r^3} \sum_{n=1}^{n_2} \sum_{m=1}^{n} m \left(\frac{a_p}{r} \right)^n \begin{bmatrix} (n+1) \sec \phi \, P_n^m \, (C_{nm} \sin m\lambda - S_{nm} \cos m\lambda) \\ m \sec^2 \phi \, P_n^m \, (-C_{nm} \cos m\lambda - S_{nm} \sin m\lambda) \\ P_n^{m'} \, (-C_{nm} \sin m\lambda + S_{nm} \cos m\lambda) \end{bmatrix} \qquad (29)$$

$$\frac{\partial \ddot{\mathbf{r}}'(C,S)}{\partial z'} = \frac{\mu}{r^3} \sum_{n=1}^{n_2} \sum_{m=1}^{n} \left(\frac{a_p}{r} \right)^n \begin{bmatrix} -(n+1) \cos \phi \, P_n^{m'} \, (C_{nm} \cos m\lambda + S_{nm} \sin m\lambda) \\ m (\sin \phi \sec^2 \phi \, P_n^m + P_n^{m'})(-C_{nm} \sin m\lambda + S_{nm} \cos m\lambda) \\ (\cos^2 \phi \, P_n^{m''} - \sin \phi \, P_n^{m'}) \, (C_{nm} \cos m\lambda + S_{nm} \sin m\lambda) \end{bmatrix} \qquad (30)$$

From Eq. (19) of Part III,

$$G^T = T \, R^T \qquad (31)$$

where R is a function of the probe position and T is a function of time. Thus,

$$\frac{\partial G^T}{\partial x} = T \frac{\partial R^T}{\partial x} \qquad x \to y, z \qquad (32)$$

Let

$$R^T = \begin{bmatrix} e_{11} & e_{12} & e_{13} \\ e_{21} & e_{22} & e_{23} \\ e_{31} & e_{32} & e_{33} \end{bmatrix} \qquad (33)$$

where the expressions for the elements may be obtained from Eq. (16) of Part III. Then

$$\frac{\partial R^{\mathrm{T}}}{\partial x} = \begin{bmatrix} \dfrac{\partial e_{11}}{\partial x} & \dfrac{\partial e_{12}}{\partial x} & \dfrac{\partial e_{13}}{\partial x} \\[2mm] \dfrac{\partial e_{21}}{\partial x} & \dfrac{\partial e_{22}}{\partial x} & \dfrac{\partial e_{23}}{\partial x} \\[2mm] \dfrac{\partial e_{31}}{\partial x} & \dfrac{\partial e_{32}}{\partial x} & \dfrac{\partial_{33}}{\partial x} \end{bmatrix} \quad x \to y, z \quad (34)$$

$$\frac{\partial e_{ij}}{\partial \mathbf{r}} = \left(\frac{\partial e_{ij}}{\partial x}, \frac{\partial e_{ij}}{\partial y}, \frac{\partial e_{ij}}{\partial z} \right) = \frac{\partial e_{ij}}{\partial \mathbf{r}'} G \quad (35)$$

and

$$\frac{\partial e_{ij}}{\partial \mathbf{r}'} = \left(\frac{\partial e_{ij}}{\partial r}, \frac{1}{r \cos \phi} \frac{\partial e_{ij}}{\partial \lambda}, \frac{1}{r} \frac{\partial e_{ij}}{\partial \phi} \right) \quad (36)$$

Differentiating each e_{ij} gives

$$\frac{\partial e_{11}}{\partial \mathbf{r}'} = \left[0, -\frac{\sin \lambda}{r}, -\frac{\sin \phi \cos \lambda}{r} \right] \quad (37)$$

$$\frac{\partial e_{21}}{\partial \mathbf{r}'} = \left[0, \frac{\cos \lambda}{r}, -\frac{\sin \phi \sin \lambda}{r} \right] \quad (38)$$

$$\frac{\partial e_{31}}{\partial \mathbf{r}'} = \left[0, 0, \frac{\cos \phi}{r} \right] \quad (39)$$

$$\frac{\partial e_{12}}{\partial \mathbf{r}'} = \left[0, -\frac{\cos \lambda}{r \cos \phi}, 0 \right] \quad (40)$$

$$\frac{\partial e_{22}}{\partial \mathbf{r}'} = \left[0, -\frac{\sin \lambda}{r \cos \phi}, 0 \right] \quad (41)$$

$$\frac{\partial e_{32}}{\partial \mathbf{r}'} = [0, 0, 0] \quad (42)$$

$$\frac{\partial e_{13}}{\partial \mathbf{r}'} = \left[0, \frac{\sin \phi \sin \lambda}{r \cos \phi}, -\frac{\cos \phi \cos \lambda}{r} \right] \quad (43)$$

$$\frac{\partial e_{23}}{\partial \mathbf{r}'} = \left[0, -\frac{\sin \phi \cos \lambda}{r \cos \phi}, -\frac{\cos \phi \sin \lambda}{r} \right] \quad (44)$$

$$\frac{\partial e_{33}}{\partial \mathbf{r}'} = \left[0, 0, -\frac{\sin \phi}{r} \right] \quad (45)$$

The terms $\partial G^{\mathrm{T}}/\partial x$, $\partial G^{\mathrm{T}}/\partial y$, and $\partial G^{\mathrm{T}}/\partial z$ are obtained by substituting Eqs. (37)–(45) into Eq. (35) to give the 27 terms of $\partial R^{\mathrm{T}}/\partial x$, $\partial R^{\mathrm{T}}/\partial y$, and $\partial R^{\mathrm{T}}/\partial z$. Given these, the desired matrices are computed from Eq. (32).

The complete formulation for computing Legendre polynomials for the oblateness acceleration terms and the corresponding partial derivatives follows.

Legendre polynomials and derivatives $(n = 1, 2, 3, \cdots, n_1)$. The Legendre polynomial P_n is computed recursively from

$$P_n = \frac{2n-1}{n} \sin \phi\, P_{n-1} - \left(\frac{n-1}{n} \right) P_{n-2} \quad (46)$$

beginning with

$$\begin{aligned} P_0 &= 1 \\ P_1 &= \sin \phi \end{aligned} \quad (47)$$

The first derivative of P_n with respect to $\sin \phi$, denoted P'_n, is given by

$$P'_n = \sin \phi\, P'_{n-1} + n P_{n-1} \quad (48)$$

starting with

$$P'_1 = 1 \quad (49)$$

Differentiation of Eq. (48) with respect to $\sin \phi$ gives

$$P''_n = \sin \phi\, P''_{n-1} + (n + 1) P'_{n-1} \quad (50)$$

beginning with

$$P''_1 = 0 \quad (51)$$

Associated Legendre functions and derivatives $(m = 2, 3, \cdots, n; \ n = 2, 3, \cdots, n_2)$. Compute $\sec^2 \phi\, P_n^m$ by first generating

$$\sec^2 \phi\, P_m^m = (2m - 1) \cos \phi\, (\sec^2 \phi\, P_{m-1}^{m-1}) \quad (52)$$

for $m = 2, 3, \cdots, n_2$, starting with

$$\sec^2 \phi\, P_2^2 = 3 \quad (53)$$

and then generating

$$\sec^2 \phi \, P_n^m = \left(\frac{2n-1}{n-m}\right) \sin \phi \, (\sec^2 \phi \, P_{n-1}^m)$$

$$- \left(\frac{n+m-1}{n-m}\right)(\sec^2 \phi \, P_{n-2}^m) \quad (54)$$

In Eq. (54), for each value of m between 2 and n_2, n is varied from $m+1$ to n_2. The general term P_a^b in Eq. (54) is zero if $b > a$.

The derivative of P_n^m with respect to $\sin \phi$, denoted $P_n^{m'}$, is computed from

$$P_n^{m'} = -n \sin \phi \, (\sec^2 \phi \, P_n^m) + (n+m)(\sec^2 \phi \, P_{n-1}^m) \quad (55)$$

Multiplying Eq. (55) by $\cos^2 \phi$ and differentiating with respect to $\sin \phi$ gives

$$\cos^2 \phi \, P_n^{m''} = -(n-2) \sin \phi \, P_n^{m'} + (n+m) P_{n-1}^{m'} - nP_n^m \quad (56)$$

Associated Legendre functions and derivations $(m = 1;$ $n = 1, 2, 3, \cdots, n_2)$.

Compute

$$\sec \phi \, P_n^1 = \left(\frac{2n-1}{n-1}\right) \sin \phi \, (\sec \phi \, P_{n-1}^1)$$

$$- \left(\frac{n}{n-1}\right)(\sec \phi \, P_{n-2}^1) \quad (57)$$

starting with

$$\sec \phi \, P_1^1 = 1 \quad (58)$$

Multiply Eq. (57) by $\cos \phi$ and $1/\cos \phi$ to give P_n^1 and $\sec^2 \phi \, P_n^1$, the latter of which is indeterminate for $\phi = 90$ deg.

Compute

$$\cos \phi \, P_n^{1'} = -n \sin \phi \, (\sec \phi \, P_n^1) + (n+1)(\sec \phi \, P_{n-1}^1) \quad (59)$$

Multiplication by $1/\cos \phi$ gives $P_n^{1'}$, which is indeterminate for $\phi = 90$ deg.

The following sums are not indeterminate when $\phi = 90$ deg, although their individual terms are

$$(\sin \phi \, \sec^2 \phi \, P_n^1 + P_n^{1'}) = \sec \phi \, P_n^2 \quad (60)$$

$$(\cos^2 \phi \, P_n^{1''} - \sin \phi \, P_n^{1'}) = -P_n^1 - 3 \sin \phi \, (\sec \phi \, P_n^2) + P_n^3 \quad (61)$$

The Legendre functions that are indeterminate for $\phi = 90$ deg appear in Eq. (29).

d. Contribution from solar radiation pressure and attitude control models. The acceleration of the probe due to the solar radiation pressure and attitude control models is given by Eq. (37) of Part III. The probe position $\mathbf{r}$ affects r_{SP}, EPS, and the unit vectors $\mathbf{U}_{SP}$, $\mathbf{X}^*$, and $\mathbf{Y}^*$. Hence,

$$\frac{\partial \ddot{\mathbf{r}}}{\partial \mathbf{r}} = -\frac{2}{r_{SP}} \ddot{\mathbf{r}}_{SRP} \mathbf{U}_{SP}^T + (\ddot{\mathbf{r}} \cdot \mathbf{U}_{SP}) \frac{\partial \mathbf{U}_{SP}}{\partial \mathbf{r}} + (\ddot{\mathbf{r}} \cdot \mathbf{X}^*) \frac{\partial \mathbf{X}^*}{\partial \mathbf{r}}$$

$$+ (\ddot{\mathbf{r}} \cdot \mathbf{Y}^*) \frac{\partial \mathbf{Y}^*}{\partial \mathbf{r}} + \frac{C_1 A_p}{mr_{SP}^2} (G_r' \mathbf{U}_{SP} + G_x' \mathbf{X}^*$$

$$+ G_y' \mathbf{Y}^*) \frac{\partial EPS}{\partial \mathbf{r}} \mu^* (t - T_{SRP}) \quad (62)$$

where

$\ddot{\mathbf{r}}$ = acceleration of probe due to solar radiation pressure and attitude control (terms of Eq. 37)

$\ddot{\mathbf{r}}_{SRP}$ = acceleration of probe due to solar radiation pressure (terms of Eq. 37 proportional to A_p)

From Eq. (38) of Part III,

$$\frac{\partial \mathbf{U}_{SP}}{\partial \mathbf{r}} = \left[\frac{\partial \mathbf{U}_{SP}}{\partial x}, \frac{\partial \mathbf{U}_{SP}}{\partial y}, \frac{\partial \mathbf{U}_{SP}}{\partial z}\right] = \frac{1}{r_{SP}}[I - \mathbf{U}_{SP}\mathbf{U}_{SP}^T] \quad (63)$$

From Eq. (39) of Part III,

$$\begin{bmatrix} \partial \mathbf{X}^*/\partial \mathbf{r} \\ \partial \mathbf{Y}^*/\partial \mathbf{r} \end{bmatrix} = \begin{bmatrix} \cos K & \sin K \\ -\sin K & \cos K \end{bmatrix} \begin{bmatrix} \partial \mathbf{T}/\partial \mathbf{r} \\ \partial \mathbf{N}/\partial \mathbf{r} \end{bmatrix} \quad (64)$$

From Eq. (42) of Part III,

$$\frac{\partial \mathbf{N}}{\partial \mathbf{r}} = \frac{1}{\| \mathbf{U}_R \times \mathbf{U}_{SP} \|} [I - \mathbf{N}\mathbf{N}^T] \left\{ \left[\mathbf{U}_R \times \frac{\partial \mathbf{U}_{SP}}{\partial x} ; \mathbf{U}_R \times \frac{\partial \mathbf{U}_{SP}}{\partial y} ; \mathbf{U}_R \times \frac{\partial \mathbf{U}_{SP}}{\partial z} \right] \right.$$
$$\left. + \left[\frac{\partial \mathbf{U}_R}{\partial x} \times \mathbf{U}_{SP} ; \frac{\partial \mathbf{U}_R}{\partial y} \times \mathbf{U}_{SP} ; \frac{\partial \mathbf{U}_R}{\partial z} \times \mathbf{U}_{SP} \right] \right\} \tag{65}$$

If the reference body B is a star,

$$\frac{\partial \mathbf{U}_R}{\partial \mathbf{r}} = \left[\frac{\partial \mathbf{U}_R}{\partial x}, \frac{\partial \mathbf{U}_R}{\partial y}, \frac{\partial \mathbf{U}_R}{\partial z} \right] = 0 \tag{66}$$

If the reference body B is a planet or the Moon, we obtain from Eq. (41) of Part III,

$$\frac{\partial \mathbf{U}_R}{\partial \mathbf{r}} = \left[\frac{\partial \mathbf{U}_R}{\partial x}, \frac{\partial \mathbf{U}_R}{\partial y}, \frac{\partial \mathbf{U}_R}{\partial z} \right] = - \frac{1}{\| \mathbf{r}_B^C - \mathbf{r} \|} [I - \mathbf{U}_R \mathbf{U}_R^T] \tag{67}$$

From Eq. (43) of Part III,

$$\frac{\partial \mathbf{T}}{\partial \mathbf{r}} = \left[\frac{\partial \mathbf{N}}{\partial x} \times \mathbf{U}_{SP} ; \frac{\partial \mathbf{N}}{\partial y} \times \mathbf{U}_{SP} ; \frac{\partial \mathbf{N}}{\partial z} \times \mathbf{U}_{SP} \right]$$
$$+ \left[\mathbf{N} \times \frac{\partial \mathbf{U}_{SP}}{\partial x} ; \mathbf{N} \times \frac{\partial \mathbf{U}_{SP}}{\partial y} ; \mathbf{N} \times \frac{\partial \mathbf{U}_{SP}}{\partial z} \right] \tag{68}$$

From Eq. (44) of Part III,

$$\frac{\partial EPS}{\partial \mathbf{r}} = \frac{1}{\sin EPS} \left[\mathbf{U}_R'^T \frac{\partial \mathbf{U}_{SP}}{\partial \mathbf{r}} + \mathbf{U}_{SP}^T \frac{\partial \mathbf{U}_R'}{\partial \mathbf{r}} \right] \tag{69}$$

where $\partial \mathbf{U}_R'/\partial \mathbf{r}$ is computed from Eq. (67) using $\mathbf{U}_R'$ instead of $\mathbf{U}_R$.

4. Computation of B Matrix

None of the terms of the probe acceleration specified in Part III are functions of the probe velocity. Hence, for Phase 1 of the DPODP,

$$B = 0 \tag{70}$$

where the zero indicates a 3 × 3 null matrix.

5. C Matrix and Integration Tables for Each Parameter

In this section, the remaining partial derivatives necessary to generate the three sum and difference arrays for

each parameter will be specified. These include the column of the C matrix and discontinuities to the columns of the Z and $\dot{Z}$ matrices for each parameter q_i.

a. Injection parameters. The method of generating the 18 sum and difference arrays for the six injection parameters has been specified in Section 2. These sum and difference arrays are also used to compute the mapping matrices $U(t, t_i)$ from Eq. (17), which in turn are used in computing the V matrix.

b. Reference parameters $(A_E, R_E, \text{ and } E \text{ only})$. The reference parameters $\mathbf{f}$ include A_E, R_E, E for each ephemeris to be corrected, and μ_E and μ_m. They affect the position vectors $\mathbf{r}_i$ of the planets, Moon, and Sun relative to the center of integration, and hence affect the Newtonian point mass and oblate acceleration of the probe due to these bodies. The partial derivative of the probe acceleration $\ddot{\mathbf{r}}$ with respect to the reference parameters $\mathbf{f}$ (due to moving the perturbing bodies) is given by

$$\frac{\partial \ddot{\mathbf{r}}}{\partial \mathbf{f}} = \sum_i \frac{\partial \ddot{\mathbf{r}}}{\partial \mathbf{r}_i} \frac{\partial \mathbf{r}_i}{\partial \mathbf{f}} \tag{71}$$

where

$$\frac{\partial \ddot{\mathbf{r}}}{\partial \mathbf{r}_i} = \mu_i \left[\frac{3\mathbf{r}_i \mathbf{r}_i^T}{r_i^5} - \frac{I}{r_i^3} \right] - \mu_i \left[\frac{3(\mathbf{r} - \mathbf{r}_i)(\mathbf{r} - \mathbf{r}_i)^T}{\| \mathbf{r} - \mathbf{r}_i \|^5} \right.$$
$$\left. - \frac{I}{\| \mathbf{r} - \mathbf{r}_i \|^3} \right] - \frac{\partial \ddot{\mathbf{r}}}{\partial \mathbf{r}} \text{ (from Eq. 22)} \tag{72}$$

The first two terms of Eq. (72) are the derivatives of the Newtonian point mass acceleration (Eq. 9, Part III) with respect to $\mathbf{r}_i$. The last term is the derivative of the probe acceleration due to the oblateness of body i with respect to $\mathbf{r}_i$. This acceleration is a function of $(\mathbf{r} - \mathbf{r}_i)$. Hence $\partial \ddot{\mathbf{r}}/\partial \mathbf{r}_i = - \partial \ddot{\mathbf{r}}/\partial \mathbf{r}$ computed from Eq. (22).

The acceleration due to solar radiation pressure and attitude control (SRP–AC) is affected by the positions of

the Sun, Earth, and reference body (for roll control) relative to the center of integration. Eq. (72) should include a term for the partial derivative of $\mathbf{r}(SRP-AC)$ with respect to $\mathbf{r}_i$ when i equals the Sun, Earth, or reference body. However, these terms are small and have been ignored.

Section 2 of Part III gives the formulas for computing corrected position and velocity vectors for the heliocentric ephemeris of a planet or the Earth–Moon barycenter or for the geocentric lunar ephemeris. Also, the corrected position and velocity vectors of the Moon relative to the Earth are broken down into the position and velocity vectors of the barycenter relative to the Earth and of the Moon relative to the barycenter. The relative position or

velocity vector between two bodies (a planet, Sun, or Moon) is computed as a sum of the above vectors (see table of Part III). Correspondingly, the partial derivative of the relative position or velocity between two bodies with respect to $\mathbf{f}$ may be computed as the sum of partial derivatives of each subvector with respect to $\mathbf{f}$. The partial derivatives of each basic position or velocity vector with respect to the reference parameters that affect it are obtained from the derivatives of Eqs. (1)–(4) of Part III:

$$\delta \mathbf{r}_p^S = \frac{\mathbf{r}_p^S}{A_E} \delta A_E + \frac{\partial \mathbf{r}_p^S}{\partial \mathbf{E}_p} \delta \mathbf{E}_p \qquad (73)$$

$$\delta \mathbf{r}_M^E = \frac{\mathbf{r}_M^E}{R_E} \delta R_E + \frac{\partial \mathbf{r}_M^E}{\partial \mathbf{E}_M} \delta \mathbf{E}_M \qquad (74)$$

$$\delta \mathbf{r}_M^B = \frac{\mathbf{r}_M^B}{R_E} \delta R_E + \frac{\mu}{1+\mu} \frac{\partial \mathbf{r}_M^E}{\partial \mathbf{E}_M} \delta \mathbf{E}_M + \frac{\mathbf{r}_M^E}{(1+\mu)^2 \mu_M} \delta \mu_E - \frac{\mu \mathbf{r}_M^E}{(1+\mu)^2 \mu_M} \delta \mu_M \qquad (75)$$

$$\delta \mathbf{r}_B^E = \frac{\mathbf{r}_B^E}{R_E} \delta R_E + \frac{1}{1+\mu} \frac{\partial \mathbf{r}_M^E}{\partial \mathbf{E}_M} \delta \mathbf{E}_M - \frac{\mathbf{r}_M^E}{(1+\mu)^2 \mu_M} \delta \mu_E + \frac{\mu \mathbf{r}_M^E}{(1+\mu)^2 \mu_M} \delta \mu_M \qquad (76)$$

---

and

$$\delta \mathbf{r} \rightarrow \delta \dot{\mathbf{r}}, \ \mathbf{r} \rightarrow \dot{\mathbf{r}}, \ \partial \mathbf{r}/\partial \mathbf{E} \rightarrow \partial \dot{\mathbf{r}}/\partial \mathbf{E}$$

In Eqs. (73)–(76), all position and velocity vectors are corrected values.

The sum and difference arrays for the reference parameters A_E, R_E, and $\mathbf{E}$ for each ephemeris to be corrected are started at the injection epoch T_{inj} and continued for the duration of the mission. The initial values of $\partial \mathbf{X}/\partial q_i$ are obtained from Eqs. (14) or (15), as appropriate. The columns of the C matrix are obtained from Eq. (71). At a change of phase (change of center of integration), $\partial \mathbf{X}/\partial q_i$ must be incremented by the following value, which necessitates a restart of the sum and difference arrays.

$$\Delta \frac{\partial \mathbf{X}}{\partial q_i} = \frac{\partial \mathbf{X}_0^N}{\partial q_i} \qquad (77)$$

where

$\mathbf{X}_0^N$ = state vector of old center of integration relative to new center of integration at time of phase change, rectangular components referred to mean Earth equator and equinox of 1950.0.

c. Gravitational constants μ_j. The gravitational constants μ_j for the planets, Sun, and Moon affect the New-

tonian point mass and oblate acceleration terms directly. The constants μ_E and μ_M are reference parameters, and hence may also affect these acceleration terms indirectly. Also, they may produce nonzero initial values at the injection epoch and discontinuities to the partials at phase changes.

The sum and difference arrays for the μ_j are started at the injection epoch with initial values given by Eqs. (14) or (15). They may be nonzero for μ_E or μ_M if the injection conditions are not referred to the center of integration. The column of the C matrix for μ_j is given by

$$\frac{\partial \ddot{\mathbf{r}}}{\partial \mu_j} = \frac{\ddot{\mathbf{r}}(\mu_j)}{\mu_j} + \sum_i \frac{\partial \ddot{\mathbf{r}}}{\partial \mathbf{r}_i} \frac{\partial \mathbf{r}_i}{\partial \mu_j} \qquad (78)$$

where $\ddot{\mathbf{r}}(\mu_j)/\mu_j$ is the sum of the Newtonian point mass and oblate accelerations due to body j, computed with $\mu_j = 1$ (one term of Eqs. 9 and 23 of Part III). The second term of Eq. (78) may be nonzero for $\mu_j = \mu_E$ or μ_M, and is obtained from Eq. (71). At a change of phase, $\partial \mathbf{X}/\partial \mu_E$ and $\partial \mathbf{X}/\partial \mu_M$ must be incremented by Eq. (77), necessitating a restart of the sum and difference arrays.

d. Harmonic coefficients (J_n, C_{nm}, S_{nm}). The acceleration terms due to the harmonic coefficients J_n, C_{nm}, S_{nm}

of an oblate body are computed only when the distance of the probe from the center of the body is less than a value specified by the user (radius of the "harmonic sphere" for that body). Thus, the three sum and difference arrays for each harmonic coefficient are started when the probe enters the harmonic sphere (or at injection) and are terminated when the probe leaves the harmonic sphere. The initial value of $\partial X/\partial q_i$ is zero. The columns of the C matrix for each J_n, C_{nm}, and S_{nm} are computed from

$$\frac{\partial \ddot{\mathbf{r}}}{\partial J_n} = \frac{\ddot{\mathbf{r}}(J_n)}{J_n} \qquad (79)$$

$$\frac{\partial \ddot{\mathbf{r}}}{\partial C_{nm}} = \frac{\ddot{\mathbf{r}}(C_{nm})}{C_{nm}} \qquad (80)$$

$$\frac{\partial \ddot{\mathbf{r}}}{\partial S_{nm}} = \frac{\ddot{\mathbf{r}}(S_{nm})}{S_{nm}} \qquad (81)$$

The acceleration due to each J_n, C_{nm}, and S_{nm} may be obtained from Eqs. (23), (27), and (28) of Part III. However, instead of dividing the acceleration term by the coefficient (which may have an *a priori* value of zero), it is simply computed using a value of unity for the coefficient.

e. Coefficients of solar radiation pressure and attitude control model.

The acceleration of the probe due to the SRP–AC model is given by Eq. (37) of Part III. The columns of the C matrix for the 15 parameters appearing explicitly in the model are

$$\frac{\partial \ddot{\mathbf{r}}}{\partial a_r} = \mathbf{U}_{SP} \qquad (82)$$

$$\frac{\partial \ddot{\mathbf{r}}}{\partial a_x} = \mathbf{X}^* \qquad (83)$$

$$\frac{\partial \ddot{\mathbf{r}}}{\partial a_y} = \mathbf{Y}^* \qquad (84)$$

$$\frac{\partial \ddot{\mathbf{r}}}{\partial b_i} = \frac{\partial \ddot{\mathbf{r}}}{\partial a_i}(t - T_{AC1}) \qquad i = r, x, \text{ or } y \qquad (85)$$

$$\frac{\partial \ddot{\mathbf{r}}}{\partial c_i} = \frac{\partial \ddot{\mathbf{r}}}{\partial a_i}(t - T_{AC1})^2 \qquad i = r, x, \text{ or } y \qquad (86)$$

$$\frac{\partial \ddot{\mathbf{r}}}{\partial G_r} = \frac{C_1 A_p}{mr_{SP}^2} \mathbf{U}_{SP}\mu^*(t - T_{SRP}) \qquad (87)$$

$$\frac{\partial \ddot{\mathbf{r}}}{\partial G_x} = \frac{C_1 A_p}{mr_{SP}^2} \mathbf{X}^*\mu^*(t - T_{SRP}) \qquad (88)$$

$$\frac{\partial \ddot{\mathbf{r}}}{\partial G_y} = \frac{C_1 A_p}{mr_{SP}^2} \mathbf{Y}^*\mu^*(t - T_{SRP}) \qquad (89)$$

$$\frac{\partial \ddot{\mathbf{r}}}{\partial G_r'} = \frac{\partial \ddot{\mathbf{r}}}{\partial G_r}(EPS), \qquad G_r \rightarrow G_r, G_y \qquad (90)$$

The three sum and difference arrays for each of the nine AC parameters are started at T_{AC1}, using zero for the initial values of the partial derivatives, and continued to the epoch T_{AC2}. The three sum and difference arrays for each of the six SRP parameters are started at T_{SRP}, using zero for the initial values of the partial derivatives, and continued for the remainder of the mission. Each time the probe passes into and out of a shadow, all sum and difference arrays must be restarted.

f. Coefficients of finite burn motor model.

The acceleration due to a finite motor burn is given by Eq. (45) of Part III. The columns of the C matrix for the polynomial coefficients F_i, α_i, and δ_i are

$$\frac{\partial \ddot{\mathbf{r}}}{\partial F_i} = \frac{t^i C}{m(t)} \mathbf{U} \qquad (91)$$

$$\frac{\partial \ddot{\mathbf{r}}}{\partial \alpha_i} = a \begin{bmatrix} -\cos\delta\sin\alpha \\ \cos\delta\cos\alpha \\ 0 \end{bmatrix} t^i \qquad (92)$$

$$\frac{\partial \ddot{\mathbf{r}}}{\partial \delta_i} = a \begin{bmatrix} -\sin\delta\cos\alpha \\ -\sin\delta\sin\alpha \\ \cos\delta \end{bmatrix} t^i \qquad (93)$$

The three sum and difference arrays for each of these parameters are started at T_0 with zero initial conditions and terminated at $T_f = T_0 + T$.

The three sum and difference arrays for $T_0(\text{UTC})$ are started at T_0 using as initial conditions:

$$\frac{\partial X(T_0)}{\partial T_0(\text{UTC})} = -\begin{bmatrix} 0(3 \times 1) \\ \hline a(T_0)\mathbf{U}(T_0) \end{bmatrix} \qquad (94)$$

The column of the C matrix for $T_0(\text{UTC})$ is

$$\frac{\partial \ddot{\mathbf{r}}}{\partial T_0(\text{UTC})} = -[\dot{a}\mathbf{U} + a\dot{\mathbf{U}}] \qquad (95)$$

where

$$\dot{a} = \frac{F_1 + 2F_2 t + 3F_3 t^2 + 4F_4 t^3}{m(t)} C$$
$$+ \frac{a}{m(t)} (\dot{M}_0 + \dot{M}_1 t + \dot{M}_2 t^2 + \dot{M}_3 t^3) \qquad (96)$$

$$\dot{\mathbf{U}} = \begin{bmatrix} -\dot{\alpha} \cos\delta \sin\alpha - \dot{\delta} \sin\delta \cos\alpha \\ \dot{\alpha} \cos\delta \cos\alpha - \dot{\delta} \sin\delta \sin\alpha \\ \dot{\delta} \cos\delta \end{bmatrix} \qquad (97)$$

and

$$\dot{\alpha} = \alpha_1 + 2\alpha_2 t + 3\alpha_3 t^2 + 4\alpha_4 t^3 \qquad (98)$$

$$\dot{\delta} = \delta_1 + 2\delta_2 t + 3\delta_3 t^2 + 4\delta_4 t^3 \qquad (99)$$

The sum and difference arrays for $T_0(\text{UTC})$ are terminated at $T_f = T_0 + T$, and the following increment to the partial derivatives is added:

$$\Delta \frac{\partial \mathbf{X}(T_f)}{\partial T_0(\text{UTC})} = \begin{bmatrix} 0(3 \times 1) \\ -a(T_f)\dot{\mathbf{U}}(T_f) \end{bmatrix} \qquad (100)$$

The initial value of the partial derivative with respect to T occurs at T_f:

$$\frac{\partial \mathbf{X}(T_f)}{\partial T} = \begin{bmatrix} 0(3 \times 1) \\ -a(T_f)\dot{\mathbf{U}}(T_f) \end{bmatrix} \qquad (101)$$

There are no sum and difference arrays for the parameter T.

g. *Parameters for instantaneous burn motor model.* A motor burn of short duration or a spring separation may be represented as a discontinuity to the probe trajectory. The rectangular components of the velocity increment $\Delta\dot{\mathbf{r}}$ and the burn time t_b are the solve-for parameters. The increment to the probe position at the maneuver epoch T_M is computed as

$$\Delta \mathbf{r} = \frac{1}{2} \Delta\dot{\mathbf{r}} t_b \qquad (102)$$

There are no sum and difference arrays for these four parameters. However, the initial values of the partial

derivatives at T_M are:

$$\left[\frac{\partial \mathbf{X}}{\partial \Delta\dot{x}}, \frac{\partial \mathbf{X}}{\partial \Delta\dot{y}}, \frac{\partial \mathbf{X}}{\partial \Delta\dot{z}}, \frac{\partial \mathbf{X}}{\partial t_b} \right] = \begin{bmatrix} \frac{1}{2}t_b & 0 & 0 & \frac{1}{2}\Delta\dot{x} \\ 0 & \frac{1}{2}t_b & 0 & \frac{1}{2}\Delta\dot{y} \\ 0 & 0 & \frac{1}{2}t_b & \frac{1}{2}\Delta\dot{z} \\ 1 & 0 & 0 & 0 \\ 0 & 1 & 0 & 0 \\ 0 & 0 & 1 & 0 \end{bmatrix}$$
$$(103)$$

h. *Parameters affecting transformation from atomic time (A.1) to ephemeris time (ET).* The parameters ΔT_{1958} and Δf_{cesium} affect the ET values of the following epochs, specified in a known time scale (A.1, UTC, UT1, or ST but usually UTC):[18]

(1) Injection, T_{inj}

(2) Unfolding of solar panels, T_{SRP}

(3) Start and stop times for attitude control polynomials, T_{AC1} and T_{AC2}

(4) Epoch of instantaneous maneuver, T_M

(5) Start time of finite burn motor, T_0

Since the acceleration versus time curve for the finite burn motor is shifted in ET, sum and difference arrays for ΔT_{1958} and Δf_{cesium} must be generated from T_0 to $T_f = T_0 + T$. Also, discontinuities to the partial derivatives with respect to ΔT_{1958} and Δf_{cesium} occur at T_{inj}, T_{SRP}, T_{AC1}, T_{AC2}, and T_M.

The partial derivatives of the ET value of an epoch T specified in the A.1, UTC, UT1, and ST time scales with respect to ΔT_{1958} and Δf_{cesium} are (see Part II; SPS 37-39, Vol. III, pp. 36–38):

$$\frac{\partial T(\text{ET})}{\partial \Delta T_{1958}} = 1 \qquad (104)$$

$$\frac{\partial T(\text{ET})}{\partial \Delta f_{cesium}} = - \frac{(\text{JD} - 243,6204.5)(86,400)}{9,192,631,770} \qquad (105)$$

An infinitesimal change in the injection epoch $dT_{inj}(\text{ET})$ is equivalent to the following changes in the injection

---

[18] All terms are defined in Parts II and III of this series.

position $\mathbf{r}_0$ and velocity $\dot{\mathbf{r}}_0$ relative to the center of integration:

$$d\mathbf{r}_0 = - \dot{\mathbf{r}}_0^B \, dT_{inj}(\mathrm{ET}) \qquad (106)$$

$$d\dot{\mathbf{r}}_0 = - \ddot{\mathbf{r}}_0^B \, dT_{inj}(\mathrm{ET}) \qquad (107)$$

where

$\dot{\mathbf{r}}_0^B$ = solve-for velocity probe relative to body B at injection epoch

$\ddot{\mathbf{r}}_0^B$ = acceleration of probe relative to body B at injection epoch

Hence, the initial values of the partial derivatives of $\mathbf{X}$ with respect to ΔT_{1958} and Δf_{cesium} at the injection epoch are

$$\frac{\partial \mathbf{X}(T_{inj})}{\partial \Delta T_{1958}} = - \begin{bmatrix} \dot{\mathbf{r}}_0^B \\ \ddot{\mathbf{r}}_0^B \end{bmatrix} \qquad (108)$$

$$\frac{\partial \mathbf{X}(T_{inj})}{\partial \Delta f_{cesium}} = \frac{[\mathrm{JD}(T_{inj}) - 243,6204.5]\,(86,400)}{9,192,631,770} \begin{bmatrix} \dot{\mathbf{r}}_0^B \\ \ddot{\mathbf{r}}_0^B \end{bmatrix} \qquad (109)$$

Similarly, at the epoch T_M of an instantaneous maneuver, $\partial \mathbf{X}/\partial(\Delta T_{1958})$ and $\partial \mathbf{X}/\partial(\Delta f_{cesium})$ must be incremented by

$$\Delta \frac{\partial \mathbf{X}(T_M)}{\partial \Delta T_{1958}} = \begin{bmatrix} -\Delta \dot{\mathbf{r}} \\ \ddot{\mathbf{r}}_1 - \ddot{\mathbf{r}}_2 \end{bmatrix} \qquad (110)$$

$$\Delta \frac{\partial \mathbf{X}(T_M)}{\partial \Delta f_{cesium}} = \frac{[\mathrm{JD}(T_M) - 243,6204.5]\,(86,400)}{9,192,631,770} \begin{bmatrix} \Delta \dot{\mathbf{r}} \\ \ddot{\mathbf{r}}_2 - \ddot{\mathbf{r}}_1 \end{bmatrix} \qquad (111)$$

where

$\ddot{\mathbf{r}}_2 = \ddot{\mathbf{r}}$ at T_M after $\Delta \mathbf{r}, \Delta \dot{\mathbf{r}}$ have been added

$\ddot{\mathbf{r}}_1 = \ddot{\mathbf{r}}$ at T_M before $\Delta \mathbf{r}, \Delta \dot{\mathbf{r}}$ have been added

At the epoch T_{SRP} where the solar panels are unfolded, the partial derivatives must be incremented by

$$\Delta \frac{\partial \mathbf{X}(T_{SRP})}{\partial \Delta T_{1958}} = - \begin{bmatrix} 0(3 \times 1) \\ \ddot{\mathbf{r}}_{SRP}(T_{SRP}) \end{bmatrix} \qquad (112)$$

$$\Delta \frac{\partial \mathbf{X}(T_{SRP})}{\partial \Delta f_{cesium}} =$$

$$\frac{[\mathrm{JD}(T_{SRP}) - 243,6204.5]\,(86,400)}{9,192,631,770} \begin{bmatrix} 0(3 \times 1) \\ \ddot{\mathbf{r}}_{SRP}(T_{SRP}) \end{bmatrix} \qquad (113)$$

Since the attitude control accelerations are extremely small, the increments to the partial derivatives at T_{AC1} and T_{AC2} have been ignored.

The three sum and difference arrays for ΔT_{1958} and for Δf_{cesium} are started at T_0 for the finite burn motor and terminated at $T_f = T_0 + T$. The initial values of the partial derivatives are given by

$$\frac{\partial \mathbf{X}(T_0)}{\partial \Delta T_{1958}} = - \begin{bmatrix} 0(3 \times 1) \\ a(T_0)\mathbf{U}(T_0) \end{bmatrix} \qquad (114)$$

$$\frac{\partial \mathbf{X}(T_0)}{\partial \Delta f_{cesium}} = \frac{[\mathrm{JD}(T_0) - 243,6204.5]\,(86,400)}{9,192,631,770} \begin{bmatrix} 0(3 \times 1) \\ a(T_0)\mathbf{U}(T_0) \end{bmatrix} \qquad (115)$$

The increments to the partial derivatives occurring prior to T_0 are mapped to T_0 and added to the above values. The columns of the C matrix are computed from

$$\frac{\partial \ddot{\mathbf{r}}}{\partial \Delta T_{1958}} = - [\dot{a}\,\mathbf{U} + a\,\dot{\mathbf{U}}] \qquad (116)$$

$$\frac{\partial \ddot{\mathbf{r}}}{\partial \Delta f_{cesium}} = \frac{[\mathrm{JD}(T_0) - 243,6204.5]\,(86,400)}{9,192,631,770} [\dot{a}\,\mathbf{U} + a\,\dot{\mathbf{U}}] \qquad (117)$$

At T_f, the partial derivatives must be incremented by

$$\Delta \frac{\partial \mathbf{X}(T_f)}{\partial \Delta T_{1958}} = \begin{bmatrix} 0(3 \times 1) \\ a(T_f)\mathbf{U}(T_f) \end{bmatrix} \qquad (118)$$

$$\Delta \frac{\partial \mathbf{X}(T_f)}{\partial \Delta f_{cesium}} =$$

$$- \frac{[\mathrm{JD}(T_0) - 243,6204.5]\,(86,400)}{9,192,631,770} \begin{bmatrix} 0(3 \times 1) \\ a(T_f)\mathbf{U}(T_f) \end{bmatrix} \qquad (119)$$

6. Conclusion

The solution to the variational equations is the matrix $\partial \mathbf{X}/\partial \mathbf{q}$ given by Eq. (11). The U matrix is computed using Eq. (16). Each column of the V matrix corresponding to

parameter q_i is obtained by one or more of the following methods:[19]

(1) Interpolation of the three sum and difference arrays for q_i.

(2) Mapping forward the final partial derivatives from discontinued sum and difference arrays, using Eq. (18).

(3) Mapping forward a discontinuity to the partial derivative using Eq. (18).

F. The JPL Double Precision Matrix Manipulation Program, *P. M. Muller*[20]

1. Introduction

As a name for this study, double precision matrix manipulation program (DPMMP) is not very descriptive, but was chosen because of similarity to the computer program that it replaces and expands. The matrix manipulation program is what is usually referred to as a normal program and is designed primarily to simulate the statistical expectations of complex deep-space missions. It will compute statistics derived from an orbit determination program (ODP) based upon real or simulated data. The ODP produces partial derivatives and other related quantities, which are then processed by DPMMP in a fashion similar to that which takes place in the ODP's own normal link. (For DPODP-related equations and discussions, see SPS 37-39, Vol. III, pp. 36–38, and subsequent issues of Vol. III.) This first article will be followed by others documenting more specific portions of the program.

2. General Program Objectives

The most important objective of the program is to have completely controllable user options which can also undergo periodic updating of the coding to include new options. This is necessary because the program is designed to simulate complex space missions, and it is impossible to specify in advance all of the capabilities that may be of interest to JPL in the design and consideration of advanced unmanned space flights. The second objective is to have an efficient program with convenient user input. Efficiency is important because of the large

number of calculations required for an engineer's study. Because of the complexity of control required, and the general lack of appreciation for programming constraints, convenient input is important. The third objective is to include an almost bewildering array of possible models, methods, and systems of calculation. These will be clarified in future articles.

3. Function of the Program

The program computes covariance matrices on various sets of parameters, based upon partial derivatives of the several data types with respect to the parameters. For the reader not familiar with the process of Bayes' estimation theory, a general description will be found in SPS 37-42, Vol. III, p. 14. The partial derivatives and other necessary input are derived from an ODP, or any similar program, and are input on tape or cards or a combination. These partial derivatives may be weighted or unweighted by data type, considering either uncorrelated or correlated data types. The resulting normal equations (or **J** matrix) are inverted to form the covariance matrix. The set of initial parameters may be mapped into several other possible sets and may be expressed in any of several coordinate systems.

A model for simulation of midcourse maneuver is available, and *a priori* conditions on the **J** matrix can be varied. Statistics resulting from data correlated with time can be accepted by the program. The statistical uncertainties on certain parameters may be held fixed. Biased data may be simulated, and data biases may be solved-for. The program will accept the residuals on the input data types at each time point and will produce a first solution after the fit by obtaining a new value for each parameter estimated. There are also a number of other minor options, as well as numerous coordinate systems for output of statistics and uncertainties.

4. Programming System

This program is written entirely in FORTRAN IV and is executed on the 7094 direct couple (7044) system. It has been structured to minimize difficulty of conversion to the new-generation computer and will handle matrix size up to and including a dimension of 50 × 50. When converted to a new computer with expanded core, the dimension may be easily increased. The DPMMP will be programmed[21] under the matrix operations programming

---

[19]For details, see Section 2, p. 33.

[20]D. Curkendall, D. Trask, G. Null, D. Grimes, K. Russell, and the author shared work on the initial program specifications and equations.

[21]Captain D. E. Hilt, who is serving his army tour at JPL, has been responsible for the logical design of this program, and will accomplish the programming.

(MOP) system documented in SPS 37-42, Vol. III, pp. 12–15, a FORTRAN IV matrix programming system. This means that the matrix algebra is highly subroutinized.

The main program will be subroutinized into four general blocks: First, read, test, and structure the user input, input tape (if any), and punched input (if any); second, accumulate the J matrix by whichever options are requested by the user; third, produce a set of covariance matrices; fourth, do the mapping of parameter sets and coordinate transformations and print the results. The program allows several examples of the basic user-input options to be submitted, and will consider and execute each option in turn. The corresponding parametric study will allow completion of an engineering report in one or two computer runs.

5. General Design Philosophy

Each option, however small, including input–output, shall be individually controllable by the user. There is a flag in the program for each option. This vector of control words is input on a punched card as (1) a single vector of integers, (2) a vector of integers for each block of the program, or (3) a flag by name (NAME = value). Under FORTRAN IV name-list input the user may have a file of cards that set the whole program, a large subset, or any individual flag, exactly as desired. The input link accomplishes logical function tests of the user input, and adjusts any flags so that the program will run thereafter without a user-induced delay. The input tape is constructed so that the program can read it regardless of which of the possible inputs are present. This universal tape format allows the program to be driven by independent sources. Card input is handled similarly via name lists, which allow any, all, or none of the input to be made with cards. With a standard set of input controls the casual user can process either a tape or card input in small or large quantities. The sophisticated user will have nearly the flexibility of a programmer running a machine-language program who sets up his coding to select program options by so-called octal correctors. The logic flow of the program is strictly linear, and new options satisfying this constraint can be rapidly coded, even on a temporary basis.

G. Capabilities Summary of the Residual Analysis Program, R. L. Motsch

1. Introduction

The residual analysis program (RAP) is a FORTRAN IV program capable of operating on JPL's IBM 7094 direct couple operating system (DCOS) installations. The purpose of the program is to form sets of residuals on the DSN tracking measurements of angles, doppler, and range, and to analyze these residuals by means of auto-correlation functions, power spectra, and various statistical measures. Output is in the form of listings, plots, or punched cards. A general flow chart of RAP is given in Fig. 23. In the paragraphs that follow, a brief description of RAP capabilities is given, following the flow of Fig. 23.

2. Program Summary

a. Input. Initial tape input to RAP is in the form of a data tape, called the TDP B1 tape,[22] and, on option, a compatible reference tape, called the PREDIX tape.[23] The TDP B1 tape is essentially a "clean" version of the DSN tracking data, while the PREDIX tape is essentially a model of what the tracking data is expected to be. Initial card input to RAP falls into three categories. First of these are the specification cards, which give RAP the following instructions:

(1) The tape, station, and data type to use.

(2) The reference options desired.

(3) The processing options desired.

(4) The output options desired.

(5) The observation period desired.

Second is an optional set of input cards that list titles to be placed on the output options, and third is a set of cards defining program parameters. Checks are made by RAP on all input, and appropriate error messages are printed if errors exist.

b. Data update. Initially, and whenever a new tracking station is specified, RAP creates a file of all the tracking data of the specified station that exist on the TDP master file. If PREDIX has been requested as a reference option, a compatible file for the specified station is also formed from the PREDIX master file.

c. Data search. Once the above file(s) has been created, the requested data type for the time range specified is collected. If the specified time range cannot be satisfied,

[22]Holzman, R. E., *Users' Guide to the Tracking Data Processor and Orbit Data Generator Programs,* Jet Propulsion Laboratory, Pasadena, Calif., May 27, 1965 (Reorder 65-205).

[23]Royer, D., *The JPL Predicts System,* Engineering Planning Document 373, Jet Propulsion Laboratory, Pasadena, Calif., May 1, 1966.

RAP picks a range that best approximates the requested range.
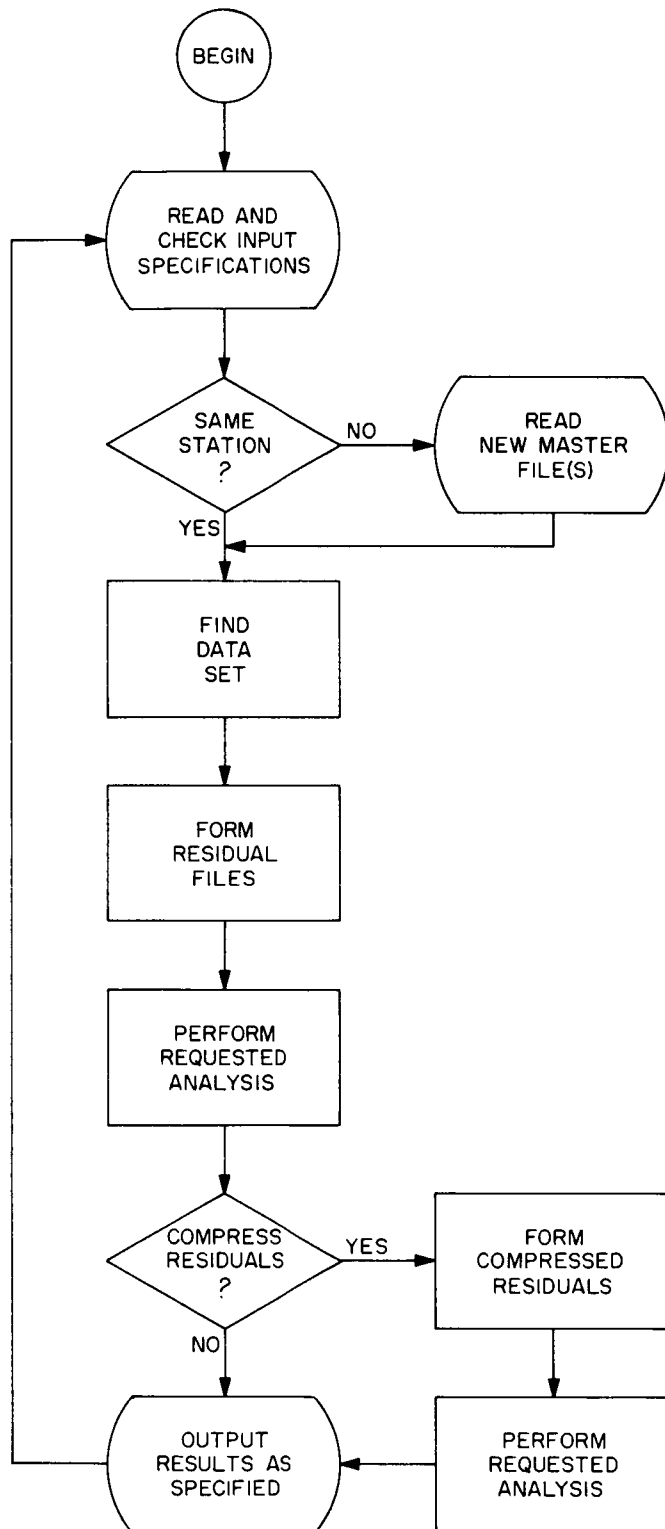
Fig. 23. RAP: General overall flow

d. Residual file formation. Residual files can be formed in three ways, depending on the user's choice of reference. As mentioned above, the PREDIX file may be used as a reference, in which case the residuals are formed by differencing the tracking data with the PREDIX values. Alternatively, RAP will fit the tracking data with one or more polynomials up to order twenty, and the residuals are then formed about these polynomials. Finally, the effect of the Earth's rotation alone may be removed by RAP from the tracking data, and the user may then optionally fit one or more polynomials up to order twenty and form residuals.

e. Residual processing. There are several ways in which RAP processes the residuals. First they are edited by use of an $n\sigma$ scheme, by which points that fall out of the $n\sigma$ bounds are considered bad, n being specified by the user and σ being the standard deviation on the "good" points. Both local sigmas and residual sums are maintained for the good data. In addition, the user may request that an autocorrelation and power spectra be run on the good data. Hamming weights are used for the power spectra computation, but can be replaced by weights of the user's chioce.

f. Residual compression. It is often useful to be able to compare the statistics of the same tracking data taken at different sampling intervals (see SPS 37-38, Vol. III, pp. 13–20, for an example of this type of analysis). To this end, RAP will form "compressed" residuals, which are simply residuals formed at count times greater than the sampling interval at which the data was taken.

g. Compressed residual processing. In addition to the analysis mentioned earlier (*e*), RAP will perform statistical comparisons of the compressed residuals. For instance, by a proper choice of data span and compression interval, RAP will determine the statistics on compressed residuals formed about zenith time, thereby making it possible to isolate ionospheric effects on the data.

h. Output. A wide range of output options is available to RAP, consisting of printouts, plots, and punched cards on all of the processing options mentioned above (*e* and *g*). One or more of the output options may be specified by the user for each of the processing options used.

3. Projected Program Usage

RAP has been written as an experimental data processing program and, as such, will be subject to periodic revisions. At these times any capabilities that may prove

to be of dubious value will be removed, and other new capabilities may be added. At present, the following capabilities are being considered for addition:

(1) A digital filtering scheme for the residuals. This would allow the removal of unwanted periodicities from the data. (See SPS 37-41, Vol. III, pp. 57–59, for an example of this type of analysis.)

(2) The addition of ODP (Ref. 7) as a reference file. This seems desirable, since ODP is the primary orbit fitting program.

(3) A method of introducing data by means of punched cards at appropriate processing junctures within RAP. At the present time, RAP will produce punched cards at any of the processing junctures. Thus, the punched data may be processed in some special way by programs other than RAP. It would be useful, however, if this process could be reversed, so that such data could be reintroduced to RAP. (See SPS 37-43, Vol. III, pp. 37–39, for an example where such procedures were necessary.)

As new methods of data-processing and parameter estimation are developed through the use of RAP, they will be introduced into the operational programs of JPL, or new operational programs will be written to exploit the new methods.

H. DSN Flight Project Support, J. P. Brenkle

1. Introduction

The DSN has provided support to outside projects including the *Atlas/Centaur* tests *A/C 2, A/C 3, A/C 5, A/C 6, A/C 8,* and *A/C 9,* the *Pioneer VI* and *VII* flights, and the *Lunar Orbiter I, II,* and *III* flights. Similar DSN support is also planned for the remaining *Pioneer* and *Lunar Orbiter* flights; however, the nature of the DSN participation in these outside projects is changing. In the past, the DSN has provided consultation service to (1) the Lewis Research Center on the conduct of the *Atlas/Centaur* tests, (2) Ames Research Center on the launch and flight operations of the *Pioneer* missions, and (3) the Langley Research Center and The Boeing Company on the conduct of launch and flight operations. The DSN is now using as well as supporting the *Pioneer* and *Lunar Orbiter* spacecraft. With two live *Pioneer* spacecraft (*Pioneers VI* and *VII*) in heliocentric orbits and two live *Lunar Orbiter* spacecraft (*Lunar Orbiters II* and *III*) in selenocentric orbits, a group of JPL DSN experiments have evolved to use these spacecraft as calibration satel-

lites. Experiments have been identified to improve the knowledge of the lunar and planetary ephemerides, the gravitational field of the Moon, the determination of station locations, the evaluation of ranging data, and the calibration of new DSN and MSFN tracking stations.

2. Pioneer Tracking Data Experiments

a. Pioneer celestial mechanics investigation. A celestial mechanics experiment[24] has been officially approved by NASA Headquarters. This gives the celestial mechanics investigation the same status as the other six *Pioneer* fields and particles experiments, and the DSN tracking data, as well as the telemetry data, are now part of the tracking and data acquisition support required by the *Pioneer* Project.

b. Pioneer VI DSS 12 tracking test. A special *Pioneer VI* tracking pass was scheduled from the DSS 12 (Goldstone Echo) 85-ft antenna on December 20, 1966. The purpose of this pass, which occurred at a time when *Pioneer VI* was at a local minimum distance from the Earth, was to determine if *Pioneer VI* could be tracked from a distance of approximately 129,000,000 km, and then to use these tracking data to update the *Pioneer VI* orbit. Since *Pioneer VI* had not been tracked from an 85-ft DSN station antenna since July 1966, it was desired to obtain a more precise orbit determination as a basis for validating the tracking data from the DSS 14 (Goldstone Mars) 210-ft antenna which were being accumulated for support of the celestial mechanics investigation. The evaluation of this special pass of DSS 12 tracking data is continuing.

c. Pioneer VI and VII DSS 14 tracking data validation. Efforts to process and calibrate tracking data from the 210-ft DSS 14 antenna for support of the celestial mechanics investigation are continuing.

d. Pioneer VII occulation experiment. The DSN *Pioneer* Flight Path Analysis and Control (FPAC) Team supported the *Pioneer VII* occultation experiment by the Stanford Tracking Station. A precise orbit determination was accomplished, and the best estimate of the orbit and the orbit uncertainties were mapped to the time of lunar occultation to predict the uncertainties in the times of lunar encounter (see Sections I and J).

A trajectory run was also made to determine which DSN stations were expected to observe the occultation

---

[24]J. D. Anderson of JPL Section 312 has been appointed the principal investigator for this experiment.

sequence. It was found that occultation as seen from the Australian stations (DSS 41 and DSS 42) would occur before the rise time for either station; however, it was determined that the Australian stations would be able to track the *Pioneer VII* spacecraft during the occultation times as seen from Stanford and Goldstone. The time of occultation as seen from Goldstone differed considerably from the Stanford observations. These differences in occultation times result from the parallax caused by different station locations on Earth and the great distance between the Moon and *Pioneer VII* spacecraft. (This situation is not the same as *Mariner* or *Lunar Orbiter* occultations which occur at about the same time for all Earth stations because of the small distance between the planet or Moon and the spacecraft.)

A separate calculation and an estimate of the predicted occultation times were made for both DSS 12 and Stanford. The actual occultation and emerge times were recorded in real time at DSS 12 and are compared in Table 9.

Table 9. Occultation time comparison

	Predicted	Actual	Actual —predicted, sec
DSS 12 occultation	05:21:17	05:21:19	2
Stanford occultation	05:30:05	05:30:33 ±10[a]	28 ±10
Stanford emergence	05:48:34	05:48:32 ±10[a]	−2 ±10
DSS 12 emergence	06:11:58	06:11:45	−13
[a] See Section J.			

e. Pioneer VII DSS 62 station location estimate. Lunar Orbiter III was the first mission scheduled for support by DSS 62. Since the station location had not been surveyed by a geodetic tie with the European Datum, it was necessary to use the orbit determination program to solve for the station location. The *Pioneer VII* spacecraft had been tracked as part of its normal support and a precise orbit determination had been accomplished. It was determined that approximately three tracking passes of *Pioneer VII* would provide sufficient tracking data to determine an accurate DSS 62 station location. It was also determined that it would be advisable to have the DSS 12 at Goldstone or other DSN stations track between the DSS 62 passes to provide strength to the orbit determination (OD) solution.

Table 10 indicates the amount of tracking data collected on a priority basis for the DSS 62 station location

Table 10. Tracking data

DSS	GMT	Date
42	0500–1345	January 24, 1967
62	1330–0100	January 24–25, 1967
12	2100–0830	January 24–25, 1967
51	1200–2130	January 25, 1967
62	1330–0100	January 25–26, 1967
42	0430–1330	January 26, 1967
62	1330–0100	January 27–28, 1967
11	2045–0430	January 27–28, 1967
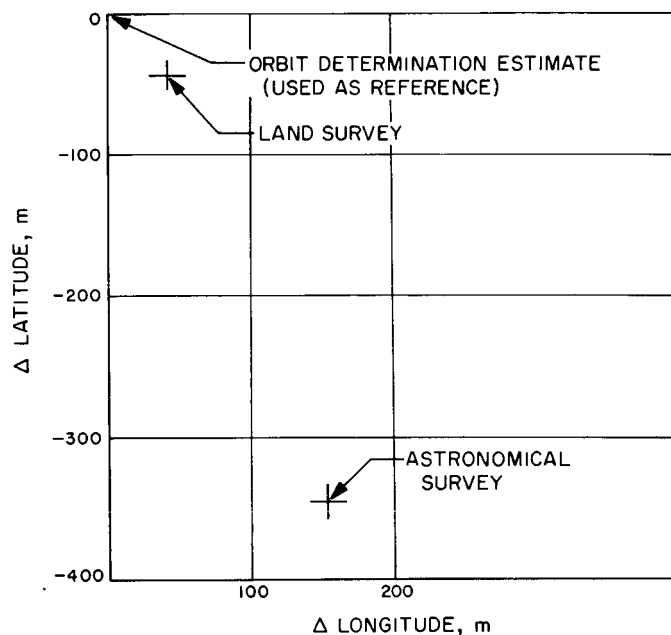
Fig. 24. Comparison of survey locations and orbit determination estimate

estimate. These data were combined with the earlier *Pioneer VII* tracking data to solve for the DSS 62 location. The results indicate that, compared with the OD estimate, the astronomical survey was in error by approximately 380 m (see Fig. 24). A land survey completed at a later date provided a comparison between the astronomical survey and the OD station location estimate. The land survey falls between the astronomical survey and the OD estimate, and approximately 60 m from the OD estimate (as shown in Fig. 24).

3. Lunar Orbiter tracking data experiments

a. Lunar Orbiter selenodesy experiment. The selenodesy experiment is the primary objective of the *Lunar*

48

Orbiter extended mission. Doppler and ranging tracking data are being processed and evaluated for the Langley Research Center and JPL selenodesy experimenters.

b. DSN station time synchronization. A procedure is being developed by the DSIF to use the Mark I ranging system to calibrate the DSN station clocks to within 10 μsec (SPS 37-42, Vol. III, pp. 61–67).

c. Mark I ranging system evaluation. The use of ranging data as a new data type has been evaluated using the *Lunar Orbiter I*, *II*, and *III* flights. Preliminary results (SPS 37-42, Vol. III, pp. 61–67, and SPS 37-43, Vol. III, pp. 24–28) indicate that the Mark I ranging system will be able to meet its accuracy specifications of ±15 m (1 σ).

d. Improved lunar ephemeris evaluation. Ranging data from the *Lunar Orbiter II* flight was used to evaluate Eckert's correction to the lunar ephemeris (SPS 37-43, Vol. III, pp. 24–28). The improved lunar ephemeris has been adopted as the new ephemeris for the *Lunar Orbiter* Project.

e. Proposed ranging calibration experiment. This experiment has been proposed to the *Lunar Orbiter* Project by the DSN Inherent Accuracy Project. The purpose of the doppler–ranging calibration experiment is to acquire doppler and ranging data from operating *Lunar Orbiter* spacecraft to:

(1) Analyze error sources that affect doppler and ranging systems differently.

(2) Demonstrate that the effects of the above error sources can be determined by use of ground calibration tests and actual flight data so that valuable calibrated tracking data can be produced for the selenodesy experiment, the lunar ephemeris improvement project, and other tracking data users.

(3) Evaluate and calibrate the Mark II planetary ranging system and develop operating procedures for handling the Mark II planetary ranging data for the *Mariner* Venus 67 Project.

It is proposed that this experiment be conducted in two phases:

Phase I: Between March 15, and April 30, 1967 (before the Lunar Orbiter D launch readiness date). Phase I of the doppler–ranging calibration experiment will utilize the Mark I A ranging system at DSS 12 (Echo, Goldstone) to obtain tracking data at rates up to 1 point/sec.

Eight passes of *Lunar Orbiter* tracking data have been requested for Phase I of the doppler–ranging calibration experiment.

Phase II: Between June 1 and the end of year 1967 (after the Lunar Orbiter D photographic mission). Phase II of the doppler–ranging calibration experiment will also use the Mark II ranging system at DSS 14 (Mars, Goldstone). The minimum objective of Phase II is the operational checkout of the Mark II ranging system for the *Mariner* Venus 67 Project. It is also anticipated that the Mark II ranging system, particularly if tracking a high-inclination, long-period *Lunar Orbiter D* spacecraft, will provide more precise results for the comparison of doppler and ranging tracking data. Use of the Mark II ranging system will reduce the data handling problem, since data rates of 1 point/min will probably be sufficient (see Sections A and D).

f. Apollo ground operational support system (GOSS) navigation qualification. A new *Lunar Orbiter* experiment is being planned, the primary purpose of which is the qualification of the *Apollo* MSFN, including the unified S-band system (USBS) and the navigation subsystem of the real time computer complex (RTCC) at Houston.[25] This experiment is divided into three phases:

Phase A: (December 15, 1966 to April 30, 1967). This will include the collection and processing by the RTCC of two-way tracking data from the DSN and three-way tracking data from the MSFN. The three-way tracking by the MSFN will be coincident with the scheduled tracking passes by the DSN.

Phase B: (May 1, 1967 to August 31, 1967). This will include two-way tracking of *Lunar Orbiter* spacecraft by the MSFN; no ranging data will be obtained. During the first half of Phase A, three passes per month are to be tracked by part of the MSFN; during the second half, two passes per month are to be tracked by the entire MSFN.

Phase C: (September 1, 1967 to December 31, 1967). This will include two-way doppler and ranging tracking data once per month by the entire MSFN.

During Phases B and C, the DSN will be scheduled to take three orbits of tracking data during each scheduled MSFN tracking pass. The first orbit will have overlapping

---

[25]*Support Instrumentation Requirements Document*, Apollo GOSS Navigation Qualification, December 15, 1967 (available from Langley Research Center).

coverage by two DSN stations (one station in a two-way mode and the other in a three-way mode) to determine a precise orbit for comparison purposes by the Manned Spacecraft Center (MSC) RTCC. This precise orbit will also be used to satisfy some of the selenodesy tracking data requirements and the *Lunar Orbiter* Project requirements for orbit updating, and may satisfy the requirements of other *Lunar Orbiter* tracking experiments.

A real challenge in the *Apollo* GOSS navigation qualification is the requirement to evaluate the *Lunar Orbiter* thrust maneuvers by use of tracking and telemetry data.

I. Pioneer VII Orbit Determination in Support of the Lunar Occultation Experiment, F. L. Paulsen

Pioneer VII was launched on August 17, 1966, and was occulted by the Moon on January 20, 1967. One week before occultation, on January 13, 1967, JPL's single precision orbit determination program (SPODP) was used to fit a trajectory over the arc of the spacecraft orbit, using the most recent data then available. In the fit, 60-sec two-way doppler data taken at DSS 12 and DSS 51 between December 27, 1966, and January 9, 1967, were used. The data included are given below. Each date represents a full pass of data.

DSS 51: December 28, December 29, December 30, January 3, January 5, January 8, January 9.

DSS 12: December 27, December 30.

The amount of data included in the fit was a compromise between (1) enough data to reduce the uncertainties in the orbit determined, and (2) not so much data that effects of a gas leak would adversely influence the determination.

The gas leak diminishes with time so the effects on the orbit are less for more recent data. A more important factor in the exclusion of early data, however, is that the model does not account for nongravitational forces that exist; therefore, as more data are included an incorrect statistical model will cause an increase in the true variances.

Data taken prior to December 27 are essentially not used in the determination of the orbit. That is, an orbit based on early December data was determined and the results of this determination are used as *a priori* information for the final orbit determination run. However, this

a priori information is degraded by 1000 km in each component of position and 1 km/sec in each component of velocity. The orbit determined on the basis of early December data is given in Table 11.

Table 11. Orbits 203 and 204 (August 19, 1966, 13:00:00.000 GMT)

Position and velocity coordinates	Orbit 203	Orbit 204	Difference
X, km	406338.26	406365.31	27.
Y, km	−22953.34	−23039.21	−86.
Z, km	−8592.08	−8635.41	−43.
DX, m/sec	1897.1528	1897.1596	−0.0060
DY, m/sec	26.6783	26.6902	−0.0080
DZ, m/sec	78.1084	78.1132	−0.0093

As explained in Section B, data noise and station location uncertainties are the main contributors to the probe angular uncertainty with respect to Earth. These effects can be treated as essentially independent. The effect of the data noise is obtained from orbit 204 which did not consider station location uncertainties; an estimate of the actual station location uncertainties can be obtained from SPS 37-43, Vol. III, pp. 3–18.

Based on orbit 204, the predicted angular uncertainties of the spacecraft on January 20, 1967, 05:30:00.000 GMT due to data noise are:

$$\sigma_{\delta_1} = 3.2 \text{ arc sec}$$

$$\sigma_{\alpha_1} = 2.1 \text{ arc sec}$$

The effective data weight on the two-way doppler is 0.1 cps based on 1 sample/min.

It was assumed that station location errors were

$$\sigma_{r_s} = 15 \text{ m}$$

$$\sigma_\lambda = 40 \text{ m}$$

where σ_{r_s} is the error in the station's distance off the spin axis and σ_λ the error in longitude.[26]

---
[26]Because orbit 204 did not use the λ recommended in SPS 37-43, Vol. III, pp. 3–18, $\bar{\sigma}_\lambda = 40$ m is used rather than the value of 30 m suggested in that article by C. J. Vegos and D. W. Trask.

The error produced in the calculation of the probe's geocentric declination, σ_{δ_2} is given by (see Section B)

$$\sigma_{\delta_2} = (\cot \delta) \left(\frac{\sigma_{r_s}}{r_s} \right) (2.06 \times 10^5 \text{ arc sec/rad}) = 1.5 \text{ arc sec}$$

where

δ is the geocentric declination of the probe = 16.4 deg

r_s is the station's distance from the spin axis = 5200 km for DSS 12

The error in right ascension is

$$\sigma_{\delta_2} = (\cot \delta) \left(\frac{\sigma_\lambda}{r_s} \right) (2.06 \times 10^5 \text{ arc sec/rad}) = 1.1 \text{ arc sec}$$

Combining these two error sources,

$$\sigma_\delta = \sqrt{\sigma_{\delta_1}^2 + \sigma_{\delta_2}^2} = 3.8 \text{ sec}$$

$$\sigma_\alpha = \sqrt{\sigma_{\alpha_1}^2 + \sigma_{\alpha_2}^2} = 3.5 \text{ sec}$$

On January 20, 1967, the Earth probe distance was 51,440,000 km; therefore, the corresponding positional uncertainties are 880 km in the declination direction and 670 km in the right ascension direction.

J. *Pioneer VII* Lunar Occultation Calculation and Error Analysis, J. F. Gallagher

1. Summary

This article discusses the methods by which the lunar occultation of the *Pioneer VII* spacecraft was predicted as well as the error analysis that was applied. A comparison of the predicted occultation times with the times observed by the Stanford experimenters shows agreement to within about 15 sec.

2. Introduction

A lunar occultation was one of several mission objectives Ames trajectory engineers sought to satisfy in their design work. Those interested were scientists and engineers at Stanford University Center for Radar Astronomy who wanted to make measurements on a possible lunar ionosphere. After much trajectory design work, it was decided on a practical basis that a lunar occultation was too difficult a matter; i.e., the required launch window was much too short, and injection errors of approximately 2 σ would cause a miss in the occultation. Therefore, it

was planned to first satisfy the other mission objectives and then try to satisfy the lunar occultation objective, if possible. The final nominal trajectory design did *not* include a lunar occultation. However, after the launch and after a good orbit determination, it was discovered that the injection errors, though well within the 3-σ limits, combined in such a way that a lunar occultation would in fact take place. The Stanford experimenters were then able to proceed with preparations for the occultation that was to take place at approximately 5^h30^m GMT on January 20, 1967. Ames trajectory engineers completed occultation time calculations in September 1966; in early October they requested that JPL verify these calculations. JPL undertook this verification as well as an error analysis of the problem.

3. Geometry at Occultation Time

The relationship of the spacecraft, Moon, Earth, and Sun at occultation time is shown in Fig. 25. The coordinates of Fig. 25 are geocentric, true equinox date, and the view is down on the Earth's equatorial plane. The vernal equinox is shown for reference, together with the meridians of Greenwich and the Stanford antenna.

4. Occultation Time Calculations: Methods and Results

a. First method. The times of enter and exit occultation were calculated in two different ways. The first, which was the simpler and more direct, was as follows: Using the JPL trajectory programs SPACE and SFPRO
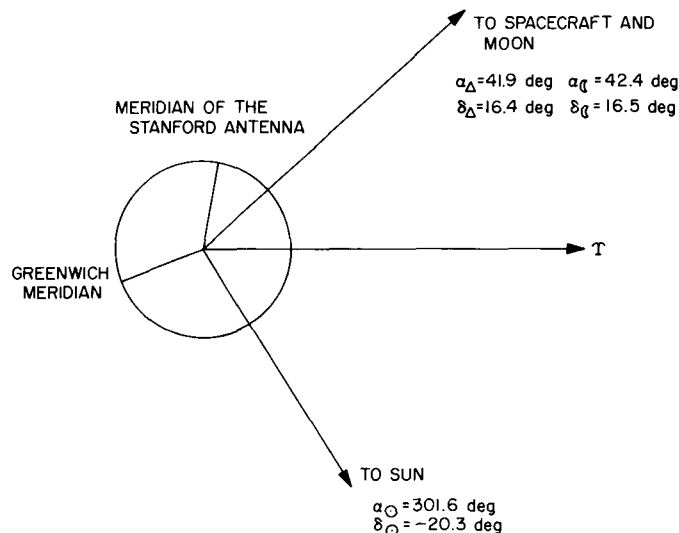
Fig. 25. Geocentric location of the spacecraft, Moon, and Sun at occultation time, January 20, 1967, 5^h30^m GMT

and using the Stanford antenna as the station, the probe–station–Moon angle γ_{psm} was calculated for a series of times during the occultation period, and a graph was drawn of this angle versus time. The angular semidiameter of the Moon as seen from the Stanford antenna, defined as α_s was carefully calculated for the occultation period. The times at which γ_{psm} fell below and rose above α_s marked the enter and exit times, respectively. The change in α_s during the occultation period was found to be small and was ignored.

The calculations outlined above were carried out for four different orbits. For the purposes of this article, they are labeled 1, 2, 3, and 4.

(1) Orbit 1 (*Pioneer VII*, orbit 201) was based on about 23 days of data taken just after completion of the step II orientation maneuver about two days after launch on August 17, 1966.

(2) Orbit 2 (*Pioneer VII*, orbit 202) was based on data taken during the last few days of October and the first few days of November 1966. This orbit was calculated to assess the size and direction of the trajectory change caused by a gas leak aboard the *Pioneer VII* spacecraft.

(3) Orbit 3 (*Pioneer VII*, orbit 203) was based on data taken during early December 1966. It, too, was done to assess the gas leak effect.

(4) Orbit 4 (*Pioneer VII*, orbit 204) was based on data taken during the last four days of December 1966 and first nine days of January 1967. This is believed to be the best description of the *Pioneer VII* orbit.

Plots of the probe–station–Moon angle for the four orbits are shown in Fig. 26. The horizontal dashed line represents the (assumed) constant value of α_s during the occultation period. It can be seen that the time spread among the four trajectories for enter and exit occultation is about 2 min. Reading the enter and exit occultation times for the fourth orbit, considered the best, shows they are $5^h30^m15^s$ and $5^h48^m36^s$, respectively.

b. Second method. The second way in which the occultation times were calculated was as follows: The *topocentric* right ascension and declination of the spacecraft and the Moon were calculated at a series of times during the occultation period with the topos at the Stanford antenna.

The difference in topocentric right ascension between the spacecraft and the center of the Moon, called α, and
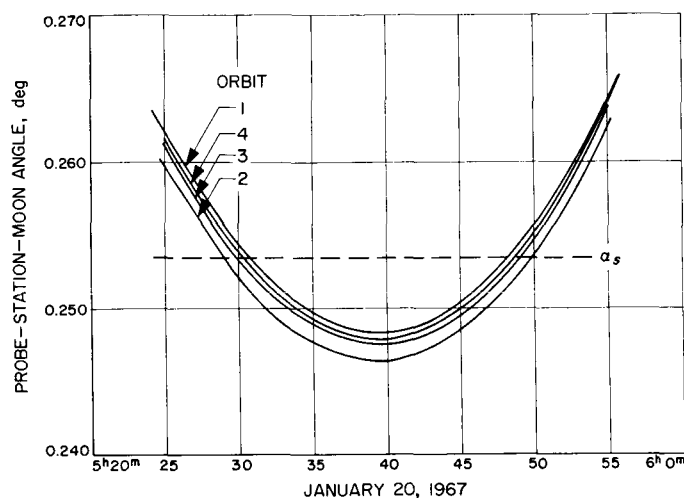
Fig. 26. Probe–station–Moon angle for *Pioneer VII* and the Stanford antenna

the similar quantity for topocentric declination, called δ, were calculated for each time point. A plot of δ versus α was then made using rectangular coordinates. The Moon's disk, being a circle on the celestial sphere, did not map as a circle in these α–δ coordinates; therefore, the α and δ values for the limb of the Moon were carefully calculated and plotted on the same graph. The result is shown in Fig. 27. The line $\alpha = 0$ deg in Fig. 27 is a segment of a meridian circle in the topocentric coordinate system whose X-Y plane is parallel to the Earth's equator. Fig. 27 presents a geometrically realistic view of the occultation as viewed by an observer at the Stanford antenna, who keeps the cross hairs of an equatorially mounted telescope fixed at the center of the Moon's disk and watches the spacecraft pass through the field of view.

Fig. 27 shows only orbits 1 and 2. Orbits 3 and 4 lie between and parallel to orbits 1 and 2 but were not plotted for the sake of neatness. Orbit 4, thought to be the best, lies about one-third of the way from orbit 1 to orbit 2. The transverse lines are lines of constant time and allow us to read the enter and exit occulation times. When we do this for orbit 4, we get about $5^h30^m20^s$ for enter occultation and about $5^h48^m45^s$ for exit occultation. These times compare very well with the times taken from Fig. 26 which can be read more accurately.

5. Error Analysis of the Problem: Method and Results

a. The method. If the spacecraft is not quite where we think it is, the occultation will, of course, occur at a time somewhat different from our predictions. Uncertainties in

52
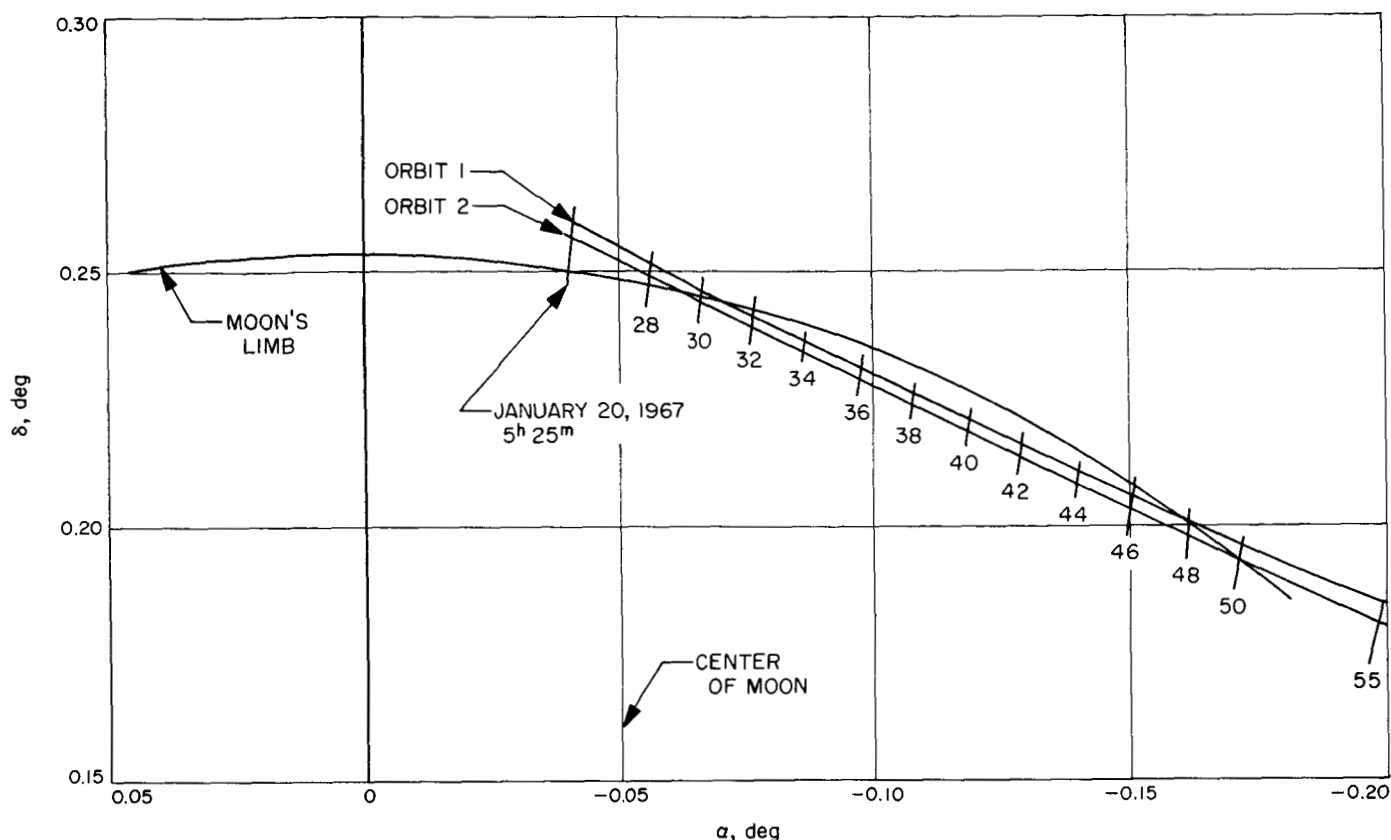
Fig. 27. Trajectory of *Pioneer VII* relative to Moon's disk as viewed by observer at the Stanford antenna

our knowledge of the position of the Moon and the Stanford antenna will also alter the occultation time. To solve the indicated error analysis problem, we select the geocentric Cartesian true equator of date coordinates of the spacecraft and the Moon and the Earth-fixed spherical coordinates of the Stanford antenna as the independent variables of the problem, and the α–δ coordinates already mentioned as the dependent variables. The α–δ system was used to express the problem in terms of coordinates that varied linearly over fairly wide intervals of the independent variables and had partials with respect to these independent variables that were quite constant over the occultation period. The probe–station–Moon angle depicted in Fig. 26 would be a natural choice as a dependent variable, but it was found to be rather nonlinear and to vary rather widely over the occultation period. The occultation times themselves might have been used, but they present problems of continuity and, in any case, are more difficult to formulate analytically.

The error analysis procedure was to write the equations expressing the geometrical relationship between α and δ on the one hand and the position coordinates of the

probe, Moon, and station on the other. Assuming small changes in the independent variables, the following relation holds:

$$\Delta\alpha = A\,\Delta\mathbf{X} \tag{1}$$

where the 9×1 column vector $\Delta\mathbf{X}$ represents the small changes in the independent variables, the 2×9 matrix A is a matrix of partial derivatives of α and δ with respect to the nine independent variables, and the 2×1 matrix represents the resulting changes in α and δ. Eq. (1) can be multiplied on the right by its transpose, and taking the ensemble average over many samples of small changes (errors) in $\mathbf{X}$, one obtains

$$\lambda = A\,\Lambda\,A^{\mathrm{T}} \tag{2}$$

where Λ is the 9×9 covariance matrix of uncertainties in the position coordinates of the spacecraft, Moon, and probe, A is as before and λ is the 2×2 covariance matrix of uncertainties in α and δ. If we make the usual assumption of normally distributed errors in the independent

variables, the errors in α and δ are then distributed normally and the familiar error ellipse results. This error ellipse can be drawn and laid on top of Fig. 27 or on an enlarged view of the occultation areas of Fig. 27, and can be used to provide an estimate of the earliest and latest occultation times for the trajectories contained within the 3-σ error ellipse.

b. The results. The matrix of partial derivatives of α and δ with respect to the nine independent variables are given in Table 12. The elements of the matrix A above were determined by both linear analysis and finite differencing.

Table 12. Partial derivative matrix A

	α	δ
X_p	-0.78×10^{-6}	-0.234×10^{-6}
Y_p	0.86×10^{-6}	-0.21×10^{-6}
Z_p	0	0.1068×10^{-5}
X_M	0.102×10^{-3}	0.300×10^{-4}
Y_M	-0.113×10^{-3}	0.27×10^{-4}
Z_M	0	-0.14×10^{-3}
r_s	0.7×10^{-4}	0.58×10^{-4}
ϕ_s	-0.7×10^{-2}	0.14×10^{-1}
θ_s	0.104×10^{-1}	0.22×10^{-2}
Units are in degrees and kilometers.		

Choosing a covariance matrix of uncertainties in the positions of the spacecraft, Moon, and station involves some guesswork. As far as the spacecraft is concerned, the best information available from the orbit determination engineers at JPL puts the 3-σ uncertainty at about 3000 km. The Moon's position is known to about 5 km, 3 σ. This amounts to about 2.5 sec of arc at the Moon's distance. Actually, the angular position of the Moon is known better than the radial position; therefore, the uncertainty in Cartesian coordinates depends upon the Moon's position. However, 5 km is a good representative figure for all three Cartesian directions. As far as the Stanford antenna is concerned, a guess was made. Generous estimates for the 3-σ uncertainties in radial and angular position of the antenna are 0.1 km and 0.01 deg, respectively. The station uncertainty estimates, generous though they are, contribute very little to the uncertainties in α and δ. The relative contributions from the nine independent variables to the uncertainty in α and δ are indicated in Table 13, which is an accumulation of absolute

Table 13. Relative contributions to uncertainties in α and δ

Increments in independent variables	α, deg	δ, deg
Spacecraft $\Delta X_p = \Delta Y_p = \Delta Z_p = 3000$ km	0.00234	0.000705
	0.00258	0.000633
	0.00000	0.003200
	0.00492	0.004538
Moon $\Delta X_M = \Delta Y_M = \Delta Z_M = 5$ km	0.000510	0.000150
	0.000565	0.000135
	0.000000	0.000700
	0.001075	0.000985
Station $\Delta r_s = 0.1$ km, $\Delta \phi_s = \Delta \theta_s = 0.01$ deg	0.000007	0.0000058
	0.000070	0.0001400
	0.000104	0.0000220
	0.000181	0.0001678
Total	0.006176	0.0056908

values of products of partial derivatives with their corresponding independent variable increments.

Combining the covariance matrix of uncertainties in the position of the probe, Moon, and station with the partial derivative matrix, in accordance with Eq. (2), results in the covariance matrix for α and δ. This is

$$0.1414 \times 10^{-5} \qquad 0.1115 \times 10^{-8}$$
$$0.1115 \times 10^{-8} \qquad 0.1301 \times 10^{-5}$$

This covariance matrix of uncertainties in α and δ was used in a two-dimensional Gaussian distribution, the adequacy of which we assume. By calculating eigenvalues and the direction of the eigenvectors, the semimajor and semiminor axes and the inclination angle of the 3-σ error ellipse can be calculated. This ellipse can then be used to estimate the earliest and latest occultation times for the set of trajectories lying in the 3-σ α–δ error ellipse. The semimajor and semiminor axes and the inclination angle of this ellipse are

$$a = 0.00357 \text{ deg}$$

$$b = 0.00342 \text{ deg}$$

$$\alpha = 0270.6 \text{ deg}$$

As can be seen, the ellipse is virtually a circle. This is to be expected from the assumption of equal uncertainties in all three Cartesian coordinates of the probe and Moon, which are the principal contributors to the uncertainties in α and δ, as shown in Table 13. Assuming that the error ellipse is a circle of 0.0035-deg radius and ignoring the small distortion of this circle due to the mapping, we may estimate the earliest and latest enter and exit occultation times in the graphical manner indicated in Fig. 28. This figure shows that the earliest and latest enter and exit occultation times may be estimated by centering the error circle on the nominal trajectory, which in this case is orbit 4, and moving the error circle along the nominal trajectory until it is tangent to the limb of the Moon. This method does not determine true 3-σ uncertainties in the occultation times, but rather the earliest and latest possible occultation times for the set of trajectories lying in the 3-σ error ellipse. Whether these times are close to the actual 3-σ uncertainties in occultation times is another problem. The determination of the true uncertainties in occultation times caused by uncertainties

in the position and velocity of the probe, Moon, and station is a more difficult problem than that dealt with in this article. A moment's reflection tells us that (1) the magnitude of the uncertainty depends strongly upon just where in the Moon's disk the occultation takes place, and (2) the uncertainty in exit occultation is a random variable that is not independent of the actual enter occultation time.

When measurements are carried out in Fig. 27 for orbit 4 in the fashion indicated by Fig. 28, we find the earliest and latest occultation times. These are given in Table 14.

Table 14. Earliest and latest occultation times

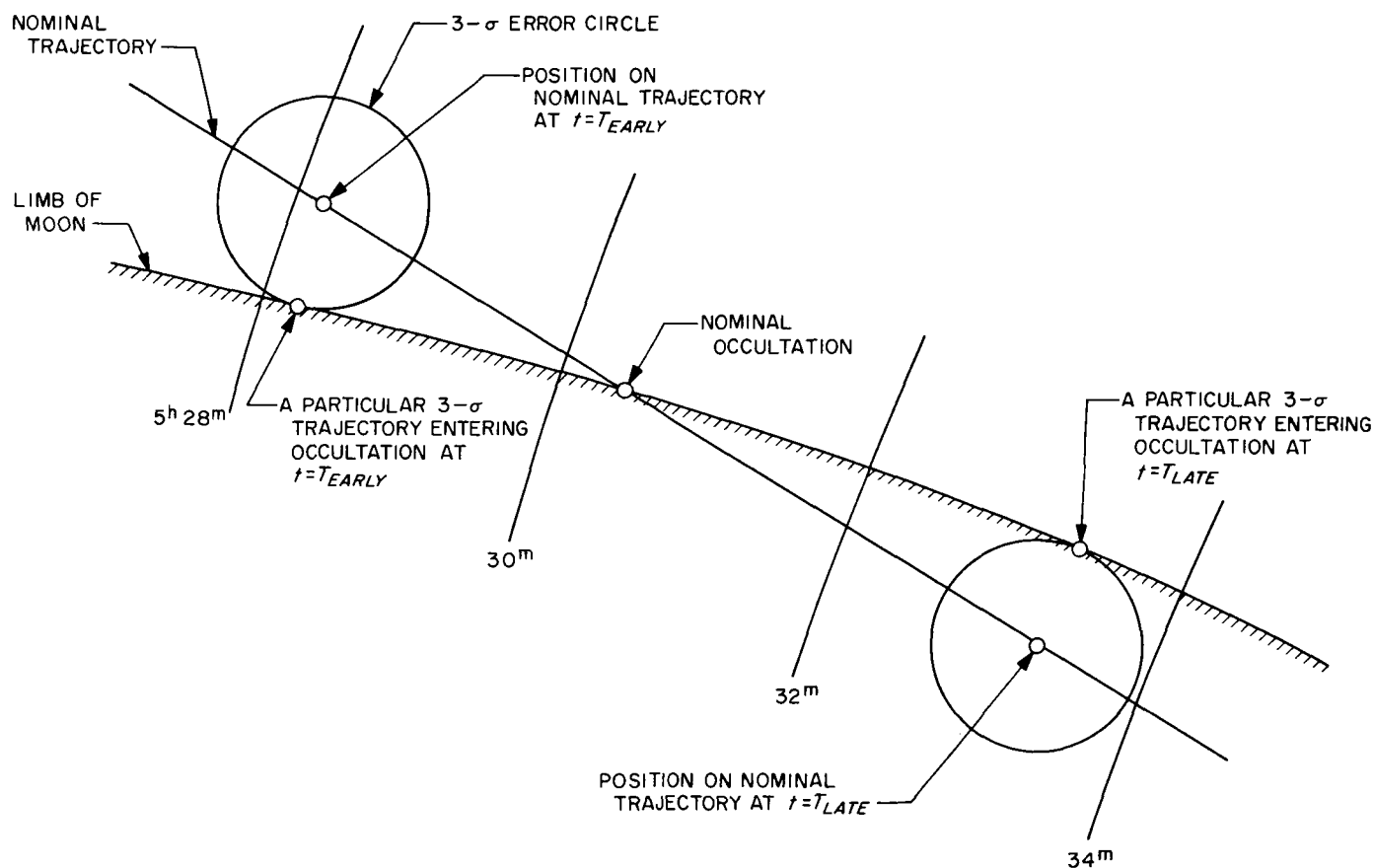| Occultations	Enter	Exit
Nominal	$5^h30^m10^s$	$5^h48^m40^s$
Earliest	5^h28^m	5^h45^m
Latest	$5^h33^m30^s$	$5^h51^m30^s$

Fig. 28. Graphical method of estimating earliest and latest occultation times for trajectories in 3-σ error circle

The occultation that occurred on January 20, 1967, allowed a test of the above prediction. The Stanford experimenters transmitted on two frequencies, 50 and 425 MHz. The signal received from the spacecraft was recorded; when it dropped 6 db, occultation was defined to occur. A similar definition applied to the exit occultation. According to H. T. Howard of Stanford University Center for Radar Astronomy, the time of immersion was $5^h30^m33^s \pm 10$ sec and the time of emersion was $5^h48^m32^s \pm 10$ sec.

The actual observed times given above agree quite well with the best predicted times as shown in Table 14. The differences between the observed and predicted occultation times are $+18^s \pm 10$ sec and $-4^s \pm 10$ sec for immersion and emersion, respectively. The predicted times in Table 14 should be altered by the light time effect which causes both enter and exit occultation to occur about 10 sec earlier. This would change the differences between the observed and predicted occultation times to about $+28^s \pm 10$ sec and $+6^s \pm 10$ sec. These differences are well within the uncertainties indicated in Table 14.

K. Pioneer VII DSS 62 Station Location Estimate,
W. L. Sjogren

The amount and quality of the doppler tracking data used for this estimate are summarized in Table 15. The data span is approximately one month of nominal DSS tracking of the *Pioneer VII* space probe. The Cebreros Deep Space Station (DSS 62) tracked only three days at the end of this period. The standard deviation and mean given respectively in the last two columns show how well all data were finally fit.

The tool used for this determination was the single precision orbit determination program (SPODP)[27] which performs a weighted least-squares fit on the doppler observables. There were eight parameters estimated: the three components of the spacecraft position, the three components of velocity, and two station location coordinates (latitude and longitude). All three station coordinates are not estimated because of the insensitivity of the tracking data to the station coordinate along the Earth's axis of rotation. Effectively, the tracking data are used to determine longitude differences between deep space stations and the distance of each station off the Earth's spin axis r_s (Ref. 17). Since only the DSS 62 coordinates were

estimated, this solution is certainly *relative* to the other tracking stations (which were originally estimated in somewhat the same manner using *Ranger* and *Mariner* data). However, these stations are known to an accuracy of 50 m, which is sufficient for estimating the new station location.

The results of the least-squares fit are shown in Table 16. The position and velocity components have been truncated and inserted so their magnitudes are displayed, whereas the latitude and longitude of DSS 62 are given exactly (column 3). The uncertainty in the parameters (shown in column 4) is derived strictly from the data weights, for no *a priori* was given to any of the estimated parameters. The data weight[28] was 0.045 Hz and takes into account error sources other than those that cause the "visible" or high-frequency data noise given in column 5 of Table 15. There are, of course, other omitted parameters which could have some secondary effect (i.e., solar pressure uncertainty, AU uncertainty), but best values from previous estimates were used and their omission should be negligible. Column 5 of Table 16 shows the stability of the solution. Final corrections are not more than one-tenth of the standard deviation. In Table 17, the correlation matrix shows that the latitude and longitude estimates are essentially uncorrelated with the other parameters.

The initial estimate that was given for DSS 62 location was an astronomical determination having an uncertainty of 500 m. The orbit determination estimate moved the astronomical value approximately 310 m in r_s and 230 m in longitude. Since this analysis, a first-order land survey has verified these estimates to at least 60 m. These values are tabulated in Table 18, column 2. It is interesting to compare the first-order land survey at DSS 61, which is only 8 mi away from DSS 62, to see if the same differences exist, as they should. In column 4 of Table 18, the survey differential locations are compared with those determined from radio tracking data. The agreement of 4 m in r_s and 3 m in longitude is encouraging in light of the expected uncertainties in the determinations. The land surveys between points this close together can easily be made to 1 m, and the 1-σ orbit determination solutions are 15 m both in r_s and in longitude differences due to orbit uncertainty and the limitations discussed in SPS 37-43, Vol. III, pp. 5–18 (i.e., ionospheric refraction, inaccuracies in the Earth–Moon ephemeris, and the wandering of the Earth's pole between various DSS 61 and DSS 62 determinations).

[27]Warner, M. R., and Nead, M. W., *SPODP—Single Precision Orbit Determination Program,* Technical Memorandum 33-204, Jet Propulsion Laboratory, Pasadena, Calif., February 15, 1965.

Table 15. Data coverage

(1) DSS	(2) Date[a]	(3) Duration, hr	(4) No. of doppler observations, 1 sample/5 min	(5) Standard deviation, Hz[b]	(6) Mean, Hz[b]
11 (Pioneer, Goldstone)	Jan. 12 14 27	11 10½ 6	226	0.011	−0.011
42 (Tidbinbilla)	Jan. 19 20 24 26	3½ ½ 8 8	233	0.0068	+0.0053
51 (Johannesburg)	Dec. 28 29 30 Jan. 3 5 6 8 9 14	8½ 9 9 9 8 9 9 7 8½	886	0.0038	+0.00013
12 (Echo, Goldstone)	Dec. 27 30 Jan. 18 19 24	1 8 1 7 10½	317	0.0103	+0.0039
62 (Cebreros)	Jan. 24 25 27	7 9 10	204	0.0083	−0.00020

[a] Dates cover December 27, 1966, through January 27, 1967.
[b] 1 Hz ≈ 65 mm/sec, except at Johannesburg where 1 Hz ≈ 20 mm/sec.

Table 16. Station location estimate

(1) Parameters estimated	(2) Units	(3) Estimated values	(4) Standard deviation	(5) Change from previous iteration
x[a]	km	0.33×10^8	68.	−6.
y	km	0.16×10^8	93.	−4.
z	km	0.72×10^7	181.	−0.4
$\dot{x}$	m/sec	3.1×10^3	0.0016	0.00007
$\dot{y}$	m/sec	6.2×10^3	0.035	0.0013
$\dot{z}$	m/sec	2.7×10^3	0.078	−0.0031
Latitude[b] 62	deg	40.26367	0.00009	−0.000004
Longitude 62	deg	355.63235	0.00006	−0.000009

[a] Epoch for position and velocity was Dec. 25, 1966, 0^h 0^m 0^s
[b] Radius of 6370.007 km held constant, 0.001 deg ≈ 100 m

Table 17. Correlations between parameters

	x	y	z	$\dot{x}$	$\dot{y}$	$\dot{z}$	Latitude	Longitude
x	1	0.20	0.03	−0.33	0.18	−0.01	0.05	−0.24
y		1	−0.29	−0.80	0.75	0.43	−0.18	−0.10
z			1	−0.27	0.60	−0.88	0.12	−0.03
$\dot{x}$				1	0.41	0.01	0.16	0.21
$\dot{y}$					1	−0.84	0.38	0.00
$\dot{z}$						1	−0.33	−0.01
Latitude							1	−0.10
Longitude								1

Table 18. Comparison of estimates on station locations

(1)	(2)		(3)		(4)	
Type of estimate	DSS 62		DSS 61		Difference between DSS 62 and DSS 61	
	r_s, km	Longitude, deg	r_s, km	Longitude, deg	r_s, km	Longitude, deg
Orbital determination (OD)	4860.810	355.63239	4862.600	355.75118	−1.790	−0.11879
Land survey (LS)	4860.862	355.63300	4862.648	355.75182	−1.786	−0.11882
Astronomical (A)	4861.128	355.63467	—	—	—	—
A minus OD	0.318	0.00228	—	—	—	—
LS minus OD	0.052	0.00061	0.048	0.00064	0.004	−0.00003

r_s = geocentric radius of the station times the cosine of latitude = distance off rotation axis.
Radius for DSS 62 = 6370.007 km for OD and 6370.026 km for LS.
Radius for DSS 61 = 6370.012 km for OD and 6370.080 km for LS.
0.001 deg ≈ 100 m.

L. Lunar Orbiter DSN Trajectory Operations,
R. A. Wallace

1. Introduction

Early in 1964, personnel in the JPL Systems Analysis Section became involved in the planning of operations for the five *Lunar Orbiters* to be launched in 1966 and 1967. The role of the DSN Trajectory Group has been twofold: (1) to provide Langley Research Center (LRC) with consulting services necessary to planning systems analysis activities for a deep space mission, and (2) to provide trajectory analysis necessary to operate the tracking and data acquisition facilities for the near-Earth portion of a *Lunar Orbiter* mission. Prior to the first launch in August 1966, the first role was of major importance. However, with the experience of each launch, less time has been required in the consulting role and the second role has assumed dominance.

This report is devoted to the activities carried on in flight path analysis and control (FPAC) by the Trajectory Group for the past, present, and future *Lunar Orbiter* missions. These activities can be divided into three groups:

(1) Preflight planning

(2) Launch phase trajectory operations

(3) Postlaunch services

Before the first launch, it was decided that JPL would direct the FPAC operations in the near-Earth phase. Thus, the primary focus for Trajectory Group activities has been in planning for trajectory support during launch

phase operations. This report will be divided into two sections: (1) operations activities prior to launch, and (2) activities after launch.

2. Prelaunch Trajectory Activities

The guiding objective for the Trajectory Group prior to a *Lunar Orbiter* launch is to become as familiar as possible with the nominal launch trajectory associated with the actual launch time. It must be remembered that there are an infinite number of trajectories associated with the launch windows in any launch period. There is, however, a one-to-one correspondence between each trajectory and the precise launch time. The object, therefore, is to be able to produce the salient characteristics of any trajectory resulting at any time during a launch window, and from these characteristics, to answer questions relating to the desired nominal trajectory. To perform such a task, several sources of information are available. Among these are:

(1) Project trajectory documents

(2) DSN near-Earth tracking coverage documents

(3) Targeted nominal trajectory data

(4) A backlog of experience and familiarity with the mission

(5) Prelaunch information from Air Force Eastern Test Range (AFETR)

The first source—project trajectory documents—gives many general characteristics of the type of trajectories to

be flown during a launch period. These documents provide a wealth of information with which the Trajectory Group is expected to be familiar. Information of a more specific nature is given in the *Tracking Station View Period Document* (published by the DSN Trajectory Group for the first launch but subsequently assumed by the LRC). This document provides information regarding nominal near-Earth trajectories simulating a launch every three degrees of launch azimuth throughout the launch windows in a given launch period.

DSN near-Earth tracking coverage documents, produced by systems analysis personnel in the Mission Analysis Group, are another source of information. These documents tell, prior to launch, what the expected near-Earth tracking coverage will be for a nominal launch. They give the Trajectory Group a good indication of the support that can be expected from the AFETR.

The targeted nominal trajectory data provide the most important source of information regarding prelaunch trajectories. The sources for this information are the *Range Safety Magnetic Tape Listings* and the *Firing Tables*. Both are produced by TRW under contract to Lockheed, the launch vehicle contractor. The data in these documents are given for every three degrees of launch azimuth, and as such cannot be used directly to determine the nominal trajectory. Two methods have been used to process the targeted data so that pertinent nominal trajectory characteristics can be obtained.

(1) Computer program in real time

(2) Trajectory listings computed prior to launch day

Historically, a computer program—called the launch trajectory program—has been used with launch time as input as soon as determined at launch. There are three disadvantages to this method: First, the Trajectory Group is totally dependent on the computer system. Second, the launch time can slip a number of times during a launch window, resulting in many different and erroneous launch trajectories. Third, a continuous comparison of nominal trajectories close to the actual nominal trajectory is not possible; i.e., when the launch time is obtained, only one trajectory is computed by the trajectory program. This method was used on *Lunar Orbiter I*, launched in August 1966.

To overcome these disadvantages, a new method was tried on *Lunar Orbiter II*; however, the computer program method was maintained as a backup. Briefly, this method compiles the targeted data and fits a fifth-degree

polynomial to the figures. These polynomials are then printed out as a function of launch time throughout the launch window. This method was used in both *Lunar Orbiters II* and *III* and enhanced considerably the analysis capability of the Trajectory Group. This disadvantage of the method lies in its prelaunch manpower requirement.

The last two sources of information relate to unpublished material obtained through meetings and discussions with personnel involved with the *Lunar Orbiter*. One example is the prelaunch information relayed as late as one hour before launch, tabulating changes in the powered flight trajectory which are required because of booster performance changes.

3. Postlaunch Activities

Just as the prime goal of prelaunch activities was to determine the nominal trajectory, the goal of postlaunch activities is to determine the characteristics of the actual trajectory. As soon as the launch time has been determined, the Trajectory Group has a nominal trajectory for which tracking station predicts can be sent to the stations. For the remainder of the launch phase it is the *prime responsibility* of the Trajectory Group to determine the actual trajectory from all possible sources. To do this the Trajectory Group has several sources of information:

(1) Real time computer system of AFETR

(2) Mark time reports from AFETR

(3) Real time flight reports from AFETR

(4) Nominal trajectory information

(5) Trajectory computer programs

The most important source of actual trajectory information comes from the real time computer system (RTCS) located at AFETR, where AFETR tracking data from launch through the first DSIF acquisition are processed and orbits are determined. The results of these orbit determinations are teletyped to the SFOF, where the Trajectory Group prepares an analysis on the orbital conditions. Complementing this analysis is another which uses the event times of the ascent trajectory reported in real time from the AFETR tracking stations. Both of these are assimulated with any other pertinent data from the other available sources, and a first actual trajectory report is made to the FPAC Director. These reports permit the FPAC Director to quickly comprehend how nominal a trajectory is being flown or, if extremely nonnominal, to determine what steps can be taken for DSIF

acquisition. These reports are made at two times, the first as soon as possible after the injection into parking orbit and the second after injection into the lunar transfer orbit.

An example may serve to illustrate this process. *Lunar Orbiter III* was launched on February 5, 1967, at 01^{h}17^m 01.120^s GMT. This launch time resulted in a nominal trajectory having a theoretical launch azimuth of 80.8 deg and a parking orbit coast time of 581.5 sec. Prior to launch, the Launch Vehicle Control Center had advised the Trajectory Group that a heavier battery than expected would be flown on the *Atlas* booster. Though the parking orbit would be reached at a later time, there would be no change in its orbital elements. There would also be no changes in either the time of injection or in the orbital elements of the transfer orbit. At the time of the first trajectory report, the trajectory seemed nominal except for one anomaly; the Mark event times indicated a 1-sec overburn for the first burn of the *Agena* engine. From studies made by the DSN Trajectory Group, it is known that an overburn of only several tenths of a second can ruin a mission. From AFETR reports it was also known that tracking coverage would be marginal for this launch azimuth. Since such coverage determines the worth of the orbital element message from the RTCS, it was with some reservations that the Trajectory Group awaited further information. This was clarified upon receipt of successive pieces of information. The orbital element message for the injection into transfer orbit was nominal (its worth labeled fair, however). The Mark event times showed a 1-sec overburn for the second *Agena* burn. At this time a voice report based on launch vehicle telem-

etry was received, indicating that pressure in the *Agena* tanks had been less than nominal. This could certainly account for the 1-sec overburns. Because the several sources of information were all consistent with a nominal mission throughout this analysis, no great amount of concern was generated. However, any one source would not have been enough to confirm whether the mission was nominal.

If the trajectory is nominal, the DSN Trajectory Group assumes a consulting role soon after first spacecraft acquisition by the DSIF. Several trajectory computer programs are available to answer necessary questions. An example of a consultant activity occurred during the *Lunar Orbiter I* flight to the Moon. During this mission, spacecraft reflection problems necessitated the use of the Earth as a reference body rather than the star Canopus. Because of this change from nominal procedure, spacecraft personnel had to obtain information on the new reference angles, which changed considerably along the trajectory from the region of near-Earth to near-Moon. A trajectory program was run and consulting analysis supplied to support the LRC in acquiring this information.

4. Conclusion

The real worth of the operational procedures used by the Trajectory Group during the *Lunar Orbiter I, II,* and *III* missions is yet to be determined. The prime goal of these procedures is to enable the DSN Trajectory Group to react to a nonnominal mission. To this date, all *Lunar Orbiter* missions have had nominal trajectories.

References

1. Sjogren, W. L., Trask, D. W., Vegos, C. J., and Wollenhaupt, W. R., *Physical Constants as Determined From Radio Tracking of the Ranger Lunar Probes,* Technical Report 32-1057, Jet Propulsion Laboratory, Pasadena, Calif., December 30, 1966.

2. Sjogren, W. L., Curkendall, D. W., Hamilton, T. W., Kirhofer, W. E., Liu, A. S., Trask, D. W., Winneberger, R. A., and Wollenhaupt, W. R., *The Ranger VI Flight Path and Its Determination From Tracking Data,* Technical Report 32-605, Jet Propulsion Laboratory, Pasadena, Calif., December 15, 1964.

References (contd)

3. Wollenhaupt, W. R., Trask, D. W., Sjogren, W. L., Piaggi, E. G., Curkendall, D. W., Winneberger, R. A., Liu, A. S., and Berman, A. L., *The Ranger VII Flight Path and Its Determination From Tracking Data,* Technical Report 32-694, Jet Propulsion Laboratory, Pasadena, Calif., December 15, 1964.

4. Wollenhaupt, W. R., Kirhofer, W. E., Piaggi, E. G., Vegos, C. J., Trask, D. W., Borncamp, F., and Liu, A. S., *The Ranger VIII Flight Path and Its Determination From Tracking Data,* Technical Report 32-766, Jet Propulsion Laboratory, Pasadena, Calif. (to be published).

5. Vegos, C. J., Kirhofer, W. E., Piaggi, E. G., Trask, D. W., Borncamp, F., and Liu, A. S., *The Ranger IX Flight Path and Its Determination From Tracking Data,* Technical Report 32-767, Jet Propulsion Laboratory, Pasadena, Calif. (to be published).

6. Warner, M. R., Nead, M. W., and Hudson, R. H., *The Orbit Determination Program of the Jet Propulsion Laboratory,* Technical Memorandum 33-168, Jet Propulsion Laboratory, Pasadena, Calif., March 18, 1964.

7. Warner, M. R., Nead, M. W., *SPODP—Single Precision Orbit Determination Program,* Technical Memorandum 33-204, Jet Propulsion Laboratory, Pasadena, Calif., February 15, 1965.

8. Eckert, W. J., Jones, R., and Clark, H. K., *Improved Lunar Ephemeris, 1952– 1959* (Prepared jointly by the Nautical Almanac Offices of the U.S.A. and U.K.), U. S. Government Printing Office, Washington, D. C., 1954.

9. Clarke, V. C., Jr., *Constants and Related Data for Use in Trajectory Calculations,* Technical Report 32-604, Jet Propulsion Laboratory, Pasadena, Calif., March 6, 1964.

10. Clemence, G. M., "The System of Astronomical Constants," in *Annual Review of Astronomy and Astrophysics: Vol. 3,* pp. 93–112. L. Goldberg, Editor, Annual Reviews, Inc., Palo Alto, Calif., 1965.

11. Anderson, J. D., *Determination of Masses of the Moon and Venus and the Astronomical Unit From Radio Tracking Data of the Mariner II Spacecraft,* Technical Report 32-816, Jet Propulsion Laboratory, Pasadena, Calif. (to be published).

12. Null, G., Haynes, N., Gordon, H., and Tito, D., *Mariner IV Flight Path and Its Determination From Tracking Data,* Technical Report 32-1108, Jet Propulsion Laboratory, Pasadena, Calif. (to be published).

13. Kovalevsky, J., *The System of the Astronomical Constants,* Gauthier-Villars, Paris, France, 1963.

14. Makemson, M. W., Baker, R. L., Jr., and Westrom, C. B., *Analysis and Standardization of Astrodynamic Constants,* Astrodynamical Report 12, University of California, Los Angeles, Calif., February 1961 (Reprint from the *Journal of the Astronautical Sciences,* Vol. 8, No. 1, pp. 1–13, Spring 1961).

15. Eckert, W. J., Walker, M. J., and Eckert, D., "The Transformation of the Lunar Coordinates and Orbital Parameters," *Astronomical Journal,* Vol. 71, pp. 314– 332, June 1966.

References (contd)

16. Garriott, O. K., Smith, F. L., III, and Yuen, P. C., "Observations of Ionospheric Electron Content Using A Geostationary Satellite," *Planetary and Space Science,* Vol. 13, pp. 829–838, August 1965.

17. Cain, D. L., and Hamilton, T. W., *Determination of Tracking Station Locations by Doppler and Range Measurements to an Earth Satellite,* Technical Report 32-534, Jet Propulsion Laboratory, Pasadena, Calif., February 1, 1964.

III. Communications Research and Development

A. Frequency Generation and Control: *Mariner* Venus 67 Precision Ranging Experiment,

G. U. Barbani and A. Sward

1. Step-Recovery Diode ×6 Frequency Multiplier,

G. U. Barbani

a. Introduction. A step-recovery diode ×6 frequency multiplier (10 to 60 MHz) has been developed to meet the requirements of the frequency synthesizer section, Side III of the *Mariner* Venus 67 precision ranging system. The output of this module is the coherent reference for the DSIF Unified S-Band RF Receiver located at DSS 14. The frequency multiplier meets a stringent set of performance requirements.

b. Performance. The mechanical structure of the ×6 frequency multiplier is very similar in appearance to the standard DSIF RF module. It is the gold-plated, cavity-type construction and is similar to previously reported RF modules. Refer to SPS 37-43, Vol. IV, p. 90 for mechanical description.

The ×6 frequency multiplier converts a 10-MHz signal into a 60-MHz +13 dbm reference signal by means of a single-stage multiplier. This is accomplished by a modified class C input limiter/amplifier that excites a step-recovery diode. The multiplied signal is amplified and filtered by a crystal bandpass filter. The output amplifier restores the 60 MHz to the +13 dbm level required. This reference signal is part of the frequency synthesizer section, side III of the MV-67 precision ranging experiment (SPS 37-43, Vol. III, p. 90 and SPS 37-42, Vol. III, p. 52).

Fig. 1 is the electronic schematic showing the input impedance matching network, the 10-MHz amplifier-limiter, a commercial step-recovery diode which is used as a harmonic generator, followed by a 60-MHz amplifier, crystal bandpass filter, and a final amplifier.

The input impedance shown in Fig. 2 demonstrates the VSWR limits as a function of the 10-MHz input signal drive level, +3 to +13 dbm.

The limiting curve of Fig. 3 demonstrates the dynamic range of the entire module. The 60-MHz output is +10 dbm for a 10-MHz variation of 10 db.

The 60-MHz output signal was analyzed for harmonic distortion; it was found that the second harmonic was down 30 db; the third harmonic down 55 db and all others down >60 db. All spurious signals are down >120 db.
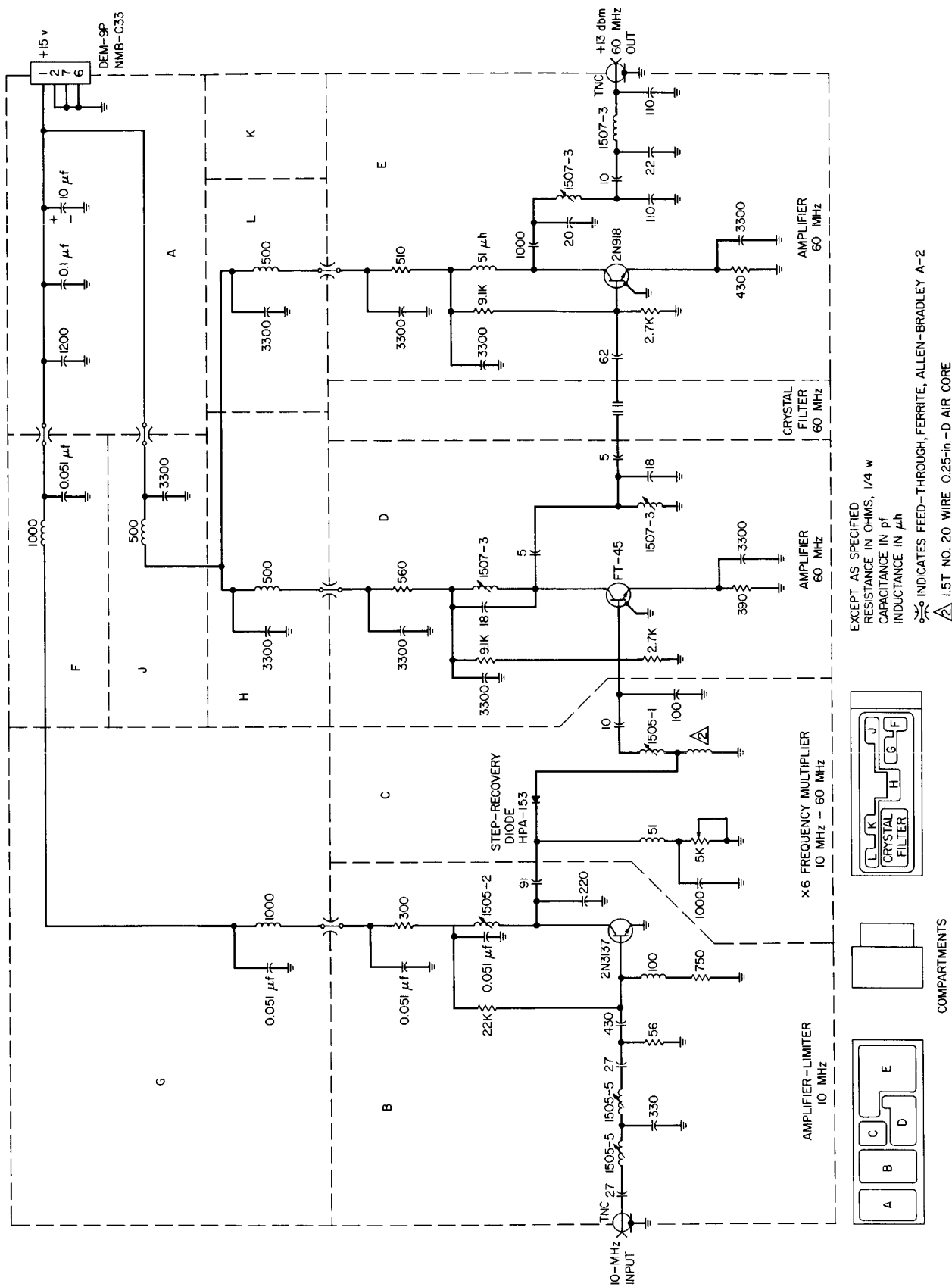
Fig. 1. ×6 Frequency multiplier (10 to 60 MHz)
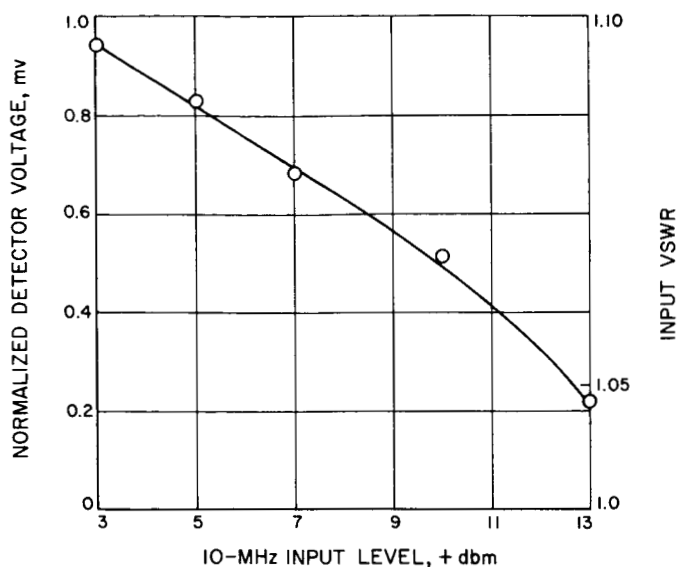
Fig. 2. Input impedance versus level
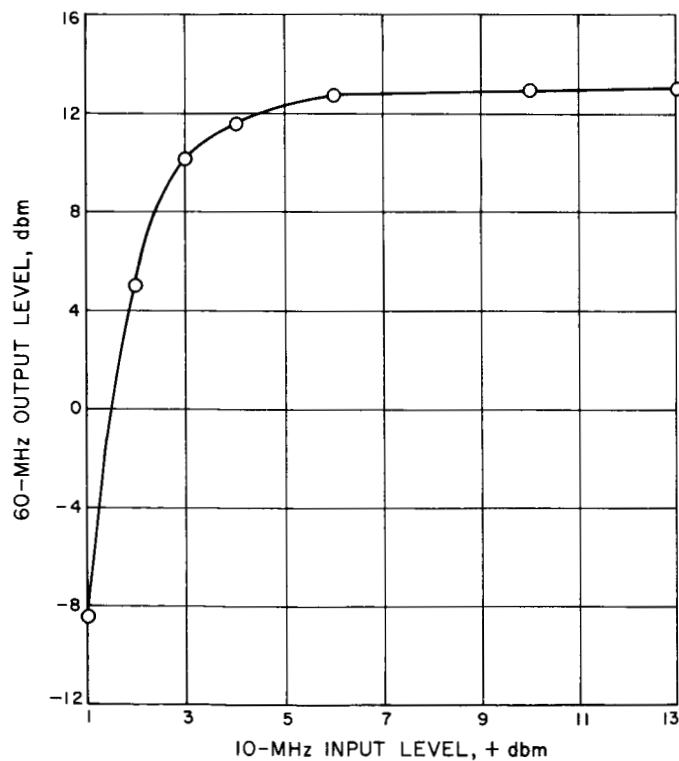
Fig. 3. Dynamic range for constant output

A spectral noise density measurement was conducted, and its level was found to be −133.5 dbm/Hz. This is below the required −130 dbm/Hz by 3.5 db.

There were no extraneous oscillations, spurious or parasitic signals due to loads, shorts, opens or combinations,

power supply variations or input signal power over the range from 0 to +16 dbm. There is no evidence of any spurious signal above the −120 dbm level in the band from 0.15 to 31 MHz.

Since the multiplier diode is relatively close to the input terminal, an attenuation measurement was performed to determine how much 60-MHz signal was present at the input terminal. A spectrum analysis showed the 60-MHz signal to be >60 db down at the full +13 dbm, 10-MHz input level.

A power supply variation of ±5% changes the usable output ±0.5 db. A 4/3 over-voltage test produced no ill effects. Power drain is 0.51 w from a +15 vdc power system for normal operation with applied signal.

The module was subjected to a temperature test from 0 to 50°C (Fig. 4). No thermal runaway was observed.
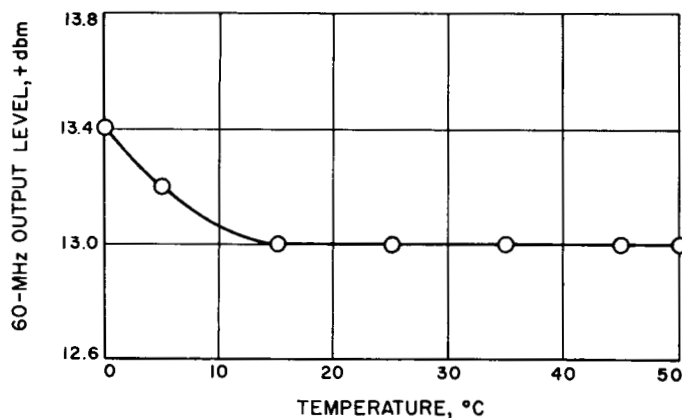
Fig. 4. Environmental variations

The step-recovery diode spectrum (Fig. 5) taken at the output of the diode multiplier (Fig. 1) shows a collection of signals at high amplitudes. Since the module is actuated by a 10-MHz signal, a spectrum of every harmonic of 10 MHz is present. Although it is not shown, this spectrum does continue at relatively high amplitudes to approximately 1 GHz.

With the occurrence of all these signals within the multiplier, a detailed RFI measurement was initiated. Leakage was checked on the power line, threaded coaxial (TNC) terminals and all external mechanical junctions, with a tuned RF voltmeter (Table 1).

Since the bandwidth of the multiplier is determined by the crystal bandpass filter, it is measured to be ±12 kHz
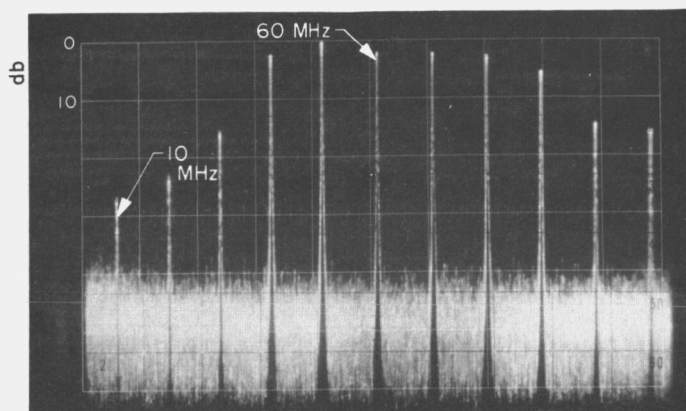
Fig. 5. Step-recovery diode spectrum

at the 3-db points, and is in good agreement with the crystal filter manufacturing data. The 10-MHz input bandwidth measures ±2.0 kHz at the 3-db points. The output impedance was measured to be 45 Ω.

c. Conclusions. The advantages of this type of frequency multiplication are: (1) the high order of multiplication available with little loss, (2) the reduced number of electronic components required for high multiplication factors, (3) high power level outputs, (4) low power requirements, (5) smaller housing assembly, and (6) reduced sensitivity to temperature changes.

Table 1. RFI Leakage at all prime frequencies

Area	Frequency						
	10 MHz, μv	20 MHz, μv	30 MHz, μv	40 MHz, μv	50 MHz, μv	60 MHz, μv	120 MHz, μv
B+	<0.5	0.9	0.5	<0.3	<0.2	<0.5	<0.1
Mechanical junctions	<0.1	0.6	0.0	0.0	0.0	<0.2	<0.1
TNC terminals	<0.1	<0.1	0.0	0.0	0.0	<0.2	<0.1

The use of step-recovery diodes as frequency multipliers has become prevalent throughout the frequency generation spectrum (Caro, E. R., "Step Recovery Diode Multiplier," SPS 37-41, Vol. III, pp. 99–101).

2. 100-kHz Square Law Detector, A. Sward

a. Introduction. One of the modules designed and built for the precision ranging system which is to be used in the *Mariner* Venus 67 mission is a square law detector. Its purpose will be to convert a 100-kHz signal to DC, which then will be fed into the digital section of the system.

b. Circuit description. The square law detector develops an output voltage which is proportional to the input power. In general, square law devices do not have a large dynamic operating range, due to their inherent limitations. However, one of the requirements for this detector was that it
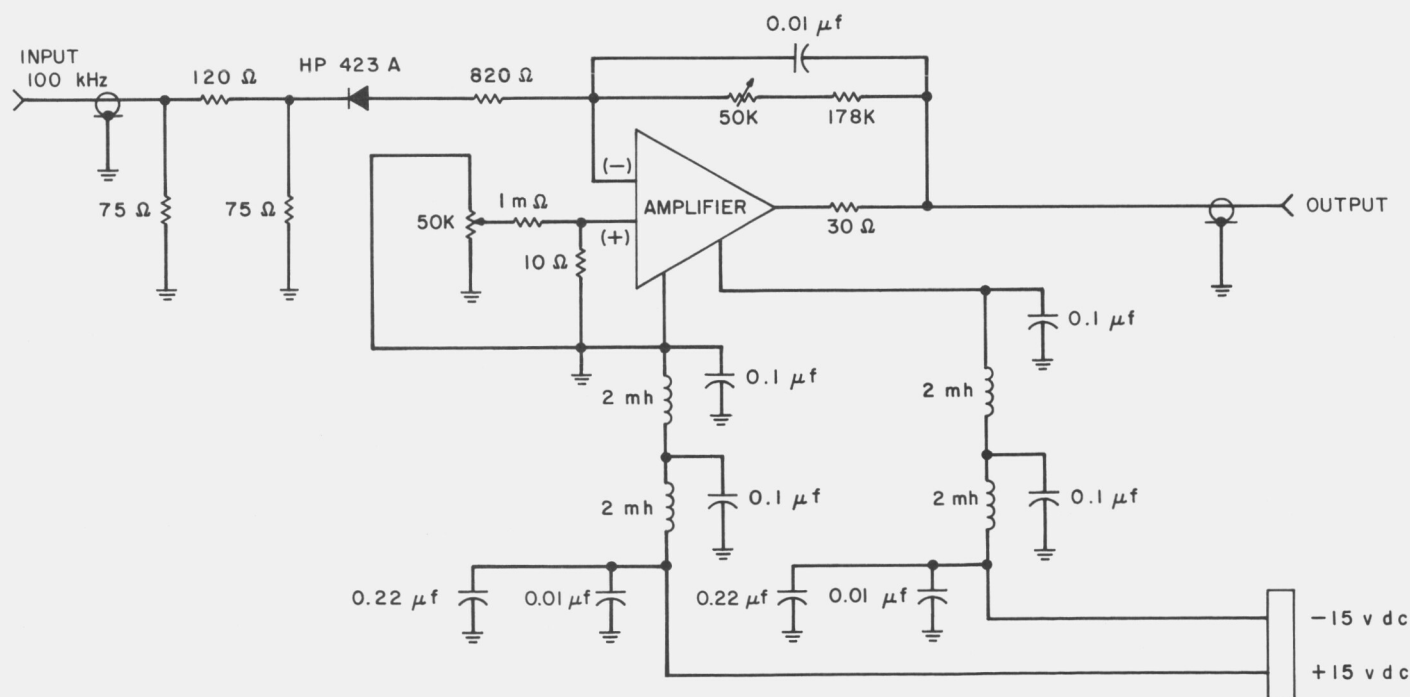
Fig. 6. 100-kHz Square law detector schematic

have a 40-db dynamic range, since the input could vary from -27 to $+13$ dbm. Several other requirements were:

(1) Output: 0 to $+10$ vdc into 500 Ω

(2) VSWR ≤ 1.1

(3) No parasitic oscillations for capacitive loading up to 3000 pf

Fig. 6 shows the circuit configuration used. A Hewlett-Packard crystal detector, Model 423A, was used as the square law device because of its large dynamic operating range. Although it is principally a microwave diode, it performed very satisfactorily at 100 kHz.

In order for the device to operate linearly, a maximum of -3 dbm input power could be tolerated, which required a 16-db attenuator to precede it. The output of the detector is filtered by the RC circuit in the feedback loop of the operational amplifier.

It was found that with the minimum input applied, the output signal of the detector was nearly masked by the noise at the input of the operational amplifier. In order to minimize the noise, several steps were taken. Glass resistors were used along with a low drift, low noise operational amplifier. In addition, current noise was minimized by using a circuit configuration which would allow smaller values of resistors to be used.

Finally, an isolation resistor was placed at the output of the operational amplifier to suppress any parasitic oscillations which might occur due to the capacitive loading of the output. The capacitive loading could be caused by coax cable at the output.

c. Circuit performance. Input power versus output voltage is shown plotted in Fig. 7. No parasitic oscillations occurred for capacitive loads of up to 10,000 pf.

3. 10.1-MHz Balanced Mixer, A. Sward

a. Introduction. The precision ranging system, which is to be used as part of the Celestial Mechanics experiment of the *Mariner* Venus 67 Mission, is nearly at the end of the module checkout phase. One of the modules that has been designed, built, and checked out is a 10.1-MHz balanced mixer which is used in the frequency synthesizer section to supply a 10.1-MHz reference signal.

b. Circuit description. Several of the design criteria to be met are: (1) output frequency of 10.1 MHz, (2) 10-MHz signal to be down 60 db or more from 10.1 MHz signal, (3) output noise density to be less than -130 dbm/Hz, and (4) output level to be between $+10$ and $+13$ dbm for all combinations of input levels over $+3$ to $+13$ dbm range.

The overall circuit consists of five sections: (1) the 10.0-MHz isolation stage, (2) the 0.1-MHz isolation stage, (3) mixer stage, (4) crystal filter, and (5) the output amplifier.
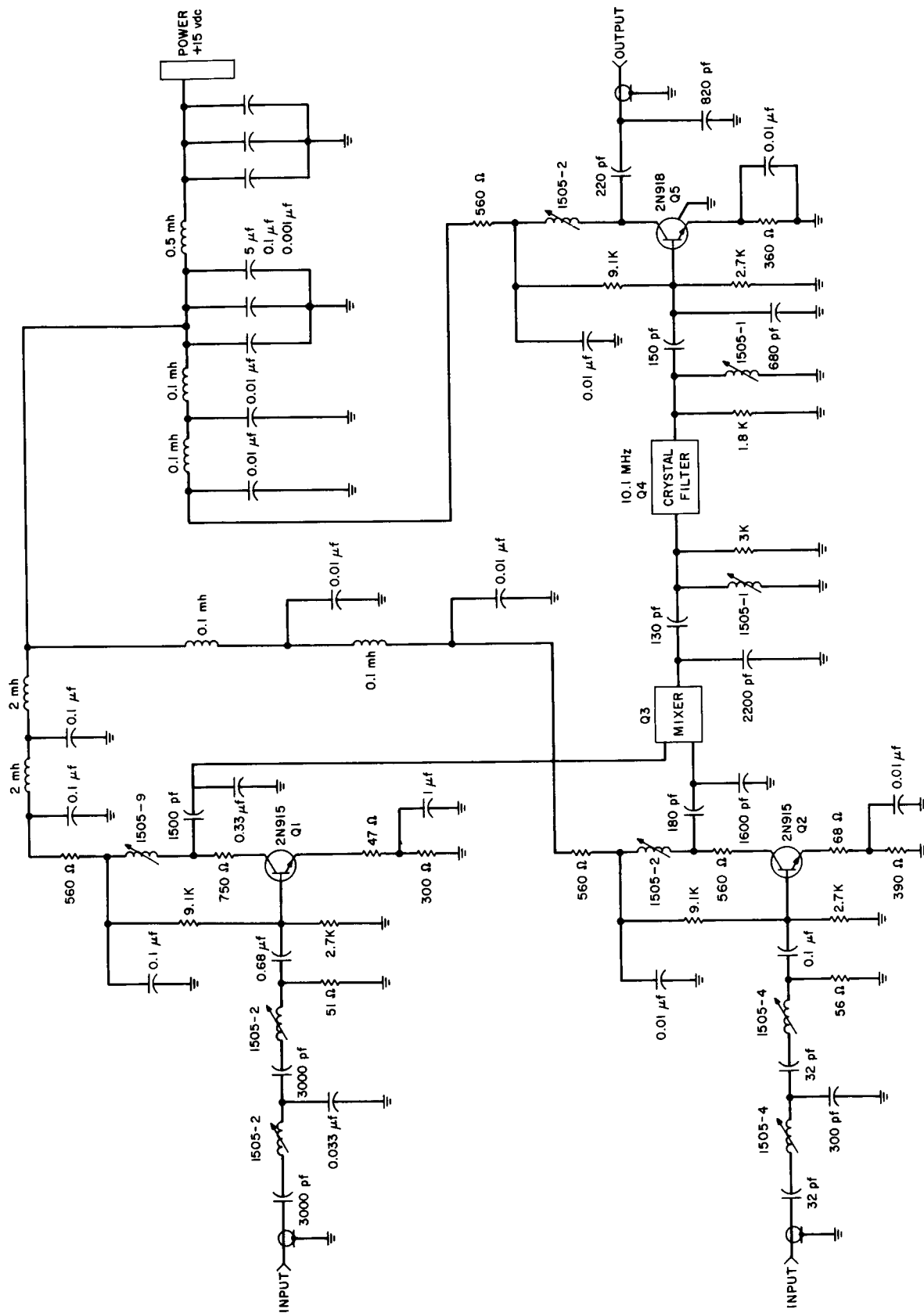
Fig. 8. Schematic of 10.1-MHz balanced mixer

Fig. 8 shows the circuit configuration. The two input isolation stages provide proper isolation between the previous module and the mixer, ensure a low input voltage standing wave ratio (VSWR), and regulate the amount of signal that is introduced into the mixer. The mixer stage consists of an HP 10514A double balanced mixer with a 45-db typical rejection of the carrier. The next stage, Q4, provides the filtering for the output of the mixer. The crystal filter has a 20-kHz bandwidth, with a 60-db rejection at ±100 kHz either side of the 10.1-MHz center frequency. The last stage, Q5, amplifies the signal to an output power of +13 dbm. A 2N918 transistor was used in the last stage in place of a 2N915 because of its increased current gain at 10.1 MHz, as well as its lower noise figure.

c. *Performance characteristic.* With a +13-dbm signal applied at each input, the output power was +12.3 dbm, causing a power drain of 240 mw from a power supply of +15 vdc.

When the harmonic content of the output was examined, only one harmonic existed. It was found to be at 20.2 MHz, down 40 db from the center frequency. The distortion was thus approximately 1%. Closer examination of the power spectrum showed all other harmonics to be down at least 70 db from center frequency, although an accurate measurement could not be made. The output noise density was measured and found to be −135.6 dbm/Hz.

The limiting curve is shown in Fig. 9 with one curve depicting decreasing power at the 10-MHz input part, and the other curve on the graph showing decreasing power at the 0.1-MHz input.
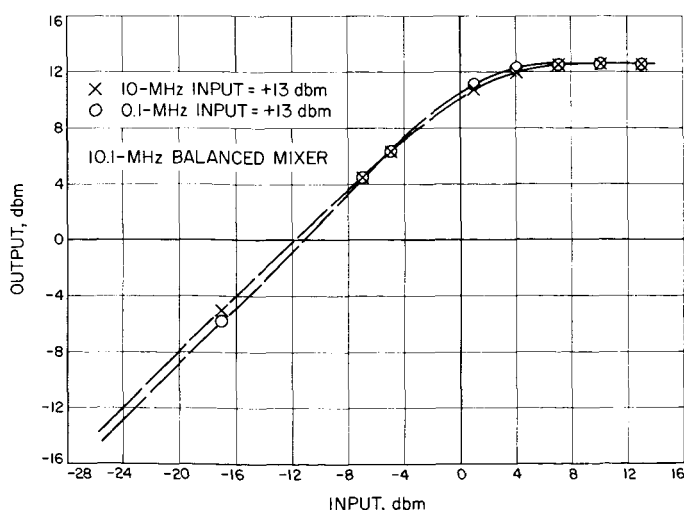
Fig. 9. 10.1-MHz balanced mixer input versus output power

B. Low Noise Receivers: Microwave Maser Development. RER Subsystem Block II TWM, *R. C. Clauss*

1. Introduction

Preparations for construction of a traveling wave maser (TWM) with a tuning range suitable for operation between 2200 and 2300 MHz are being made. A 3-in. test unit has been fabricated and tested to provide necessary design data. Experimental results are compared with previously used TWM's. Unfortunately the configuration used to obtain highest gain degrades isolator performance and results in high forward loss. Single-crystal yttrium iron garnet (YIG) isolators have been tested. The improvement obtained by the use of single-crystal YIG (polycrystalline YIG was previously used) enables the use of a comb configuration that yields higher gain than can be obtained with previous designs.

2. Design Goal

The design specifications for the Block II TWM are shown in Table 2. The maser will be a ruby-loaded comb structure. A gain adjustment trim coil (Ref. 1) will be used to trade excess gain for additional bandwidth. The specification indicates that 30-MHz 3-db bandwidth and 20-MHz 1-db bandwidth will be available at a net gain of at least 35 db. The indicated tuning range will provide coverage of any 20-MHz portion (flat within 1 db) within the 2200 to 2300 MHz range. The 6°K maximum noise temperature is defined at the waveguide input to the maser package and applies to the 1-db bandwidth (center frequency ±10 MHz).

Table 2. Design specifications for Block II TWM

Net gain	35-db min.
Tuning range	2210-2290 MHz
Instantaneous bandwidth, 1 db	20 MHz min.
Instantaneous bandwidth, 3 db	30 MHz min.
Noise temperature	6°K max.

3. Test Unit

The 3-in. test unit is shown in Fig. 10. It is used to optimize the various parameters which affect the performance of the TWM. It is one fourth the proposed length of the Block II TWM (and previously used S-band TWM's). This reduces fabrication work for tests involving isolator configurations and loading techniques.

Experience and data obtained from previously used TWM's (Ref. 1) and published information about C-band
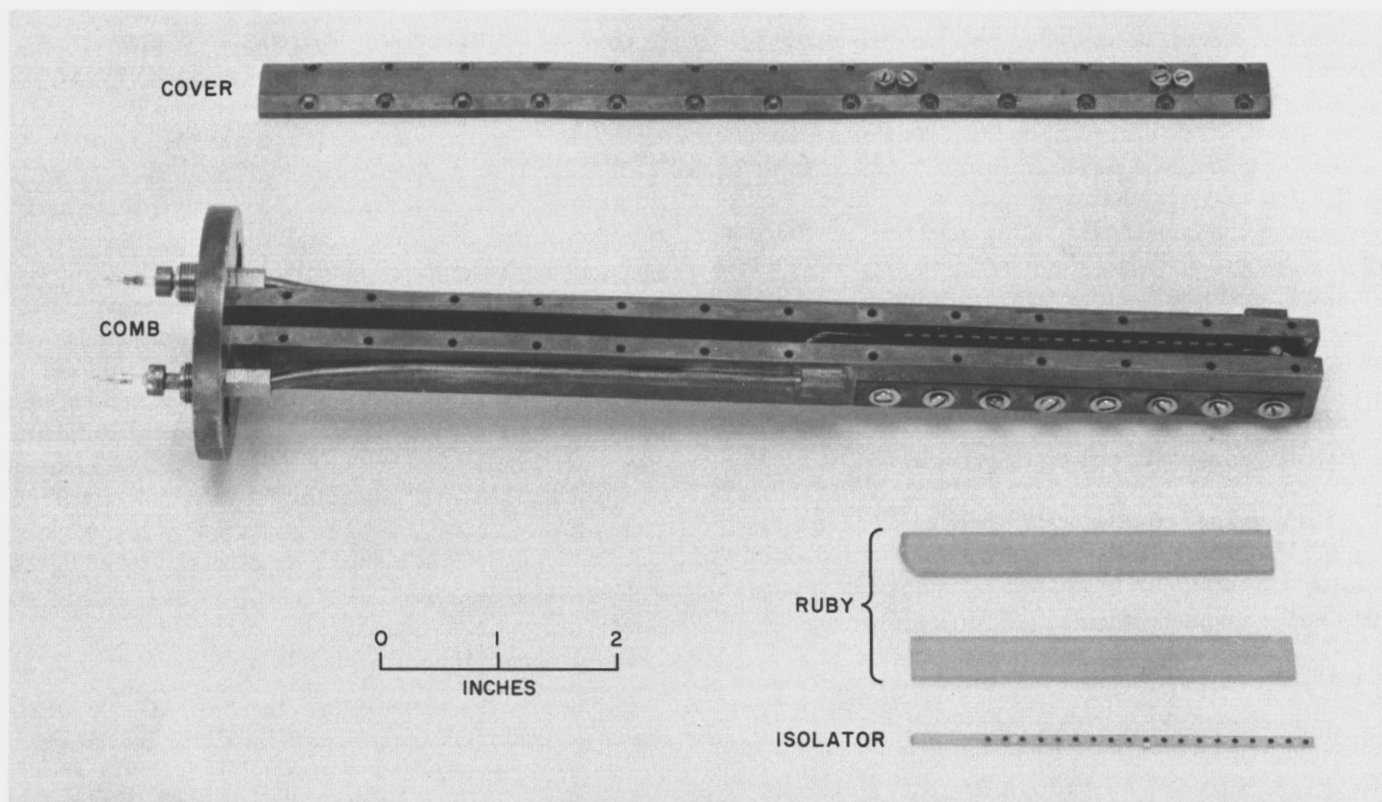
Fig. 10. Block II TWM 3-in. test unit

TWM's (Ref. 2) have resulted in the design of a comb shape with improved gain per unit length. Fig. 11 shows the Mars and Venus DSS TWM's and the test unit comb configurations as viewed from the top. Net gain in db per inch is shown across the tunable range in Fig. 12. In the Block II application it is necessary to have net maser gain exceeding 60 db prior to stagger tuning in order to meet the bandwidth requirement. An additional requirement is low forward loss. High forward loss seriously degrades the net gain versus bandwidth trade-off, and also increases the noise temperature of the TWM. The comb design best suited for high gain across a wide tuning range has very small regions of circular polarization, and results in high forward loss due to the isolator. Single-crystal yttrium iron garnet (YIG) has been used to build an improved isolator.

4. Single-Crystal YIG Isolators

The reverse to forward loss ratio, R, of a resonant isolator is (Ref. 3):

$$R = \left(\frac{4f}{\gamma \Delta H}\right)^2 \qquad (1)$$

where

$$f = \text{resonant frequency}$$

$$\gamma = \text{gyromagnetic ratio}$$

$$\Delta H = \text{isolator line width}$$

Polycrystalline YIG isolators used in S-band TWM's have a line-width of approximately 400 MHz at 4.2°K. An isolator made of single-crystal YIG has been tested and has a line-width of approximately 100 MHz. The improvement in the reverse-to-forward-loss ratio, however, is not as predicted. In order to provide sufficient reverse loss the isolator disk is 0.046-in. in diameter and extends into regions where the RF magnetic field polarization is elliptical. A comparison of performance for single-crystal and poly-crystalline YIG isolators (at 4.2°K in the 3-in. test unit) is shown in Table 3 and Fig. 13.

The resonant frequency of the isolator is determined by the shape of the YIG and the applied magnetic field. For maser operation the magnetic field is determined by the maser material (ruby in this case) and the YIG shape
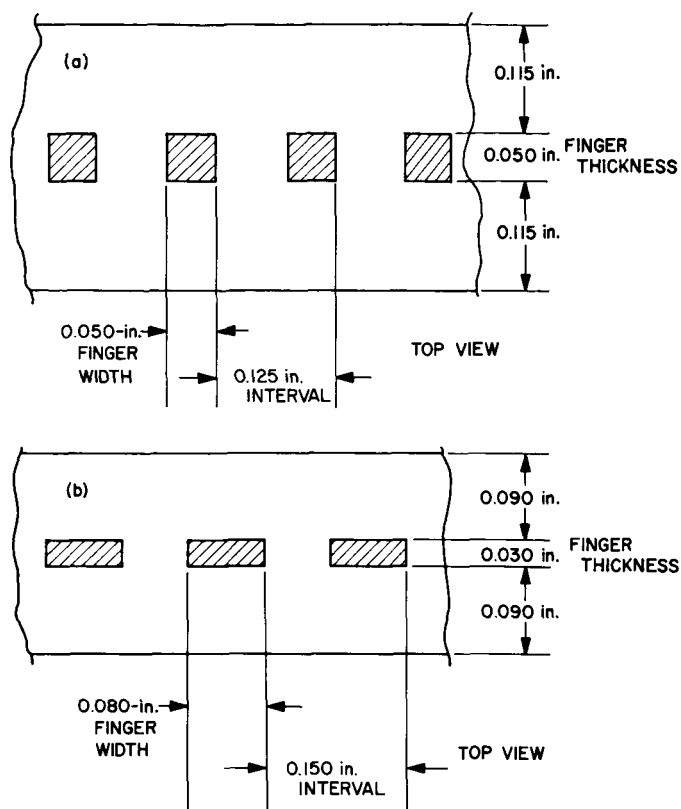
Fig. 11. TWM comb configurations (a) for Mars and Venus DSS (b) for Block II 3-in. test unit
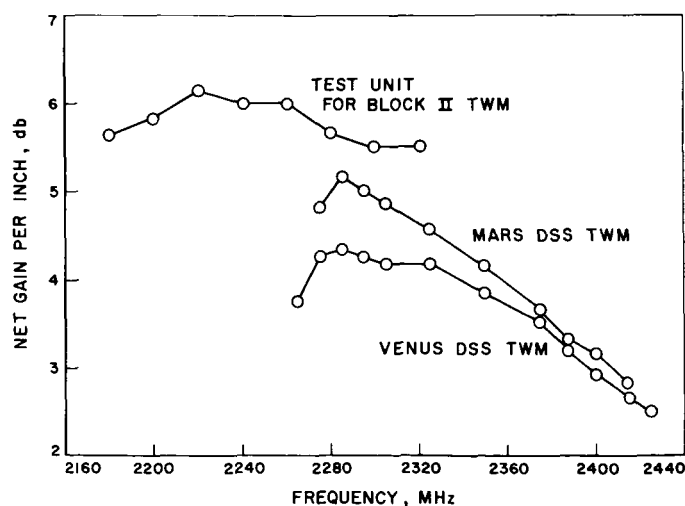
Fig. 12. TWM gain comparison

Table 3. Isolator comparison

Frequency, MHz	Single-crystal YIG[a]		Polycrystalline YIG[b]	
	Forward loss, db	Reverse loss, db	Forward loss, db	Reverse loss, db
2160	17	79	14	55
2180	9.5	76	8.5	55
2200	5.5	76	5	54
2220	3.7	80	2.5	54
2240	2	83	2	56
2260	2	86	2	59
2280	2.2	>86	4	62
2300	4.5	>86	9.5	>65

[a]19 disks at 0.046-in. D and 0.0065 in. thickness. Total isolator volume = 2.05 × 10⁻⁴ in.³

[b]19 disks at 0.063-in. D and 0.0081 in. thickness. Total YIG volume = 4.79 × 10⁻⁴ in.³
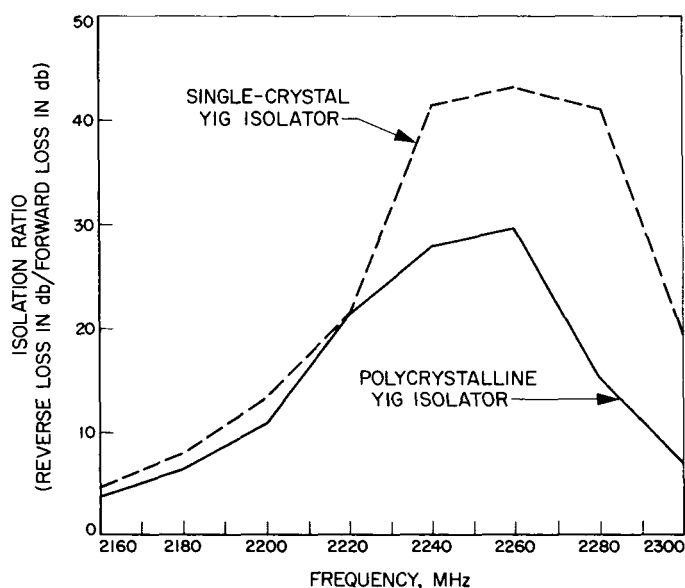
Fig. 13. Isolation ratio

maser material over a 100-MHz tuning range and the allowable error in adjustment of resonant frequency is approximately 10 Mc, or 0.00003 in. in thickness tolerance.

Dimensional measurement techniques used for polycrystalline YIG are not suitable for the single-crystal YIG isolator. The single-crystal YIG disks are checked for resonant frequency, one at a time, at room temperature. Fig. 14 shows a block diagram of the test equipment used for this measurement. The thickness of individual disks is adjusted by lapping the surface with No. 600 silicon carbide paper.

is adjusted for resonance at the proper frequency. A disk with 0.046-in.-D and 0.0065-in. thickness changes resonant frequency approximately 300 MHz for a 0.001-in. thickness change. The isolator ($\Delta H = 100$ MHz) must track the
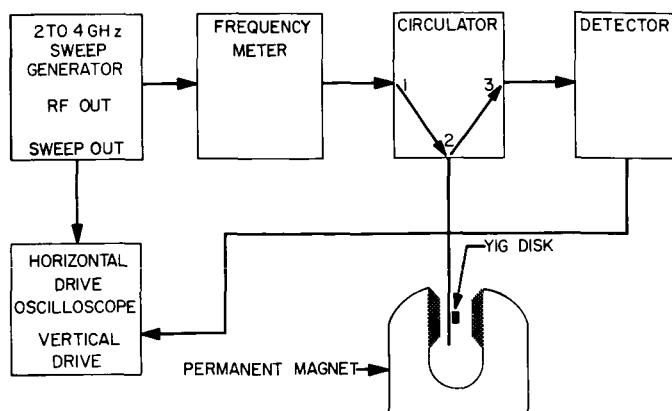
Fig. 14. Test equipment used for measurement of isolator resonant frequency

The process is fairly simple and requires little time. Even disks with broken edges can be adjusted for resonance at the proper frequency. A single-crystal isolator and a polycrystalline isolator for the 3-in. test unit are shown in Fig. 15.

5. Mechanical Considerations

A comb structure TWM could be built to provide a wider tuning range and higher gain per unit length than is obtained with the 3-in. test unit. Such a design would result in a comb with closer interval and with fingers of less strength. Distortion resulting from contraction and expansion when cooling the maser to 4.2°K and warming the unit to room temperature (many times) could permanently damage such an amplifier. Mechanical design considerations for the Block II TWM are: rugged construction to ensure reliability, ease of fabrication, and ease of assembly.

C. Improved Calibration Techniques: X-Band Noise Temperature Calibrations, *T. Y. Otoshi and C. T. Stelzried*

1. Introduction

This article presents results of absolute antenna and maser noise temperature calibrations of an X-band feed horn assembly and maser assembly which were used in three different antenna receiving system configurations. These are:

(1) Horn receiving system

(2) Cone-on-ground receiving system

(3) 85-ft antenna Cassegrain receiving system

A description as well as calibration results for each antenna receiving system will follow. An overall comparison of the noise temperatures of the three receiving systems is presented at the end of the article.

In this article an antenna receiving system will be referred to as one which basically consists of: (1) an antenna assembly, (2) antenna-to-maser interconnecting transmission line, (3) maser assembly, and (4) follow-up receiver. The overall system temperature is comprised of the individual noise temperatures contributed by each of the above components.

Although for most operational purposes knowledge of only the overall system temperature is of real concern, it is often desirable that the system temperature be separated into its component temperatures. Component temperature calibrations provide data which make it possible to analyze and isolate component problems should they arise in a particular system. Knowledge of the component
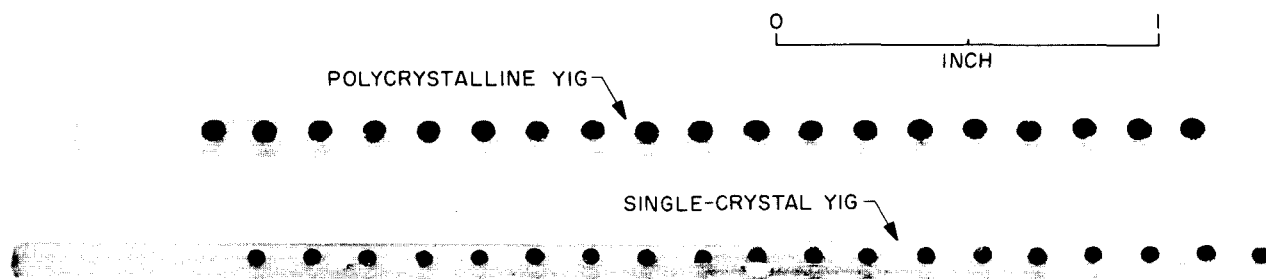
Fig 15. Isolators for 3-in. test unit

temperatures also enables a more thorough comparison to be made on the performances of different receiving systems. Additionally, information is provided so that attention can be focused on the needed areas for system performance improvement.

2. Measurement Technique

One of the methods used for absolute noise temperature calibrations of the individual components of system temperature is the Y-factor technique involving the use of two thermal noise standards. This measurement technique has been previously discussed in detail in SPS 37-39, Vol. III, pp. 86–91 and in SPS 37-40, Vol. IV, pp. 202–209. A block diagram of the basic calibration system may be found in the referenced SPS.

Temperature symbols used throughout this article are defined as follows:

T_A' = antenna temperature, °K

T_L = temperature contributed by the dissipative loss of the transmission line between the antenna output and the maser input reference flanges, °K

T_M'' = maser temperature, °K

T_F'' = follow-up receiver temperature contribution, °K

$T_{SA}'' = T_A' + T_L + T_M'' + T_F''$

= system temperature when the maser input is switched to the antenna, °K

T_{EL}'' = excess noise temperature of the low gas tube injected into the maser, °K

T_{EH}'' = excess noise temperature of the high gas tube injected into the maser, °K

T_{02c} = physical temperature of the ambient load and receiving system transmission lines, °C

T_{02} = physical temperature of the ambient load and receiving system transmission lines, °K

Double-primed symbols indicate temperatures defined at the maser input reference flange; all single-primed symbols refer to temperatures defined at the antenna output reference flange. The double- and single-primed temperatures are related by the dissipative loss of the transmission line which connects the antenna to the maser.

3. Horn Receiving System

For maximum accuracy in calibrating antenna and maser noise temperatures, the antenna and thermal load assemblies should be connected directly to the maser input without interconnecting transmission lines so that: (1) all noise temperatures can be defined at the same reference plane, and (2) any uncertainties in transmission line loss calibrations can be eliminated. In an attempt to obtain best accuracy in calibrating the X-band horn antenna and maser noise temperatures, an experimental horn receiving system was assembled. The horn antenna and maser assemblies for this system were connected together with as short a length of low-loss transmission line as was practical. Switching of the horn and thermal load assemblies to the maser input was performed manually so that the added line loss of a mechanical switch could be avoided and a minimal loss transmission line system could be realized.

A photograph of two horn receiving systems for noise-temperature calibrations may be seen in Fig. 16. These receiving systems were located outside of the X-band cone in an isolated area on the roof of JPL Building 238. This test area provided a simulated on-the-ground environment for the receiving systems.

The horn antenna assembly for the first horn receiving system [Fig. 16(a)] consisted of: (1) feed horn, Part No. 235, (2) mode generator, (3) turnstile junction, and (4) a 4.00-in. length of waveguide transmission line. The turnstile junction was operated in the RCP receive mode. This horn assembly was connected to the maser assembly by a well-matched, low-loss, 90-deg waveguide bend which was accurately calibrated.

The horn antenna assembly for the second horn receiving system [Fig. 16(b)] consisted of: (1) feed horn, Part No. 232, (2) mode generator, and (3) a circular-to-CPR 112 waveguide transition. This horn assembly was connected directly to the maser assembly. Both the feed horn and mode generator were believed to be mechanically and electrically identical to those of the first horn receiving system. This second horn system operated in a linear polarization receive mode in contrast to the first system which operated in the RCP mode.

The X-band maser assembly, which was the same used in all of the calibrated X-band receiving systems, was described in SPS 37-42, Vol. III, p. 42. The maser input reference flange is defined at the input to the low-pass X-band filter section.
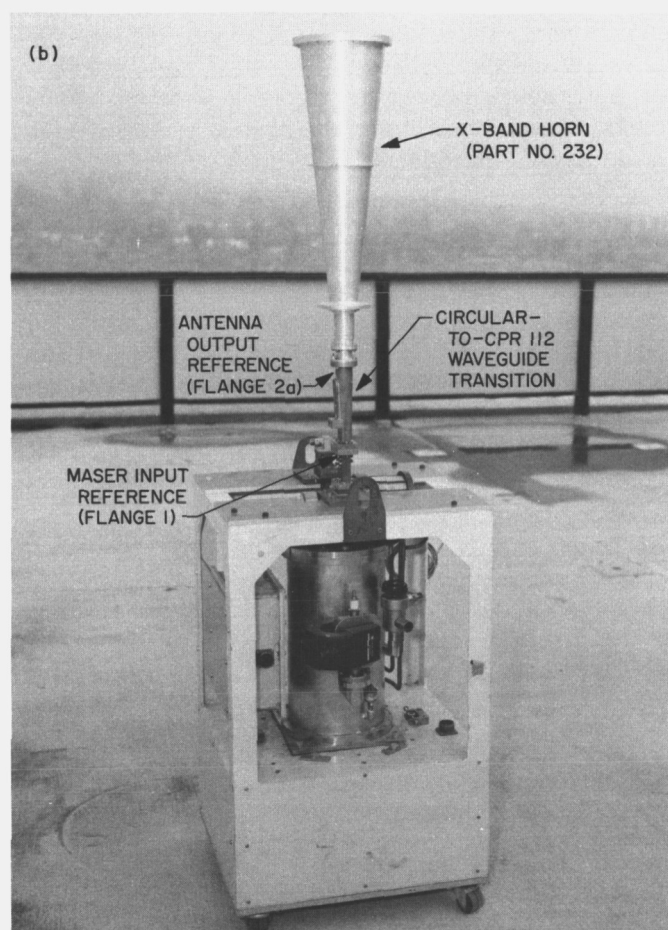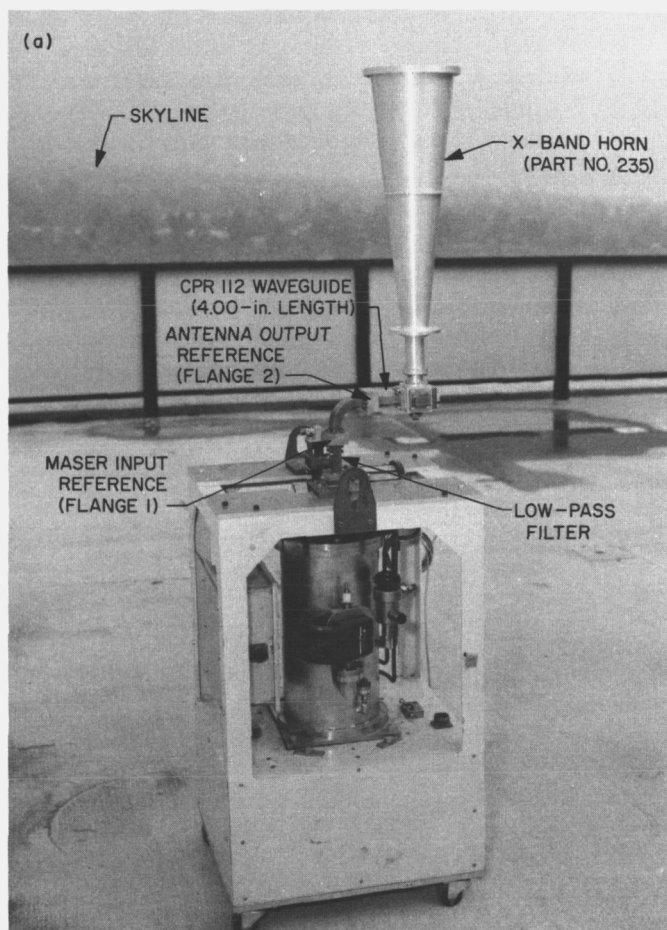
Fig. 16. X-Band horn receiving system (a) X-band horn Part No. 235 (b) X-band horn Part No. 232

The described first and second horn receiving systems will be referred to as the Horn 235 and Horn 232 receiving systems, respectively. As may be seen in Figs. 16(a) and 16(b), the flanges defined to be the antenna output reference flanges in the Horn 235 and 232 receiving systems are defined at different points in the system. Assuming that all environmental conditions remain the same during calibrations, the differences in calibrated antenna temperatures of the two horn systems should be due primarily to the loss of the turnstile junction.

Calibrations were performed with the use of thermal waveguide load assemblies of the types shown in Fig. 17. Figs. 17(a) and 17(b), respectively, show ambient waveguide and liquid-nitrogen-cooled waveguide load assemblies connected to the system at the same reference flange to which the Horn 235 antenna assembly was connected. Fig. 17(c) shows a liquid-helium-cooled waveguide load connected to the system at the same reference flange also, but through an additional length of waveguide line whose

loss was accurately calibrated. All critical system and component reflection coefficients were precisely measured.

For the horn receiving system calibrations, switching was done manually and therefore the relatively long switching periods increased the possibility of calibration errors occurring as a result of maser gain changes. However, if the long-term maser gain is changing in one direction, the effects of this gain change can be partially cancelled by reversing the switching sequence each time a set of Y-factors has been obtained. The noise temperatures for each set of Y-factors can be individually computed and then an average is computed from all of the Y-factor sets in the run. This measurement procedure was adopted for all of the X-band receiving system calibrations.

Noise temperature calibrations were made on an hourly basis to observe any effects due to periodic-type variations in the sky temperatures. These calibrations were
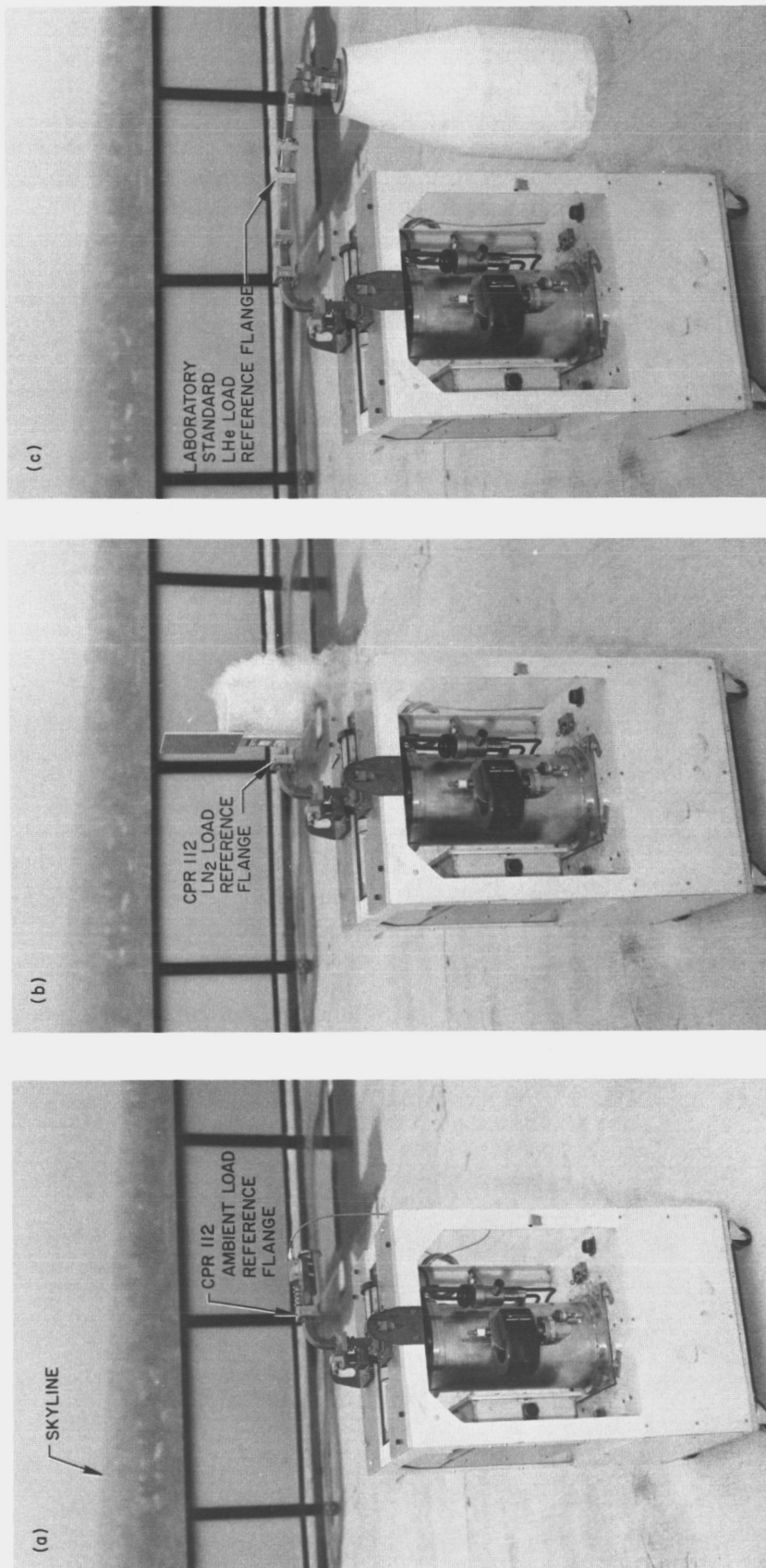
Fig. 17. X-Band thermal load standards (a) CPR 112 ambient load assembly (b) CPR 112 LN₂ load assembly (c) laboratory standard LHe load assembly

made with the horn pointed at the zenith position. A sample hourly run plot of calibrated noise temperatures for the Horn 235 receiving system is shown in Fig. 18. This sample plot includes only runs made over a three-day period (other runs were also made with liquid nitrogen and liquid helium loads on days subsequent to those shown on the plot). Each data point on the plot represents the average of approximately four sets of Y-factors. The limits indicated on a particular antenna temperature data point represent the total probable error of the associated average value. It is suspected that some of the larger variations in antenna temperatures seen on the plot may be due to calibration errors while some of the smaller variations could have been caused by changes in weather conditions. At X-band and higher frequencies, it can be shown that physical temperature and humidity changes of the atmosphere have significant effects on the sky noise temperature (refer to equations in article entitled, "System Noise Temperature as a Function of Meteorological Conditions" in SPS 37-43, Vol. III, p. 63).

A summary of noise temperature calibration results for the Horn 235 and 232 receiving systems at 8448 MHz are presented in Tables 4 and 5, respectively. Separate mean values based on calibrations with liquid-nitrogen–cooled and liquid-helium–cooled terminations are tabulated as well as the combined averages. Some calibration runs were not considered in the averaging process; these were runs whose antenna temperature values appeared to deviate significantly ($> \pm2°K$) from the mean value as calibrated with a particular cryogenic load. Deviations greater than $\pm2°K$ from the mean antenna temperature were considered to be due either to large calibration errors or to inclement weather conditions.
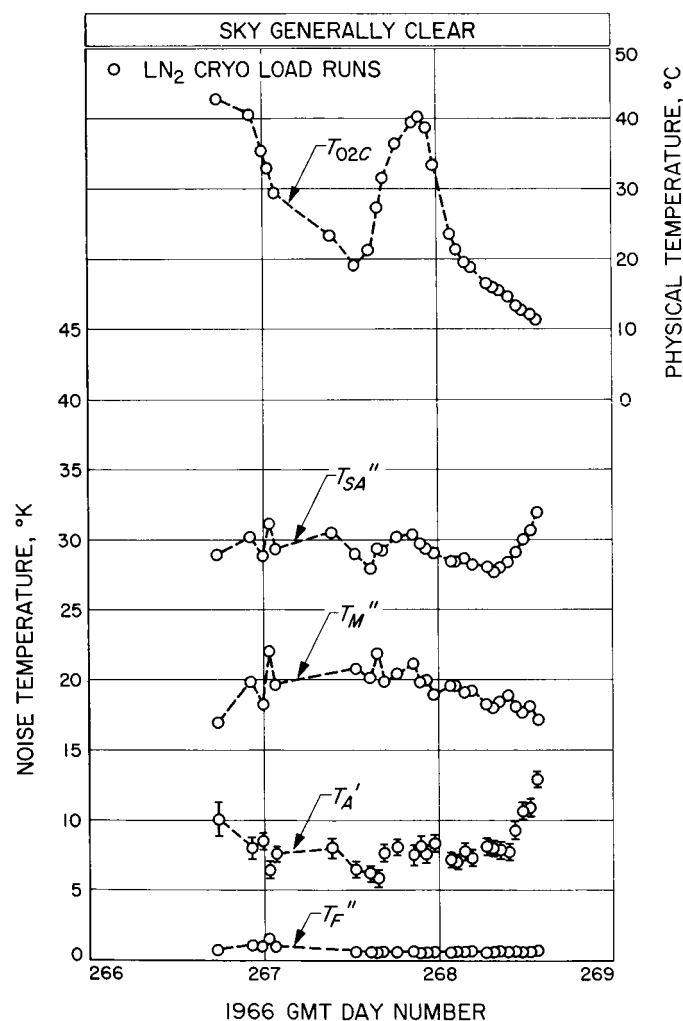
A combined average was obtained by taking an unweighted average of the two mean values obtained with the two types of cryogenic loads. Although calculations were also made of weighted average antenna and maser temperatures, as based on independent probable errors, a subsequent comparison made of the weighted and unweighted averages showed no significant differences. A decision was made to use the unweighted instead of weighted averages because, for the case considered, the calculated total probable errors associated with the unweighted averages were found to be somewhat more conservative. For calculations of the total probable errors $(pe)_T$, considerations were given to the measurement dispersion errors $(pe)_D$, and the bias probable errors $(pe)_B$ caused primarily by uncertainties in the cryogenic load reference temperature, ambient load temperature, Y-factor ratios, and mismatches.

As given in Tables 4 and 5, the unweighted average antenna and maser temperature values are 8.5 and 19.0°K, respectively, for the Horn 235 receiving system, and 6.8 and 18.5°K, respectively, for the Horn 232 receiving system. The antenna temperature for the Horn 235 receiving system is approximately 1.7°K higher than that obtained for the Horn 232 receiving system. If it is assumed that there were no differences in the antenna environments during calibrations, the loss contributed by the Horn 235 turnstile junction at approximately 30°C would be 1.7°K with an associated total probable error of $\pm1.0°K$.

4. Cone-on-Ground Receiving System

After completion of tests of the horn receiving systems and insertion loss calibrations of the X-band cone transmission lines, the final phase of cone receiving system

Fig. 18. Sample hourly run noise temperature plot: X-band Horn 235 receiving system

1	2	3	4	Combined average	
Temperature	Reference flange No. [Fig. 16(a)]	Average of 23 LN$_2$[a] cryogenic load runs, °K	Average of 3 LHe[b] cryogenic load runs, °K	Unweighted average of Cols. 3 and 4, °K	$(pe)_T$[d], °K
Zenith T_A'	2	7.94 ± 0.09 $(pe)_D$[c]	8.97 ± 0.05 $(pe)_D$	8.5 ± 0.4 $(pe)_D$	±0.7
T_L		0.84	0.80	0.8	
T_M''	1	19.71 ± 0.15 $(pe)_D$	18.24 ± 0.24 $(pe)_D$	19.0 ± 0.5 $(pe)_D$	±0.9
T_F''	1	0.94 ± 0.05 $(pe)_D$	1.68 ± 0.06 $(pe)_D$	1.3 ± 0.2 $(pe)_D$	±0.2
T_{SA}''	1	29.42 ± 0.14 $(pe)_D$	29.69 ± 0.30 $(pe)_D$	29.6 ± 0.1 $(pe)_D$	
$(T_{02} - 273.2°K)$		27.9 ± 1.4 $(pe)_D$	33.4 ± 1.3 $(pe)_D$	30.7 ± 1.9 $(pe)_D$	

[a] LN$_2$ cryogenic load used was Maury Microwave Corporation (MMC) Model 8023, SN 013.
[b] LHe cryogenic load used was the Laboratory Standard LHe Load (SPS 37-23, Vol. IV, pp. 206–208).
[c] $(pe)_D$ denotes the probable error of the mean due to dispersion of the data points.
[d] $(pe)_T$ denotes the probable error of the mean due to dispersion and bias errors.

1	2	3	4	Combined average	
Temperature	Reference flange No. [Fig. 16(b)]	Average of 8 LN$_2$ cryogenic load runs, °K	Average of 6 LHe[b] cryogenic load runs, °K	Unweighted average of Cols. 3 and 4, °K	$(pe)_T$, °K
Zenith T_A'	2a	6.78 ± 0.14 $(pe)_D$	6.72 ± 0.05 $(pe)_D$	6.8 ± 0.02 $(pe)_D$	±0.7
T_L		1.20	1.21	1.2	
T_M''	1	18.52 ± 0.17 $(pe)_D$	18.57 ± 0.05 $(pe)_D$	18.5 ± 0.02 $(pe)_D$	±0.7
T_F''	1	0.98 ± 0.01 $(pe)_D$	1.37 ± 0.01 $(pe)_D$	1.2 ± 0.1 $(pe)_D$	±0.1
T_{SA}''	1	27.48 ± 0.12 $(pe)_D$	27.87 ± 0.05 $(pe)_D$	27.7 ± 0.1 $(pe)_D$	
$(T_{02} - 273.2°K)$		27.9 ± 0.9 $(pe)_D$	30.2 ± 1.1 $(pe)_D$	29.1 ± 0.8 $(pe)_D$	

[a] LN$_2$ cryogenic load used was MMC 8023, SN 013.
[b] LHe cryogenic loads used were Laboratory Standard LHe Load and Goldstone LHe Load (SPS 37-30, Vol. III, p. 59).

installation and noise temperature calibrations were initiated. The X-band cone receiving system consists basically of the Horn 235 antenna assembly, maser and follow-up assemblies, cone transmission lines, and thermal load assemblies. A detailed description and block diagram of the X-band cone receiving system were presented in SPS 37-43, Vol. III, pp. 56–60. The results of measurements of all critical system and component reflection coefficients and transmission line losses were also reported in the same SPS article.

The cone assembly area on the roof of JPL Building 238 was used as a convenient location for noise temperature calibrations of the cone in a ground-type environment. The antenna receiving system, as assembled in the cone on JPL Building 238 roof, will be referred to as the cone-on-ground receiving system. In this receiving system the antenna output and maser input reference flanges are the same as those for the Horn 235 receiving system. A partial view of the cone transmission line, which connects the horn antenna assembly to maser assembly, may be seen
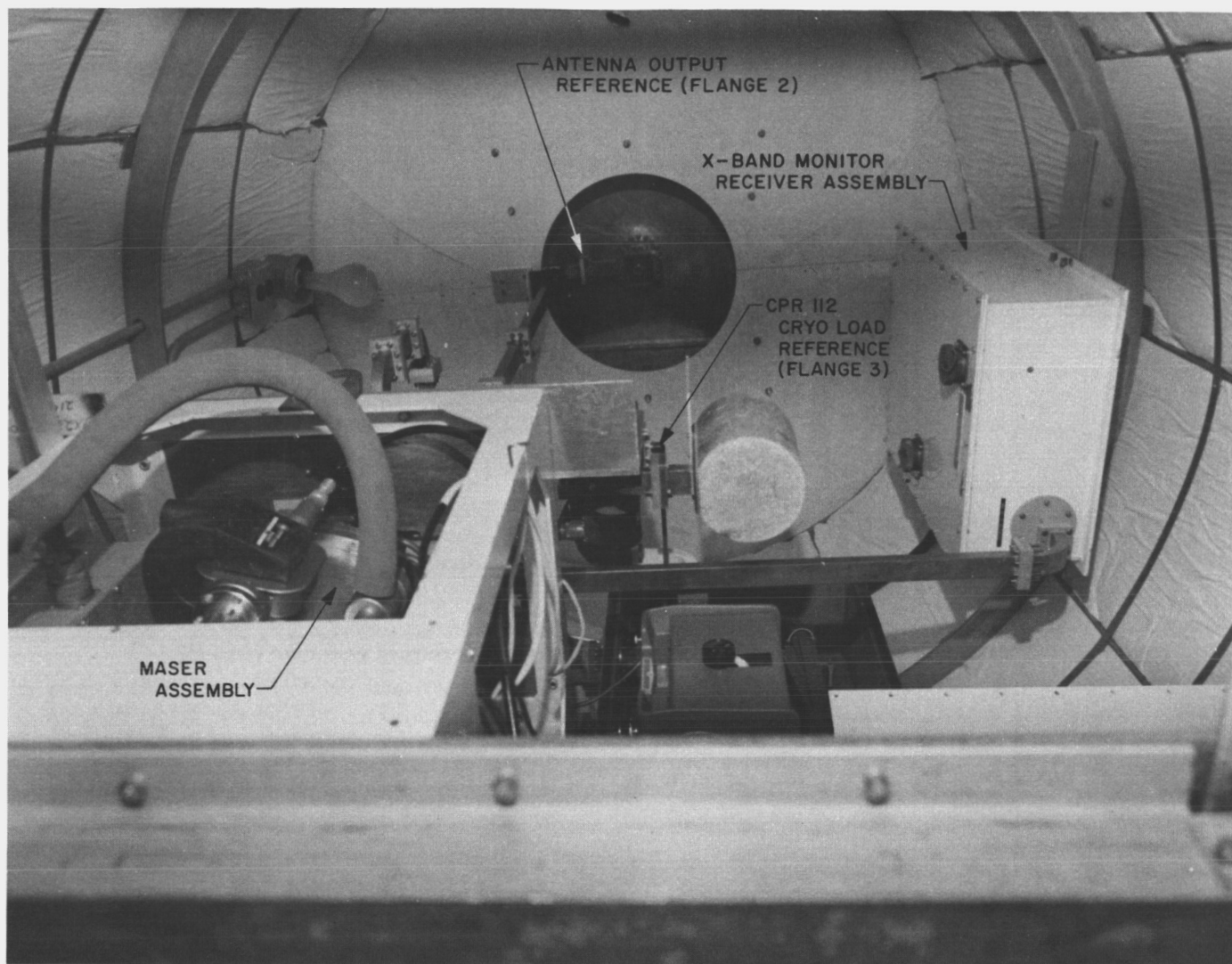
Fig. 19. X-Band cone interior

in Fig. 19. The loss of this transmission line should be the major source of system noise temperature differences for the Horn 235 and cone-on-ground receiving systems.

A sample of an hourly run plot of the cone-on-ground receiving system noise temperatures may be seen in Fig. 20. There appears to be some correlation between maser temperature and the physical cone temperature in this plot. Each data point in the plot represents the average of six or more sets of Y-factor measurements. The limits shown on the individual antenna temperature values indicate total probable errors.

A summary of the average noise temperatures for the cone-on-ground receiving system at 8448 MHz is tabu-

lated in Table 6. The averages of runs made with liquid nitrogen and liquid helium loads are tabulated separately. Comparison of the associated probable errors of weighted and unweighted averages again resulted in a decision to use the unweighted average technique for calculating the combined averages. There were no significant differences between weighted and unweighted averages.

Temperatures of primary interest in Table 6 for the cone-on-ground receiving system are the combined average values of 9.1, 16.9, and 36.9°K for the antenna, maser, and system temperatures, respectively. Values of the calibrated low and high gas tube temperatures may also be found in this table. This measurement system will have larger bias errors than the Horn 235 receiving system due
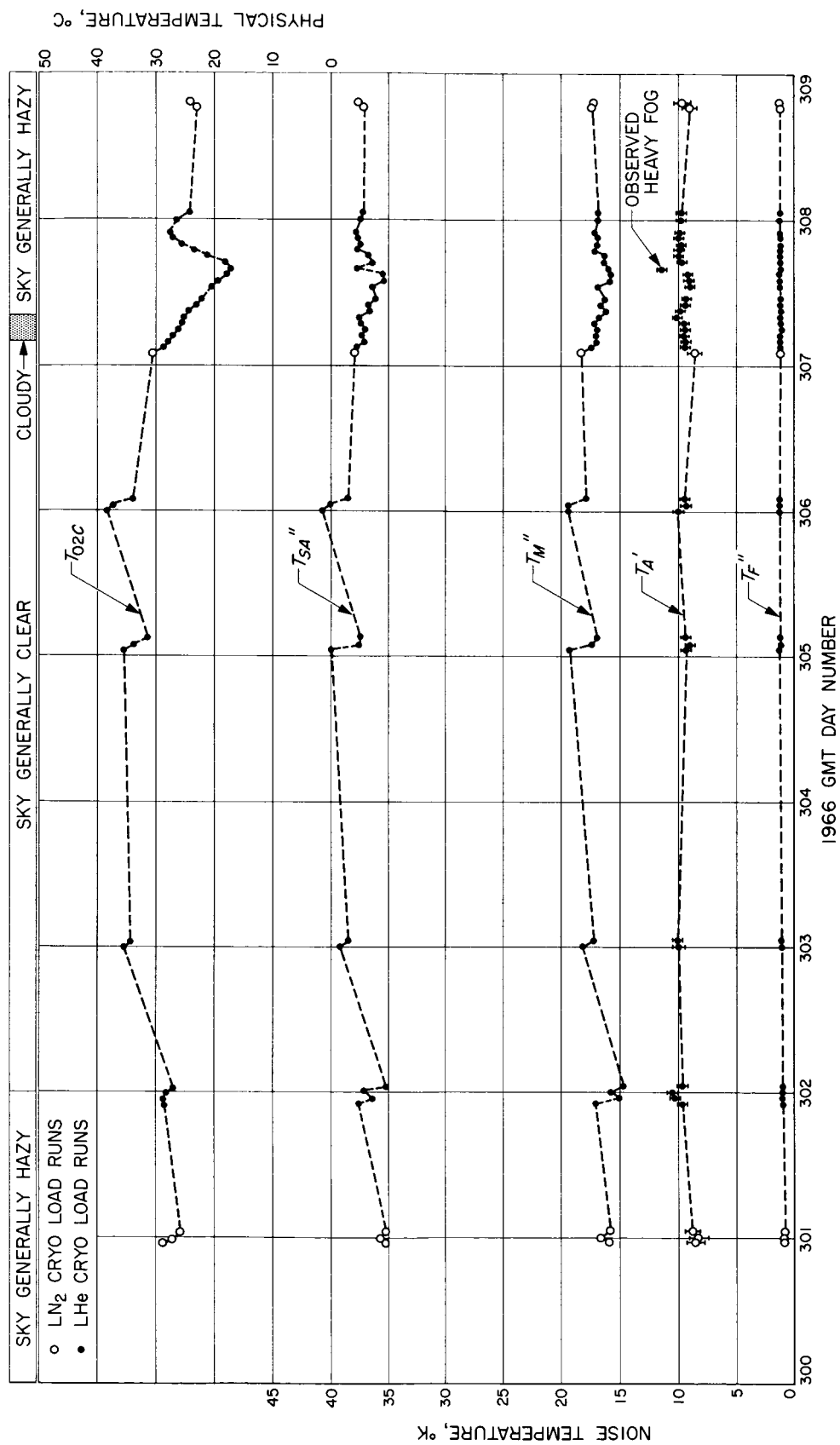
Fig. 20. Sample hourly run noise temperature plot: X-band cone-on-ground receiving system

Table 6. Summary of average temperatures for cone-on-ground receiving system at 8448 MHz

1	2	3	4	Combined average	
Temperature	Reference flange No.[a]	Average of 6 LN$_2$[b] cryogenic load runs, °K	Average of 29 LHe[c] cryogenic load runs, °K	Unweighted average of Cols. 3 and 4, °K	$(pe)_T$, °K
Zenith T_A'	2	8.75 ± 0.12 $(pe)_D$	9.47 ± 0.04 $(pe)_D$	9.1 ± 0.2 $(pe)_D$	±0.7
T_L		9.87	9.86	9.9	
T_M''	1	16.85 ± 0.24 $(pe)_D$	16.94 ± 0.13 $(pe)_D$	16.9 ± 0.03 $(pe)_D$	±0.8
T_F''	1	0.99 ± 0.04 $(pe)_D$	1.12 ± 0.01 $(pe)_D$	1.1 ± 0.04 $(pe)_D$	±0.1
T_{SA}''	1	36.46 ± 0.31 $(pe)_D$	37.38 ± 0.16 $(pe)_D$	36.9 ± 0.3 $(pe)_D$	
$(T_{02} - 273.2°K)$		26.6 ± 0.8 $(pe)_D$	27.0 ± 0.7 $(pe)_D$	26.8 ± 0.1 $(pe)_D$	
T_{EL}''	1	3.89 ± 0.04 $(pe)_D$	4.02 ± 0.02 $(pe)_D$	4.0 ± 0.04 $(pe)_D$	
T_{EH}''	1	38.56 ± 0.13 $(pe)_D$	39.33 ± 0.06 $(pe)_D$	38.9 ± 0.3 $(pe)_D$	

[a]See Fig. 14, p. 60 of SPS 37-43, Vol. III.
[b]LN$_2$ cryogenic load used was MMC 8023, SN 013.
[c]LHe cryogenic load used was Laboratory Standard LHe Load.

to the waveguide transmission line and switch loss measurement inaccuracies but better measurement resolution due to the rapid switching available with the waveguide switches. The difference in the antenna temperatures measured for the cone-on-ground and Horn 235 receiving systems can be due to either measurement inaccuracies, differences in weather conditions, or ground contributions.

5. 85-Ft Antenna Cassegrain Receiving System

After completion of calibrations of the cone-on-ground receiving system, the X-band cone was transported to the Venus DSS and installed on the 85-ft-D paraboloid to complete the assembly of the 85-ft antenna Cassegrain receiving system (Fig. 21).

The antenna output and maser input reference flanges for this system are the same as for the cone-on-ground receiving system. The noise temperature difference between the two systems should be principally due to the antenna temperature because of the effects of spillover, etc.

Noise temperature calibrations made on the 85-ft antenna Cassegrain receiving system consisted of hourly runs made with the hyperboloid subreflector in the following positions: (1) S-band hyperboloid reference position

of 1.840 in., (2) initial X-band focus position of 2.440 in., and (3) final X-band focus position of 2.660 in. All calibrations were made with the 85-ft antenna pointed at the zenith position.[1]

A sample plot of hourly runs for the hyperboloid at the 2.440-in. position may be seen in Fig. 22. Each data point in the figure represents the result of 10 sets of Y-factor measurements. The limits on the individual antenna temperatures indicate total probable errors.

Table 7 presents a summary of the 8448-MHz average noise temperatures for the 85-ft antenna Cassegrain receiving system with the hyperboloid at the S-band reference position of 1.840 in. The combined averages in Table 7 are the unweighted averages of the means obtained with liquid nitrogen and liquid helium loads. Comparison of weighted and unweighted averages showed no significant differences. Table 7 shows the unweighted antenna temperature to be 12.1 ±0.8°K $(pe)_T$ for this receiving system with the hyperboloid at the S-band reference position.

The noise temperature values calibrated with the hyperboloid at the X-band far-field focus positions of 2.440

---

[1]Most of the noise temperature calibrations on this system were performed by Venus DSS personnel.
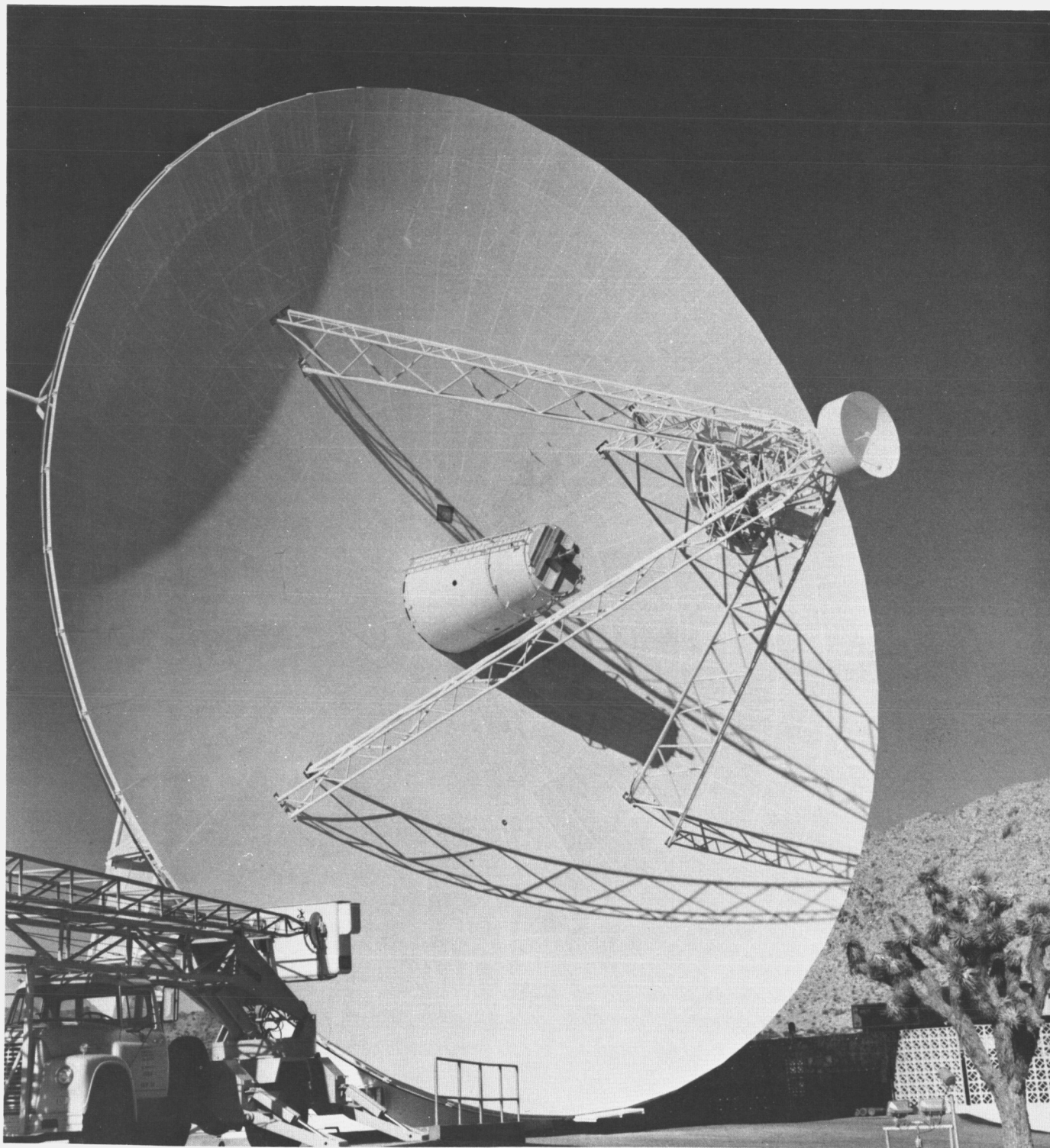
Fig. 21. X-Band cone on 85-ft-D paraboloid
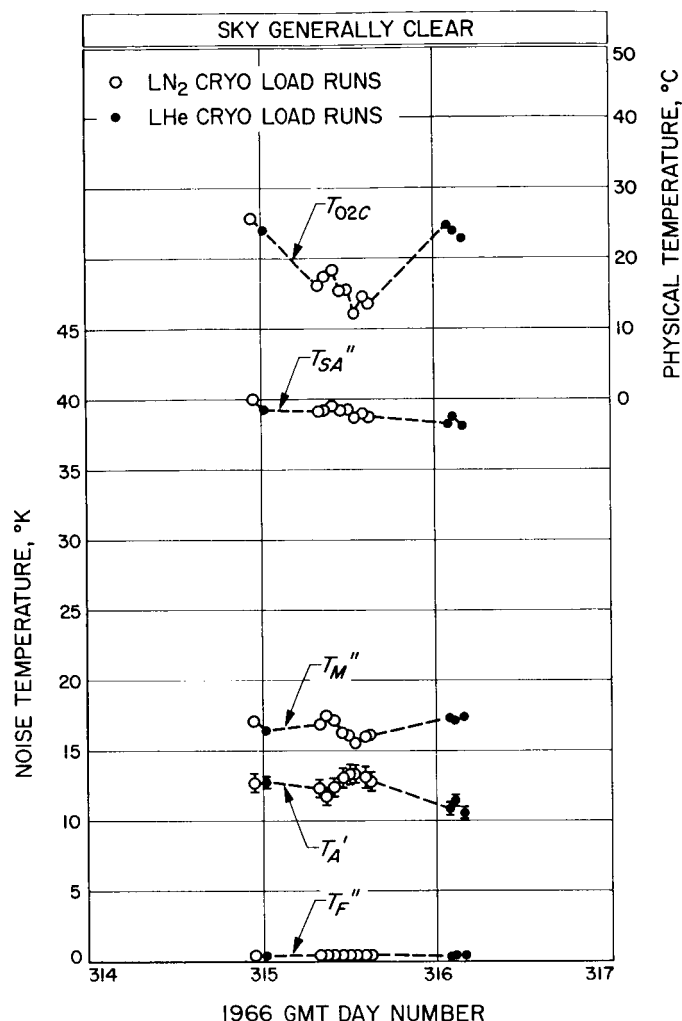
Fig. 22. Sample hourly run noise temperature plot: 85-ft antenna Cassegrain receiving system (hyperboloid at the 2.440-in. reference position)

and 2.660 in. may be found in Table 8. The average calibrated antenna temperatures as given in Table 8 for the two far-field focus positions of 2.440 and 2.660 in. are 13.6 ±0.4°K $(pe)_T$ and 13.3 ±0.4°K $(pe)_T$, respectively. The lower total probable errors for these averages are due to the use of only the more accurate liquid helium cryogenic reference load for calibrations.

6. Comparison of Receiving Systems

A comparison of average noise temperatures of the various receiving systems which were calibrated is given in Table 8. The average antenna temperatures tabulated for the various receiving systems should be considered as the best calibrated values which were obtained with the

amount of data taken (limited in some cases), and for the environmental conditions which existed during the measurement periods. No effort was made to correlate the measurements to atmospheric temperature and humidity variations.

An independent method, which was proposed for calibrating the loss of the antenna-to-maser transmission line for the X-band cone, is based on measurements of system temperatures. The mathematical relationship is expressed as follows:

$$(T_L)_{cone} = (T_L)_{Horn\ 235} + [(T_{SA}'')_{cone} - (T_{SA}'')_{Horn\ 235}]$$
$$- [(T_A')_{cone} - (T_A')_{Horn\ 235}]$$
$$- [(T_R'')_{cone} - (T_R'')_{Horn\ 235}] \qquad (1)$$

where

$$(T_R'')_{cone} = (T_M'')_{cone} + (T_F'')_{cone}$$
$$(T_R'')_{Horn\ 235} = (T_M'')_{Horn\ 235} + (T_F'')_{Horn\ 235}$$

If the assumption is made that

$$(T_A')_{cone} = (T_A')_{Horn\ 235}$$

and if it is assumed that the values of receiver temperatures are different but precisely known for the two systems, then substitution of values from Table 8 into Eq. (1) gives a nominal line loss of 10.4°K as compared to the 9.9°K value based on actual insertion loss measurements. Except for the error caused by rounding off temperature values, the difference in the two line-loss values is precisely the difference in calibrated antenna temperatures for the two systems. The difference in calibrated antenna temperatures could be real, since the horn environments for the two systems were somewhat different. On the other hand, the antenna temperatures of the two systems could actually be the same and the measured difference can be accounted for by the probable errors. If it had been assumed in Eq. (1) that both the receiver and antenna temperatures were the same for the two systems, then substitution of values into Eq. (1) would have given 8.1°K due to line loss of the X-band cone. This assumption, however, would have been erroneous, due to the fact that the maser magnet was changed in orientation after the horn experiments. A subsequent lowering of calibrated maser temperature was noted at that time. The difference in calibrated maser temperatures for the horn and cone-on-ground receiving systems is partly attributed to the change in magnet orientation and partly to calibration errors.

Table 7. Summary of average temperatures for 85-ft antenna Cassegrain receiving system at 8448 MHz
(hyperboloid at S-band reference position of 1.840 in.)

1	2	3	4	Combined average	
Temperature	Reference flange No.[a]	Average of 9 LN₂ cryogenic load runs, °K	Average of 4 LHe cryogenic load runs, °K	Unweighted average of Cols. 3 and 4, °K	(pe)$_T$, °K
Zenith T_A'	2	12.77 ± 0.12 (pe)$_D$	11.43 ± 0.33 (pe)$_D$	12.1 ± 0.5 (pe)$_D$	±0.8
T_L		9.40	9.69	9.5	
T_M''	1	16.54 ± 0.15 (pe)$_D$	17.11 ± 0.14 (pe)$_D$	16.8 ± 0.2 (pe)$_D$	±0.8
T_F''	1	0.50 ± 0.01 (pe)$_D$	0.42 ± 0.02 (pe)$_D$	0.5 ± 0.03 (pe)$_D$	±0.05
T_{SA}''	1	39.21 ± 0.09 (pe)$_D$	38.65 ± 0.19 (pe)$_D$	38.9 ± 0.2 (pe)$_D$	
$(T_{02} - 273.2°K)$		16.7 ± 0.9 (pe)$_D$	24.0 ± 0.3 (pe)$_D$	20.4 ± 2.5 (pe)$_D$	
T_{EL}''	1	4.00 ± 0.07 (pe)$_D$	4.06 ± 0.02 (pe)$_D$	4.0 ± 0.02 (pe)$_D$	
T_{EH}''	1	39.53 ± 0.07 (pe)$_D$	39.70 ± 0.31 (pe)$_D$	39.6 ± 0.06 (pe)$_D$	

[a]Reference flange numbers are same as for cone-on-ground receiving system.
[b]LN₂ cryogenic load used was MMC 8023, SN 013.
[c]LHe cryogenic load used was Laboratory Standard LHe Load.

Table 8. Overall comparison of average noise temperatures of X-Band receiving systems at 8448 MHz

Receiving system	Reference table	Calibration period (1966 GMT Day No.)	Total No. of runs	Zenith T_A', °K	T_L, °K	T_M'', °K	T_F'', °K	T_{SA}'', °K	T_{EL}'', °K	T_{EH}'', °K	T_{02t}, °C
Horn 232	5	271–275	14	6.8 ± 0.02 (pe)b ± 0.7 (pe)t	1.2	18.5 ± 0.02 (pe)b ± 0.7 (pe)t	1.2 ±0.1 (pe)b ±0.1 (pe)t	27.7 ± 0.1 (pe)b			29.1 ± 0.8 (pe)b
Horn 235	4	266–270 and 281–282	26	8.5 ± 0.4 (pe)b ± 0.7 (pe)t	0.8	19.0 ± 0.5 (pe)b ± 0.9 (pe)t	1.3 ±0.2 (pe)b ±0.2 (pe)t	29.6 ± 0.1 (pe)b			30.7 ± 1.9 (pe)b
Cone-on-ground	6	300–308	35	9.1 ± 0.2 (pe)b ± 0.7 (pe)t	9.9	16.9 ± 0.03 (pe)b ± 0.8 (pe)t	1.1 ±0.04 (pe)b ±0.1 (pe)t	36.9 ± 0.3 (pe)b	4.0 ±0.04 (pe)b	38.9 ± 0.3 (pe)b	26.8 ± 0.1 (pe)b
85-ft antenna Cassegrain (hyperboloid at 1.840 in.)	7	314–316	13	12.1 ± 0.5 (pe)b ± 0.8 (pe)t	9.5	16.8 ± 0.2 (pe)b ± 0.8 (pe)t	0.5 ±0.03 (pe)b ±0.05 (pe)t	38.9 ± 0.2 (pe)b	4.0 ±0.02 (pe)b	39.6 ± 0.06 (pe)b	20.4 ± 2.5 (pe)b
85-ft antenna Cassegrain (hyperboloid at 2.440 in.)		328–332	18[a]	13.6 ± 0.1 (pe)b ± 0.4 (pe)t	9.5	16.1 ± 0.1 (pe)b ± 0.6 (pe)t	0.43 ±0.003 (pe)b ±0.03 (pe)t	39.7 ± 0.2 (pe)b	4.0 ±0.01 (pe)b	39.9 ± 0.03 (pe)b	20.7 ± 0.6 (pe)b
85-ft antenna Cassegrain (hyperboloid at 2.660 in.)		356	3[a]	13.3 ± 0.1 (pe)b ± 0.4 (pe)t	9.4	15.0 ± 0.06 (pe)b ± 0.6 (pe)t	0.5 ±0.01 (pe)b ±0.04 (pe)t	38.2 ± 0.07 (pe)b	4.0 ±0.03 (pe)b	39.4 ± 0.1 (pe)b	18.6 ± 0.04 (pe)b

[a] All runs were made with the Laboratory Standard LHe Load.
[b] Any difference between T_{SA}'' and the sum $= T_A' + T_L + T_M'' + T_F''$ are due to round-off errors.

Comparison of the values of antenna temperature in Table 8 shows that the antenna temperature increased when the X-band cone was used on the 85-ft antenna Cassegrain system instead of on the ground. The increases were 3.0, 4.5, and 4.2°K, respectively, with the hyperboloid at the 1.840-, 2.440-, and 2.660-in. positions, respectively. Some of the increases in antenna temperatures are due to hyperboloid scattering, leakage through the dish surface, quadrapod blockage, and spillover.

More calibrations of the 85-ft antenna Cassegrain receiving system are expected to be made in the near future. The data given in Table 8 may undergo further refinements and the results reported in a future SPS.

D. Improved RF Calibration Techniques: Daily System Noise Temperature Measurements,
C. T. Stelzried

The daily noise temperature calibration technique used at the Mars and Venus DSS's has been discussed in detail (SPS 37-42, Vol. III, p. 25). Noise temperature calibrations are made by switching the maser input with a waveguide switch between the antenna and a waveguide ambient termination. The principal advantage of this technique is long-term stability and reliability of the ambient waveguide termination. Another advantage is that it is not necessary to evaluate the waveguide losses if the system temperature is defined at the maser input. This technique does depend on a previous calibration of the maser input noise temperature, although a 10% error in this parameter results in only about a 1% error in the system temperature measurement for a typical Goldstone installation.

The principal results of the daily noise temperature calibrations are tabulated in Figs. 23 and 24 for the period of October 24 (Day No. 297), 1966 to February 9 (Day No. 40), 1967. This does not include the data taken at the Mars DSS when used in the standard DSIF mode of operation. A summary of the system noise temperature and maser gain averages is tabulated in Table 9. The probable errors of the measurement dispersions are identified as $(pe_i)_D$ for the individual measurements and $(pe)_D$ for the mean. The errors do not include bias errors, such as those due to nonlinearities, etc. These are the first reported daily system noise temperature calibrations for the X-Band cone (previously described in SPS 37-42, Vol. III, p. 46). The system temperature averages were computed using only data which were acquired as follows:

(1) Antenna at zenith.

(2) Clear weather.

(3) No RF spur in receiver pass-band.

It is interesting to note that even though atmospheric effects are greater at X-Band ("Efficient Antenna Systems: System Noise Temperature as a Function of Meteorological Conditions," SPS 37-43, Vol. III, p. 63) than S-Band, the daily individual measurement dispersion was the lowest with the X-Band data. Apparently, at least for this particular period of time, the equipment, personnel, and operational procedures were the overriding source of error and noise temperature instabilities. The maser gain averages were computed using all data points. The maser gain was optimized prior to each calibration except for the post calibrations.

Table 9. Summary of the system temperature and maser gain averages and measurement dispersions

DSS	Frequency, MHz	System temperature, °K	Maser gain, db
Venus	2388.0	22.9 $\begin{array}{l}\pm 3.2\ (pe_i)_D\\\pm 0.13\ (pe)_D\end{array}$ 33 data points	39.8 $\begin{array}{l}\pm 0.54\ (pe_i)_D\\\pm 0.07\ (pe)_D\end{array}$ 50 data points
Venus	8448.0	37.9 $\begin{array}{l}\pm 1.7\ (pe_i)_D\\\pm 0.13\ (pe)_D\end{array}$ 17 data points	40.4 $\begin{array}{l}\pm 0.63\ (pe_i)_D\\\pm 0.13\ (pe)_D\end{array}$ 23 data points
Mars	2388.0	27.4 $\begin{array}{l}\pm 3.2\ (pe_i)_D\\\pm 0.21\ (pe)_D\end{array}$ 15 data points	38.4 $\begin{array}{l}\pm 0.43\ (pe_i)_D\\\pm 0.08\ (pe)_D\end{array}$ 28 data points
Mars	2297.6	28.1 $\begin{array}{l}\pm 2.5\ (pe_i)_D\\\pm 0.15\ (pe)_D\end{array}$ 19 data points	40.6 $\begin{array}{l}\pm 0.17\ (pe_i)_D\\\pm 0.03\ (pe)_D\end{array}$ 30 data points

STA.	DAY NO.	OPER.	FREQ. (GHZ)	TEST PRE	TEST POS	CLEAR WTHR.	ZENITH	RF SPUR	REFLECTO-METER(DB) AMB.	ANT.	GAIN (DB)	TF (DEG,K)	TS (DEG,K)	PETSA (DEG,K)	COMMENTS
13	298	SCA	2388	1	1	2	2	1	46.7	39.9	39.4	.4	22.0	.21	NO SPIKES OBSERVED
13	299	SCA	2388	1	1	2	2	1	47.3	39.9	39.3	.4	21.9	.21	NO SPIKES OBSERVED
13	300	HNK	2388	1	1	2	2	1	47.7	40.3	36.4	.5	22.7	.22	
13	301	WOO	2388	2	1	2	2	1	44.6	33.7	37.4	.4	22.2	.33	
13	303	LJW	2388	2	1	2	1	1	44.6	41.2	40.1	.4	22.3	.22	
13	310	F G	2388.0	1	1	2	2	1	44.7	41.7	38.3	.6	20.5	.20	FIRST DAILY AFTER CONE CHANGE,COOLDOWN
13	317	LJW	8448.0	1	1	2	2	1	38.2	35.8	41.1	.3	36.5	.34	
13	318	LJW	8448.0	1	1	2	2	1	38.8	37.3	41.4	.4	37.2	.30	
13	319	LJW	8448	1	1	2	2	1	44.5	38.5	41.7	.4	39.5	.32	
13	321	NMK	8448	1	1	2	2	1	42.9	37.2	41.7	.3	38.9	.31	
13	323	LJW	8448	1	1	2	2	1	41.5	37.0	41.0	.4	39.2	.32	
13	324	NMK	8448	1	1	2	1	1	42.9	37.5	41.3	.4	39.5	.31	
13	325	NMK	8448	1	1	1	1	1	39.4	36.1	41.1	.4	38.4	.31	
13	326	NMK	8448	1	1	1	1	1	37.0	34.7	41.0	.4	38.2	.31	
13	327	MHK	8448	1	1	2	1	1	37.2	34.7	40.5	.4	38.7	.31	
13	333	HJK	8448.00	1	1	1	2	1	42.8	37.0	41.1	.4	39.4	.32	
13	336	CBW	2388	1	1	2	2	1	41.0	38.0	39.3	.5	22.3	.21	
13	337	CBW	2388	2	1	1	2	1	41.2	37.7	40.2	.3	25.4	.23	
13	338	CBW	2388	2	1	2	2	2	43.7	37.9	40.4	.4	24.6	.26	
13	339	CBW	2388	2	1	1	2	1	40.9	37.0	40.6	.5	22.6	.27	
13	340	CBW	2388	2	1	1	2	1	43.3	38.7	40.3	.4	21.1	.21	
13	341	LJW	2388	2	1	1	2	1	42.0	37.2	38.5	.8	23.3	.29	
13	343	LJW	8448	1	1	2	2	1	31.3	30.5	40.0	.6	37.4	.31	
13	344	LJW	8448	1	1	2	2	1	37.2	35.4	40.5	.4	37.1	.31	
13	345	LJW	8448	1	1	2	2	1	38.5	35.0	40.9	.4	37.4	.30	
13	346	LJW	8448	1	1	2	2	1	39.5	36.8	39.5	.6	37.5	.30	
13	347	LJW	8448	2	1	2	2	1	38.0	35.0	39.5	.6	37.8	.31	
13	348	NMK	8448	1	1	2	2	1	40.2	35.4	39.5	.6	37.2	.30	
13	349	NMK	8448	1	1	2	2	1	41.2	36.3	39.4	.6	38.1	.34	
13	350	NMK	8448	1	1	2	2	1	39.0	35.0	39.0	.6	37.5	.31	
13	351	FAG	8448	2	1	2	2	1	40.2	37.0	39.0	.6	38.3	.31	
13	352	M K	8448	1	1	2	2	1	40.0	37.5	39.0	.6	38.2	.32	
13	353	M K	8448	1	1	2	2	1	42.0	39.6	39.0	.4	38.1	.32	
13	355	M K	8448	1	1	1	2	1	41.2	38.7	41.0	.4	37.9	.31	
13	356	M K	8448	1	1	2	2	1	41.9	37.9	40.2	.5	38.4	.31	

Fig. 23. Tabulated results of the Venus DSS daily noise temperature calibrations

13	357	CBW	2338	2	1	2	2	1	40.8	43.3	40.4	.4	23.5	.23	FIRST CALIB. AFTER COOL DOWN OF MASER
13	361	CBW	2338	1	1	2	2	1	40.3	44.7	38.9	.5	23.8	.26	1ST CAL.AFT.HOLIDAYS 2ND AFT.MASER CLDN
13	362	CBW	2338	1	1	1	2	1	41.7	37.4	40.0	.5	22.1	.21	SPACE HEATER WAS ON IN THE CONE
13	363	CBW	2338	1	1	2	2	1	41.8	37.5	40.0	.5	23.4	.22	HEAT ON IN CONE
13	365	F G	2388	1	1	1	2	1	43.1	38.0	40.9	.5	26.3	.24	
13	3	CBW	2388	1	1	1	2	1	42.5	37.7	39.4	.5	24.0	.23	
13	4	LJW	2388	1	1	2	2	1	42.0	35.2	40.1	.6	23.9	.23	
13	5	LJW	2388	1	1	1	2	1	42.2	35.5	40.4	.5	24.8	.24	
13	7	LJW	2388	1	1	1	2	1	42.2	35.4	38.8	.7	24.0	.23	
13	8	LJW	2388	1	1	2	2	1	41.4	37.2	39.5	.6	25.3	.42	
13	10	RLB	2388	1	1	2	2	1	30.1	28.0	40.0	.5	22.2	.22	
13	11	NMK	2388	1	1	2	2	1	41.8	38.4	40.0	.5	22.3	.22	
13	12	RLB	2388	1	1	2	2	1	41.0	37.7	39.9	.6	22.2	.22	
13	13	NMK	2388	1	1	2	2	1	42.2	38.2	39.5	.5	26.4	.26	
13	15	NMK	2388	1	1	2	2	1	42.5	39.2	39.7	.5	23.7	.22	
13	16	RLB	2388	1	1	2	2	1	43.5	38.5	39.9	.5	21.9	.21	
13	17	NMK	2388	1	1	2	2	1	41.4	37.0	40.0	.5	22.9	.22	
13	18	KAM	2388	1	1	2	2	1	41.2	37.2	40.0	.5	22.6	.22	
13	19	KAM	2388	1	1	2	2	1	42.7	37.3	40.2	.4	22.1	.21	
13	20	RLB	2388	1	1	2	2	1	42.1	38.6	40.2	.5	25.0	.28	WIND 20 TO 30 MPH
13	21	RLB	2388	1	1	2	2	1	40.0	37.4	40.2	.5	22.4	.22	WIND 20 TO 30 MPH
13	22	RLB	2388	1	1	2	2	1	43.4	37.8	40.0	.5	23.7	.22	
13	23	KAM	2388	1	1	1	2	1	42.1	37.2	39.5	.5	18.9	.19	WET,RAINING PAST 12 HOURS
13	24	NMK	2388	1	1	1	2	1	42.6	37.6	40.2	.4	24.9	.24	
13	25	RLB	2388	1	1	1	2	1	42.1	37.4	40.0	.5	21.8	.22	WIND GUSTS TO 20 MPH INTERMITTENT RAIN
13	27	RLB	2388	1	1	1	2	1	41.5	37.4	40.5	.4	23.2	.24	
13	28	RLB	2388	1	1	1	2	1	42.8	38.2	40.7	.4	23.1	.23	
13	29	F G	2388	1	1	2	2	1	42.8	37.8	40.6	.5	23.4	.25	
13	30	RLB	2388	1	1	1	2	1	41.5	37.5	40.0	.5	22.0	.22	
13	32	LJW	2388	1	1	2	2	1	42.6	35.8	40.4	.5	22.8	.22	
13	33	LJW	2388	1	1	2	2	1	41.4	36.0	40.3	.5	22.1	.23	
13	34	LJW	2388	1	1	2	2	1	41.6	36.2	40.3	.5	22.3	.22	
13	35	RLB	2388	1	1	1	2	1	42.0	38.5	39.8	.5	22.6	.24	
13	36	RLB	2388	1	1	2	2	1	42.0	38.2	39.9	.5	23.4	.31	
13	37	LJW	2388	1	1	2	2	1	42.6	35.6	39.4	.6	23.3	.23	
13	38	RLB	2388	1	1	2	2	1	42.8	37.6	40.0	.5	24.1	.24	
13	39	NMK	2388	1	1	2	2	1	41.2	37.2	39.8	.5	23.3	.22	
13	40	LJW	2388	1	1	2	2	0	41.1	37.3	40.0	.5	23.3	.28	

Fig. 23 (contd)

STA.	DAY NO.	OPER.	FREQ. (GHZ)	TEST PRE	TEST POST	CLEAR WTHR.	ZENITH	RF SPUR	REFLECTO-METER(DB) AMB.	REFLECTO-METER(DB) ANT.	GAIN (DB)	TF (DEG,K)	TS (DEG,K)	PETSA (DEG,K)	COMMENTS
14	297	LJ	2297.5	2	1	2	2	1	40.7	31.7	40.0	.7	28.0	.25	
14	297	C S	2297.5	1	2	2	2	1	41.7	32.0	40.2	.8	28.1	.25	
14	299	LJW	2297	2	1	2	2	1	39.4	31.5	40.6	.7	27.8	.25	
14	299	LJW	2297.5	1	2	2	1	1	40.7	31.8	40.7	.7	28.4	.25	
14	300	NMK	2297.5	2	1	2	2	1	40.4	31.8	40.6	.6	25.5	.51	
14	300	LJW	2297.5	1	2	2	2	1	40.3	31.9	40.7	.7	28.0	.27	
14	301	HNK	2388.0	2	1	2	2	2	20.7	24.8	38.8	.6	245.5	4.66	STRONG SIG 2388.86
14	304	NMK	2297.5	2	1	2	2	1	39.6	31.5	40.9	.6	27.7	.25	
14	304	NMK	2297.5	1	2	2	2	1	40.0	31.9	40.9	.6	27.8	.25	
14	306	C W	2297.0	2	1	2	1	1	38.3	31.0	40.8	.7	27.4	.26	
14	306	NMK	2297.0	1	2	1	2	1	38.8	31.6	40.7	.6	27.7	.25	
14	307	HNK	2297.5	2	1	1	1	1	39.9	31.7	40.9	.6	30.4	.27	
14	308	HNK	2297.5	1	2	1	2	1	39.8	31.8	40.9	.6	28.2	.26	
14	313	LJW	2297.5	2	1	2	2	1	41.2	31.9	40.4	.7	26.6	.24	
14	313	C W	2297.6	1	2	2	2	1	40.8	31.8	40.2	.7	28.4	.25	
14	315	C W	2297.6	1	2	1	2	1	40.8	31.7		.7	29.0	.26	
14	325	NMK	2297.5	2	1	2	2	1	39.6	31.2	40.3	.8	27.9	.25	
14	325	LJW	2297.5	1	2	2	2	1	37.8	31.0	40.4	.8	29.5	.26	
14	336	LJW	2388.	1	2	1	2	1	20.7	25.0	40.4	.8	27.0	.24	
14	340	KAM	2388.	1	2	1	2	1	20.8	25.0	38.6	.7	27.9	.66	
14	346	LJW	2297.59	2	1	2	2	1	40.1	31.2	40.5	.7	28.5	.26	
14	346	CBW	2297.59	1	2	1	2	1	41.1	32.0	40.3	.7	29.5	.26	
14	349	NMK	2297.5	2	1	2	2	1	39.4	31.3	40.3	.6	27.5	.25	
14	349	LJW	2297.59	1	2	2	2	1	40.2	31.8	40.6	.7	28.1	.25	
14	354	M K	2297.5	2	1	2	2	1	39.9	31.0	40.8	.7	29.5	.26	
14	354	LJW	2297.59	1	2	2	2	1	40.3	31.4	40.8	.7	29.5	.27	
14	355	M K	2297.5	2	1	1	2	1	39.3	30.8	40.8	.7	29.6	.26	
14	355	KAM	2297.6	1	2	2	2	1	41.1	31.7	40.7	.7	29.7	.26	
14	361	M K	2297.59	1	2	1	2	1	39.0	31.5	40.4	.8	28.3	.26	
14	362	CBW	2297.59	2	1	2	2	1	40.1	31.3	40.9	.5	35.5	.29	
14	363	M K	2388.0	2	1	2	2	1	20.7	25.0	38.5	.8	27.0	.25	
14	364	LJW	2388.0	1	2	1	2	1	20.8	24.8	38.2	.8	25.2	.24	
14	5	LJW	2388.	2	1	1	2	1	20.7	24.4	39.1	.7	28.8	.26	
14	7	LJW	2388.	2	1	1	2	1	20.7	24.8	37.4	1.1	29.3	.26	
14	8	KAM	2388.	1	2	2	2	1	20.7	24.9	37.4	1.1	28.6	.26	

Fig. 24. Tabulated results of the Mars DSS daily noise temperature calibrations

14	10	KAM	2388.	2	1	2	2	1	20.8	24.9	38.2	.8	26.5	.24	
14	10	LJW	2388.	1	2	2	2	1	20.7	24.9	37.9	.9	26.9	.24	
14	12	KAM	2388.	2	1	2	2	2	20.8	24.9	38.3	.8	360.0	2.17	STRONG SPUR 2388.8
14	12	NMK	2388.	1	2	2	2	1	20.9	24.6	38.3	.8	29.0	.26	PRECAL RF SPUR DUE
															TO EXC/REC CH23 ON
14	14	KAM	2388.	2	1	2	2	1	20.8	25.0	38.2	.8	27.4	.26	
14	14	NMK	2388.	1	2	2	2	1	20.8	24.9	37.9	.9	25.6	.24	
14	14	LJW	2388.	2	1	2	2	1	20.6	24.4	38.5	.7	26.4	.24	
14	15	NMK	2297.6	2	1	2	2	1	40.0	31.2	40.6	.7	26.6	.24	NO RF SPUR
14	15	LJW	2297.6	1	2	2	2	1	39.4	31.6	40.4	.8	28.8	.26	
14	26	LJW	2388.	2	1	2	2	1	18.7	16.2	39.7	.8	27.8	.26	
14	26	RLB	2388.	1	2	1	2	1	17.2	17.3	38.2	.9	23.7	2.69	
14	28	NMK	2388.	2	1	1	2	1	22.6	20.8	38.0	.9	31.0	.27	
14	28	RZB	2297.6	2	1	1	2	1	22.0	22.2	40.5	.8	28.1	.27	
14	28	KAM	2297.6	1	2	1	2	1	22.3	22.6	41.0	.6	26.9	.25	
14	29	RLB	2388.	1	2	2	2	1	22.8	20.5	38.2	.8	27.5	.29	
14	29	KAM	2388.	2	1	1	2	1	17.0	20.7	37.9	.9	28.0	.25	
14	30	NMK	2388.	1	2	1	2	1	22.7	20.7	37.9	.9	28.2	.25	
14	31	NMK	2388.	2	1	1	2	1	22.7	20.6	38.1	.9	28.8	.26	
14	31	RLB	2388.	1	2	2	2	1	22.9	21.0	37.5	1.0	27.5	.25	
14	36	KAM	2388.	2	1	2	2	1	20.9	24.7	38.5	.8	29.4	.26	
14	36	LJW	2388.	1	2	2	2	2	21.1	24.7	38.8	.8	32.1	.70	UNKNOWN SIGNAL AP-
															PEARS IN ANT.PO.ONLY
14	38	KAM	2388.	2	1	2	2	1	20.9	23.7	38.2	.8	29.7	.26	
14	39	RTB	2388	2	1	2	2	0	20.9	25.2	39.0	.8	26.6	.24	
14	40	KAM	2388	1	2	2	2	0	20.8	25.2	38.4	.9	26.5	.24	

Fig. 24 (contd)

E. Improved Calibration Techniques: Calibration of S-Band Rotary Vane Attenuator, T. Y. Otoshi and D. L. Welling

1. Introduction

This article presents preliminary results of calibrations made on an S-band rotary vane attenuator (SPS 37-24, Vol. IV, pp. 156–161) used in the Mars DSS 210-ft antenna gain measurement experiment. A description of the unique gain comparison measurement system, which used *Surveyor I* spacecraft on the Moon as a far field collimation facility, is given in "Efficient Antenna Systems: Gain Measurements of the Advanced Antenna System Using *Surveyor I* Signals," Part G of this SPS.

Following the gain measurement experiment, the rotary vane attenuator was returned to JPL for final calibrations. Relative attenuation measurements were performed at the various indicated vane angle settings required for final calculations of antenna gain. Three independent methods used for calibration of the attenuator were: (1) IF substitution, (2) AC substitution, and (3) DC substitution techniques. All calibrations were performed at 2295 MHz.

Discussions and calibration results of these three independent methods are presented. After careful considera-tion of various calibration errors present in the three independent methods, the various results were weighted and combined to produce grand average calibration values.

2. Measurement Procedures

a. IF substitution system. An IF substitution method was used in the first measurement system. This system uses linear detection to measure changes in the IF signal level before and after the attenuator is inserted in the system. For rotary vane attenuator calibrations, the attenuator remains in the system, and IF signal levels at various indicated vane angle settings are compared.

A block diagram of the IF system used is shown in Fig. 25. A PRD 915 was used as the receiver. The IF calibrations were cross-checked, using three different external IF attenuators, an AIL 2220-29D5 attenuator and two Weinschel PA-2 attenuators, as the attenuation standards. The RF source and load assemblies were matched to less than 1.014 VSWR, and their flange faces were lapped before taking any measurement data. Data were taken in sets of approximately eleven measurements. All attenuation measurements at required vane angle settings were made relative to the 0.000-deg indicated vane-angle setting. The results, using each of the three IF attenuators,
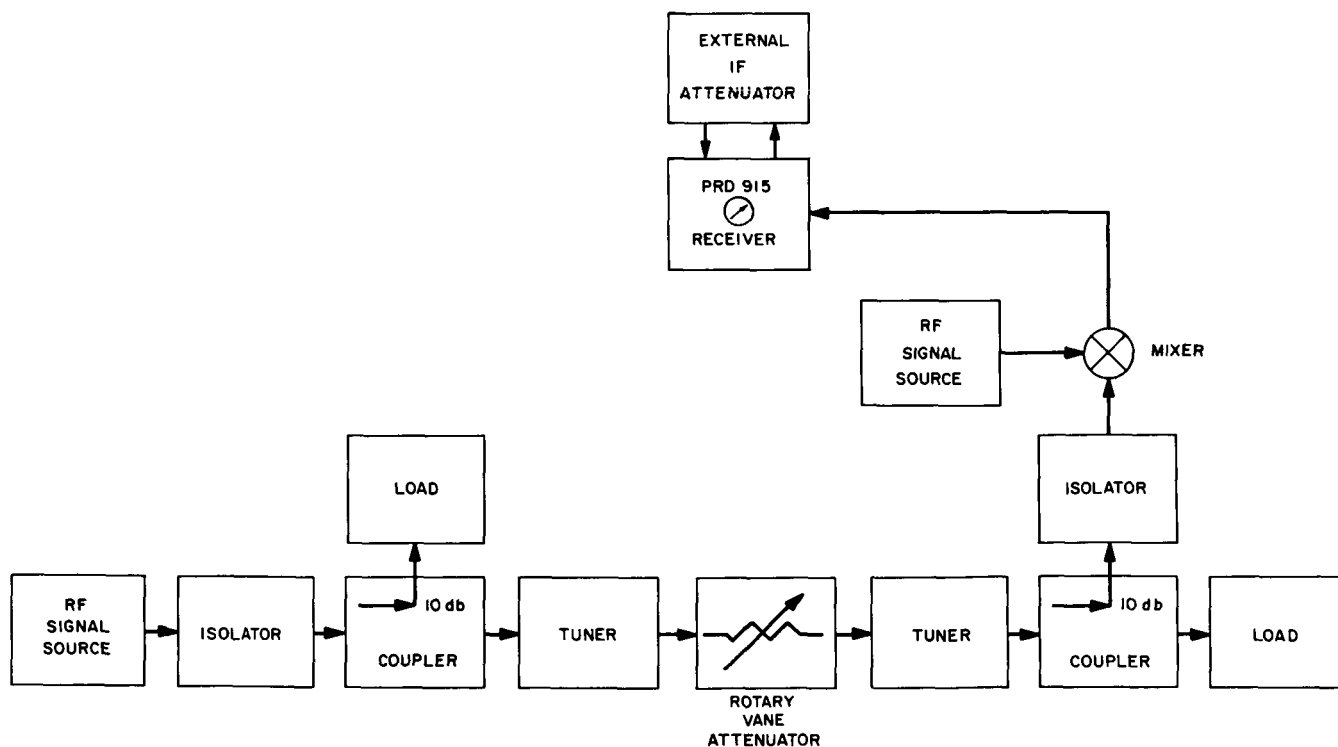

Fig. 25. Block diagram of IF substitution system

were analyzed with respect to their associated probable errors. Overall weighted averages and associated probable errors for the IF system were then calculated for the required indicated vane angle settings.

b. AC substitution system. An AC insertion loss set for precision insertion loss measurements (Ref. 4) was used in the second independent measurement system for the rotary vane attenuator calibrations.

This system employs AC substitution techniques and uses an AC ratio transformer as the AC attenuation standard. Fig. 26 shows a block diagram of the system. The RF input signal is 100% square wave modulated at 1 kHz. Input and output RF powers are detected in a dual channel bolometer system. The RF power levels in both bolometers were kept slightly under 0.1 mw to ensure linear operation. For relative attenuation measurements the detected AC signal levels at the various vane angle settings are compared on a high precision ratio transformer.

The RF source and load assemblies were matched to better than 1.002 VSWR, and the flange faces were lapped

before any data were taken. Data were taken in sets of seven measurements. Calibrations of large attenuations between indicated vane-angle settings were made in nominal steps of 10 db, with the maximum measured step being 13 db. This procedure ensured use of the most accurate range of the ratio transformer and minimization of bolometer nonlinearity errors. Several data sets were taken for each step of attenuation. The averages of these step values of attenuation and the associated probable errors were compiled. Using these values, overall weighted averages and associated probable errors for the required vane angle settings were then calculated.

c. DC substitution system. A DC insertion loss set for precision insertion loss measurements (Ref. 5) was used in the third independent measurement system. This system is a dual channel measurement system which uses a thermistor detector mount and HP 431B power meter in each channel. The DC output voltages from the power meters for this system are essentially linear with RF signal level and are fed into a divider network containing a high-precision DC potentiometer which is used as the attenuation standard in this system. To compare the DC
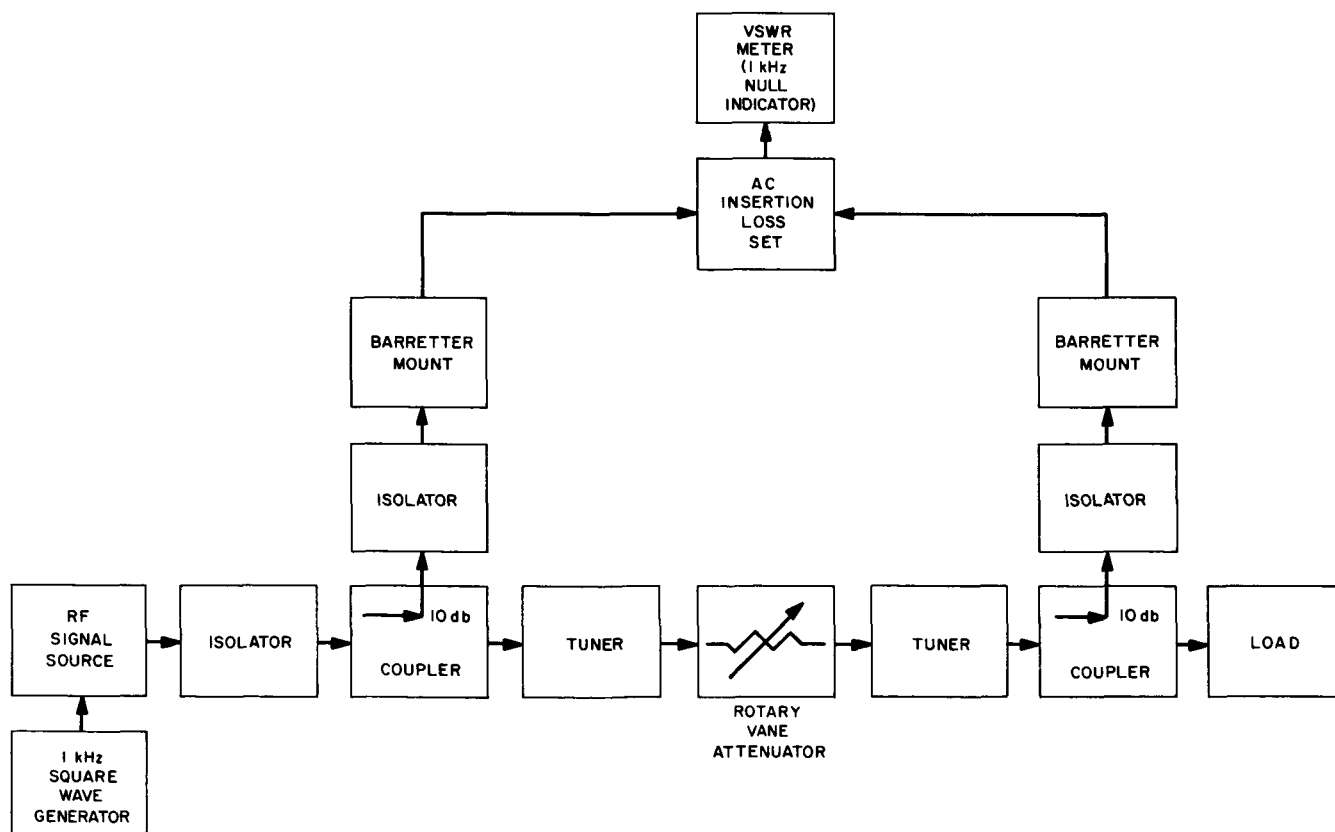

Fig. 26. Block diagram of AC substitution system

outputs, the potentiometer is adjusted for a null indication before and after a change of attenuation is made in the RF system.

The RF source and load assemblies were matched to 1.002 VSWR, and the flanges were lapped before data were taken. The step attenuation measurement technique and data analysis procedure for the DC system were the same as those used for the AC system.

3. Discussion and Results

Calibration of the rotary vane attenuator was conducted in three phases:

(1) Electrical calibration with the IF and AC substitution systems.

(2) Mechanical calibration of indicated vane angles by the JPL Inspection Department.

(3) Electrical calibrations with the AC and DC substitution systems.

Electrical cross-checks of the attenuator reflection coefficients and the zero-degree vane-angle misalignment error before and after inspection were made to verify that the attenuator calibrations were not altered during mechanical inspection. Results of the voltage reflection coefficient measurements made before and after inspection are shown in Figs. 28 and 29, respectively. The input and output ports of the attenuator as used for these curves are defined in Fig. 7 of Ref. 4. Comparison of Figs. 28 and 29 shows slight differences in reflection coefficients, which are attributed to slight detuning of the tuning screws. These were found to produce very small changes in mismatch error uncertainties. The check of misalignment error before and after inspection showed no change.

Table 10 shows the weighted calibrated attenuation values and associated probable errors for the individual measurement techniques and the grand mean. In compiling these averages for the IF, AC, and DC systems consideration was given to probable errors due to mismatch, measurement scatter, and system nonlinearity. Using these error considerations, weighted averages and their associated probable errors were calculated for each system.
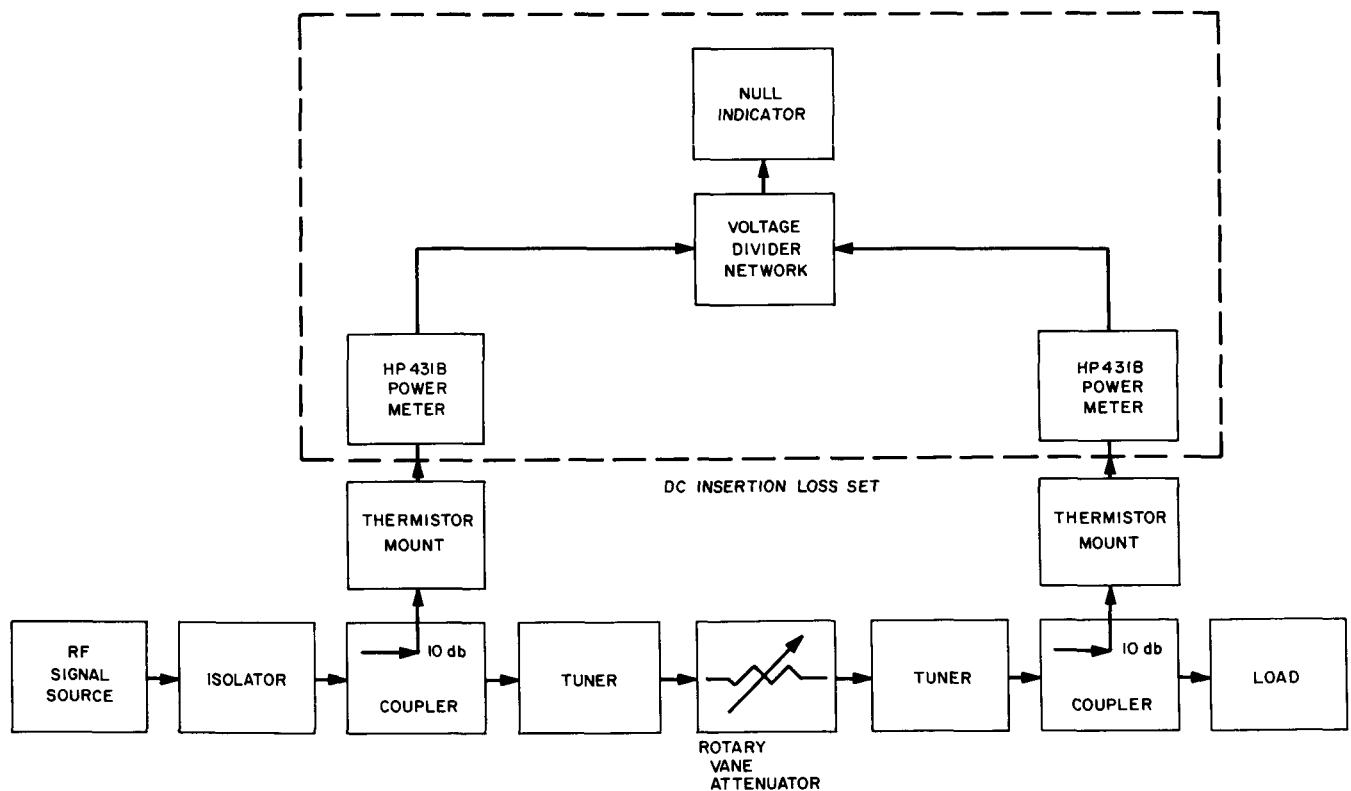

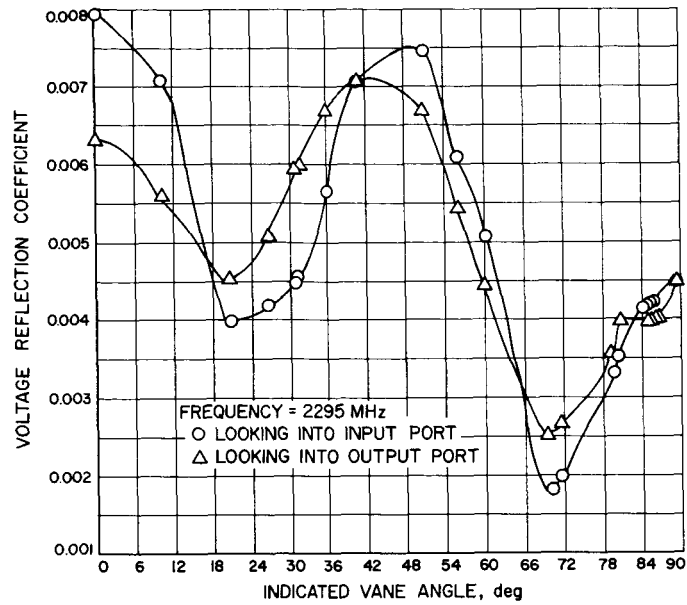Fig. 27. Block diagram of DC substitution system

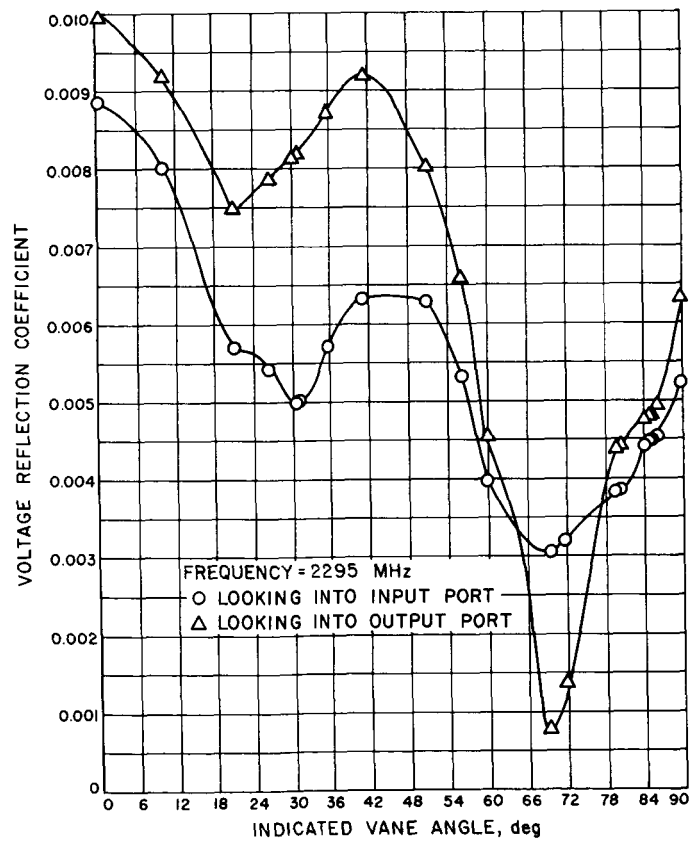**Fig. 28. Voltage reflection coefficient curves before mechanical inspection**

Fig. 29. Voltage reflection coefficient curves after mechanical inspection

Table 10. Comparison of measured attenuations on the S-band rotary vane attenuator at 2295 MHz

Indicated vane angle, deg	Indicated theoretical attenuation, db	Weighted average of measured attenuations relative to zero-deg indicated vane angle, db			
		AC substitution system	DC substitution system	IF substitution system	Grand mean
25.710	1.8110	1.7988 ± 0.0018	1.8007 ± 0.0018	1.7978 ± 0.0065	1.7997 ± 0.0013
30.600	2.6050	2.5900 ± 0.0026	2.5924 ± 0.0026	2.5954 ± 0.0061	2.5916 ± 0.0018
35.500	3.5726	3.5562 ± 0.0036	3.5594 ± 0.0034	3.5954 ± 0.0077	3.5615 ± 0.0024
55.782	9.9999	9.974 ± 0.010	9.979 ± 0.010	—	9.9763 ± 0.0071
71.565	20.0000	19.965 ± 0.020	19.936 ± 0.027	—	19.955 ± 0.016
79.757	30.0005	29.936 ± 0.030	29.905 ± 0.035	—	29.923 ± 0.023
84.261	40.0005	39.896 ± 0.040	39.843 ± 0.044	—	39.872 ± 0.030
84.650	41.2160	41.099 ± 0.041	41.045 ± 0.045	41.033 ± 0.031	41.054 ± 0.022
84.970	42.2845	42.165 ± 0.043	42.106 ± 0.046	42.109 ± 0.030	42.123 ± 0.021
85.300	43.4605	43.347 ± 0.044	43.263 ± 0.047	43.289 ± 0.031	43.298 ± 0.022
90.000	—	—	—	88.49 ± 0.72	88.49

Tolerances shown for the AC, DC, and IF systems are total probable errors associated with the average values. Tolerances shown for the grand mean values are grand mean probable errors (Ref. 6).

From these weighted averages for each system a grand mean attenuation and associated grand mean probable error (Ref. 6) were calculated for each of the indicated test angles.

Fig. 30 shows curves of measured attenuation deviation from indicated theoretical attenuation. Measured deviation is defined as follows:

$$(\text{measured deviation})_{db} = (A_I)_{db} - (A_M)_{db}$$

where

$(A_I)_{db}$ = indicated theoretical attenuation, db

$(A_M)_{db}$ = weighted average of measured attenuations at the indicated vane angle, db

The limits given on each curve account for the probable error associated with each weighted average.

At present, the grand mean averages are being further refined by a fourth calibration technique. This technique involves corrections to the indicated theoretical attenuation values through consideration of: (1) zero-degree misalignment error, (2) readout errors, and (3) transmission errors. The results of these corrections and resultant refinement of the grand mean calibration values will be presented in a future SPS.

F. Efficient Antenna Systems: X-Band Gain Measurements, D. A. Bathker

1. Introduction

An experimental program has begun to investigate the behavior of the DSIF antennas as they approach gain limit (SPS 37-42, Vol. III, p. 40). Gain measurements were previously conducted at S-band. In the future these tests will be planned for C- and K-bands.

Initially, the 85-ft AZ-EL reflector at Venus DSS will be evaluated by using the Tiefort Mountain collimation
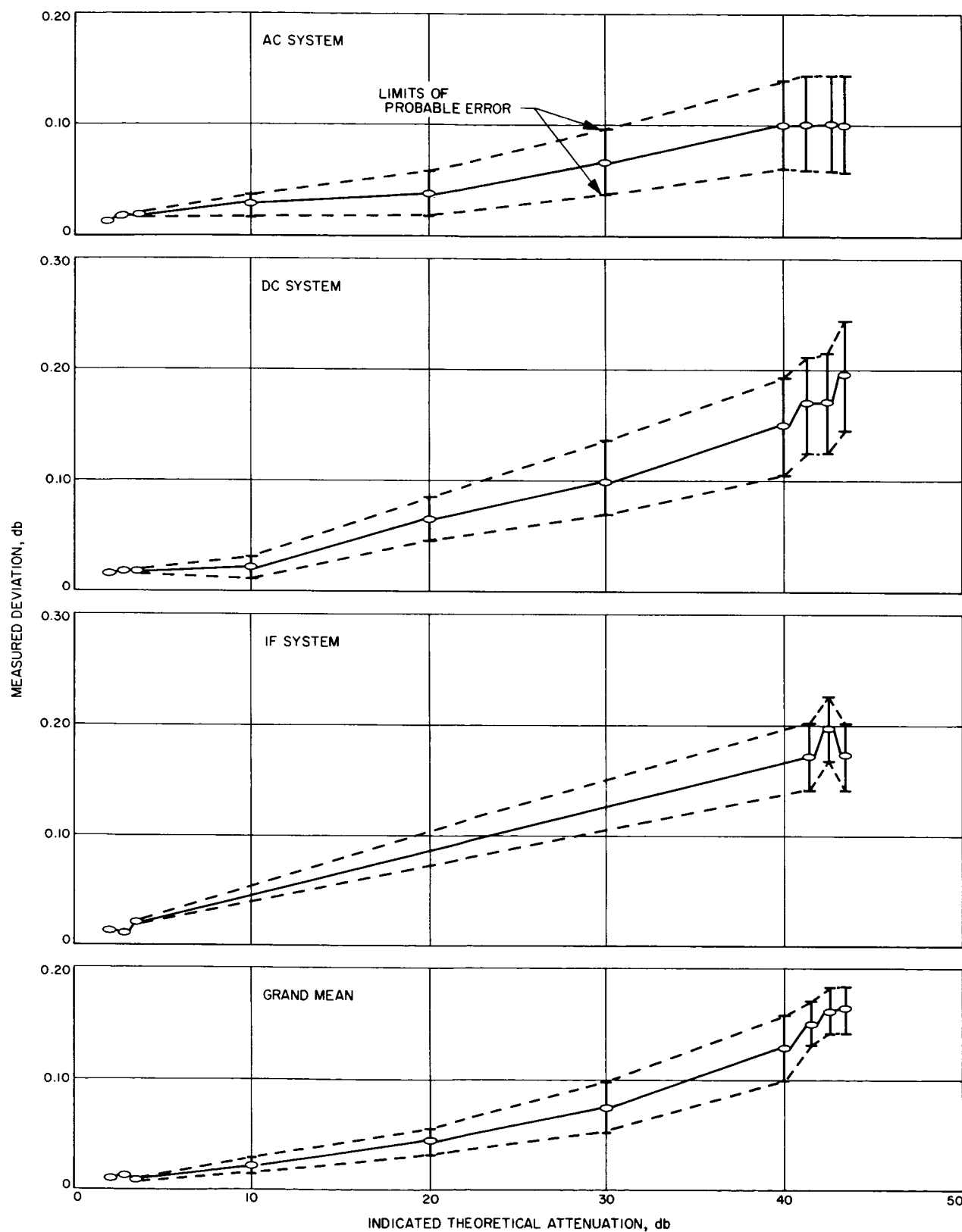
Fig. 30. Deviation of measured attenuation from indicated theoretical attenuation

facility and radio star flux density measurements. Equipment to be used at Venus DSS, including precision calibration of a thermistor-type power meter for the gain tests has been described (SPS 37-43, Vol. III, p. 61). This reporting will describe final evaluations of the gain standard horn antennas to be used in the X-Band Cassegrain feedcone and at Tiefort Mountain. Development and preliminary evaluations of a large-aperture gain standard horn to be tried at the Tiefort Mountain facility are also discussed.

2. Current 22-db Horn Calibrations

JPL has conducted far-field absolute gain measurements of the Venus DSS reflectors (30-ft and 85-ft), based on the establishment of a known flux density at the Tiefort Mountain facility. Because flux density is a function of transmitter power and illuminator antenna gain, the accurate knowledge of both is mandatory. Transmitter power calibration has been discussed in detail in the last reporting. In order to know the illuminator antenna gain accurately and reliably, it has been our approach to discriminate against any antenna type having appreciable (order of 0.1 db) dissipative loss and/or mechanical complexity. For the above reasons, simple horn radiators are a reasonable choice. A substantial improvement in the radiation pattern characteristics of horn antennas is available by allowing the propagation of certain higher-order waveguide modes within the horn (Ref. 7). This technique, implemented using two modes, has been applied to conical horns at JPL for both paraboloidal reflector feed

and gain standard horn functions with excellent results (SPS 37-22, Vol. III, pp. 11–15).

More important, perhaps, than the general desirability of the dual-mode conical horn as either a paraboloidal reflector feed or gain standard horn, are the results obtained by Ludwig (Ref. 8). Ludwig has shown that the radiation pattern in all space (and, therefore, the gain) for any antenna having physical circular symmetry and the proper excitation may be completely specified by measuring the usual E- and H-plane radiation patterns. Thus, we have the fortuitous situation of an analyzable structure having desirable properties.

Using a JPL-developed computer program (SPS 37-26, Vol. IV, pp. 200–208) horn gain for the X-Band Cassegrain feed and the Tiefort Mountain illuminator (both 4.671 λ aperture dual-mode conical horns) was computed using carefully obtained experimental E- and H-plane radiation patterns. The technique of moving the test antenna with respect to the center of rotation of the antenna rotator was used as a semi-independent check. Correction terms due to space loss of 0.50 to 1.00 db are necessary and accurately determined for a measurement of this kind. As the Table 11 results show, the X-band equipment is consistent with all previous JPL determinations. Random measurement error for the 6-1966 set of 4 S-band measurements is 0.075 db p.e., while the 9-1966 set of three X-band measurements is 0.015 db p.e., an achievement in combined antenna pattern recording and data reduction technique of 0.35%.

Table 11. Experimental gain data summary on 4.671 λ aperture dual-mode horn

| Date	Frequency, MHz	Experimentors	Method	Far-field gain, db	Application
6-63	2388	FEM/PDP	Two-horn space loss	22.16	Venus radar calibration
				22.16	
				22.14	
				22.21	
6-63	2388	FEM/PDP	Pattern integration[a]	21.95	Venus radar calibration
6-64	16330	DAB	Pattern integration[b]	21.91	AAS scale model calibration
6-66	2295	ACL/REC	Pattern integration[b]	21.77	AAS *Surveyor I* gain calibration
				21.95	
				21.69	
				22.00	
9-66	8448	DAB/HFR	Pattern integration[b]	21.87	X-band Cassegrain feedcone
9-66	8448	DAB/HFR	Pattern integration[b]	21.83	X-band Tiefort Mountain illuminator
				21.87	
				21.82	

[a]Planimeter.
[b]Machine.
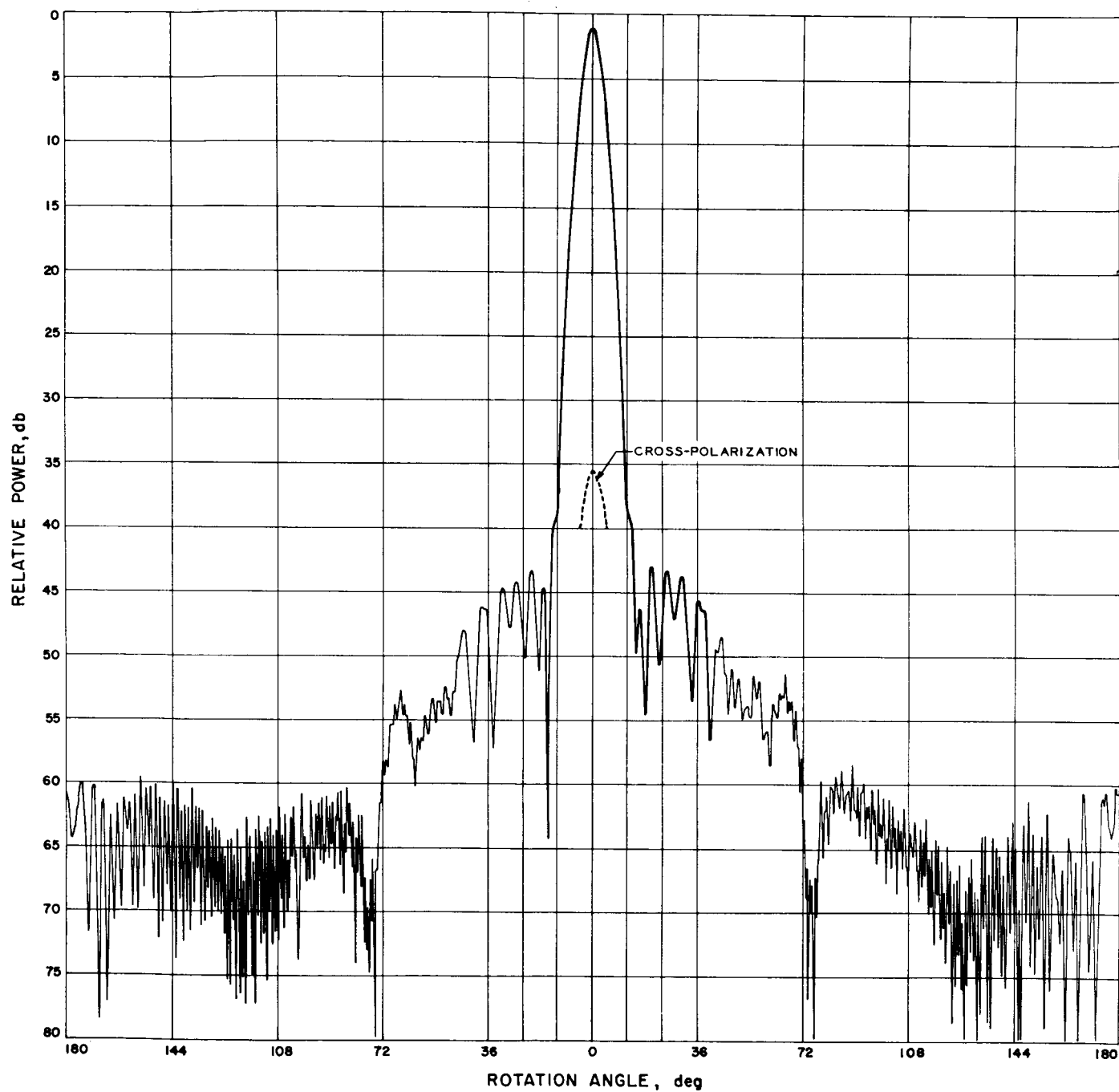
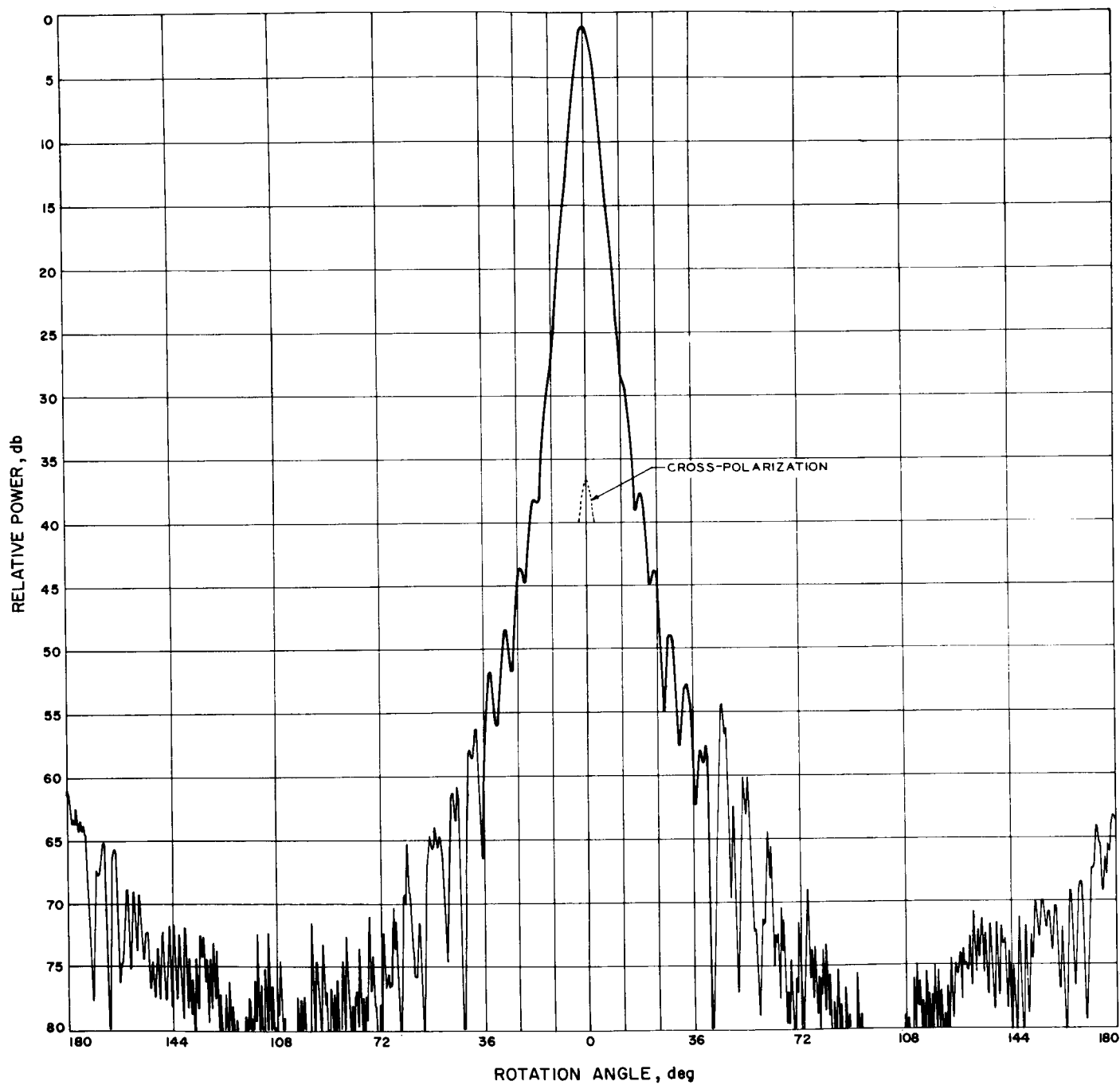Fig. 31. Radiation pattern, large-aperture gain standard horn, E-plane

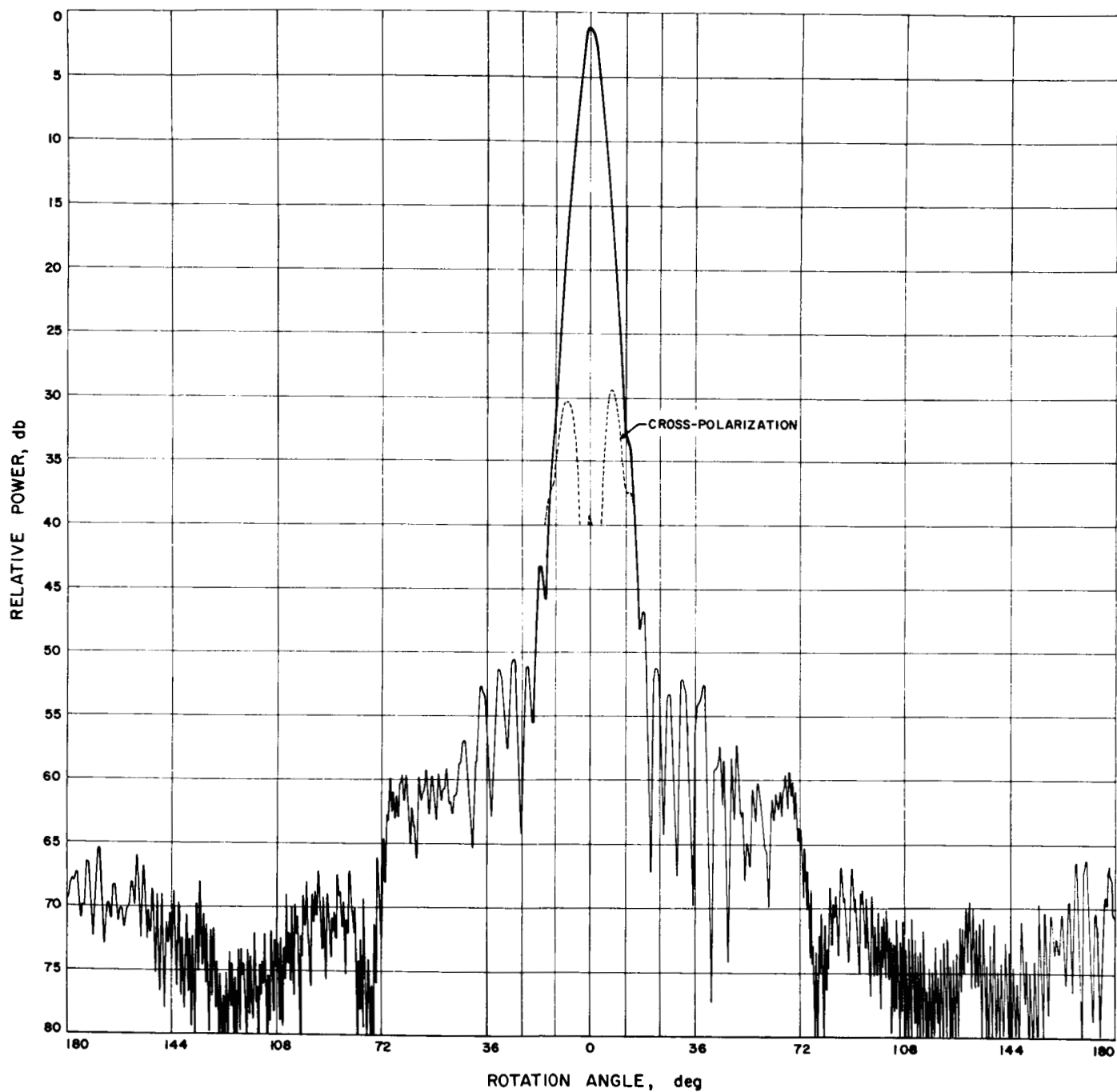Fig. 32. Radiation pattern, large-aperture gain standard horn, H-plane

Fig. 33. Radiation pattern, large-aperture gain standard horn, 45-deg plane

Calculated dissipation loss for the 22 db X-band Tiefort illuminator horn, not including the complex turnstile junction but using practical values of RF conductivity, is 0.013 db.

3. Large Aperture Horn

As discussed in the previous reporting (SPS 37-43, Vol. III) the method of gain measurement to be used requires the accurate determination of the difference between two RF power levels, approximately +30 dbm at the Tiefort Mountain collimation facility and −20 dbm at the Venus DSS. The technique requires use of a power meter having known linearity over a 30-db range. Although laboratory results proved excellent, past field experience has shown thermal drifts to be a serious problem on the most sensitive ranges of the instrument used. For this reason primarily, and for possible improvement in a multipath environment, the development of a large-aperture-gain standard horn was initiated.

An existing conical horn of 6° 15′ 15″ flare angle and 12.548 λ aperture at 8448 MHz was modified to mate with existing dual-mode generators. Because differential phase-shift calculations, when applied to conical horn radiators, apparently fail due to aperture effects, a spacer kit in 15-deg differential phase-shift increments was fabricated
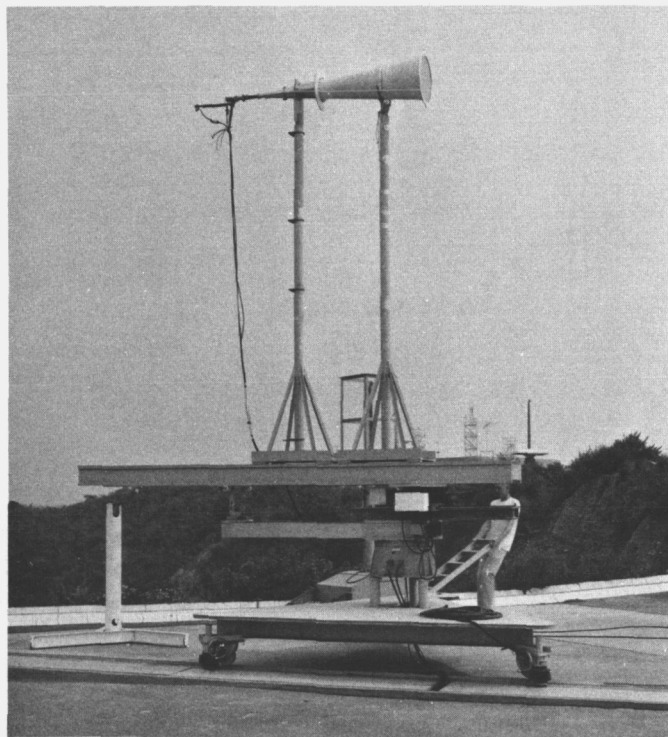

Fig. 34. Large-aperture gain standard horn test

and a new mode generator length was empirically determined. Figs. 31 through 33 show the E-, H- and 45-deg plane radiation patterns of the large aperture assembly. As the figures show, the patterns are entirely acceptable. A precision set of three patterns was made to apply the semi-independent pattern integration method of gain determination. The results of these computations were 29.50, 29.52 and 29.51 db for an extremely small random experimental error. Space loss correction terms were approximately 0.25 db for this case. The computations included only that energy contained down to the 40-db points; the remainder was input as zero field. A second computation was completed using the on-phase center (29.52 db gain) pattern data including all sidelobe energy to ±180 deg; the resultant gain was 29.51 db.

Calculated dissipation loss for the large-aperture horn, not including the complex turnstile junction as before, and using the same RF conductivity values mentioned above is 0.023 db. Fig. 34 shows the large-aperture horn undergoing Mesa Antenna Range tests.

G. Efficient Antenna Systems: Gain Measurements of the Advanced Antenna System Using Surveyor I Signals, G. S. Levy, D. A. Bathker, and A. C. Ludwig

1. Introduction

The S-band telemetry signals of *Surveyor I* transmitted from the lunar surface provided an opportunity for making an accurate gain measurement of the Advanced Antenna System (AAS). The field strength at Goldstone was great enough to permit reception on a low gain horn. The received signal level at the gain standard horn was compared to that received by the AAS. The measured value of gain was (61.62 ±0.27) db, 2σ, and a weighted mean of measured and theoretical is (61.81 ±0.32) db, 2σ.

2. Description of Experiment

The setup for the experimental gain measurement is shown schematically in Fig. 35 and pictorially in Figs. 36 and 37. The measurement is basically a comparison of the gain of the 210-ft-D antenna and a gain standard horn. The unique feature of the measurement is the use of the *Surveyor* spacecraft as a Moon-based source. The major advantages of this source are: (1) it is in the far field of the 210-ft-D antenna $(2D^2/\lambda = 39 \text{ mi})$; (2) the source appears at elevation angles at which the antenna will normally be operated; (3) the signal is strong enough to acquire with a
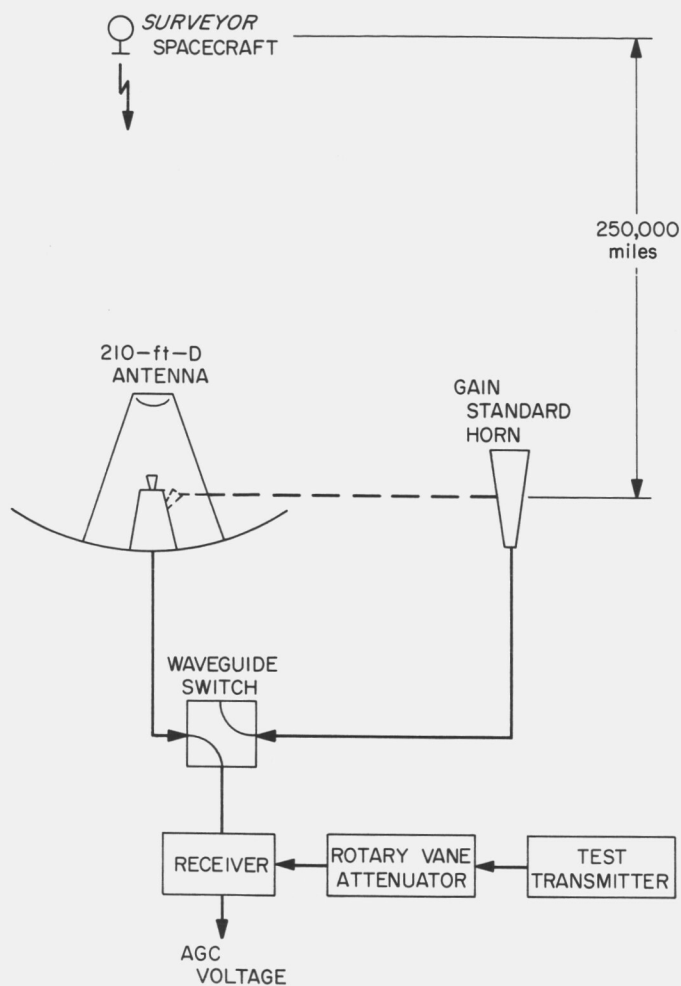
Fig. 35. Experimental gain measurement schematic

Fig. 36. Test horn installation, View 1

Fig. 37. Test horn installation, View 2

low-gain horn; (4) the tracking rate is slow and allows several repetitions of the measurement per view period. This combination of features cannot be obtained with a collimation tower, radio star, or satellite; and the *Surveyor* mission provided a rare opportunity for obtaining a good operational gain measurement. Preliminary measurements and system checkout were made July 7, 1966, and the actual tests were conducted on July 8. One 2-hr period was made available from 09:30 to 11:30 GMT and a second period from 13:00 to 15:40. The elevation angle went from 31 to 44 deg in the first period and 44 to 26 deg in the second period. During the measurements the *Surveyor* was transmitting an unmodulated CW signal at low power (+20 dbm) on its high-gain planar array antenna.

The measurement technique was: (1) acquire the *Surveyor* signal, boresight the large antenna, and obtain an indication of signal level from the AGC voltage; (2) using the very narrow bandpass of the receiver as a
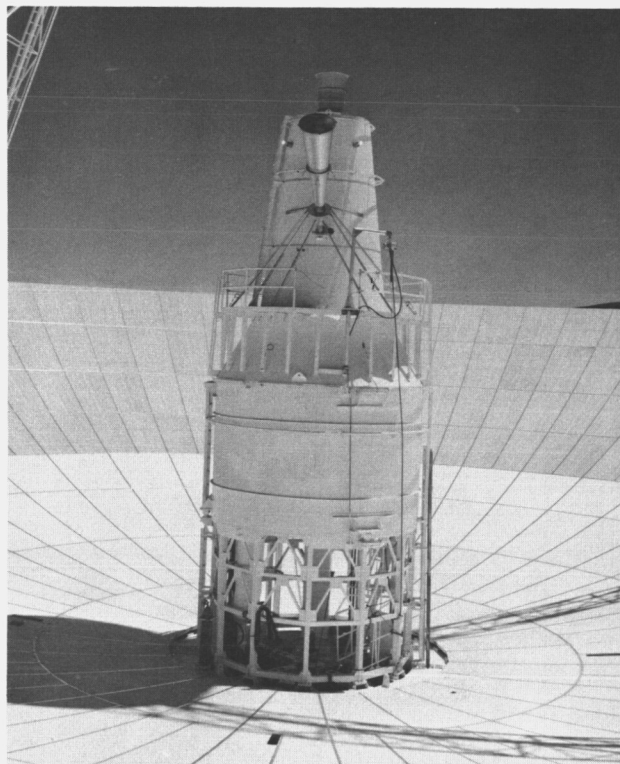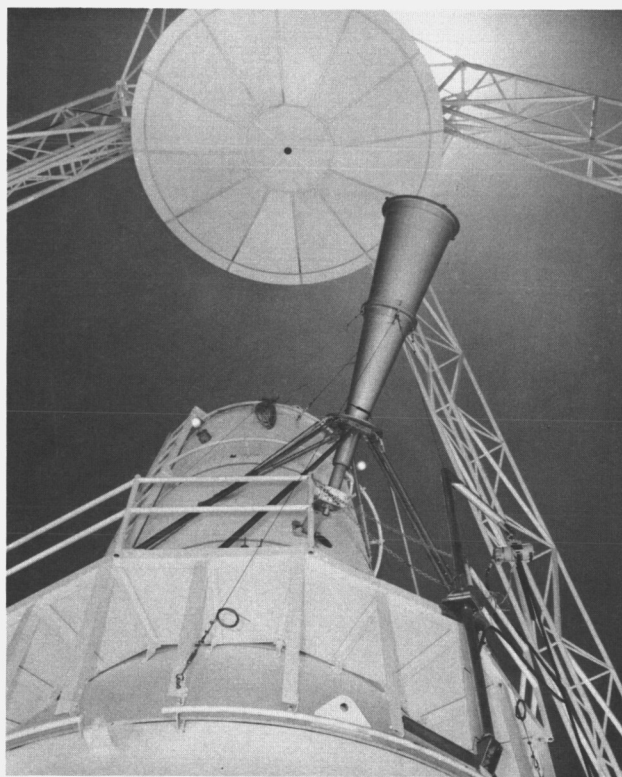
switch, tune to the test transmitter (the difference in frequency was 8 to 50 kHz) and adjust the rotary vane attenuator to obtain an identical AGC voltage; (3) repeat steps (1) and (2), except for boresight, five times; (4) repeat the entire process with the gain standard horn on the *Surveyor*. This sequence provides one set of antenna/horn data. The difference in the settings of the rotary vane attenuator which make the test signal equal to the antenna and horn received signals, respectively, provides the difference in gain between the antenna and standard gain horn.

The accuracy of the measurement of the gain difference is a function of: (1) stability of the spacecraft signal, test transmitter signal, and receiver gain as indicated by the AGC voltage; (2) the calibration and repeatability of the rotary vane attenuator; (3) boresight accuracy; (4) systematic errors introduced by ellipticity (the radiation is nominally RCP for all antennas). The accuracy of the net value for gain is in addition a function of the calibration of the gain standard horn. These limitations will be discussed in detail.
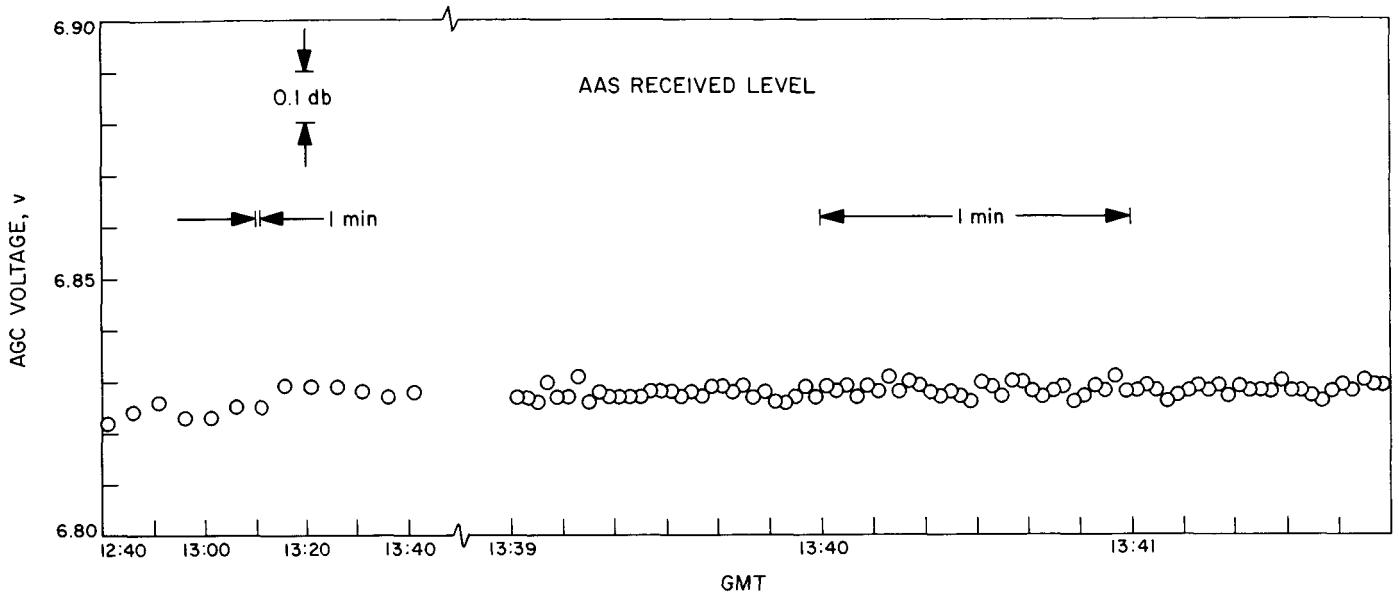

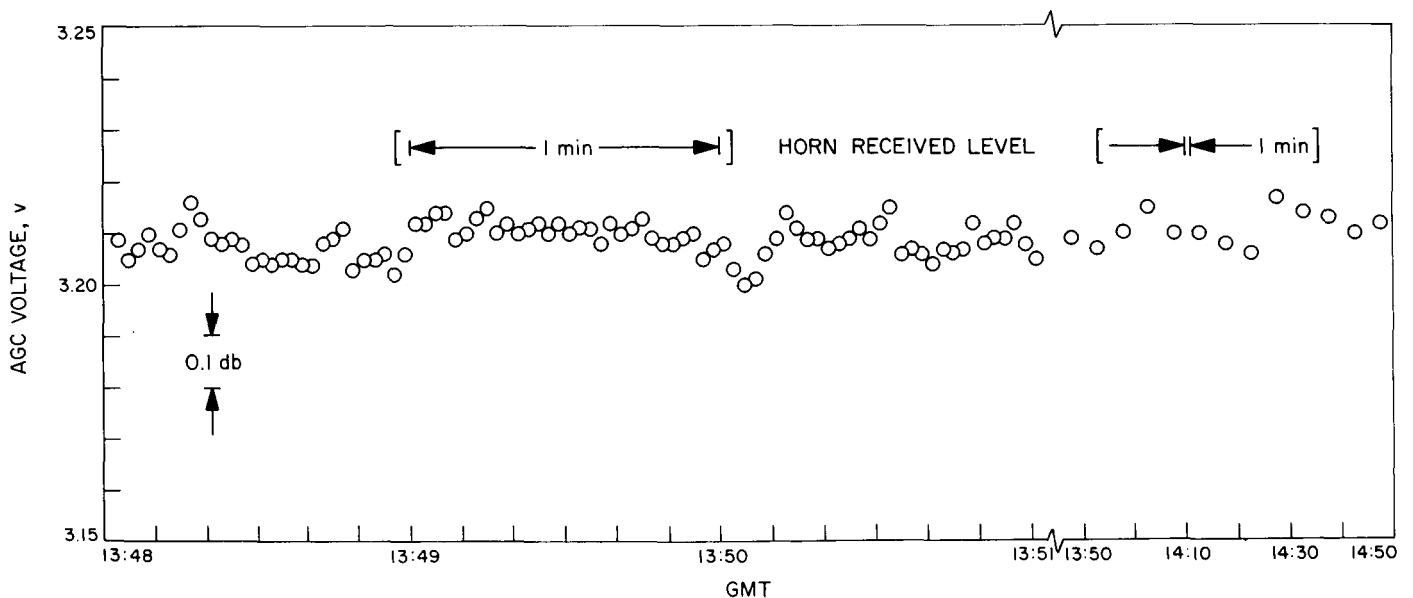Fig. 38. Test transmitter/AGC stability, AAS-received level (July 13, 1966)

Fig. 39. Test transmitter/AGC stability, horn-received level (July 13, 1966)
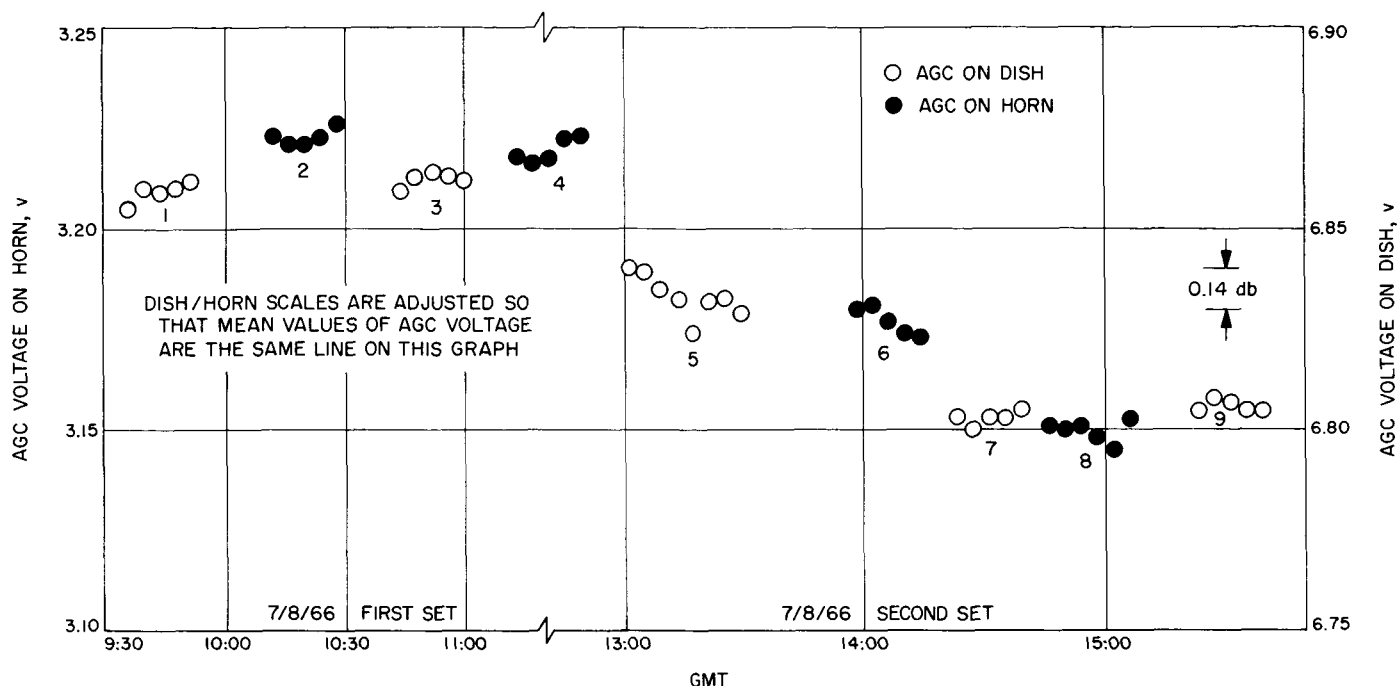
Fig. 40. Received AGC signal versus time

3. Experimental Data

The measurement technique employed depends on the stability of the *Surveyor* transmission and test transmitter over the period of observation between the gain standard horn and the 210-ft antenna. Stability tests were run with the test transmitter and receiver system AGC output at the signal levels received on the AAS and gain standard horn. Figs. 38 and 39 show the results of test runs. The standard deviation of the points taken for 1 hr at 5-min intervals was found to be 0.026 db for the same signal level as received by the large paraboloid and 0.030 db for the gain standard horn. Fig. 40 shows the measured AGC indicated power levels as a function of time. The AGC voltages are normalized to have both the AAS and gain standard signals on the same scale. During the first period there appears to be very little drift between points. Between the first and second period (observations 4 and 5), there appears to be a drift in signal level. There also appears to be a drift in signal level between observations 6 and 7.

Measurements were made using an S-band rotary vane attenuator to set the output of the test transmitter to the same level as the received signal as indicated by the AGC. Fig. 41 presents the uncorrected attenuator setting versus time with the attenuator scales normalized for the nominal gain difference. After these measurements the rotary vane

attenuator was subjected to an extremely careful evaluation, which is described in Sect. III E of this SPS. Further evaluation of the rotary vane attenuator will be attempted, and if any new data is obtained, it will be published in the SPS. The probable errors to the corrections obtained from the attenuator readings are: 0:0214 db, p.e. at 42 db and 0.0012 db, p.e. at 2 db. The corrected difference between successive observations is tabulated, except for the 4–5 and 6–7 measurements.

Measurement No.	Signal difference, db	p.e., db
1–2	39.755	0.037
2–3	39.691	0.032
3–4	39.785	0.026
5–6	39.659	0.042
7–8	39.725	0.017
8–9	39.663	0.016

RMS (39.713 ± 0.014) db, p.e.

The gain standard horn was mounted on the Cassegrainian support structure and offset 45 deg in azimuth. A computer program was used to prepare a punched tape to drive the antenna servo when using either the large paraboloid or the gain standard horn. The boresight error of the small horn was found to be below threshold on
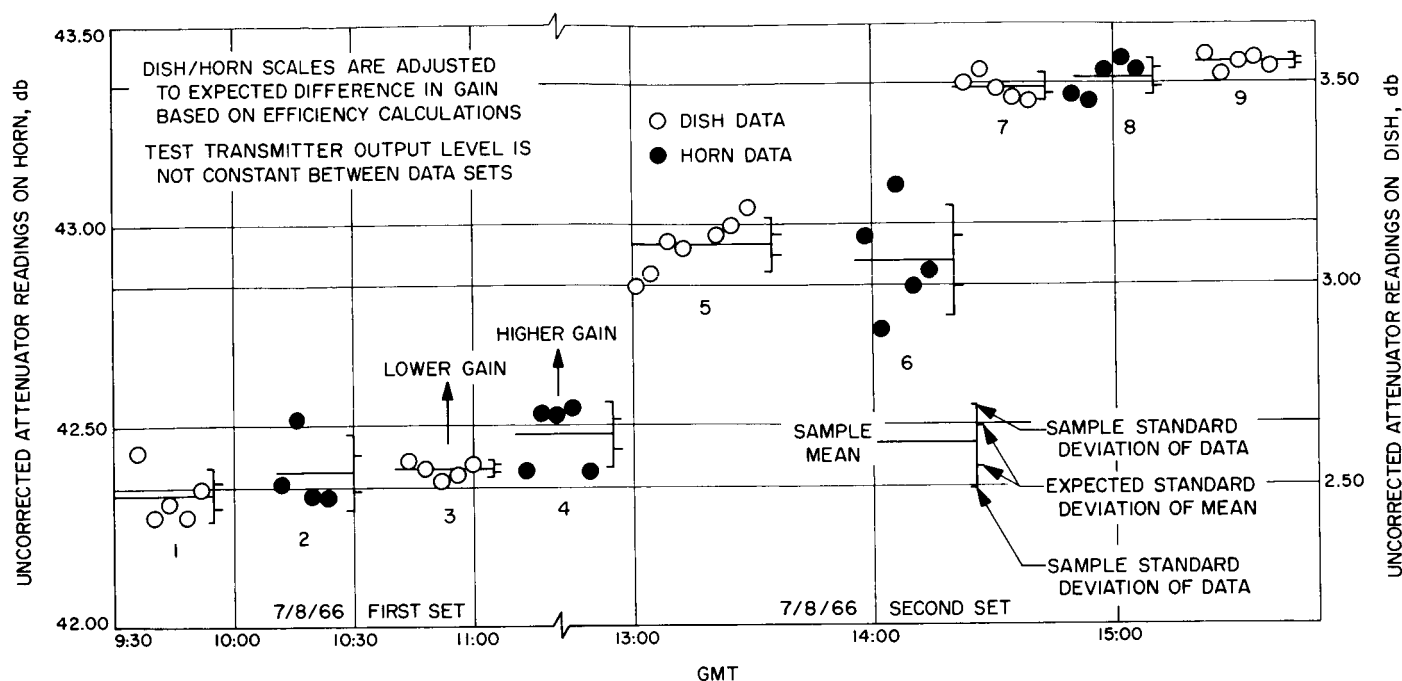
Fig. 41. Uncorrected attenuator readings versus time

elevation and only off 0.33 deg in azimuth. Because of the large beamwidth of this horn it was decided that it was not necessary to boresight before each pass. The gain standard horn was connected to the receiver system with waveguide from the horn to the liquid nitrogen port of the calibration switch. SPS 37-38, Vol. IV, pp. 180–186 gives the insertion loss of the waveguide run from the maser to the regular AAS feed horn as (0.1496 ± 0.0015) db, p.e., and from the maser to the nitrogen load port as (0.0627 ± 0.0007) db, p.e. The additional waveguide from the waveguide switch to the standard horn was measured and found to be (0.0206 ± 0.0013) db, p.e. The total gain standard run is therefore (0.0887 ± 0.0011) db, p.e., and the differential loss is (0.0609 ± 0.0019) db, p.e. In addition to the errors already discussed, the probable error due to the ellipticities of the spacecraft antenna as well as the AAS feed horn and gain standard horn was found to contribute ± 0.008 db, p.e.

The gain standard horn used has been carefully measured, using several different techniques which are described earlier in this report under X-band calibrations as well as in Ref. 8. The best gain measurements give a value of (21.85 ± 0.086) db, p.e. The error due to antenna pointing was minimized by boresighting before each run on the paraboloid. The estimated gain error due to boresight is ± 0.01 db, p.e.

The measured gain is therefore:

Measured difference	39.713	± 0.014	p.e.
Attenuator calibration		± 0.021	p.e.
Differential waveguide loss	0.0609	± 0.0019	p.e.
Ellipticity		± 0.008	p.e.
Pointing errors		± 0.01	p.e.
Gain standard horn	21.85	± 0.086	p.e.
	61.62	± 0.0905	db, p.e.

This gain is referenced to the input of the feed horn mode generator.

SPS 37-42, Vol. III quotes a theoretical computation for the gain of the AAS as $(61.90 + 0.19 - 0.17)$ db, where the tolerances are 2σ values. Converting the measured value to a 2σ tolerance we have (61.62 ± 0.27) db. Taking a weighted mean we get (61.81 ± 0.32) db, 2σ.

This gain measurement technique appears to overcome several of the difficulties normally encountered in gain measurements. The two largest sources of error are the gain standard horn which, as discussed in a previous section of this report, is known quite accurately; and the rotary vane attenuator which also proved to be very difficult to calibrate. But now that the technique has been

mastered, this appears to be a very good method for gain measurement of large antennas. This technique should prove particularly useful when permanent *Apollo* packages are landed on the lunar surface. The possibility of landing transmitters in other frequency bands is also very attractive.

References

1. Clauss, R. C., *A Traveling Wave Maser for Deep Space Communication at 2295 and 2388 MHz*, Technical Report 32-1072, Jet Propulsion Laboratory, Pasadena, California, February 15, 1967.

2. Chen, F. S., and Tabor, W. J., "Filling Factor and Isolator Performance of the Traveling-Wave Maser," *The Bell System Technical Journal*, pp. 1005–1033, May 1964.

3. Microwave, Inc., *Microwave Engineers Handbook*, 1963, p. T-163, Horizon House, Brookline, Mass.

4. Finnie, C. J., Schuster, D., and Otoshi, T. Y., *AC Ratio Transformer Technique for Precision Insertion Loss Measurements*, Technical Report 32-690, Jet Propulsion Laboratory, Pasadena, Calif., November 1966.

5. Stelzried, C. T., Reid, M. S., and Petty, S. M., "A Precision DC Potentiometer Microwave Insertion Loss Test Set," *IEEE Transactions on Instrumentation and Measurement*, Vol. IM-15, No. 3, September 1964.

6. Worthing, A. G., and Geffner, J., *Treatment of Experimental Data*, John Wiley and Sons, Inc., New York, N. Y., December 1960, pp. 195–196.

7. Potter, P. D., "A New Horn Antenna with Suppressed Sidelobes and Equal Beamwidths," *Microwave Journal*, Vol. VI, No. 6, pp. 71–78, June 1963.

8. Ludwig, A., "Gain Computations from Pattern Integration," to be published in *IEEE Transactions on Antennas and Propagation*, 1967.

N67-25064

IV. Communications Development Engineering

A. 85-ft Az-El Antenna Structure Deformations From Gravity Loads, M. S. Katow

1. Introduction

Distortion of the 85-ft Az-El reflector structure in terms of rms (root mean square) of the ½ RF path length errors and a contour picture of the normal errors from gravity loads, as calculated by the STAIR structural computing program, were presented in SPS 37-29, Vol. III, p. 49. Normal deformations were pictured as offsets from the circumferential line at radial positions on the reflector structure.

Because the rms best-fitting program can draw contour levels, using the SC-4020 plotter (SPS 37-40, Vol. IV, p. 176), results of the previous work and studies on the 85-ft reflector structure are now presented in the form of contour level maps.

With the added capability of the rms program to best fit, using the focal length as a parameter, the deformation picture with respect to a paraboloid of a slightly changed focal length is also presented. The computed results show that RF performance evaluation may account for possible changes in the focal point with respect to the main reflector structure.

2. Recent Work

Since the 85-ft Az-El reflector (Fig. 1) structure is symmetrical about the Y-Z plane (a plane perpendicular to the elevation axis and passing through the vertex of the paraboloid), only 1/2 of the structure is analyzed, using proper restraints at the cutting plane. All contour maps look into the right half face of the reflector and show the map of deformation for only the top joints in the reflector structure. To obtain the total distortion affecting the RF
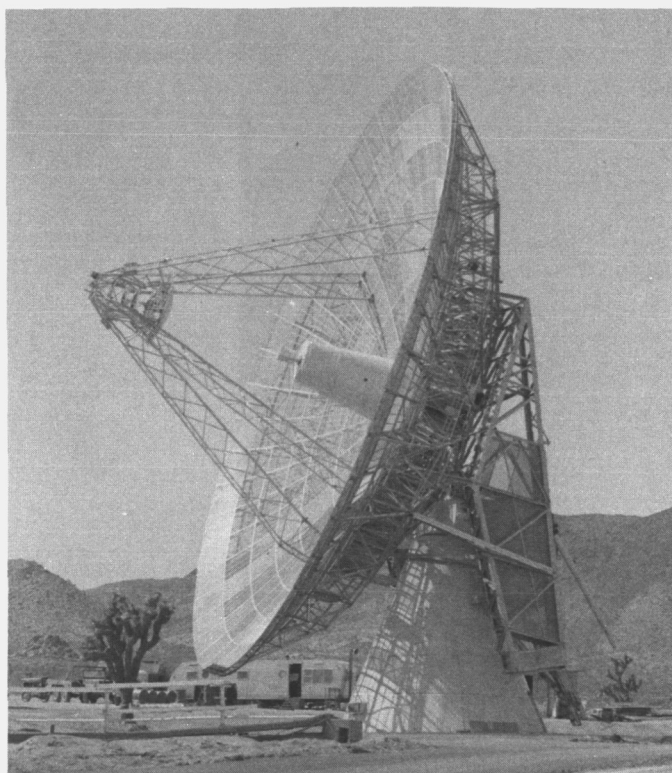
Fig. 1. 85-ft Az-El antenna

performance, the surface panel errors, as well as the errors from the hyperboloid subreflector, must be accounted for in the evaluation. Furthermore, at present, the error budget must include the effects of distortions from the hysteresis effects due to looseness in the bolt joints. As shown by results from extensometer tests, as reported before (SPS 37-24, Vol. III, pp. 39–43), the bolted joints are loose enough to produce measurable hysteresis effects.

Also, there are additive deflections in the actual antenna over the computed results caused by compromises made to ease fabrication. Specifically, in this antenna, the centroid of the hoop members misses the work points of the rib trusses by a long distance. This prevents the development of tension forces in the hoop members to aid the rib trusses in keeping the deflections low for the symmetric gravity loading condition. To obtain a closer agreement among the deflections, smaller hoop areas could have been used in the computer simulation. However, this was not done; and the optimum condition of the centroid of all structural members joining exactly at the work points was assumed, as required by the STAIR computer analysis.

Fig. 2 shows the contour map of 1/2 path length errors. The same data were used that produced the normal deflec-

tion error map presented in Fig. 16 of the SPS 37-29, Vol. III, p. 53. As shown before, the effect of the counterweight tie to the reflector structure is perceptible. The effect on the rms when the focal length is allowed to vary should also be noted. It follows that the optimum design goal is to obtain a structure that deforms but always remains within a paraboloid form.

The deformation map when the panels are set to a perfect paraboloid shape at 45-deg elevation angle in the normal gravity field, as the structure exists in the field and rotated to the horizontal look position, is shown in Fig. 3.

Studies of computed deformations, following proposed changes in the structure, are illustrated by Fig. 4, the structural ties between the reflector structure and the counterweight having been removed. Here, the tie removal effect is to reduce the deformation in the horizon look case. Table 1 outlines the changes in rms effected by the proposed change.

Since the removal of the ties obviously changes the restraints on the counterweight, alternate methods of restraining the counterweights must be found. After analyzing the bar-stress output of the computing program for the different load directions of the gravity force, it is concluded that a few additional reinforcing bars could perform the function of the removed ties without connecting them to the reflector structure.

Table 1. Computed change effects in rms

Case No.	Antenna [a] position and counterweight support		Distortion [b] after best fit-rms-in.		New focal length
			Rigid body	Focal length	
1	Zenith look	Normal	0.024	0.018	432.194
2		Counterweight ties removed	0.021	0.019	432.090
3	Horizontal look	Normal	0.036	0.026	431.709
4		Counterweight ties removed	0.021	0.014	431.813

[a]The starting condition for all cases is at 45-deg elevation angle with the surface panels set to a perfect paraboloid shape of 432-in. focal length. The distortion is then evaluated, after rotation in the gravity field, to the stated condition.

[b]Only the distortion data of the work points in the reflector structure are used to best fit the paraboloid and compute the rms distortion number and focal length change.

CONTOUR DEFINITIONS
1/2 RF PATHLENGTH

ERROR, in.	LABEL
− 0.1600	A
− 0.1500	B
− 0.1400	C
− 0.1300	D
− 0.1200	E
− 0.1100	F
− 0.1000	G
− 0.0900	H
− 0.0800	I
− 0.0700	J
− 0.0600	K
− 0.0500	L
− 0.0400	M
− 0.0300	N
− 0.0200	O
− 0.0100	P
0.0000	Q
0.0100	R
0.0200	S
0.0300	T
0.0400	U
0.0500	V
0.0600	W
0.0700	X
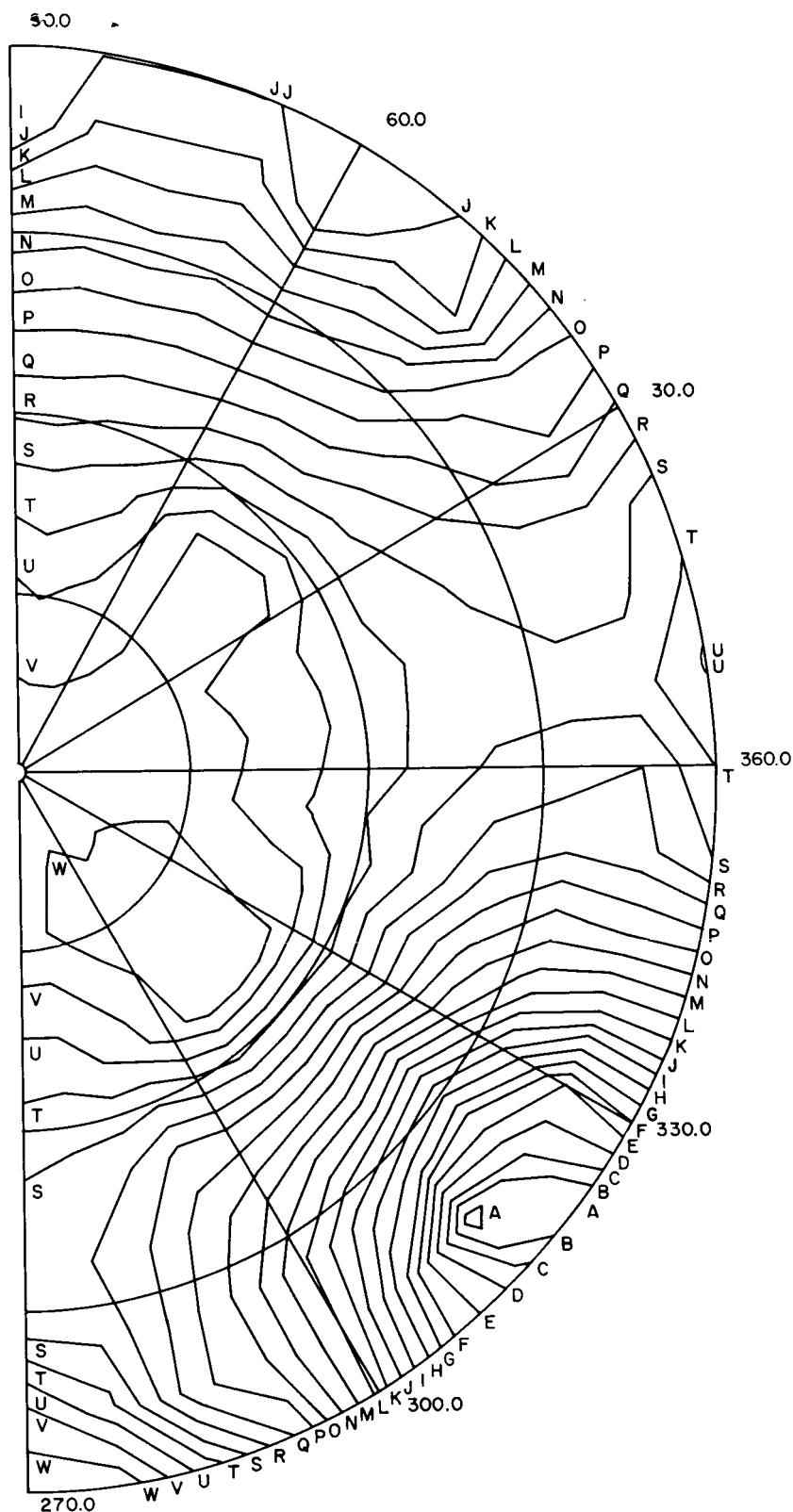
Fig. 2. 85-ft Az-El antenna — normal antenna — zenith look, gravity off to on
(rigid body fit, rms = 0.046)

CONTOUR DEFINITIONS
1/2 RF PATHLENGTH

ERROR, in.	LABEL
−0.130	A
−0.120	B
−0.110	C
−0.100	D
−0.090	E
−0.080	F
−0.070	G
−0.060	H
−0.050	I
−0.040	J
−0.030	K
−0.020	L
−0.010	M
0.000	N
0.010	O
0.020	P
0.030	Q
0.040	R
0.050	S
0.060	T
0.070	U
0.080	V
0.090	W
0.100	X
0.110	Y
0.120	Z

Fig. 3. 85-ft Az-El antenna — normal antenna — panels set at 45 deg. Horizontal look (focal length fit, rms = 0.026)

CONTOUR DEFINITIONS
I/2 RF PATHLENGTH

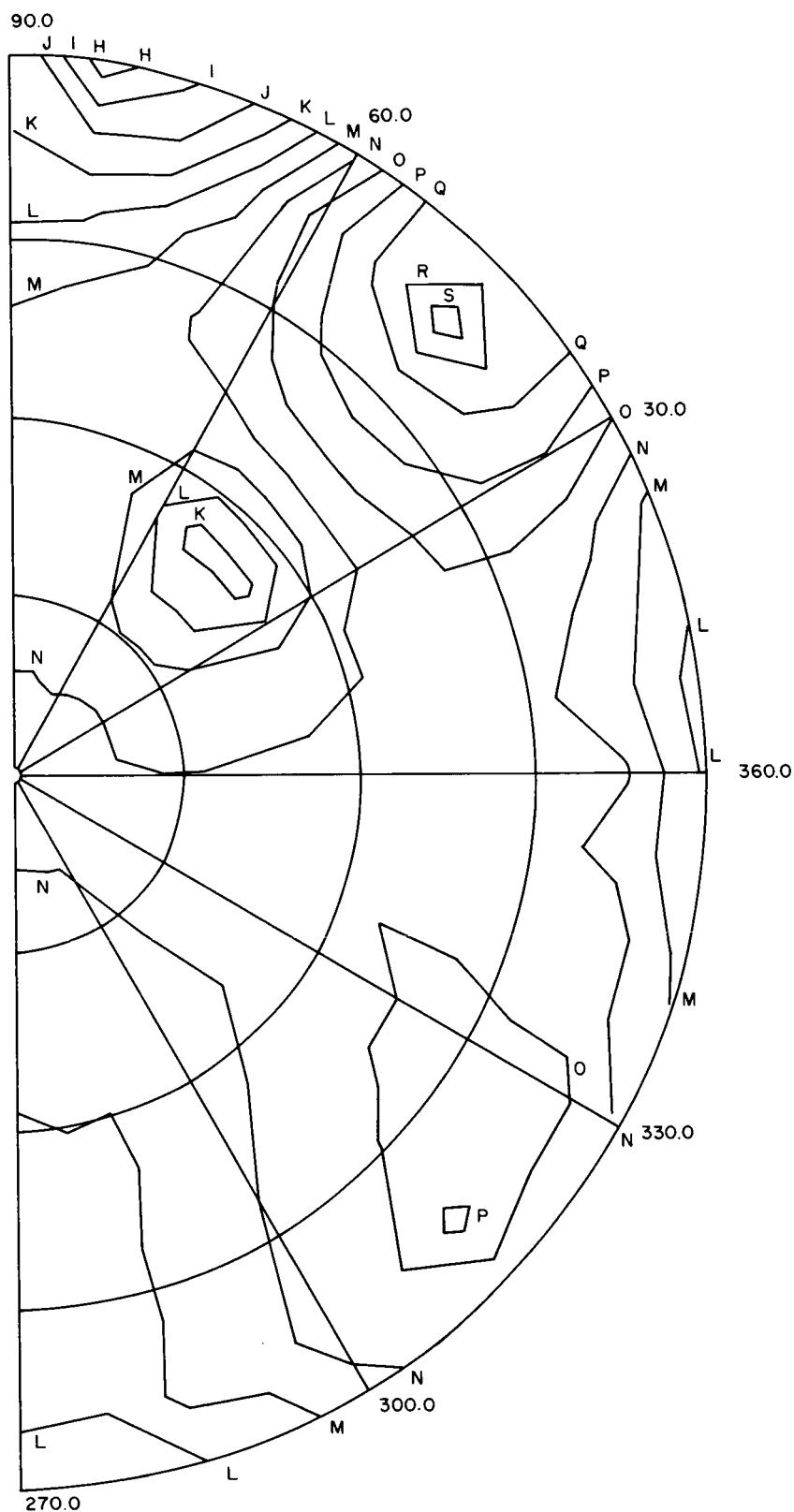| ERROR, in.	LABEL
-0.130	A
-0.120	B
-0.110	C
-0.100	D
-0.090	E
-0.080	F
-0.070	G
-0.060	H
-0.050	I
-0.040	J
-0.030	K
-0.020	L
-0.010	M
0.000	N
0.010	O
0.020	P
0.030	Q
0.040	R
0.050	S
0.060	T
0.070	U
0.080	V
0.090	W
0.100	X
0.110	Y
0.120	Z

Fig. 4. 85-ft Az-El antenna with counterweight ties removed. Panels set at 45 deg. Horizontal look
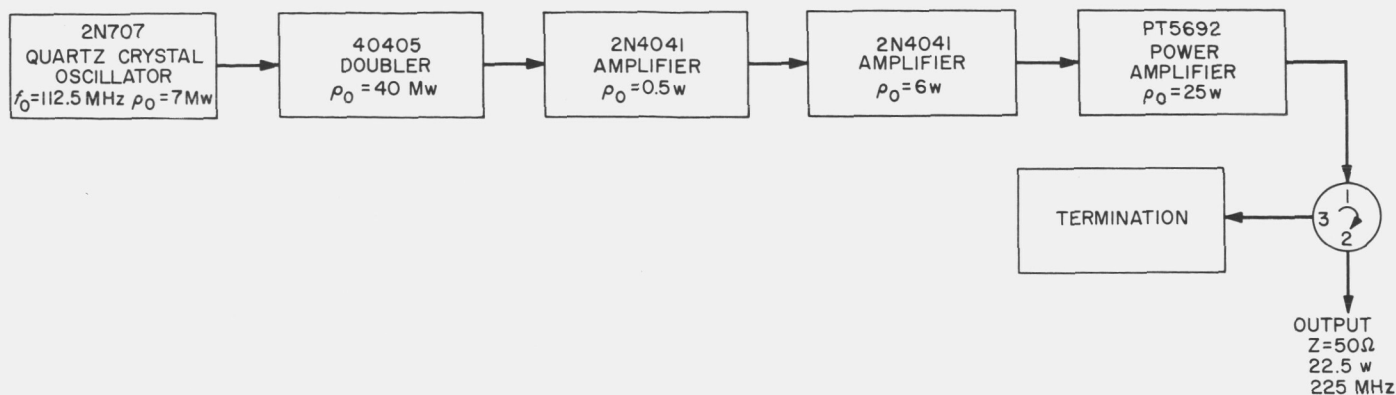(focal length fit, rms = 0.014)
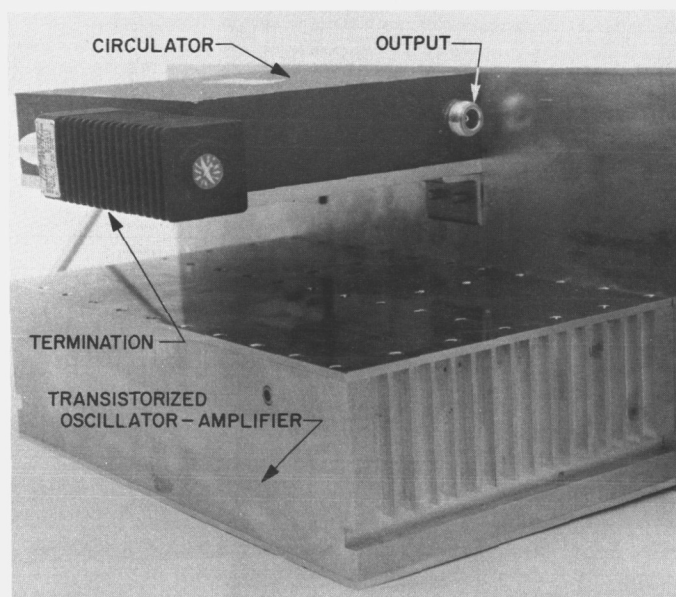
Fig. 5. Block diagram of transmitter

Fig. 6. Solid state RF exciter for hydrogen maser

B. Frequency Generation and Control: Atomic Hydrogen Frequency Standard, W. H. Higa and S. N. Petty

To improve the reliability of the atomic hydrogen maser, it is planned to replace all vacuum tubes with solid state devices. The vacuum tube oscillator used to excite the RF discharge in the dissociator (SPS 37-43, Vol. III) was recently replaced by a transistorized unit.

This unit consists of a five-stage transistor transmitter with an output circulator and delivers up to 22½ w at a frequency of 225 MHz. A block diagram of the complete transmitter is shown in Fig. 5.

The quartz crystal oscillator provides 7 mw of RF power to the doubler. The doubler stage contains a potentiometer which can vary the output power of the transmitter from 8 to a maximum of 22.5 w. The output frequency of the transmitter varies less than 1 kHz over the full range of output power. Two 225-MHz amplifier stages drive the power amplifier at the rated power output. The output circulator is required to prevent transmitter damage under possible open or short circuit conditions. Figure 6 shows the complete transmitter and output circulator.

Work is now in progress on a more compact version of this transmitter. The operating characteristics of the unit are summarized as follows:

Output power (with circulator). . . 8 to 22.5 w
Frequency . . . . 225.00 MHz
DC power input . . . . 28 v DC @ 2 amp max
Spurious AM sidebands . . . . > 20 db down
Spurious harmonics . . . . > 27 db down

Both hydrogen masers are now operating, and plans are being made to conduct the short-term stability measurements.

N67-25065

V. Facility Engineering and Operations

A. Flight Project Support, J. Orbison

1. Surveyor Project

Preparations for the *Surveyor* mission C tracking at DSS 11 include system interface compatibility testing. Installation of the multiple mission support equipment into the station S-band system necessitated new interface testing. In addition, the TV-1/TV-11 interface verification, and the control data console command transmitted and word error rate tests were accomplished. Through February the mission independent equipment/control data console compatibility testing continued, as system performance evaluation and personnel training.

2. Mariner Mars 1964 Project

Tracked jointly by DSS 14 and DSS 13, the *Mariner IV* spacecraft continues to provide telemetry data. Using the JPL experimental maser and receiver (SPS 37-39, Vol. III, p. 112) DSS 14 tracks in the receive-only mode, microwaving the telemetry data to DSS 13 for processing.

3. Mariner Venus 67 Project

The read-write-verify (R-W-V) command and ground telemetry equipment installed at DSS 11 (SPS 37-43, Vol. III, p. 121) are receiving intensive operational and interface testing. Additional read-write-verify command subsystems are being installed at DSS 12 and DSS 14. Because of *Lunar Orbiter III* commitments, the DSS 12 read-write-verify equipment operational testing began in March. A school was held at DSS 11 in January for personnel who will operate the read-write-verify equipment

during the mission. Personnel from local and overseas stations attended.

4. Lunar Orbiter Project

a. Lunar Orbiter II mission. *Lunar Orbiter II* spacecraft tracking continues. Two special tests were conducted at DSS 12 with this spacecraft. During pass 61, on January 8, a spacecraft transponder oscillator drift characteristic test was accomplished preparatory to multiple tracking of the *Lunar Orbiters*. During pass 82, on January 31, spacecraft transponder interference and silent acquisition tests were accomplished to obtain more information concerning dual tracking.

Three passes of the spacecraft were used for DSS 12 operational training and testing, in preparation for the *Lunar Orbiter III* mission.

Two special short tracks of the *Lunar Orbiter II* were accomplished on passes 92 and 94, February 9 and 11. During passes 5 and 7, *Lunar Orbiter III* was occulted by the Moon. For 40 min during the occultation, *Lunar Orbiter II* was turned on and successfully tracked. Tracking of *Lunar Orbiter II* continued on a special schedule basis through February 28.

b. Lunar Orbiter III mission. *Lunar Orbiter III* spacecraft was launched from Cape Kennedy, Florida, February 4, 1967. DSS 12 acquired the spacecraft at 14:23 GMT, February 5, for the start of pass 1. The initial lunar orbiting deboost was accomplished by a command from

DSS 12 February 8. On February 14, the video test leader was read out at DSS 12.

5. Pioneer Project

a. Pioneer VI mission. The *Pioneer VI* spacecraft completed a year in space December 16, 1966 (SPS 37-43, Vol. III, p. 120). Currently, DSS 14 is tracking it.

Personnel from Thompson-Ramo-Wooldrige and the NASA/AMES Laboratory were at Goldstone in January, updating the *Pioneer* computer program scheduled for use with later *Pioneer* missions. A portion of the testing was accomplished using the current spacecraft.

b. Pioneer VII mission. In the seventh month of its mission on February 28, the *Pioneer VII* spacecraft tracking continues. The DSS 12 commitment with *Lunar Orbiter III* caused the prime tracking of the *Pioneer VII* to return to DSS 11 on February 1. Multiple mission support is provided from DSS 12 *Pioneer* ground operational equipment and the telemetry and command processing equipment via microwave.

A lunar occultation by *Pioneer VII* occurred during pass 156 January 19. A special experiment was conducted by Stanford University, using equipment provided by the experimenters and installed at DSS 12.

Prime tracking was moved to DSS 14 February 20, with DSS 12 providing multiple mission support.

B. Facility Construction and Equipment Installation, J. Orbison

1. DSS 11

Installation of two 500-kw diesel-engine-generators is in progress (Fig. 1). When completed, the installation will provide DSS 11 with 1300 kw of back-up power.
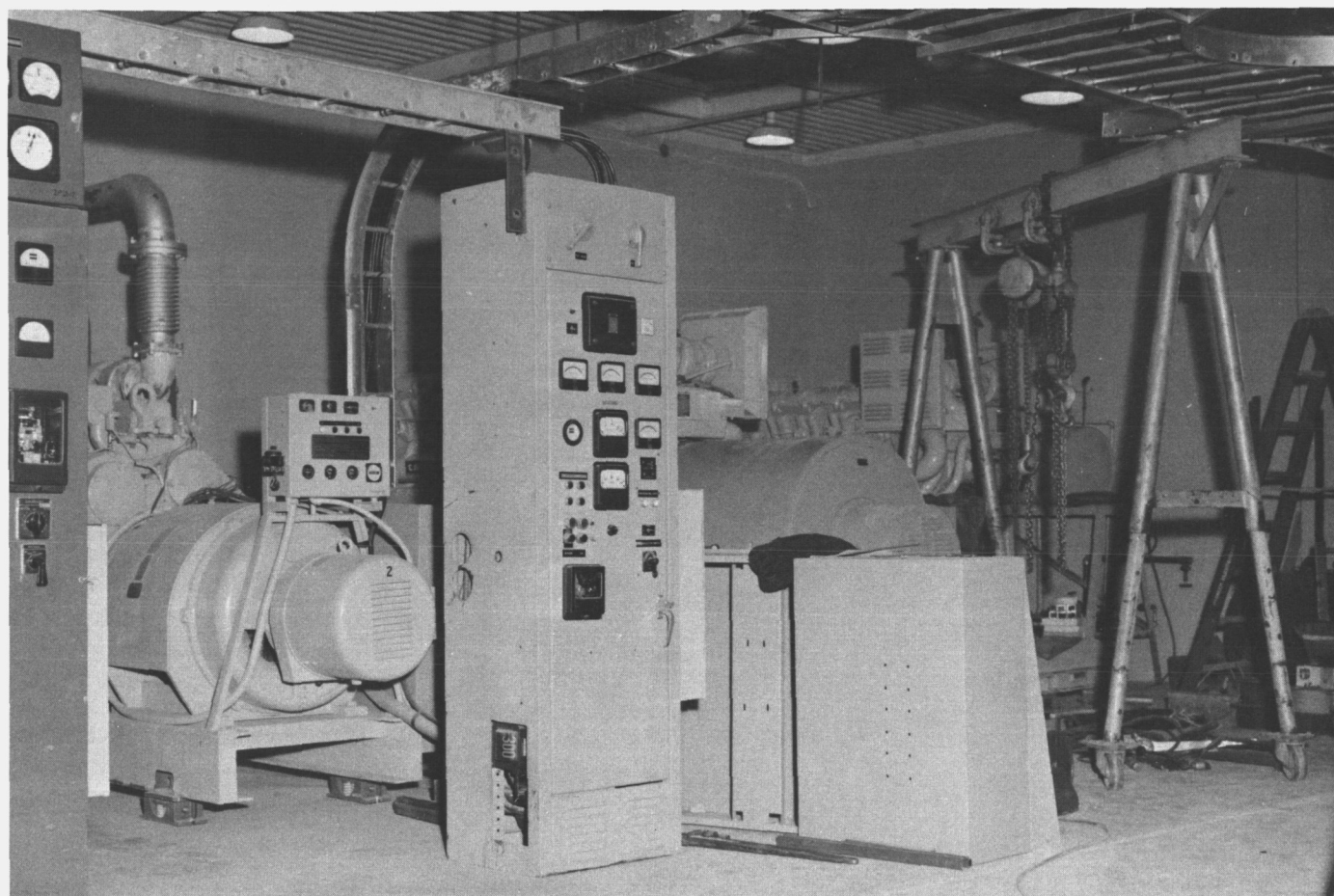

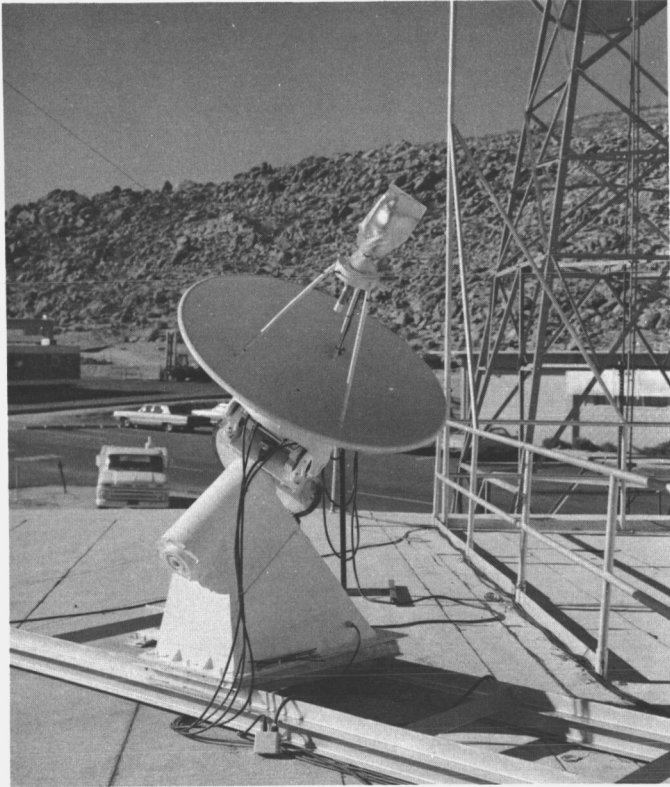**Fig. 1. New generator at Pioneer Station**

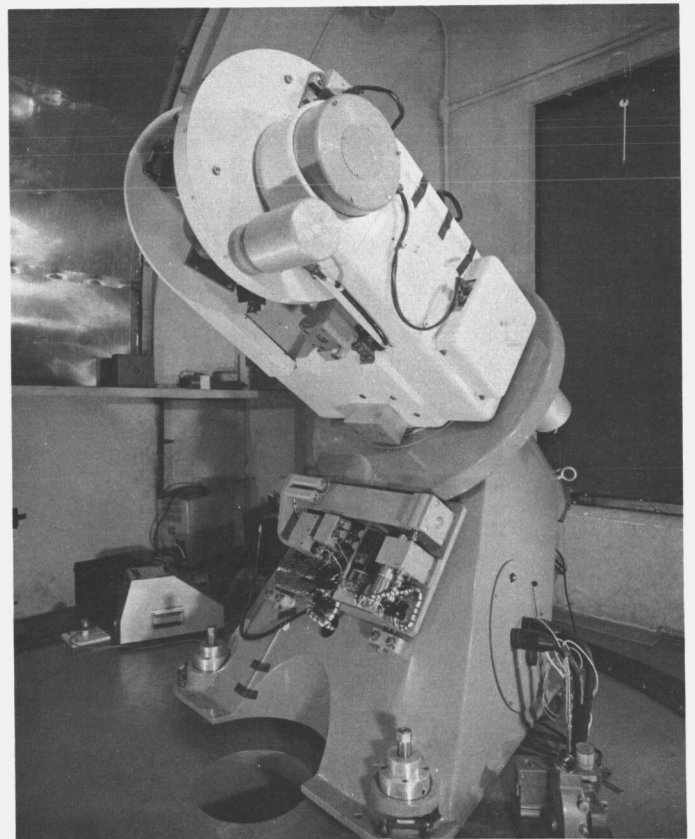Fig. 2. Four-foot antenna used for time synchronization experiments

Fig. 3. Master equatorial installation at Mars Station

The S-band system has been augmented by an additional telemetry and command processing computer and interim antenna pointing system installations. Both subsystems are in the process of operational testing.

2. DSS 12

A 4-ft diameter HA-Dec paraboloid antenna was installed on the roof of building G-33 at DSS 12 (Fig. 2) in January. Time synchronization experiments were conducted between the DSS 12 and DSS 13 30-ft antenna via the inter-site passive microwave link.

3. DSS 14

The S-band system installation continued with most major elements of the subsystems operational. Arriving January 10, the rubidium frequency standard was installed, tested, and placed in operation, assuring the operations of a local prime frequency standard. The digital instrumentation subsystem communications buffer arrived January 16 and was installed and placed in operation. Installation of the telemetry and command data handling transfer racks is in progress in conjunction with the *Mariner* Venus 67, and subsequent multiple mission projects.

Station personnel are assisting JPL and contractor engineers to align and test the hydrostatic bearings supporting the alidade structure. The master equatorial/intermediate reference structure antenna pointing testing continues. Located in an observation room at the top of the instrumentation tower (Fig. 3), the master equatorial provides a precision angle data system for the 210-foot antenna (SPS 37-27, Vol. III, p. 133).

A 500-kw diesel engine-generator unit was delivered in February. Installation is progressing and completion will bring the total available back-up diesel-electric power to 2000 kw.

C. Venus Deep Space Station Operations,

M. A. Gregg, E. B. Jackson, and A. L. Price

1. Experimental Activities

From December 13, 1966 through February 14, 1967 the Venus Station 85-ft antenna was used primarily in planetary radar experiments bistatic with the Mars Station and in the *Mariner IV* spacecraft reception. Also, it was used for radio source evaluation at X-band and radio source tracking at S-band (8448 and 2388 MHz, respectively). The 30-ft antenna was used with a receiving antenna located at the Echo Station to conduct experiments on the X-band time synchronization system involving transmission of PN code-modulated signals via the Moon.

2. Subsystem Performance

a. Receiving systems. During this period the Mod. IV receiver was used in its bistatic configuration for reception of signals from the *Mariner* spacecraft and for Venus and Jupiter planetary radar experiments. In each case, signals from the appropriate Mars station R&D receiver were fed, via the microwave link, into the 455-kHz portion of the Venus Station's Mod. IV receiver.

The Venus Station 2388-MHz receiver and the Venus Station *Mariner* receiver were used in a special test in an effort to resolve discrepancies in computer-measured signal strength levels in the open- and closed-loop modes. Testing will continue as the tracking schedule permits.

The X-band 8448- to 30-MHz converter remained in the 85-ft antenna feed cone. It was used, in conjunction with the 30-MHz portion of the Mod. IV receiver, in various antenna pattern measurements.

One component failure occurred in the Mod. IV receiver during this period. This involved the automatic gain control amplifier in the main loop channel of the receiver. The amplifier was replaced with a spare, and normal operation was restored.

A hardware failure also occurred. This concerned a broken flex line which supplies coolant water to the cold-plate in receiver cabinet no. 2. The leak was repaired before there was any over-heating or water damage.

A leak in the *Mariner* receiver cooling system was repaired by replacement of one of the plumbing fittings. No damage resulted from the leak, and normal operation was restored.

Operation of the central frequency synthesizer remained good throughout this period with no lost time due to equipment failures. Reference signal cabling to the new X-band programmed oscillator has been completed and is now in use. Intermittent problems with the voltage monitoring circuitry for the +30-v power supply have occurred. Troubleshooting is continuing.

b. R&D 100-kw transmitter. The R&D transmitter has been operating during this reporting period for the Venus and Jupiter bistatic radar experiments. Both the Varian VA885 S/N 4 and the Eimac 5-KM 300 SI S/N A6-17 were used.

Some failures were experienced during this operating time. The time lost to these failures was 45 min due to failure of a reflected power amplifier and recalibration of the replacement unit. Some time was also lost because of the high voltage cable breakdown in the crowbar cabinet.

c. Mariner 100-kw transmitter. For this reporting period, the *Mariner* transmitter has operated without failures.

3. System Improvement

a. Receiving systems. A 2388-MHz test transmitter is being checked out for possible use as a collimation tower signal generator. The generator would be used for quick spot checks of the S-band receiver operation.

b. Transmitting systems. The Eimac klystron 5-KM 300 SI S/N A6-17 was installed in the R&D cone with an external resistor for the modulating anode. A modification, the installation of a vacuum relay to switch the modulating anode from cathode to ground, has been delayed because the switch, damaged in shipment to the Venus Station, was returned to the manufacturer for repair.

D. DSIF Station Control and Data Equipment,
R. Flanders, E. Bann, G. Jenkins, A. Burke, and H. Baugh

1. Introduction

The status of the DSIF station control and data equipment implementation is reported in each issue of the SPS. The subsystems included in the DSIF station control and data equipment are the Antenna Pointing Subsystem (APS), Digital Instrumentation Subsystem (DIS) Station Monitor and Control Console (SMC), Telemetry and Command Processor (TCP), and the Frequency and Timing Subsystem (FTS). In this issue the reported status of the implementation of this equipment is current as of February 1967.

2. Antenna Pointing Subsystem

The antenna pointing subsystem has been implemented in the DSIF stations to provide the capability to point antennas under computer control in addition to the existing servo automatic tracking and manual control modes of pointing. The primary function of the APS is to point

an antenna in the direction of a spacecraft or celestial body (ephemeris) the location of which has been computed by the subsystem or supplied by external pointing prediction data on punched paper tape. The APS consists of a scientific data systems (SDS) model 910 computer with associated peripheral equipment, interface equipment and a subsystem control panel. The APS operates in conjunction with the servo assembly of the antenna mechanical subsystem and the antenna angle readouts of the tracking data handling subsystem.

The APS adds the following capabilities to the DSIF: (1) rapid radio signal acquisition, (2) tracking when there is no radio signal or when radio signal level is too low for automatic tracking operations, and (3) more flexibility and precision in control of antenna movement.

The interim APS has been implemented in DSSs 12, 14, 41, 42, 61, and 62. Stations 11 and 72 will be completed during March 1967. The interim APS makes use of existing equipment to provide antenna pointing support on an interim basis.

The APS phase I implementation is the second step which will provide increased capability over the interim subsystem. APS phase I requires additional computer interface equipment to perform its function. The increased capability provided by APS phase I consists of: (1) a planetary/spacecraft mode which permits tracking of spacecraft in Earth orbit and improved tracking of spacecraft in planetary orbit, and (2) an injection condition mode, which provides tracking of spacecraft by computing an ephemeris based on injection conditions at time of launch. This mode is particularly useful in spacecraft acquisition during the first pass before predict data are available.

APS phase I has been implemented at DSS 14 and is scheduled to be implemented at DSSs 11, 12, 41, 42, 61, 62, and 72 at one month intervals, starting in May 1967. Computer interface equipment for APS phase I is in the procurement stage, in addition to new control panels which will provide increased capability for operator control of the APS. Both the interface racks and control panels are scheduled for delivery beginning May 15, 1967, with units arriving at one month intervals thereafter.

3. Digital Instrumentation Subsystem, Phase II

Implementation of the Digital Instrumentation Subsystem (DIS), Phase II is proceeding in the areas of the subsystem hardware procurement, DSIF System Monitor Program preparation, and documentation procurement.

The purpose of the DIS Phase II, together with the SMC Phase II, is to provide system monitoring facilities at each station in the DSIF. The DIS Phase II is to perform the following functions:

(1) Present station performance and status data in real time or near real time for evaluation of data validity and verification of station operating configuration.

(2) Provide alarm monitoring of critical station parameters, comparing actual performance with pre-established criterion data for initiation of corrective action where conditions exceed nominal limits or present a failure indication.

(3) Maintain a complete permanent record of station performance and failure data throughout the duration of a mission to facilitate real time and post-mission analysis of the system operation.

The present effort is directed toward the establishment of hardware and software compatibility between interfacing equipment. Functional interfaces with mating equipment have been identified, and are being translated to electrical and mechanical characteristics to provide the functions described in (1) and (2) above. Software interfaces, including the format and content of the monitor criterion data message, and station periodic and alarm messages, are presently being defined, primarily for function (2) above. The documentation requirements for the subsystem have now been established, with the effort separated into the two distinct phases of: (1) subsystem assembly and subassembly drawing generation, and (2) subsystem operation and maintenance manual preparation.

4. Station Control and Monitor Console

The SMC phase I is intended to provide for the display and control of station performance from a central location, for use by the station manager at each station. Furthermore, the SMC displays information to indicate nonstandard system or subsystem performance. SMC phase II calls for added functions, as follows: (1) displaying selected station parameters, (2) providing an English text printout of station performance and status, (3) providing system alarm monitoring under control of the DIS to indicate station failures, and (4) providing a teletype page printer. Completion of phase I implementation requires only the countdown clock. The first countdown clock should be operational no later than August 1967.

Phase II development is underway and delivery of the prototype X-Y plotter is scheduled for April 1967. This unit is scheduled to undergo thorough evaluation at both JPL and Goldstone prior to procurement of follow-on units. The plotter is intended to display actual vs predicted performance data. The program alarm and control panel is undergoing an extensive redesign, which incorporates an audible alarm and now uses JPL Hi-Rel digital modules in lieu of the original Computer Control Company (3-C) cards. The first unit should be operational by June 1967. Implementation of the program alarm and control panel is planned for five stations in FY 67. Actual delivery, however, will be early in FY 68.

Page and line printers are on order and delivery to five stations is planned for the first quarter of FY 68.

5. Telemetry Command Processor, Phase II

The TCP phase II provides the DSIF with a mission independent telemetry and command data processing capability for real time operation. The TCP phase II assembly interfaces with the mission dependent project equipment and provides the capability to decommutate, process, edit, alarm monitor, and format spacecraft telemetry data for transmission to the Space Flight Operations Facility (SFOF), and to process and verify command data, received at the DSIF station from the SFOF, for transmission to the spacecraft.

The TCP phase II is in the process of being expanded and in order to recognize how each station is equipped, the following configurations are being established:

a. TCP phase II-B.

(1) Addition of Analog-to-Digital Converters (ADC). The ADC will interface directly with the mission independent equipment and is part of the capability to provide digital tapes of telemetry data to the flight projects, in lieu of analog tapes previously supplied.

(2) Core expansion of the TCP phase II SDS 920 computer from 8K to 12K memory. This is also part of the capability to provide digital tapes to the flight projects.

(3) The TCP phase II-B is scheduled for implementation at all DSS's with the exception of DSS-51. The detailed implementation schedule will be established when hardware delivery information becomes available.

b. TCP phase II-C.

(1) Core expansion of the TCP phase II-B SDS 920 computers from 12K to 16K memory and an additional analog-to-digital converter for each computer.

(2) Addition of digital control equipment for telemetry bit synchronization.

(3) The TCP phase II-C is scheduled for implementation at DSSs 12, 41, 62, 71, and 14.

Implementation of the TCP phase II-B and -C will expand the DSIF capability to support flight projects and will considerably reduce the amount of mission dependent equipment required at the deep space stations.

6. Frequency and Timing Subsystem, Phase II

During the last two months there has been little technical progress on this project. Instead, the principal effort has been in the area of component procurement for modules, and in the initiation of procurement for other subsystem components. For instance, an order was placed for a digital driver-isolation amplifier assembly, to be evaluated as a possible approach to assuring that all systems using timing signals will be completely isolated from one another. The first unit will be installed at one of the Goldstone tracking stations for thorough testing in an operational environment.

E. Operational Scheduling and Utilization Forecasting System, B. W. Dysart

1. Introduction

The deep space network (DSN) provides tracking and telemetry support for several independent missions simultaneously. The arrangement of the various mission activities in an order such that launch schedules can be met and flight spacecraft can be tracked requires careful planning and efficient assignment of the available DSN resources.

The DSN management compares projects' plans and detects impending overloads of the network's support capability. Critical conflicts in planned facility use may occur at any of one thousand or more independent elements of the DSN; however, decisions of which activities to support can only be made by considering the relative importance of these activities within and among all of the projects involved. Therefore, the DSN management is required to consider in great detail a large number of project activities of varying priorities. When necessary, alternative plans are recommended to project managers.

a. 7-day schedule. All of the work done at all of the stations and at the SFOF is scheduled by the DSN operations control chiefs and the DSN scheduling office located in the SFOF. The various project inputs must be compatible with each other in order that comparisons can be made and conflicts detected. Requests for support are placed ten to fourteen days in advance of the period covered by the 7-day schedule, which allocates all DSN resources on an hour-by-hour basis.

b. 12-week DSN utilization schedule. Prior to the submission of the 7-day schedule requests, the projects make requests to the 12-week schedule, where potential conflicts are detected on a week-by-week basis. The level of facility detail considered is the same as the 7-day schedule, but the time scale is in hours per week. Conflicts detected by the 12-week schedule are considered far enough in advance to allow some rescheduling of activities into the slack time, which is made visible by the same process. When rescheduling is not possible, the conflicting projects must solve these problems outside the DSN's area of responsibility.

c. 16-month loading schedule. While the 12-week schedule covers project planned activities from one to four months in advance, this time is usually insufficient to install project-peculiar equipment at the selected tracking stations. The planning device used to allocate complete station tracking coverage and SFOF computer loading is the 16-month schedule, which covers the period from the third through the sixteenth month in the future. This schedule, because it is primarily concerned with tracking coverage, uses a much less detailed set of system elements.

For each time span considered, the project scheduling effort is commensurate with what confidence the project has in it, and the visibility is commensurate with the system alterations that are possible at that lead time. In addition, the input forms for each schedule and the output forms from that scheduling effort maintain a continuity that permits rapid and efficient planning by the flight projects. Fig. 4 shows the information and processing involved in the various schedules.

2. 12-Week DSN Utilization Schedule

All planning and scheduling systems concern themselves with information and decisions. The 12-week schedule deals in requests from many sources for DSN operational support and the decisions necessary to most efficiently provide that support. The DSN is committed to the flight projects long in advance of the detailed planning. When the detailed plans are made, the DSN, as the only common point of contact, will correlate requests and detect

INFORMATION:
1. LAUNCH DATES
2. TRAINING REQUIREMENTS
3. NECESSARY SPECIAL EQUIPMENT
4. MILESTONES

AVAILABLE DSN
FACILITIES PRESENT
AND FUTURE

SEVERAL
INDEPENDENT
FLIGHT
PROJECTS AND
DSN DESIGN
AND DEVELOPMENT
GROUPS

16-MONTH
INPUT
FORMAT

16-MONTH
SCHEDULE
PROCESS

COMPATIBLY ALLOCATED
FACILITIES

UNSCHEDULABLE
REQUESTS

TRACKING
AND
COMPUTER
LOADING
SCHEDULES

MORE DETAILED
FACILITY LIST

1. PROJECT TRAINING PLANS
2. EQUIPMENT INSTALLATION DATES
3. ASSIGNED TRACKING STATIONS
4. COMPUTER PROGRAM DEVELOPMENT AND
   CHECKOUT DATES
5. PRIOR 12-WEEK SCHEDULE REQUESTS

12-WEEK
SCHEDULE
INPUT
FORMAT

1. LIST OF FACILITIES FOR WHICH
   REQUESTS HAVE BEEN MADE
   (THAT DO NOT EXCEED MAXIMUM
   ELEMENT LOADING)

12-WEEK
SCHEDULE
PROCESS

2. LIST THAT EXCEEDS LOADING LIMITS
3. DICTIONARY OF CONFIGURATIONS
4. PROJECTS' LISTS OF REQUESTS

PLANNED
STATION
AND SFOF
EQUIPMENT
UTILIZATION
SCHEDULE

SPECIFIC HOURS OF SPECIFIC
DAYS FOR PLANNED ACTIVITIES

ADDITIONAL REQUESTS NOT
COVERED BY 12-WEEK
SCHEDULE PROCESS

7-DAY
SCHEDULE
PROCESS

MINUTE BY MINUTE EQUIPMENT
ALLOCATION FOR SPECIFIC PROJECT
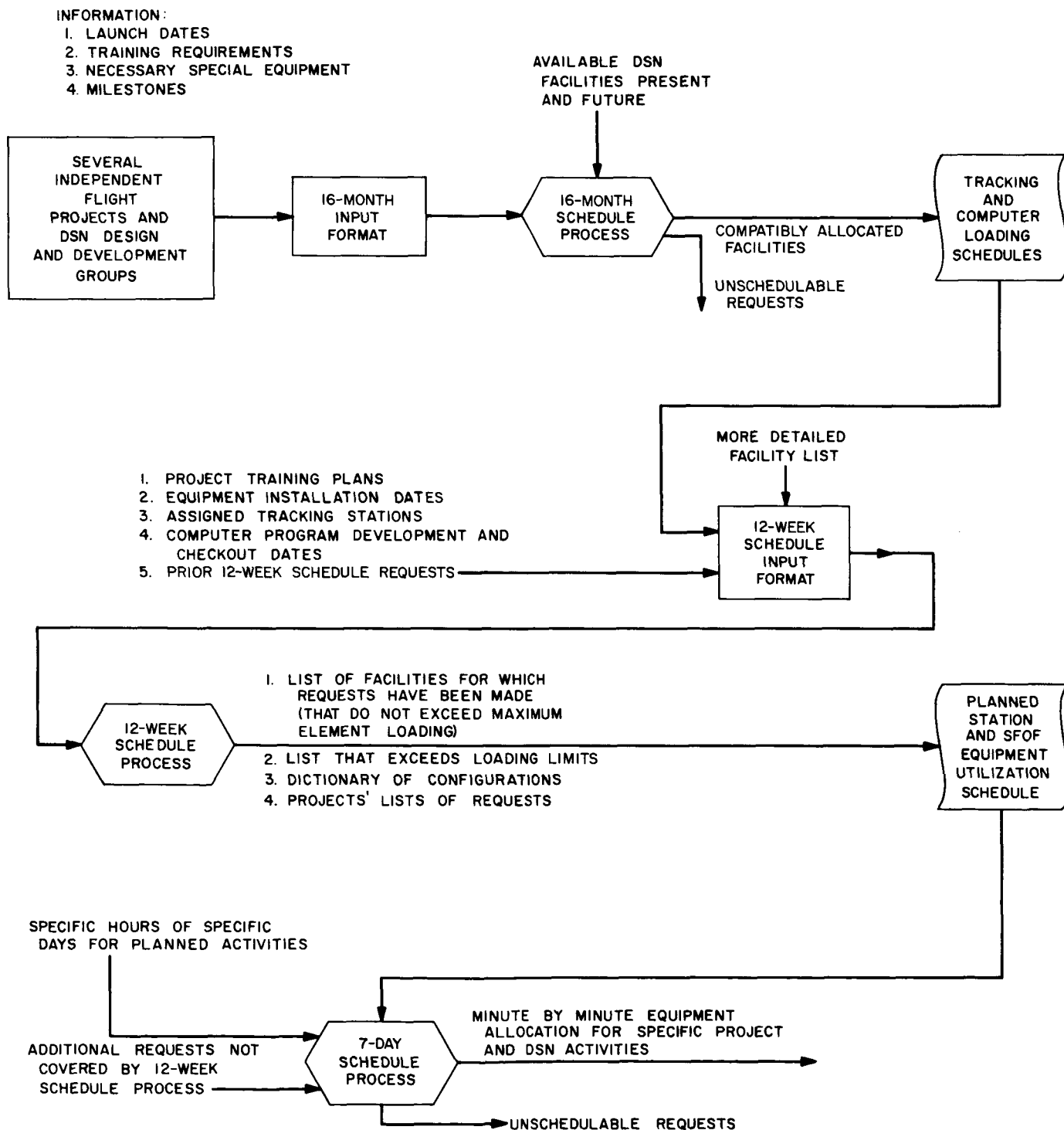AND DSN ACTIVITIES

UNSCHEDULABLE REQUESTS

Fig. 4. DSN scheduling system flow chart

potential conflicts in facility usage. If there are no conflicts, the DSN will provide equipment and support at the committed level, and, where possible, will endeavor to provide additional requested support on a noninterference basis. If there are conflicts the DSN will use the several scheduling systems to advise of possible problem solutions, but it remains with the projects involved to finally resolve these conflicts.

The 12-week DSN utilization schedule, presently in development, is being operated in real time in order to uncover both practical improvements to production methods and possible alterations in information presentation and gathering. Also, it provides management and planning information during the development period.

a. Program function description. The DSN 12-week schedule conflict detection and resolution process uses a 7094 COBOL program to accept brief, organized input requests and generate extensive lists of DSN equipment utilization. At the same time, using relatively simple criteria, it detects potential overloads on an individual DSN element basis and generates a conflict list in a form usable by the DSN project representatives. A meeting is then held among these representatives. The DSN project engineers and DSN project managers consider the potential overloads, and solutions to the various equipment utilization conflicts are recommended. The program is then used to generate a revised list of equipment utilization and sets of individual project request data. This output of the 12-week schedule program is used by the projects in preparing their subsequent requests to the 7-day scheduling system and for revising their inputs to future 12-week schedule issues.

The same 7094 program, through the use of alternate instruction options, is later used in the 7-day scheduling system.

b. Input information and methods. From the DSN elements available for scheduling, each DSN user selects a set that will be used for his activity. The size of a DSN element is based on possible simultaneous use for different purposes. If an element can be used by independent users for different purposes simultaneously, then that element is divided into smaller nonsharable elements. For example, DSS 61 is divided into: antenna, transmitter, receiver No. 1, receiver No. 2, etc. These elements can be used independently but not their internal parts. The user then defines a set of elements for future use, and a DSN schedule reference number is assigned. A configuration library is maintained; unless changes are made to these configura-

tions, the user can always refer to them in the future by requesting them by the reference number. A dictionary of previously requested configurations is supplied to the user as part of each month's 12-week schedule output.

Requests for DSN support are made by filling in a one line format that describes the activity in English, such as "*Pioneer VII* track, DSS 41"; the number of hours needed, such as "16 Hr"; the week of the year, "Wk 16"; and the predefined set of elements needed to support the activity, "Configuration P410." Many independent requests for support can be made on the same form, each line of the form resulting in a separate request IBM card.

c. Processing and output presentation. The 7094 COBOL program then examines the configurations specified in all requests and generates a list of all the requested elements of the DSN for each week. Each element appears in the list as shown in Fig. 5.

A subtotal of each project's hours is printed to the right of the request hours, and a complete total appears at the bottom. The program's conflict detection criterion is simple; if the total for any element exceeds 168 hrs in a week, the element is identified as conflicting and is extracted for listing in the conflict portion of the output. This process does not detect those conflicts that arise from simultaneous use at specific hours of specific days, the period covered is too far in the future to warrant filling in request forms to that detail. Reorganization of requests, such as scheduling *Pioneer* tracking passes at DSS 42 instead of DSS 41, relieves the load on the 7-day schedule process to a marked degree.

The L089 entries under both maser and paramp are the result of a single request. All elements defined in the configuration L089 will contain the 9-hour request for this week. If the decision is made to delete this request (perhaps because of a conflict shown elsewhere) all entries for this request will automatically be removed.

In addition to the basic element list and the conflict list, the 7094 program produces two project-oriented planning aids: an updated dictionary of the project's predefined configurations, and a week-by-week list of requests similar to a single line of the element schedule.

After a conflict resolution meeting, the program is run again with the deleted requests appearing with a configuration suffix "D" and overprinted with dashes as shown in Fig. 6.

TWELVE WEEK ELEMENT SCHEDULE   01/28/67   PAGE 686

ELEMENTS DURING WEEK NO. 13 (03/26/67 TO 04/01/67)

          FACILITY   ACTIVITY   DURATION   PROJECT TOTAL

DSS 12MASER

          L089   LO EXTENDED MISSION CRUISE - 12   009 00   009 00
          P009   PIONEER 7 TRACK DSS 12   032 00
          P009   PIONEER 7 TRACK DSS 12   032 00   064 00
          T014   STATION MAINTENANCE STATION 12   024 00
          T014   STATION NOT AVAILABLE STAT 12   048 00   072 00

                                           TOTAL   145 00

DSS 12PARAMP

          L089   LO EXTENDED MISSION CRUISE - 12   009 00   009 00
          P009   PIONEER 7 TRACK DSS 12   032 00
          P009   PIONEER 7 TRACK DSS 12   032 00   064 00
          T014   STATION MAINTENANCE STATION 12   024 00
          T014   STATION NOT AVAILABLE STAT 12   048 00   072 00

                                           TOTAL   145 00

Fig. 5. Sample of computer printout

TWELVE WEEK ELEMENT SCHEDULE   01/28/67   PAGE 104

ELEMENTS DURING WEEK NO. 06 (02/05/67 TO 02/11/67)

          FACILITY   ACTIVITY   DURATION   PROJECT TOTAL

DSS 12XMTR

          L020   LO CRUISE 12,41,62 SFOF   096 00   096 00
          P009D   PIONEER 7 TRACK DSS 12 (GONE TO 11)   032 00
          T014   STATION NOT AVAILABLE STAT 12   048 00
          T014   STATION MAINTENANCE STATION 12   024 00   072 00

                                           TOTAL   168 00

Fig. 6. Sample of computer printout showing deleted request

These deleted requests are recommendations to the projects of feasible solutions to the conflict. Note that the hours originally requested are still visible along with an inserted note "(Gone to 11)." Decision information has been kept visible for use by both the project and the DSN. The sequence of operations for 12-week schedule
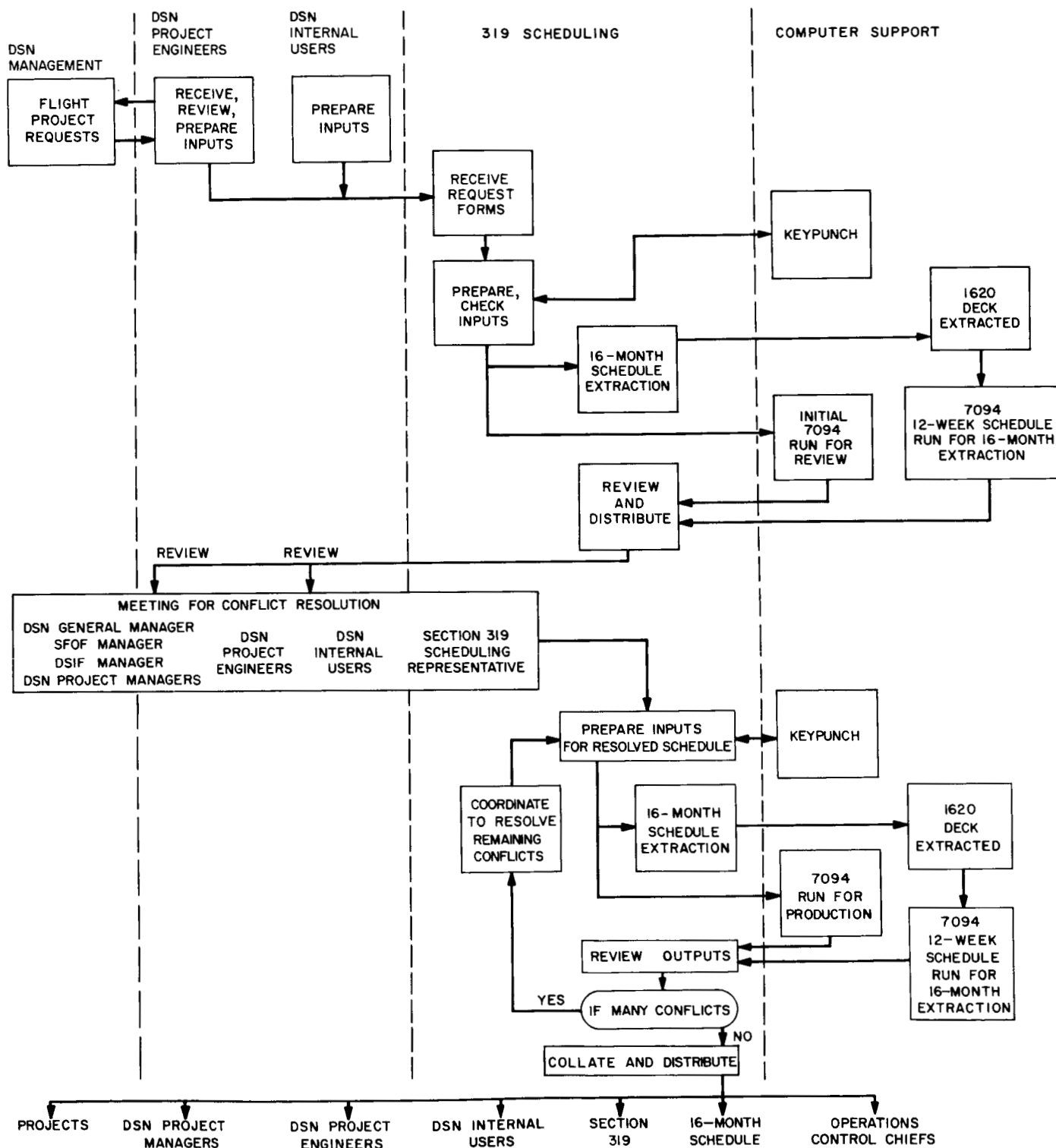

Fig. 7. 12-week DSN utilization schedule procedures

production along with a responsibility breakdown is shown in Fig. 7.

d. Summary of present status. The 12-week DSN utilization schedule operating system is presently being operated by development personnel and is providing management planning data on a regular monthly basis. In the immediate future a set of standard practice instructions will be introduced, and the system will be handed over to operational scheduling personnel. At the same time, because of intimate experience with the problems that arise from detail of input and output information, quality of such information, management and operating personnel loading, etc., several major and many minor changes to the program and operating system will be designed and installed. It is planned that new models of the scheduling system will be run in parallel with the existing one and when proven to be an improvement, will be installed with updated standard practice instructions. Several presently planned areas of development are:

(1) Output format changes, two dimensional charts rather than the present essentially one dimensional tabulations.

(2) More flexibility in input request handling.

(3) More rapid turn around in order to preserve the timeliness of planning data.

(4) Development of the correspondence between the computer's internal model and in the corresponding segments of the real schedulable world.

(5) Automation of some of the present manual aspects of the system operation.

A description of the 16-month scheduling system and its interaction with the complete scheduling and forecasting system will be given in the next report.

F. Star Clock for Use in Antenna Calibrations,
J. Rothwell

1. Introduction

Before a program of star tracking is considered, it is necessary to determine what portion of the sky is within the field of view of the observing station. Then suitable stars are selected from within this section of sky and their positions relative to the local horizon mask are checked, as some may be obscured by the horizon although they are within the general field of view. These calculations are relatively simple but are tedious and susceptible to errors, especially when done in a hurry to cope with last minute changes in the program.

A mechanical device has been developed at DSS 42 to assist in star selection. This is semiautomatic and includes a provision for the longitude and horizon mask of the observing station, which would be the only variables from station to station.

The star clock can be used to perform several functions:

(1) It can display the stars within the field of view of the observing station (taking the horizon mask into account) and will indicate the local hour angles (LHA) of these stars to within about 1 deg, and maintain this accuracy for several hours.

(2) It can be used to determine the rise and set times and meridian crossings etc. of any star.

(3) It can be used to determine the LHA of the Moon and planets within about 1 deg, and maintain this accuracy for a limited period.

(4) It will indicate sidereal time to an accuracy within a few minutes for several hours.

(5) It can be used as in (1) or (2) for radio stars.

2. Operation

The operation of the clock is based on two formulae found under "Explanation" at the back of the Nautical Almanac.

$$\text{LHA} = \text{Greenwich hour angle (GHA)} \quad \begin{matrix} + \text{ East longitude} \\ \\ - \text{ West longitude} \end{matrix} \quad (1)$$

$$\text{GHA of star} = \text{GHA of Aries} + \text{sidereal hour angle (SHA) of star} \quad (2)$$

By combining these two formulae we have

$$\text{LHA} = \text{GHA} \quad \begin{matrix} + \text{ E. long.} \\ \\ - \text{ W. long.} \end{matrix} \quad (1)$$

$$\text{GHA (star)} = \text{GHA (Aries)} + \text{SHA (star)} \quad (2)$$

$$\text{LHA (star)} = \text{GHA (Aries)} + \text{SHA (star)} \quad \begin{matrix} + \text{ E. long.} \\ \\ - \text{ W. long.} \end{matrix} \quad (3)$$
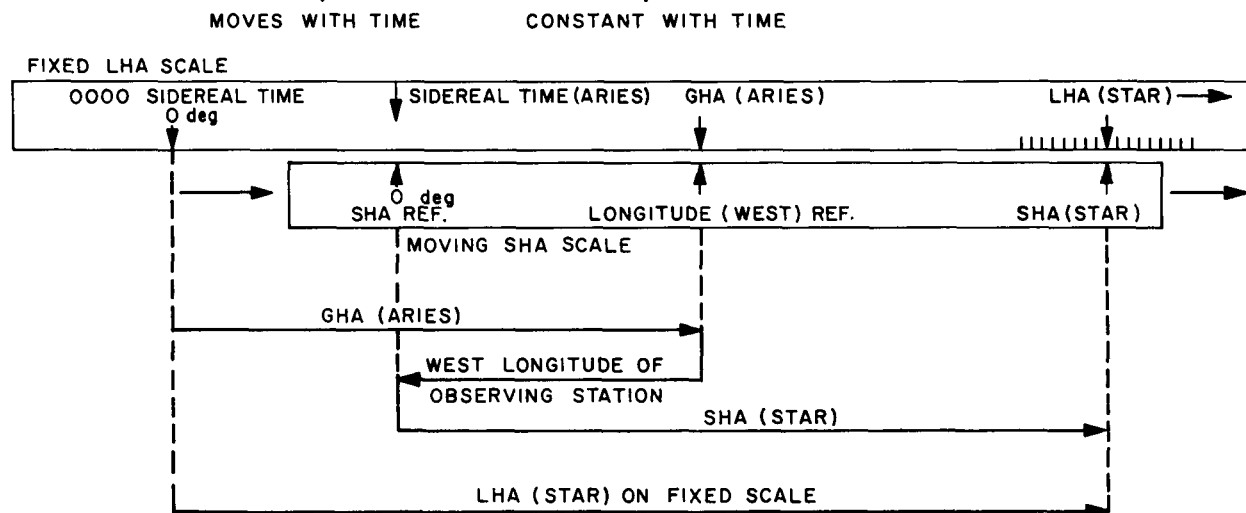
FORMULA IS : LHA (STAR) = GHA (ARIES) + SHA (STAR) + EAST LONGITUDE

(a)
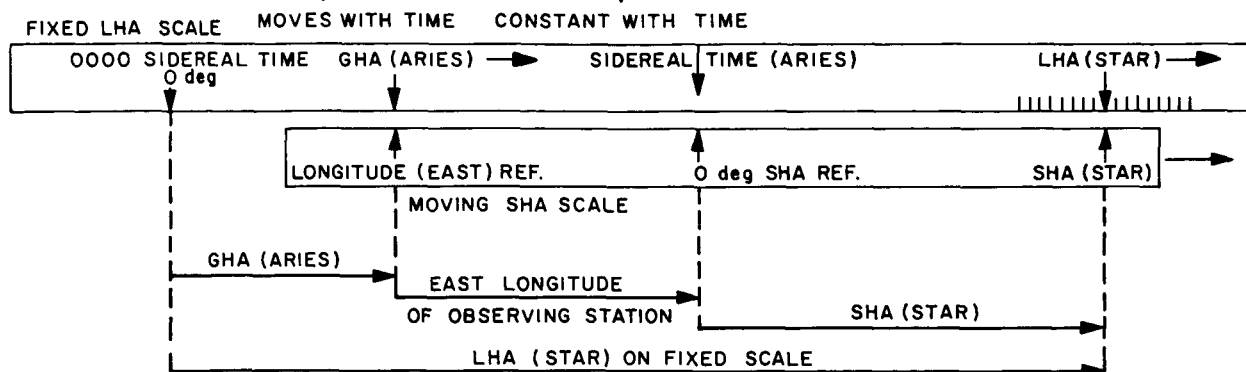
FORMULA IS : LHA (STAR) = GHA (ARIES) + SHA (STAR) − WEST LONGITUDE

(b)

FORMULA IS : LHA (SUN, MOON, PLANET) = GHA (SUN, MOON, PLANET) + EAST LONGITUDE
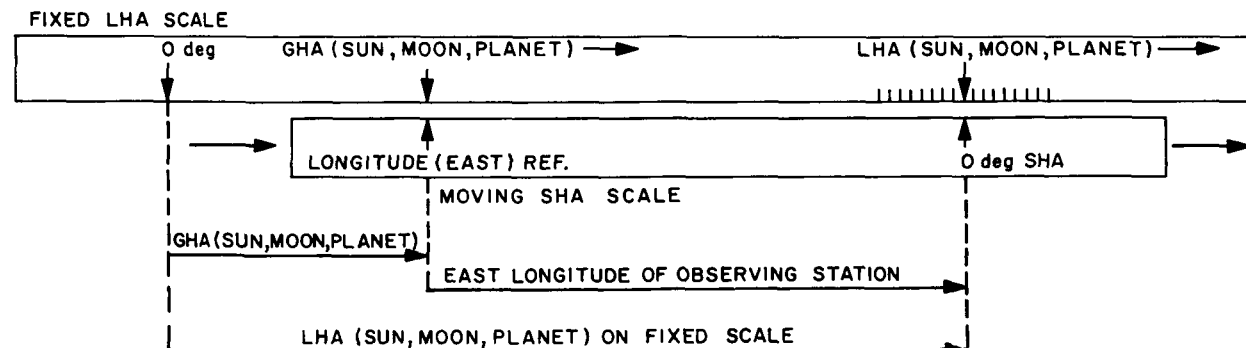
(c)

Fig. 8. Schematic operation star clock: (a) determination of LHA (star) for observation station with east longitude; (b) determination of LHA (star) for observing station with west longitude; (c) determination of LHA (Sun, Moon or planet).

By arranging two scales as shown in Fig. (8) it is clear that formula (3) can be solved. Now if the scales are formed into concentric circles, any multiple of 360 deg in the result will be automatically eliminated. Since GHA of Aries (and LHA of star) advances by approximately 361 deg every 24 hr then one of the circular scales can be driven by a 24 hr clock while the other is held stationary, and thus a reasonably correct time relationship will be maintained for short periods. Since in the circular form the LHA scale is a fixture, by adding a concentric declina-tion scale the local horizon mask can be drawn in. If now the lengths of the radial lines representing stars on the SHA scale can be scaled according to the declinations of the stars, the point at which the stars cross the horizon (or antenna limits) can be seen.

The point of 0 deg SHA is marked as a reference on the SHA scale, and it can be used to indicate the local position of the Sun, Moon and planets, if the longitude reference pointer is set to the solar, lunar, or planetary GHA given in the Nautical Almanac (formula (1) and Fig. 8c). If the longitude reference pointer is set to the GHA of Aries, the 0-deg SHA reference will indicate the sidereal time on the outer 24-hr time scale (Fig. 8a and b).

Table 1. Stars selected for star clock

Star	SHA, deg	Magnitude
Fomalhaut	16	1.3
Al Na'ir	28½	2.2
Deneb	50	1.3
Altair	63	0.9
Vega	81	0.1
Kaus Australis	84½	2.0
Theta Scorpii	96	2.0
Atria	109	1.9
Antares	113	1.2
Alphecca	127	2.3
Rigil Kent	141	0.1
Arcturus	146	0.2
Hadar	150	0.9
Alkaid	153½	1.9
Spica	159	1.2
Mimosa	168½	1.5
Gacrux	173	1.6
Acrux	174	1.1
Denebola	183	2.2
Delta Leonis	192	2.6
Regulus	208	1.3
Miaplacidus	222	1.8
Delta Velorum	229	2.0
Avior	234½	1.7
Gamma Velorum	238	1.9
Pollux	244	1.2
Procyon	246	0.5
Castor	247	1.6
Adhara	256	1.6
Sirius	259	−1.6
Alhena	261	1.9
Canopus	264	−0.9
Betelgeuse	272	0.1 − 1.2
Alnitak	275	1.9
Alnilam	276	1.8
Bellatrix	279	1.7
Capella	281½	0.2
Rigel	282	0.3
Aldebaran	291½	1.1
Mirfak	309½	1.9
Hamal	329	2.2
Achernar	336	0.6
Diphda	349½	2.2
Alpheratz	358	2.2

3. Description

A star clock has been made at DSS 42 with the outer LHA scale (and 24-hr time scale) containing the horizon mask fixed and the inner SHA scale driven by a solar time clock mechanism 24-hr shaft. The DSS 42 star clock is shown in Fig. 9, and a list of the stars selected for the star clock is contained in Table 1. A small disc is driven by the 1-min shaft of the clock mechanism only to provide an indication that the clock is operating. A manual adjusting knob is available in the clock mechanism for initial setting up, and adjustment of the inner, transparent scale.

A list of the stars included on the SHA disc together with their SHA's and magnitudes is shown in Table 1. Stars selected were magnitude 2.0 or brighter, in general, but some extra stars down to magnitude 2.6 have been included to fill in large gaps.

No radio stars have been included on this disc to avoid overcrowding; a second interchangeable disc might be used for the radio stars.

4. Method of Use

a. To survey the field of view and indicate the LHAs of all stars (Fig. 8a and b).

(1) Look up the GHA of Aries for the current time from the Nautical Almanac. (This information is tabu-lated at hourly intervals and interpolation can be carried out by allowing 1 deg for every 4 min of time.)

(2) Manually set the longitude reference pointer to the appropriate angle on the fixed scale for GHA of Aries.
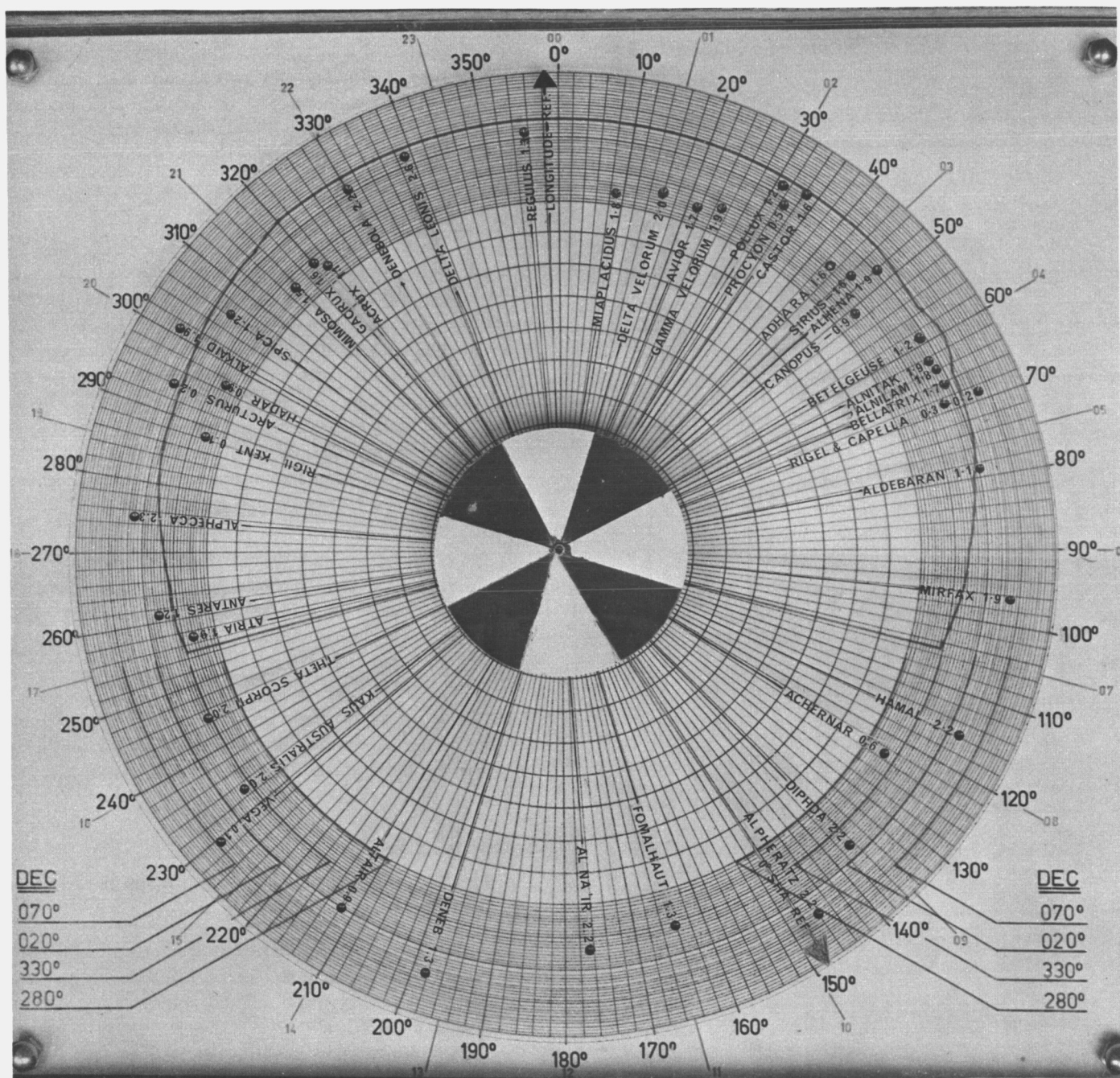
Fig. 9. Star clock—front face closeup

(3) The stars within the field enclosed by the LHA limits and the horizon mask are now obvious, and their LHA's may be read from the outer scale.

(4) The 0 deg SHA reference will indicate sidereal time (see d. below).

(5) The clock mechanisms will maintain the correct relationship with an error of approximately 1 deg in 24 hr.

b. To determine the rise or set time of a particular star.

(1) Rotate the inner disc using the manual adjusting knob until the selected star crosses the appropriate horizon or meridian.

(2) Read off the GHA of Aries against the longitude reference pointer.

(3) Consult the Nautical Almanac for the time corresponding to the GHA of Aries read off. This is the time of the horizon or meridian crossing.

c. To determine the LHA of the Moon, Sun or planets (Fig. 9).

(1) Determine the GHA for the appropriate time of the body in question from the Nautical Almanac.

(2) Manually set the longitude reference pointing to the appropriate angle for the GHA of the body.

(3) Read off the LHA of the body against the 0 deg SHA reference.

(4) The clock mechanism will retain this relationship for a period of hours.

d. To read sidereal time.

(1) Determine the GHA of Aries for the current time from the Nautical Almanac.

(2) Set the longitude reference pointer to the appropriate angle for GHA of Aries.

(3) Read off the sidereal time against the 0 deg SHA reference pointer. This relationship will be maintained with an error of 4 min per 24 hr.

5. Errors

Because a solar time clock mechanism is used, there is an error of 1 deg in angle or 4 min in time every 24 hr. This is not considered serious as the scale can only be read to an accuracy of about 1 deg, and a star tracking program is unlikely to last longer than about 12 hr. The clock can be readjusted manually prior to the start of each program. However, if it is desired to reduce this error it is suggested that a clockwork mechanism might be used which could be regulated to lose 4 min per day.

6. Conclusion

It is felt that this is an extremely useful device to assist in the selection of suitable stars for tracking. It gives a rough position for the stars which helps to eliminate any gross errors from precise calculations. It is extremely simple to use and to fabricate, and should be of benefit to all stations in the DSN as well as to similar agencies.

N67 - 25066

VI. Operations Programming

A. SFOF Conversion Project: *Surveyor* and *Lunar Orbiter* Mission-Dependent Software, H. W. Alcorn

1. Introduction

The implementation of the software system for the *Lunar Orbiter* and *Surveyor* projects was reported in SPS 37-43, Vol. III, p. 131. It is the purpose of this article to report the present status of this conversion effort.

2. Surveyor Software System

The development of the mission dependent programming task has accomplished all scheduled milestones. The system has undergone rigid testing with simulated data inputs from the telemetry processing station and the communication processing station. These data have simulated transmission from the various DSS stations. The simulated tests have served to verify the congruity of the mission-independent/mission-dependent interface. Minor program errors have been isolated and corrected within the *Surveyor* mission-dependent programs. The input/output interfaces have been exercised and verified against the *Surveyor* request for proposal. The overall result of this phase of testing has increased the confidence level of the *Surveyor* software system.

The next phase of development is acceptance testing, which will cover a 1½ mo period. During this period the software system will be certified and accepted by the *Surveyor* project. Upon certification and acceptance the entire software system will be declared operational and released to the *Surveyor* project for mission operations testing.

The final phase of development will be the publication of the final documentation. The documentation package will consist of a compilation of all documents published during the development of the task (updated where necessary), program listings, and final flowcharts of the individual programs.

3. Lunar Orbiter Software System

This task has been officially cancelled by NASA[1]. The results of the development prior to the official cancellation have been documented[2].

---

[1]TWX TN 406 from H. R. Brockett to W. H. Bayley, Jan. 25, 1967.
[2]W. Walker, *Preliminary Lunar Orbiter Software Design for SFOF 7044 Redesign*, Jet Propulsion Laboratory, Pasadena, Calif., Dec. 12, 1966.

B. Computer Programming Technology, W. Thomas

1. Introduction

A research effort was initiated in 1966 in the application of advanced programming techniques to flight operations data handling problems. A principal area of investigation has been the improvement of telemetry data recovery methods. The initial approach to this problem dealt with refinement of pulse code modulation (PCM) telemetry frame synchronization techniques. Data pattern recognition techniques were employed in a frame synchronization algorithm which enabled more timely and efficient recovery of data. A generalized serial bit manipulation programming technique evolved from these studies and was reported in SPS 37-43, Vol. III, p. 146.

2. Current Approach to Data Recovery

Efficient recovery of telemetry data is strongly dependent upon the integrity of the reconstructed (demodulated) PCM serial bit stream. A method has been developed which effectively combines the functions of frame synchronization and demodulation of phase shift keyed PCM telemetry data. A digital computer program has been written which achieves coherency (lock) by utilizing a known pattern within the data stream which was intended for frame synchronization of the demodulated bit stream.

Historically, the first work and demonstration of results of demodulation of telemetry data by digital programming methods, using a different algorithm, evolved from a communications research and development task conducted by Dr. R. Goldstein and G. A. Morris. This work is not yet reported.

3. Characteristics of the Method

The procedure, combining the functions of demodulation and frame synchronization, has the following unique attributes:

(1) Coherency is not dependent upon the signal to noise ratio of the signal.

(2) Optimum frame synchronization is established during the demodulation process; this simplifies the task of data decommutation.

(3) After establishing initial lock with the data, the procedure will track variations of the data subcarrier with little additional effort.

(4) Multiplication or divide hardware is not required of the computer performing the algorithm.

(5) The inherent modularity of the algorithm makes it practical to share, if required, the total computational load of the procedure between several computers or special hardware.

If the numerical value from which bit decisions are made is recorded, the following data processing operations are feasible:

(1) Optimum determination of subcommutation sync using block code type cross correlation methods.

(2) Statistically controlled merging of overlapped tracking data streams to produce a composite output more reliable than any of the single data inputs.

4. Method

The algorithm consists of a two dimensional matrix of demodulators (Fig. 1) each having an Earth reference input of $4fs$, which is slightly different in phase from the others. Additionally, each of the demodulators will have a slightly different limit of integration, though the duration of integration will be the same for all.

One of these demodulators will be nearly coherent with the data stream, and may be detected as follows:

$$IB_{kk}^{\alpha,\phi} = Y_L^{\alpha,\phi} + IB_{kk}^{\alpha,\phi}$$

where

$L = $ bit index $L = 0, 1, \cdots n$

α is the index of variation for the limits of integration

ϕ is the index of variation for phase angles

$kk = 1 + (L \text{ modulo } m)$

$m = $ number of bits in a frame (For *Mariner IV* Mode II, $m = 420$)

$n = nn \cdot m - 1$

$nn = $ number of frame-wise summations needed

$Y = $ value of integrand (See Fig. 1).

Then

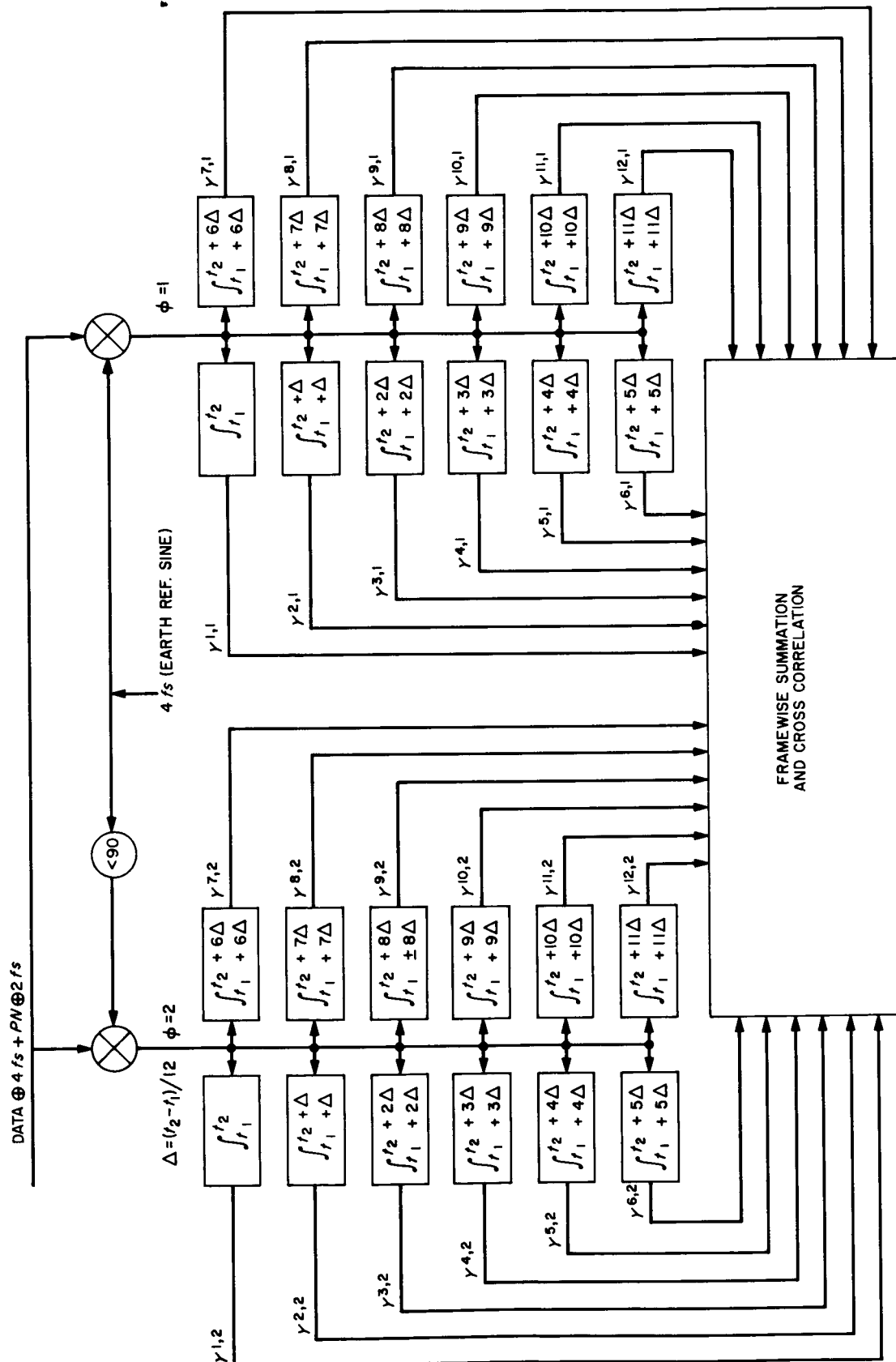$$C_j^{\alpha,\phi} = \sum_{i=1}^{m} IB_k^{\alpha,\phi} \cdot IP_i$$

Fig. 1. Demodulator matrix

where

$$j = 0, 1, 2, \cdots (m - 1)$$

$$k = j + i \text{ for } j + i \leqq m$$

$$k = j + i - m \text{ for } j + i > m$$

$IP_i = +1$ if bit i of the frame is a known one bit

$\quad = -1$ if bit i of the frame is a known zero bit

$\quad = 0$ if bit i of the frame is unknown.

The $C_j^{\alpha, \phi}$ with the largest magnitude determines which of the demodulators is most nearly coherent. The α index of this coefficient is defined as αm and the j index of this coefficient defined as jm. In addition, jm determines frame synchronization of the bit stream.

The size of this two dimensional array of demodulators is determined by the maximum signal to noise degradation acceptable as a result of this approach. In the computer program operating on the IBM 7094, $\alpha = 1, 2, \cdots 12$, which results in a maximum degradation of 0.73 db.

Only two variations of the $4fs$ are required since $Y^{\alpha m, 1}$ and $Y^{\alpha m, 2}$ can be combined to produce a single output which has an optimum signal to noise ratio. These two variations are combined as follows:

$$I3 = \text{SIGN} (MFX_1) \cdot Y^{\alpha m, 1} \cdot | MFX_1 / MFX_2 |$$
$$+ \text{SIGN} (MFX_2) \cdot Y^{\alpha m, 2}$$

where

$$MFX_1 = \sum_{L=0}^{n} Y_L^{\alpha m, 1} \cdot P_L$$

$$MFX_2 = \sum_{L=0}^{n} Y_L^{\alpha m, 2} \cdot P_L$$

$\quad P_L$ is $+1$ if bit$_L$ sent is a zero

$\quad P_L$ is -1 if bit$_L$ sent is a zero

$\quad P_L$ is 0 if bit$_L$ sent is unknown

In fact

$$MFX_1 = C_{jm}^{\alpha m, 1}$$

$$MFX_2 = C_{jm}^{\alpha m, 2}$$

Once MFX_1, MFX_2, and αm have been determined, as specified above, the bit decisions (data reconstruction) can be made based upon the sign of $I3$; $+ I3$ is a one, $- I3$ is a zero.

As the demodulation process is performed, new values of MFX_1, MFX_2, and αm are computed via a computationally simpler algorithm[3].

Often during a mission several stations are able to track a spacecraft at the same time. If the corresponding digital values of "$I3$" for two overlapping data streams are added as follows, up to a 3-db improvement in the signal to noise ratio is possible (SPS 37-36, Vol. IV),

$$S_L = k \cdot I3_L^1 + I3_L^2$$

To optimize the signal to noise ratio of S, k is determined as follows:

$$k = (\sigma_2^2 \cdot u_1) / (\sigma_1^2 \cdot u_2)$$

where σ_2, u_2, σ_1 and u_1 are computed from the $I3$'s[3].

Since the $I3^1$ and $I3^2$ are grouped independently into frames, the time mass reference tolerance required to perform station summation is $\pm$ one quarter of a frame time (for the 8⅓ bit rate this is 12 sec). At present, the time accuracy of an analog tape recorded at a DSS is ± 12 msec.

---

[3] For a complete description of the algorithm, see W. J. Thomas, *Digital Demodulator Program*, EPD 315-R-13, Jet Propulsion Laboratory, Pasadena, Calif.